ABSTRACT

Title of Thesis: COMPUTATIONAL FLUID DYNAMICS SIMULATIONS OF A PIPELINE ROTOR-STATOR MIXER

Author: Benjamin A. Minnick
Master of Science, 2017

Directed by: Professor Richard V. Calabrese
Department of Chemical and Biomolecular Engineering

Rotor-stator mixers provide high deformation rates to a limited volume, resulting in intensive mixing, milling, and/or dispersion/emulsification. CFD simulations of mixers provide flow field information that benefit designers and end users. This thesis focuses on transient three-dimensional simulations of the Greerco pipeline mixer, using ANSYS FLUENT. The modeled unit consists of two conical rotor-stator stages aligned for axial discharge flow. Flow and turbulence quantities are studied on a per stator slot and per rotor stage basis. Comparisons are made between the LES and RANS realizable k-ε model predictions at various mesh resolutions. Both simulations predict similar mean velocity, flow rate, and torque profiles. However, prediction of deformation rates and turbulence quantities, such as turbulent kinetic energy and its production and dissipation rates, show strong dependencies on mesh resolution and simulation method. The effect of operating conditions on power draw, throughput, and other quantities of practical utility are also discussed.

COMPUTATIONAL FLUID DYNAMICS SIMULATIONS OF A PIPELINE ROTOR-STATOR MIXER

By

Benjamin A. Minnick

Thesis submitted to the Faculty of the Graduate School of the
University of Maryland, College Park in partial fulfillment
of the requirements for the degree of
Master of Science
2017

Advisory Committee:
Professor Richard V. Calabrese, Chair
Professor Jeffery Klauda
Professor Kyu Yong Choi
Professor Johan Larsson

Acknowledgements

First I would like to thank Chemineer at the National Oilwell Varco (NOV) who provided the standard SCIS text (SAT) file containing information on the Greerco pipeline mixer geometry. A special thanks to Robert Strong and Eric Janz at NOV for their support and high performance computing cluster (HPCC) time.

I would also like to acknowledge the Deep Thought HPCC available on the University of Maryland campus: “The authors acknowledge the University of Maryland supercomputing resources (http://www.it.umd.edu/hpcc) made available for conducting the research reported in this paper.”

I am also grateful for the advice and support from my lab members, Kanan Ghaderzadeh, Derrick Ko, and Jung Kim. Their assistance at the beginning of this project in the development and study of a coarse tetrahedral for the Greerco pipeline mixer was instrumental in my research and later work.

Of course, a special thanks to Dr. Richard V. Calabrese for the opportunities he has provided me. Thank you for teaching me fluid mechanics and turbulence both as a professor and as an advisor.

And finally, last but by no means least, I am grateful for my friends and family for their encouragement and emotional support throughout this endeavor. To my mother and father. Whom without your mentorship none of this would be possible. To my girlfriend, Kayla, for her never-ending encouragement and trust.

Table of Contents

List of Tables

List of Figures

List of Symbols and Abbreviations

Symbols:

$A\ (m^2)$	Area
$a_{ij}\ (m^2/s^2)$	Anisotropy Tensor
$b_{ij}\ (-)$	Normalized Anisotropy Tensor
C	Coefficient
$D\ (m)$	Rotor Diameter
E	Error
$F\ (kg\ m\ s^{-2})$	Force
G	Generation Term
G_k	Turbulent Kinetic Energy Production Rate
$g\ (m\ s^{-2})$	Acceleration due to Gravity
J	Flux
$K\ (m^2\ s^{-2})$	Total Kinetic Energy
$k\ (m^2\ s^{-2})$	Turbulent Kinetic Energy
$L\ (m)$	Characteristic Length
$l\ (m)$	Mixing Length
M	Integer Value
$N\ (s^{-1})$	Rotor Speed
$N_{Po}\ (-)$	Power Number
$N_Q\ (-)$	Flow Number
$N_{sh}\ (-)$	Shearing Number
$P\ (Pa)$	Instantaneous Pressure
$p\ (Pa)$	Fluctuating Pressure
$Po\ (W)$	Power
$Q\ (m^3 s^{-1})$	Flow Rate
$Re\ (-)$	Reynolds Number
$r\ (m^2\ s^{-3})$	Residual Energy Rate
$r\ (m)$	Radius, Moment Arm
S	Source Term
$S_{ij}\ (s^{-1})$	Strain Rate Tensor
$T\ (Nm)$	Torque
$T_j\ (m^3\ s^{-3})$	Turbulent Kinetic Energy Flux
$t\ (s)$	Time
$U_i\ (m\ s^{-1})$	Instantaneous Velocity
$u_i\ (m\ s^{-1})$	Fluctuating Velocity
$V\ (m^3)$	Volume
$W\ (J)$	Work
$w\ (m)$	Shear Gap Width
$x_j\ (m)$	Position
$y\ (m)$	Vertical Distance

Greek Letters:

Γ	Filter Kernel
Δ	Deviation
δ_{ij} *(m)*	Kronecker Delta
ϵ *(m^2 s^{-3})*	Turbulent Energy Dissipation Rate
ε_{ijk} *(-)*	Permutation Operator
ζ *(Pa s)*	Dilatational Viscosity
θ *(degrees)*	Angle, Rotor Position
κ *(m^{-1})*	Wave Number
μ *(Pa s)*	Viscosity
ν *(m^2 s^{-1})*	Kinematic Viscosity
ν_t *(m^2 s^{-1})*	Turbulent Eddy Viscosity
ν_t^s *(m^2 s^{-1})*	Subgrid-Scale Eddy Viscosity
ρ *(kg m^{-3})*	Density
σ *(-)*	Viscosity Ratio
τ_{ij} *(Pa)*	Stress Tensor
τ_{ij}^s (m^2 s^{-2})	Subgrid-Scale Stress Tensor
φ	General Flow Variable
Ω_{ij} *(s^{-1})*	Vorticity Tensor
ω *(rad/s)*	Angular Velocity

Abbreviations:

CFD	Computational Fluid Dynamics
CFL	Courant-Friedrichs-Lewy
DES	Detached Eddy Simulation
DNS	Direct Numerical Simulation
Hex	Hexahedral
HPCC	High Performance Computing Cluster
LDA	Laser Doppler Anemometry
LES	Large Eddy Simulation
LHS	Left Hand Side
NOV	National Oilwell Varco
PIV	Particle Image Velocimetry
PS	Primary Slot
RANS	Reynolds-Averaged Navier-Stokes
RHS	Right Hand Side
RNG	Renormalization Group
RSM	Reynolds Stress Model
SA	Spalart-Allmaras
SGS	Subgrid-Scale
SIS	Secondary Inner Slot
SMS	Secondary Middle Slot
SOS	Secondary Outer Slot
Tet	Tetrahedral
WALE	Wall-Adapting Local Eddy

1 Introduction

1.1 Rotor-Stator Mixers

Rotor-stator mixers have industrial applications in a variety of fields, including chemical pharmaceutical, biochemical, and food processing industries. They are commonly used in high intensity processing such as dispersion, grinding, chemical reactions, and even cell disruption. A feature that distinguishes rotor-stator mixers from other mixing devices is the intensity of mixing in the relatively small gap region between the rotor and stator pieces known as the *shear gap* [1]. Large deformation and local turbulent energy dissipation rates develop as a result. Another feature of these rotor-stator mixers is their ability to be used for inline processing with high throughput.

Rotor-stator mixers can differ in geometry and operating conditions. These different configurations can result in different throughputs, power requirements, and deformation rates. For a given stage (one rotor and one stator), rotor-stator mixers are classified by the direction the flow moves away from the rotor blade. Radial discharge impellers have the rotor set within the stator which has slots directed radially outwards. An axial discharge impeller, as the one discussed in this thesis, has stator slots directing the flow further downstream. Additional stages, consisting of another rotor-stator set, can be included in these devices to improve mixing further. Operating conditions that are typically varied are rotor speed and/or pressure loss/gain across the mixer.

Those that design and use rotor-stator mixers are interested in certain properties, such as throughput and power requirements. A mixer with high power draw will have high intensity of mixing and a large range of scales important for mixing. There are several methods employed to quantify these metrics. Torque measurements on the shaft can be used to quantify power draw. Experimental methods such as particle image velocimetry (PIV) or laser Doppler anemometry

(LDA) resolve the flow field within the mixer. Computational fluid dynamics (CFD) is another method which solves a set of governing equations that model the flow field.

1.2 Problem Statement

The Reynolds-averaged Navier-Stokes (RANS) equations provide information about the time-averaged flow field. These equations have been solved using CFD methods and have been applied to various rotor-stator mixers. Although the mean velocity field is of interest, it does not readily provide information regarding the fluctuations observed in turbulent flow. The RANS equations also provide estimates to turbulent quantities which are based on the fluctuating velocity field, but these estimates are governed by assumptions are arguably inaccurate.

Large eddy simulations (LES) which filter the larger scales in turbulent flow, describe a resolved velocity field which contains a fluctuating component. The filtered Navier-Stokes equations have also been solved using CFD methods but, to the author's knowledge, have yet to be applied to axial-discharge rotor-stator mixers. Since turbulent fluctuations are simulated in a LES, no assumptions are made to relate the mean quantities to the fluctuating component as observed for RANS simulations. This is thought to make a LES model more rigorous than a RANS model. The computational effort required by a LES is too expensive to be used routinely in industry, however as computing speeds increase, LES will likely become the standard model for CFD methods.

1.3 Scope of Current Project

In this work, the desired flow characteristics and scales of turbulence in mixing are estimated by solving both the RANS and filtered Navier-Stokes equations for an axial-discharge rotor-stator mixer. The modeled unit, the Chemineer Greerco pilot-scale tandem shear pipeline mixer, is simulated using ANSYS FLUENT. This project attempts to:

- Investigate time averaged mean fluid flow behavior in rotor and stator regions by solving the RANS equations.
- Describe level of spatial resolution required by LES to provide an adequate representation of mixer performance.
- Compare slot flow rate and torque time profiles of the modeled mixer as predicted by RANS and LES at different backpressures.
- Compare turbulent statistics predicted by RANS and LES in various regions of interest.
- Investigate the adequacy of the modeling assumptions made in the RANS equations using LES predictions.

1.4 Layout of Thesis

The first chapter introduces the topic, describes how the problem of this current study relates, and the general approach taken to solve this problem. Chapter 2 provides dimensions of the studied rotor-stator mixer and relevant operating scenarios. Simulating this mixer in ANSYS FLUENT is also described in chapter two. Chapter 3 reviews metrics for rotor-stator mixers, the RANS and filtered equations, and concludes with the finite volume equations and methods of convergence necessary to simulate flow within a rotor-stator mixer using ANSYS FLUENT. Chapter 4 discusses literature results from stirred tank and rotor-stator simulations. These simulations provide perspective when studying the flow within the Chemineer Greerco pilot-scale tandem shear pipeline mixer. Proceeding the theoretical discussion and review, chapter 5 and 6 present results from the RANS and large eddy simulations respectively. The results shown include the average and instantaneous velocity field, flow rate, and power draw. Results from RANS are

compared to statistics computed by LES in chapter 7. This thesis concludes with a discussion of important results and future work.

2 Mixer Geometry and Simulation Components

Provided in this chapter is a description of the mixer discussed in this work. Before presenting results of the simulation it is important to understand the geometry, the naming convention used throughout this review, and operating scenarios of interest. Computational considerations are also presented in this chapter. Such considerations are the separation of fluid zones, the mesh used for the simulations, the boundary conditions imposed, and the specifications of the machine used to perform the calculations.

2.1 Mixer Geometry

The Chemineer Greerco "4-inch" tandem shear pipeline mixer is a two-stage inline rotor- stator mixer. Starting from the inlet, the flow moves into the primary stage, then the final secondary stage, then discharged to the volute and outlet pipe. This overall flow is summarized in Figure 2.1 below.

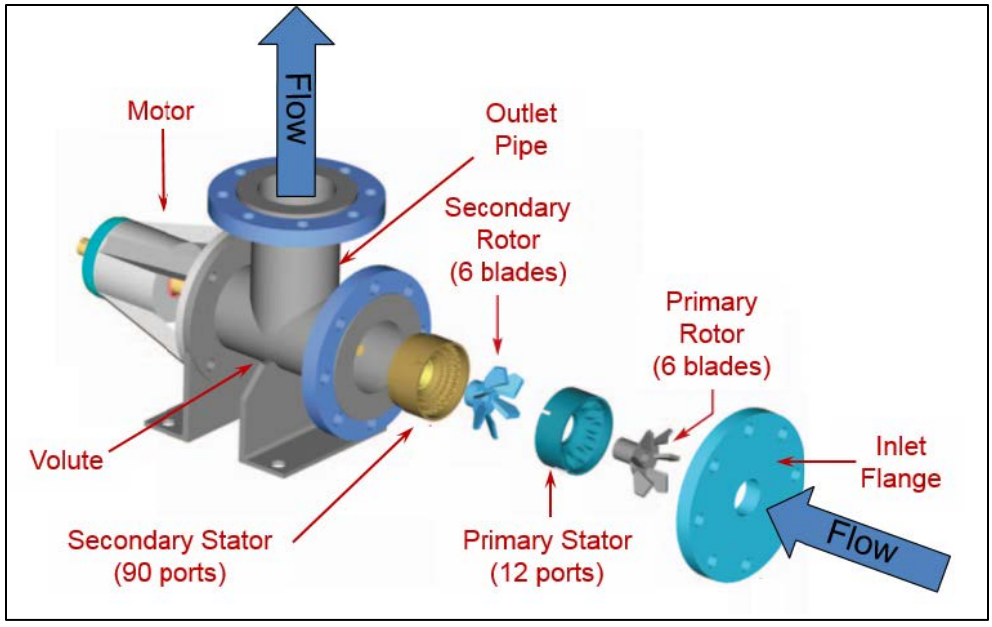

Figure 2.1 – Flow schematic of the Greerco pipeline mixer.

The inlet pipe is concentric to the mixer, however the outlet pipe is perpendicular to this centerline. It is convenient to place the cylindrical coordinate system on this centerline at the entrance of the inlet with the z-axis in the direction of flow. The primary stage involves a rotor with 6 pitched blades and a stator with 12 slanted cylinders as stator slots. The secondary stage involves a rotor geometrically similar to the primary rotor and the secondary stator involves 90 slots. Although the secondary rotor is similar to the primary rotor in regard to shape and number of blades, it is offset by 24 degrees from the primary rotor. These 90 slots are cylindrical, however not slanted as in the primary stage. Of the 90 secondary stator slots, there are 3 rows, each row containing 30 slots. With 6 blades in both rotors, there are 6 rotor periods with each complete rotor revolution. The rotors rotate counterclockwise around the z-axis. Without the outlet pipe, the mixer would be symmetrical in 6 parts. By design of the rotor blades, the shear gap between the rotor and stator is conical in shape. Some quantitative characteristics of the mixer geometry are presented in table 2.1 below.

Table 2.1 – Characteristic dimensions of the Greerco pipeline mixer.

Component	Characteristic	Value
Inlet	Diameter	61.5 mm
Outlet	Diameter	78.0 mm
Primary and Secondary Rotor	Outer Diameter	96.6 mm
Primary Stator Slot	Base Diameter	16.3 mm
Secondary Stator Outer Slot	Diameter	7.14 mm
Secondary Stator Middle Slot	Diameter	5.55 mm
Secondary Stator Inner Slot	Diameter	4.00 mm
Primary and Secondary	Slope (Angle)	1.43 (55.0°)
Shear Gap	Width	0.25 mm

Another view is provided in figure 2.2 below. Provided in this figure are various characteristic dimensions, the coordinate system, and the slot naming convention. The origin is as placed in figure 2.2a, at the inlet flange. The length of the inlet pipe extends beyond the inlet flange

in the negative axial direction. A shortened portion of the inlet and outlet pipes are shown in figure 2.2a.

The rotors rotate in the positive angular direction which is counter clockwise and indicated by the “rotation” arrow in figure 2.2. The slot naming convention is used to distinguish the stator slots. The slot to the direct left of the slot at $\theta = 0°$ in the primary stator (figure 2.2b) is named “PS1”. The naming convention continues in the positive angular direction. Concentric rows of the secondary stator will be referred to as inner, middle, and outer row, for increasing radial positions respectively. A *column of secondary stator slots*, which includes an inner, middle, and an outer slot, will be named “SS”. As an example, the column of secondary stator slots at the $\theta = 0°$ position is “SS30”. The outer slot of column SS30 is named “SOS30”, the middle slot is named “SMS30”, and the inner slot is named “SIS30”. Similar to the primary stator, the naming convention of the secondary stator continues in the positive angular direction. Every other column of secondary stator slots is labeled in figure 2.2c.

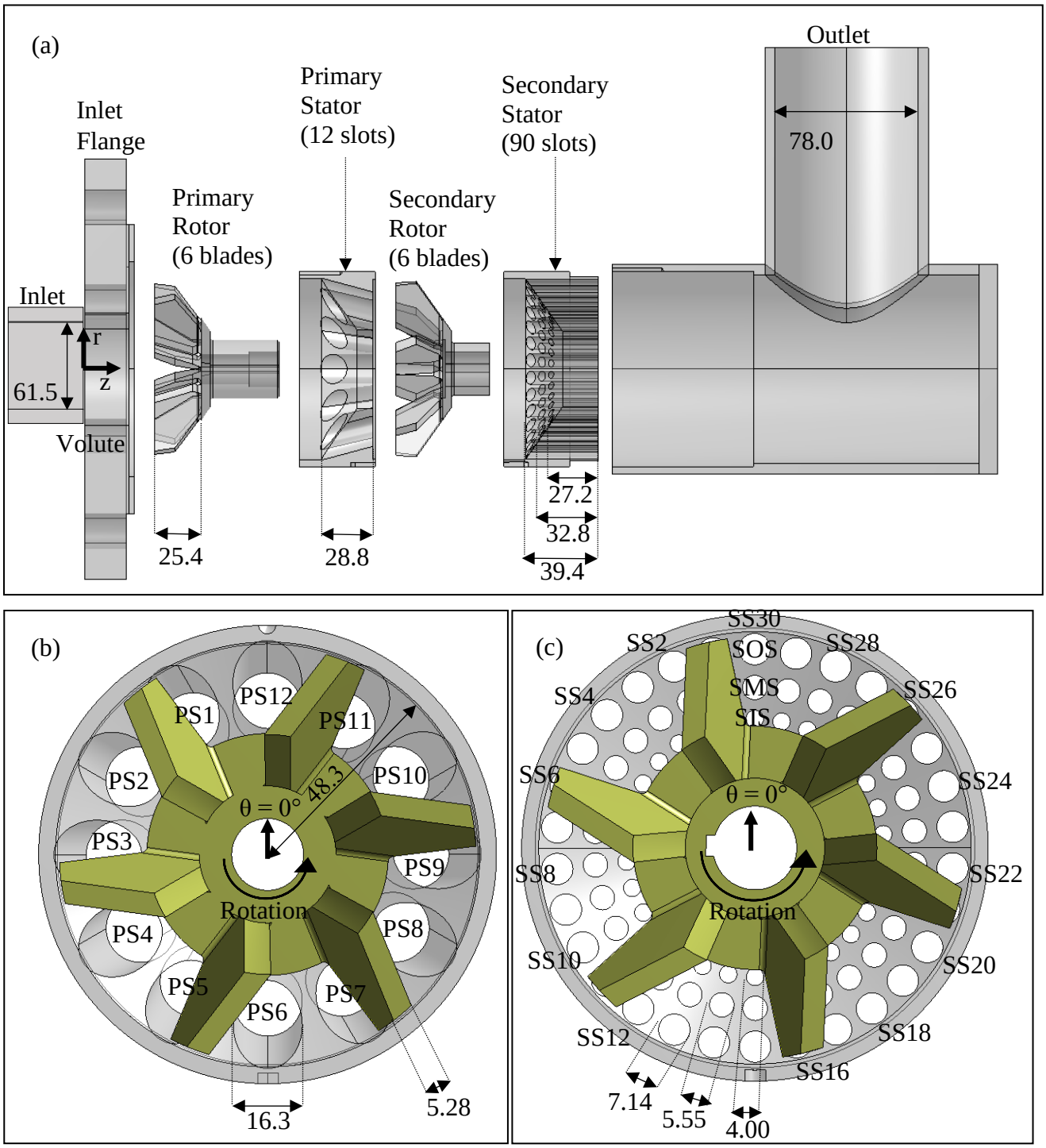

Figure 2.2 – (a) Expanded view of mixer assembly including (b) primary stage and (c) secondary stage. Dimensions in mm.

2.2 Operating Scenarios

As mentioned in the previous chapter, throughput is of interest to the study of flow within inline rotor-stator mixers. Varying pressure across the inlet or outlet planes would alter the throughput within the mixer. Therefore an operating condition to be varied to study the flow within this mixer is the pressure drop across the modeled unit. Due to the pitched rotor blades, this mixer is free pumping and therefore the mixer can operate with no pressure drop or with a given backpressure. Since we are only considering a specified backpressure for this mixer, the pressure drop will instead be defined as the pressure at the outlet minus the pressure at the inlet,

$$\Delta P = P_{outlet} - P_{inlet} \tag{2.3-1}$$

The pressure at the inlet is consistently set at 0-psi, the pressure at the outlet will be varied from 0- psi to 7-psi with 3- and 5- psi as intermediate scenarios. The inlet plane which the 0-psi pressure boundary condition is applied to is not located at the origin, z = 0 mm, but in the negative axial direction at the entrance of the inlet pipe. Another operating condition that is typically varied with rotor-stator mixers is the rotor speed. However for this particular mixer the rotor speed will be kept constant at 3600 rpm (tip speed of 18.2 m/s) for all backpressure scenarios. The working fluid is water (ρ = 998.2 kg/m^3 and $\nu = 1.00 \times 10^{-6}$ m^2/s).

2.3 Fluid Zones and Interfaces

This simulation is comprised of 8 fluid zones, with interfaces placed between each fluid zone. Shown in figure 2.3 is the 8 fluid zones and the location of the interfaces. For this simulation to properly model the rotating and stationary components of this mixer, fluid zones are separated into rotating and stationary zones. Another consideration for separating fluid zones is the ability to control the mesh in a particular area. The shear gap is the location expected to have the highest velocity gradients and so requires a controlled and refined mesh. For this reason, a shear gap fluid

zone is needed to separate the rotor and stator fluid zones. Furthermore, the shear gap fluid zone is subdivided into rotating and stationary fluid zones. A more detailed description of the mesh within the shear gap is described in section 2.5.

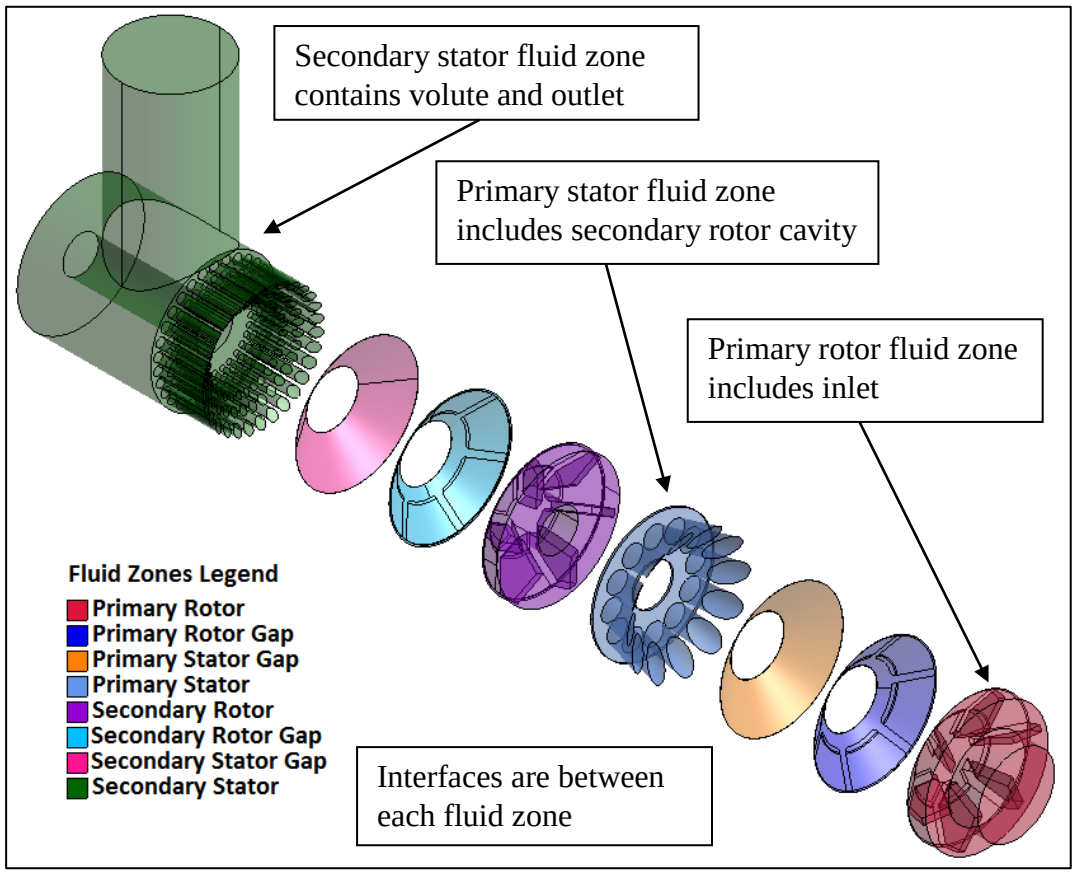

Figure 2.3 – Expanded view of the fluid zones and interfaces of the Greerco mixer simulation.

The primary rotor, primary rotor gap, secondary rotor, and secondary rotor gap are designated as rotating fluid zones in the simulation. The remaining fluid zones (the primary stator gap, primary stator, secondary stator gap, and secondary stator) are stationary fluid zones. The primary rotor fluid zone contains both the inlet pipe and primary rotor. The secondary stator fluid zone contains the secondary stator slots, volute and outlet pipe. It should be noted that both rotating walls and stationary walls can be contained in either a rotating or stationary fluid zone. The wall

will be specified as rotating or stationary as a different input in the simulation. See section 2.7 for more details.

The mesh at the surfaces between fluid zones may not match directly. This is especially true for the interfaces between a rotating and stationary fluid zone where the mesh of the rotating fluid zone rotates with each time step. At these non-conformal interfaces, FLUENT utilizes interpolation methods to move computational quantities from one fluid zone to the next. Another consideration when placing interfaces is computational time. The interpolation method employed by FLUENT becomes more computationally expensive with more interface area.

2.4 Initial Study with Tetrahedral mesh

The mesh of a simulation is a network of cells in which a set of equations, describing desired properties, are solved. There are a variety of ways to generate different types of mesh used for CFD simulations. In this work, the mesh is generated with the software package called ANSYS Workbench Meshing Version 13. ANSYS provides a "push button" mesher which quickly develops a mesh with minimal user inputs. After the push button mesher generates an initial mesh, the user can make edits as needed.

Computational time is dependent on the size of the computational mesh. Although a more refined mesh may provide a more accurate solution, more time is required to provide that solution. Several meshes were developed each with increasing number of cells and increasing manual refinement. A flow field can be initialized from another simulation using an *interpolation* file. This file takes information from the old simulation and fits it to the mesh. If cells of the new mesh are between cells of the old mesh, an interpolation scheme is used to fill that cell with the given flow field information. By initializing the flow field of a new simulation with that of a converged simulation, computational time is greatly reduced.

The initial mesh and preliminary simulations were developed in collaboration with more experienced colleagues. Chemineer provided a SAT file which was then used to develop an ANSYS Design Modeler geometry file of the Greerco mixer geometry. This geometry file described detailed dimensions of the solid parts within the mixer. Once the geometry was imported into ANSYS Design Modeler, the solid parts of the mixer were removed and only fluid volumes remained. The remaining fluid volumes were meshed into a relatively coarse tetrahedral (tet) grid of cells. The tet mesh that was developed with more experienced colleagues (see Acknowledgements) is shown in figure 2.4 below.

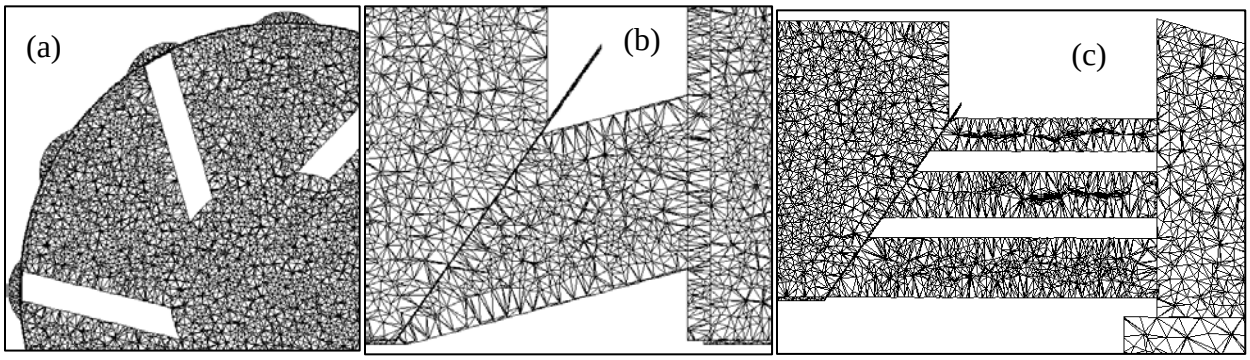

Figure 2.4 – Tetrahedral mesh with approximately 2.5 million cells. Regions shown are the (a) top left quadrant of the primary rotor, (b) primary stage, and (c) secondary stage regions.

This coarse tet mesh contained roughly 2.5 million cells with a varying number of cells across the shear gaps, from 2 to 3. The length of the inlet pipe was 23.9 mm, and the length of the outlet pipe was 127.7 mm. This mesh was developed to initialize the simulation so that the mean velocity field could be interpolated to a more refined hex mesh. Only the RANS equations were solved on this coarse tet mesh. It should be noted that the fluid zones of this tet mesh were divided differently than in figure 2.3. This mesh was relatively coarse with few user controls designating the location of computational cells. For this reason, the goal of this mesh was to initialize the RANS flow field,

determine mean flow pattern in the stator slots, and to evaluate mean throughput at different backpressures. This computational mesh was not used to conduct a LES.

2.5 Refined Hexahedral Meshes

Majority of results presented in this work were computed from two computational meshes. The first of these is a hexahedral (hex) mesh with approximately 4.2 million cells, which will be referred to as “hex 4.2M”. This mesh is shown in figure 2.5. This mesh was initialized using an interpolated flow field from the tet mesh with 2.5 million cells discussed in section 2.4. The inlet pipe was extended to the new length of 307.6 mm and the outlet pipe was extended to the new length of 283.5 mm. The purpose of the hex mesh was to quantify the mean velocity gradients in the shear gaps and still capture the macroscopic properties observed in the tet mesh. To describe the velocity field in the shear gap, more user control is required to place cells in that region. For this reason this mesh required more time to develop than the tet mesh.

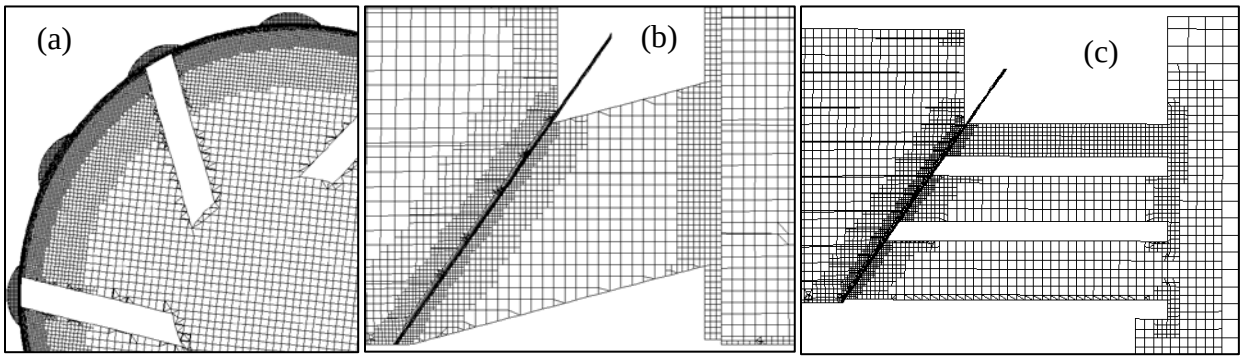

Figure 2.5 – Hexahedral mesh with approximately 4.2 million cells. Regions shown are the (a) top left quadrant of the primary rotor, (b) primary stage, and (c) secondary stage regions.

Succeeding the hex 4.2M mesh was a more refined 20 million hex cell mesh which will be referred to as hex 20M. Both hex 4.2M and hex 20M are used to simulate the mean and filtered flow fields. The controls in this mesh mimicked those in the previous, but with more refinement in the rotor and stator regions, and with a coarser inlet, outlet, and volute regions. A *rotor period*

worth of stator slots (two primary stator slots and 15 secondary stator slots) were further refined. The amount of slots in a period worth of slots for a given stage is the number of slots per rotor blades. The location of these slots is shown in figure 2.7 and the computational mesh in these slots is shown in figure 2.5 below. The hex 20M flow field was initialized from the hex 4.2M simulation.

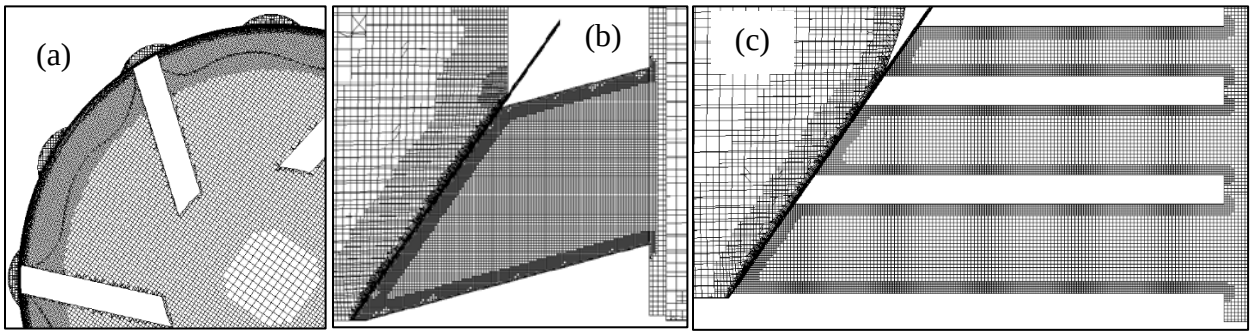

Figure 2.6 – Hexahedral mesh with approximately 20 million cells. Regions shown are the (a) top left quadrant of the primary rotor, (b) primary stage, and (c) secondary stage regions.

Reported in table 2.2 is the average cell density in each zone for the hex 4.2M and 20M computational meshes. This average cell density was calculated by counting the number of cells in that given component and then dividing by the given volume. A higher cell density indicates a more refined volume. The values in the table show that as the mesh progresses the inlet, volute, and outlet become coarser and the rotor and stator regions become more refined. If the cell size was uniform throughout a given volume, then the average cell density would be an exact representation of the number of cells per unit volume. However with inflation and other forms of adaption, the mesh is not uniform. The significant meshing constraints are listed in table 2.3 below. The number of additional cells as a result of the refinement in the period worth of stator slots in the hex 20M mesh is not included in the values provided in table 2.2.

Table 2.2 – Average cell density (number of cells/cm^3) in each computational zone.			
Component	Volume (cm^3)	Hex 4.2M	Hex 20M
Inlet	910	400	60
Primary Rotor	160	4800	12000
Primary Stator Slots	53	9500	15000
Secondary Rotor	120	8800	14000
Secondary Stator Slots	76	6500	34000
Volute	810	200	400
Outlet	1350	40	16

The average cell density in the shear gap regions is not considered in table 2.2 above. Instead, the number of cells across the shear gap quantify the amount of resolution in the shear gap. Hex 4.2M has six uniform cells across the shear gap and hex 20M has 14 cells across the shear gap. To develop the computational mesh in the shear gap region of hex 20M, adaption was used so that further mesh refinement is present near the rotor and stator wall.

Table 2.3 – Meshing constraints applied for each fluid zone.		
Fluid Zone	Region	Constraint
Inlet	No constraint	NA
Primary Rotor	Wall and interface	Inflation
Primary Rotor Gap	Width	Number of cells
Primary Stator Gap	Width	Number of cells
Primary Stator Slots	Stator slots opening	Area sizing
	Stator slot walls	Inflation
Secondary Rotor	Wall and interface	Inflation
Secondary Rotor Gap	Width	Number of cells
Secondary Stator Gap	Width	Number of cells
Secondary Stator Slots	Stator slots opening	Area sizing
	Stator slot walls	Inflation
Volute	No constraint	NA
Outlet	No constraint	NA

2.6 Sampling Rotor Position

As discussed in the previous section, the final hex 20M computational mesh has a refined rotor period worth of slots. One rotor period worth of slots is two in the primary stator and five rows in the secondary stator. The refined slots are farthest away from the outlet pipe and are the

numbered slots in figure 2.7 below. The position of the rotors relative to the slots in figure 2.7 resemble the rotor position in which some results are shown and compared in later sections. Samples from LES are collected for time-averaging statistics at this rotor position. A RANS simulation models these time-average statistics and are therefore readily available. A LES simulates a fluctuating component which can be removed by averaging across a set of samples. Data planes are presented from each refined slot. Primary slot 6 is considered to be closed as a rotor blade covers a portion of the slot, while primary slot 7 is open. Secondary slot 18 is closed while secondary slots 14 through 17 are open but vary in distance from the blade covering slot 18.

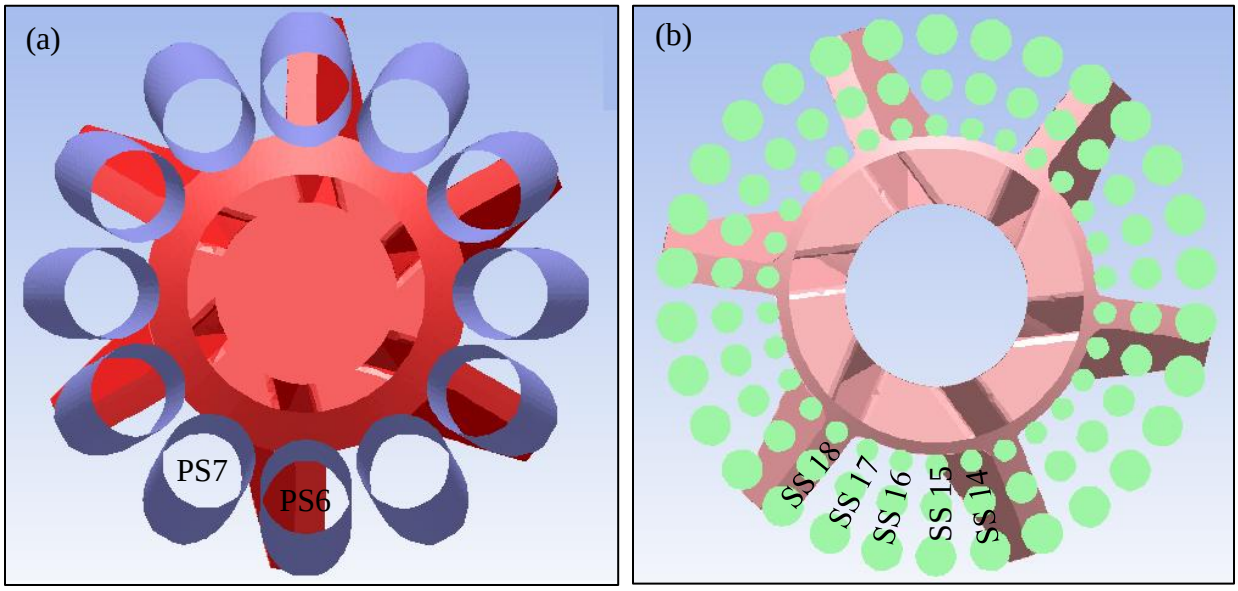

Figure 2.7 – Data plane sampling position for the (a) primary rotor and (b) secondary rotor relative to the corresponding stator pieces. The period of refined mesh slots for the hex 20M simulations is indicated by the slot numbers shown.

2.7 Boundary Conditions

Before initializing the computational model and then running the simulation, boundary conditions are required from which to start the governing equations describing the flow within the fluid zones and across the interfaces. These boundary conditions are needed to reflect the geometry of the mixer, as well as the particular operating scenario. No-slip boundary conditions are specified

at the walls within the mixer. For the rotating parts, including both rotors and the shaft within the volute region, these walls will be specified as rotating at the desired rotor speed of 3600 rpm. In a similar fashion, stationary walls including the stators, inlet and outlet pipe wall, and mixer casing will be specified as stationary walls. A surface describing the inlet and outlet of the mixer was not defined as a wall but instead at a specified pressure given by the particular operating scenario.

2.8 Computer Specifications

Computing resources are an important consideration for CFD simulations. The RAM clock speed and other computer specifications determine the computational time required for the simulation. Two computers, each with 8 processors, were used in a parallel configuration for the work presented in this thesis. Both computers share similar specifications which are summarized in table 2.4 below.

Table 2.4 – Specifications for in house machine used to conduct simulations.

Component	Value
RAM Size	48 GB each
RAM Speed	1066 MHz
Motherboard	Asus Z8PE-D12 Dual LGA1366 Xeon
Workstation	Intel Xeon Quad Core E5520 2.26 GHz 1333 MHz
Operating System	Windows

As stated previously, larger computational meshes require more computational time. A large amount of time is required to simulate flow on the hex 20M mesh on the machines specified in table 2.4. For this reason, high performance computing clusters (HPCC) were used. Two HPCC were used to provide results in this work, the University of Maryland Deep Thought II cluster and the National Oilwell Varco (NOV) cluster (see Acknowledgements). Sixty processors were used on both HPCC. The Intel Xeon E5-2680 v2 processor was used on the Deep Thought II cluster, with a processor speed of 2.80 GHz. The Linux operating system was used on the Deep Thought II cluster.

3 Theoretical Background

This chapter introduces the fundamental concepts of fluid dynamics and turbulence theory necessary for the discussion of flow within rotor-stator mixers. First, metrics that can be easily computed and are commonly used to compare rotor-stator mixers is discussed. Then quantities used to describe the flow and energy dissipated in the mixer is presented. The velocity field, which is necessary to compute these quantities, is presented in the form of conservation equations. As this is a turbulent flow problem, these conservation equations are modeled in a time-averaged sense. After this is discussed, the concept of filtering the conservation equations are presented and then modeled. The discussion that follows involves a description of how these model equations are manipulated into discrete form and thereby implemented into a fluid dynamics solver code. This chapter concludes by discussing the various methods that can be applied to quantify how converged the simulation is and thereby how accurate the results are.

3.1 Rotor-Stator Metrics

There are a variety of rotor-stator mixers with different throughput, power draw, mixing intensity, and other properties. To quantitatively compare these, various metrics have been developed to describe a particular rotor-stator mixer. The most common dimensionless number in fluid mechanics, the *Reynolds number*, Re, can be used as such a metric. This dimensionless quantity is a ratio of inertial and viscous forces and is defined by the kinematic viscosity of the fluid and a characteristic length and velocity (or rotational speed multiplied by the length),

$$Re = \frac{UD}{\nu} \qquad Re = \frac{ND^2}{\nu} \tag{3.1-1}$$

The Reynolds number describes the intensity of the flow and is a common metric to classify the flow regime. At low Reynolds numbers, viscosity dominates, and the flow is classified as laminar. At high Reynolds numbers, inertia dominates, and the flow is classified as turbulent. For flow

through pipes a Reynolds number above 4,000 is considered to be turbulent. For the rotor-stator mixer considered in this thesis, the Reynolds number based on the maximum rotor diameter is Re = 5.6×10^5.

For complicated geometries, as rotor-stator mixers often have, a single Reynolds number is not sufficient to describe the intensity of the flow throughout the entire mixer. Two different expressions of the Reynolds number can be used, one describing flow intensity in a slot and the other in the shear gap. The characteristic length and velocity of these regions in a rotor-stator mixer can be significantly different and therefore provide different Reynolds numbers.

$$Re_{slot} = \frac{U_{slot} D_{slot}}{\nu} = \frac{4Q}{\pi \nu D_{slot}} \qquad Q = U_{slot} A_{slot} = U_{slot} \frac{\pi}{4} {D_{slot}}^2 \tag{3.1-2}$$

$$Re_{gap} = \frac{U_{tip} w}{\nu} = \frac{\pi N D_{rotor} w}{\nu} \qquad U_{tip} = \omega R_{rotor} = \pi N D_{rotor} \tag{3.1-3}$$

The slot Reynolds number uses the average fluid velocity given by the throughput in the slot and the slot diameter as the characteristic velocity and length respectively. The gap Reynolds number uses the speed of the blade tip and the width of the shear gap, *w*. The rotor diameter of the conical rotors in the Greerco pipeline mixer changes in the axial direction. The tip speed therefore changes in the axial direction. In this thesis, the maximum rotor diameter is used in equation 3.1-3.

As indicated by the slot Reynolds number, throughput (or flow rate) is another important metric for rotor-stator mixers. This quantity can be nondimensionalized by the speed and diameter of the rotor. This quantity is termed the flow number and is expressed as by equation 3.1-4. The

$$N_Q = \frac{Q}{N D_{rotor}^3} = \left(\frac{\pi D_{slot}}{2 D_{rotor}}\right)^2 \frac{1}{N_{sh}} \qquad N_{sh} = \frac{U_{tip}}{U_{slot}} \tag{3.1-4}$$

which is a ratio of throughput in the mixer and speed of the rotor. It should be noted that the flow number can be expressed as the inverse of the shearing number and a ratio of slot and rotor diameter using the conversions expressed in equations 3.1-2 and 3.1-3 above. The shearing

number, ratio of rotor tip speed and slot velocity, is another metric commonly used for rotor-stator mixers. It can be further shown that the shearing number, and by extension the flow number, can be written as a ratio of the slot and gap Reynolds number.

To spin the rotor, a torque is applied which requires power. This power requirement is another characteristic metric for rotor-stator mixers. Similar to the flow number, the power can be nondimensionalized by the dimensions of the rotor and properties of the flow [1],

$$N_{Po} = \frac{Po}{\rho N^3 D_{rotor}^5} \tag{3.1-5}$$

This dimensionless group describes a ratio between resistance forces and inertial forces. The power to rotate the rotor and shaft can be rewritten in terms of torque. Taking the centerline of the mixer as the axis of rotation, any forces acting on a rotating wall provide a moment. The sum of these moments is the rotor torque, T. To convert rotor torque to power we take the scalar product of the torque and rotational speed, which amounts to multiplying the magnitude of both since these vectors act in the same direction,

$$Po = \boldsymbol{\omega} \cdot \boldsymbol{T} = 2\pi N \|\boldsymbol{T}\| \tag{3.1-6}$$

By Newton's third law of motion, there is an equal and opposite reaction force to the force exerted by the fluid on the rotating walls. This reaction force describes the torque applied from a motor to the rotor. Therefore equation 3.1-6 can be used to describe the power requirement to the rotor-stator mixer.

The force exerted by the fluid on the rotating walls can be decomposed into pressure and viscous force terms. The moment of both these forces contributes to the torque applied to the rotor. However in this work the viscous force is negligible (less than 2% of the total force), and is therefore not discussed in this section although is included in the total torque presented in the results sections. The pressure force can be computed by integrating the fluid pressure across the

surface of the rotating walls. The torque is then computed by taking the cross product of this force with the moment arm [2]. This formulation is shown in the equation below.

$$\boldsymbol{T} = \boldsymbol{r} \times \boldsymbol{F}_P = \boldsymbol{r} \times \iint_A P \, d\boldsymbol{A} \approx \boldsymbol{r} \times \sum_{\forall cells} P_i \cdot \boldsymbol{A}_i \tag{3.1-7}$$

Where the moment arm is given by the vector r and the area term is treated a vector normal to the surface being integrated. This work involves discretizing the fluid volume into cells, and so the surface integral is approximated by the sum of discrete pressure forces.

3.2 Throughput and Flow Work

In the previous section the throughput was expressed as a characteristic velocity times the cross-sectional area through which the fluid traveled. This simple expression is useful when describing rotor-stator metrics, but a more rigorous expression should be used to quantify the flow rate in a rotor-stator mixer. The flow rate can be mathematically expressed as the surface integral of the velocity [2],

$$Q = \iint_A \boldsymbol{U} \cdot d\boldsymbol{A} \approx \sum_{\forall cells} \boldsymbol{U}_i \cdot \boldsymbol{A}_i \tag{3.2-1}$$

Similar to equation 3.1-7, the surface integral can be discretized. The flow rate can therefore be approximated by the sum of discrete cell flow rates. The discrete cell flow rate is expressed as the cell velocity multiplied by the surface area of the cell side whose normal vector is in the direction of the velocity.

Throughput can be used further to quantify the *flow work* within the rotor-stator mixer. Flow work describes the energy required to push the fluid into or out of the device. Since this is a transient system, this energy requirement will be expressed as a power,

$$Po_{flow} = \frac{dW_{flow}}{dt} = \frac{d}{dt}[V(P_2 - P_1)] = Q(P_2 - P_1) \tag{3.2-2}$$

where we have assumed that the pressure drop is constant with time. Another work term that can be described by throughput is the *work due to acceleration*. This term describes how much the flow has accelerated between the inlet and outlet. Again we express this in terms of power,

$$Po_{accel} = \frac{dW_{accel}}{dt} = \frac{d}{dt}[\rho V(U_2^2 - U_1^2)] = \rho Q(U_2^2 - U_1^2) \tag{3.2-3}$$

where we have assumed that density and average inlet/outlet velocity are constant in time. It should be noted that subscript 2 denotes the outlet and subscript 1 denotes the inlet for the pressure drop and change in velocity. The rate of flow work and rate of work due to acceleration can be a significant power requirement for rotor-stator mixers.

3.3 Discrete Fourier Transform

Flow rate and torque, given by equations 3.2-1 and 3.1-7 respectively, in a rotor-stator mixer can show cyclic behavior due to the motion of the rotor blades. Therefore the flow rate and torque time profiles can be expressed as a linear combination of sines and cosines (or complex exponentials). The amplitude and frequency of these time profiles would provide another description of the flow rate and torque in a rotor-stator mixer. To extract this information, the discrete Fourier transform is applied. The discrete Fourier transform is used in this work since a CFD model discretizes flow rate and torque on a time step basis.

Applying the discrete Fourier transform to a signal [3], such as the flow rate or torque, can be expressed as,

$$\Phi_k = \sum_{m=0}^{M-1} \phi_m e^{-2\pi i k \frac{m}{M}} \tag{3.3-1}$$

Where ϕ_m represents the signal with a length of *M* time steps. Although the signal may be in the real domain (as flow rate and torque are real quantities), the transformed signal, Φ_k, can contain both real and imaginary components due to the use of the complex exponential. However in this work, the magnitude of the transformed signal is used. Then by conjugate symmetry, the magnitude of the transformed signal is shown to be symmetrical. For this work, the one-sided spectrum is shown.

To understand the usefulness of this transformed signal, the inverse discrete Fourier transform is shown [3],

$$\phi_m = \frac{1}{N}\sum_{k=0}^{M-1} \Phi_k e^{2\pi i m \frac{k}{M}} \tag{3.3-2}$$

By applying the inverse discrete Fourier transform, the original signal is reconstructed as a linear combination of complex exponentials. The amplitude of a complex exponential with a given frequency is the transformed signal. Therefore, if the magnitude of the transformed signal at a given frequency is larger than at other frequencies, that given frequency is contributes more to the shape of the original signal.

3.4 Velocity Gradients and Energy Dissipation

Fluid velocity describes quantities such as throughput and intensity of mixing. Similarly, spatial changes in fluid velocity describe how energy dissipates and how the fluid element deforms. From a computational perspective, the magnitude of velocity gradients may govern the mesh size since more cells are required to resolve larger gradients. The three velocity components can vary in three directions, therefore all velocity gradients can be expressed as a second order tensor. This tensor can be decomposed into symmetric and antisymmetric components. Einsteinian notation is used to discuss these concepts. This notation is used from section 3.4 to 3.13.

$$\frac{\partial U_i}{\partial x_j} = S_{ij} + \Omega_{ij} \tag{3.4-1}$$

$$S_{ij} = \frac{1}{2}\left[\frac{\partial U_i}{\partial x_j} + \frac{\partial U_j}{\partial x_i}\right] \tag{3.4-2}$$

$$\Omega_{ij} = \frac{1}{2}\left[\frac{\partial U_i}{\partial x_j} - \frac{\partial U_j}{\partial x_i}\right] \tag{3.4-3}$$

where the symmetric component, S_{ij}, is the *strain rate tensor*, and the antisymmetric component, Ω_{ij}, is the *vorticity tensor*. The strain rate tensor describes deformation rates and the vorticity tensor describes rigid-body rotation. Although not a useful quantity to describe mixing, vorticity can be used to describe and model turbulent flow. Mixing occurs by fluid deformation, and by this reasoning, the strain rate tensor is useful to quantify the smallest scales in which mixing occurs.

The strain rate tensor has six unique elements. The three elements along the diagonal, S_{ii}, describe compression or tension of the fluid element. The off-diagonal elements describe shear and angular deformation. These tensor components can be analyzed individually, or expressed as a scalar quantity. A useful measure is the magnitude of the strain rate tensor,

$$\|S_{ij}\| = \sqrt{2S_{ij}S_{ij}} \tag{3.4-4}$$

Another metric is the *nominal shear rate* which is a simplified quantity assuming plane Couette flow in the shear gap. This assumption implies a linear velocity profile between the rotor blade and stator, the gradient of this Couette flow is then expressed as [1],

$$S_{nom} = \frac{U_{tip}}{w} \tag{3.4-5}$$

Measuring the strain rate magnitude and relating it to the nominal shear rate provides a comparison between the observed shear gap velocity profile and the plane Couette velocity profile. As indicated in equation 3.1-3, the tip speed is a function of rotor diameter which changes in the axial

direction for the Greerco pipeline mixer. The nominal shear rate therefore changes relative to the local rotor diameter.

3.5 Conservation Equations

We are interested in the flow behavior of this rotor-stator mixer, therefore our model equations should reflect what we wish to solve for. The motion of fluid particles within the mixer can be modeled with mass and momentum conservation equations. The momentum conservation equation can be thought of as a force balance on a fluid particle [4]. This balance involves the acceleration of the particle, given by the left hand side (LHS) of the second equation and the viscous stress, pressure, and gravity forces on the right hand side (RHS).

$$\frac{\partial \rho}{\partial t} + \frac{\partial (\rho U_i)}{\partial x_i} = 0 \tag{3.5-1}$$

$$\rho \left[\frac{\partial U_i}{\partial t} + U_j \frac{\partial U_i}{\partial x_j} \right] = \frac{\partial \tau_{ij}}{\partial x_j} - \frac{\partial P}{\partial x_i} + \rho g_i \tag{3.5-2}$$

Although FLUENT solves the integral form of these conservation equations, the differential form is conceptually easier to understand and discuss.

These equations can be simplified for the problem we are considering in this work. We consider Newtonian, incompressible flow with constant physical properties. By assuming the flow is incompressible, the time derivative and spatial influence of the density, ρ, in the mass conservation equation can be set to zero. This assumption simplifies the mass conservation equation into the well-known equation of continuity for incompressible flow [4],

$$\frac{\partial U_i}{\partial x_i} = 0 \tag{3.5-3}$$

The momentum conservation equation can also be simplified. By assuming Newtonian flow the viscous stress is proportional to the rate of deformation, and so the stress tensor is written as [4],

$$\tau_{ij} = 2\mu S_{ij} + \left(\zeta - \frac{2}{3}\mu\right)\left(\frac{\partial U_i}{\partial x_i}\right)\delta_{ij} \tag{3.5-4}$$

Newton's law of viscosity can be simplified further before substituting it into the momentum conservation equation. We have previously shown that the continuity equation is valid for our system, so substituting the continuity equation into the second term of Newton's law of viscosity reveals that for an incompressible Newtonian fluid,

$$\tau_{ij} = 2\mu S_{ij} \tag{3.5-5}$$

We now substitute this expression for the stress tensor into the momentum conservation equation. Also, we assume the effects of gravity are negligible and can therefore be removed from the force balance. By these assumptions the momentum conservation equation becomes a simplified version of the Navier-Stokes equations,

$$\frac{\partial U_i}{\partial t} + U_j \frac{\partial U_i}{\partial x_j} = \nu \frac{\partial^2 U_i}{\partial {x_j}^2} - \frac{1}{\rho}\frac{\partial P}{\partial x_i} \tag{3.5-6}$$

It is important to note that the LHS of the Navier-Stokes equations, concerning accumulation, cannot be eliminated because the flow is expected to be turbulent. The diffusion term on the RHS is expected to play an important role near the solid walls of the mixer where the no-slip boundary condition is applied.

We consider the flow within the mixer to be turbulent for various reasons. From experience we expect the high rotor speed and relatively large pipe diameter to produce and maintain turbulence. Not only is this expected, it is necessary for the effective operation of the mixer, turbulence is to be used to mix the flow. For these reasons the computational model should reflect the turbulence within the mixer, this can only occur if the simulation solves a set of equations that describe turbulent behavior. The remainder of this chapter focuses on how the equation of continuity and the Navier-Stokes equations are manipulated to describe turbulence in mixing.

3.6 Reynold's Averaged Navier-Stokes Equations

A simple manipulation of the conservation equations that is still in use today is the process of *Reynolds-averaging*. The first step in this process is to decompose the quantities of interest into its average and fluctuating components [4]. In this work those quantities are the three velocity components and the pressure,

$$U_i = \bar{U}_i + u_i \qquad P = \bar{P} + p \tag{3.6-1}$$

In this thesis, an instantaneous flow variable is denoted by a capital symbol, the mean flow variable has an overbar, and the fluctuating component is denoted by a lowercase symbol. These decompositions are substituted into the governing equations and those equations are then time-averaged. The resulting equations are termed the RANS equations. Performing this procedure on the equation of continuity we obtain,

$$\frac{\partial \bar{U}_i}{\partial x_i} = 0 \tag{3.6-2}$$

Where we have used the fact that the average gradient of the fluctuating velocity approaches zero. The equation of continuity shows that if a term is linear and is time-averaged, a similar expression results but in terms of the average quantity.

We now time-average the Navier-Stokes equations. As with the equation of continuity, any linear term that is time-averaged can quickly be written as its averaged counterpart. This is done for the entire RHS and the time derivative on the LHS. This time-averaging process does not yield a similar conclusion for the convection term on the LHS. Since this term is nonlinear, after substituting the velocity decomposition and averaging across, only some terms are eliminated. An additional term appears which has been moved to the RHS, this term is known as the *Reynold's stress*. Here are the RANS equations [4],

$$\frac{\partial \overline{U}_i}{\partial t} + \overline{U}_j \frac{\partial \overline{U}_i}{\partial x_j} = \nu \frac{\partial^2 \overline{U}_i}{\partial {x_j}^2} - \frac{1}{\rho}\frac{\partial \bar{P}}{\partial x_i} - \frac{\partial \overline{u_i u_j}}{\partial x_j} \tag{3.6-3}$$

The Reynold's stress, $\overline{u_i u_j}$, adds a complication to our mathematical discussion. The RANS equations cannot be solved unless all terms can be evaluated. The average product of two fluctuating velocity components cannot be directly evaluated using mean quantities and so the Reynold's stress is modeled. Using turbulence model equations to describe the Reynold's stress is known as closing the RANS equations.

Several types of RANS closure methods are used in engineering and turbulence applications. The most common are the *turbulent eddy viscosity* closure models. These closures model the Reynold's stress using the Boussinesq approximation, which is similar to the Newton's law of viscosity for the stress tensor shown in equation 3.5-4. This approximation claims that the deviatoric component of the Reynold's stress is proportional to the gradients of the mean velocity [4]. The deviatoric component is defined as the turbulent kinetic energy, $k = \frac{1}{2}\overline{u_i u_i}$, which is discussed in more detail in the next section.

$$\overline{u_i u_j} - \frac{2}{3} k \delta_{ij} = -2\nu_t \bar{S}_{ij} \tag{3.6-4}$$

The constant of proportionality relating the mean velocity gradient to the Reynold's stress tensor is termed the turbulent eddy viscosity, ν_t. For this turbulent model to be used, the turbulent eddy viscosity must be modeled and computed. The LHS of equation 3.6-4 is often referred to as the *anisotropy tensor* and will be denoted a_{ij}. The $\frac{2}{3} k \delta_{ij}$ term can be thought of as an isotropic stress since it is a tensor that contains equal normal components. Therefore by subtracting this term from the Reynold's stress tensor, the remaining stress term involves anisotropy. Since the isotropic stress can be added to the pressure term in equation 3.6-3, only the anisotropic component of the Reynold's stress contributes to the transport of momentum.

3.7 k-ε Closure

One of the most common turbulent eddy viscosity models is the k-ϵ closure which uses conservation equations for the turbulent kinetic energy, k, and turbulent energy dissipation rate, ϵ, to determine the turbulent eddy viscosity. This two equation closure model is used in this work. From a dimensionality perspective, the ratio of turbulent kinetic squared and the turbulent energy dissipation rate results in units of diffusivity [4]. This argument is used to compute the turbulent eddy viscosity as,

$$\nu_t = C_\mu \frac{k^2}{\epsilon} \tag{3.7-1}$$

Where $C_\mu = 0.09$ is a model constant. Although the eddy viscosity is now quantified, the turbulent kinetic energy and energy dissipation rate must be computed. As mentioned previously, this is done using their conservation equations.

In classical physics, kinetic energy is described as mass times velocity squared. In turbulence theory, the turbulent kinetic energy is the sum of the squared velocity fluctuation components, then time-averaged. The turbulent kinetic energy can be described as the intensity of turbulence in the flow. The turbulent kinetic energy is proportional to the sum of the velocity variances. The conservation of this quantity can be derived by manipulating the Navier-Stokes equation, given by equation 3.5-6. Taking the dot product of the Navier-Stokes equation with the velocity gives an expression for total kinetic energy of the flow. Similar to the velocity decomposition used in equation 3.6-1, the total kinetic energy decomposes into the mean kinetic energy and the turbulent kinetic energy,

$$\overline{K} = \frac{1}{2}\overline{U_i^2} = \frac{1}{2}\overline{(\overline{U}_\iota + u_\iota)^2} = \frac{1}{2}\overline{U}_i^{\,2} + \overline{u_\iota^{\,2}} = K_{avg} + k \tag{3.7-2}$$

Where various averaging rules were used to decompose the total kinetic energy in this fashion. This decomposition shows that the turbulent kinetic energy is the total kinetic energy without the mean energy. The total kinetic energy conservation equation is subtracted by the mean kinetic energy conservation equation, which is derived by taking the dot product of the RANS equations (equation 3.6-3) and the mean velocity. This difference gives the conservation equation for the turbulent kinetic energy [4],

$$\frac{\partial k}{\partial t} + \bar{U}_J \frac{\partial k}{\partial x_j} + \frac{\partial}{\partial x_j}\left[T_j - \nu \frac{\partial k}{\partial x_j}\right] = G_k - \epsilon \tag{3.7-3}$$

The first two terms on the LHS describe the accumulation of turbulent kinetic energy. The remaining gradient terms on the LHS represent an energy flux which transports turbulent kinetic energy. Aside from the transport of turbulent kinetic energy by diffusion, the energy flux is given by,

$$T_j = \frac{\overline{u_\iota u_\iota u_J}}{2} + \frac{\overline{p u_J}}{\rho} \tag{3.7-4}$$

which describes the transport of turbulent kinetic energy by velocity and pressure fluctuations. The two terms on the RHS of equation 3.7-3 represent the production and dissipation of turbulent kinetic energy.

To understand the dissipation term in equation 3.7-3, we take the tensor product of the strain rate tensor with itself and then time-average. This tensor product has more properties other than the magnitude of velocity gradients, as shown by equation 3.4-4. Energy is dissipated from friction within the fluid, this is quantified by velocity gradients. It can be shown that after time-averaging the square of the strain rate tensor,

$$2\nu\overline{S_{\iota J} S_{\iota J}} = \nu\left(\frac{\partial \bar{U}_\iota}{\partial x_j}\right)^2 + \epsilon + \nu \frac{\partial \bar{U}_\iota}{\partial x_j}\frac{\partial \bar{U}_j}{\partial x_\iota} + \nu\overline{\frac{\partial u_\iota}{\partial x_j}\frac{\partial u_j}{\partial x_\iota}} \tag{3.7-5}$$

Where the first term on the RHS is termed the mean energy dissipation rate. The second term on the RHS is the turbulent energy dissipation rate [4],

$$\epsilon = \nu \overline{\frac{\partial u_\iota}{\partial x_j} \frac{\partial u_\iota}{\partial x_j}} \tag{3.7-6}$$

The remaining two terms represent the product of cross velocity gradient terms. These terms are zero for homogeneous incompressible flow. The first two terms are commonly expressed in terms of power dissipated into the fluid,

$$Po_{diss} = Po_{mean} + Po_{turb} = \mu \iiint_V \left\| \bar{S}_{ij} \right\|^2 dV + \rho \iiint_V \epsilon \, dV \tag{3.7-7}$$

In rotor-stator mixers, due to the high speed rotor and relatively small shear gap volume, the power dissipated is significantly larger than the flow work and work to accelerate the fluid shown by equations 3.2-2 and 3.2-3, respectively.

Before discussing how the turbulent kinetic energy conservation equation is modeled, we look to the conservation equation for the isotropic dissipation rate. In *homogeneous turbulence*, statistics involving the fluctuating velocity field do not change with position. With this assumption the turbulent kinetic energy conservation equation is reduced to the relatively simple expression [4],

$$\frac{dk}{dt} = G_k - \epsilon \tag{3.7-8}$$

Suggesting turbulent kinetic energy is produced and dissipated by these quantities. The expression for the production of turbulent kinetic energy is,

$$G_k = -\overline{u_\iota u_j} \frac{\partial \bar{U}_\iota}{\partial x_j} = -a_{ij} \bar{S}_{ij} \tag{3.7-9}$$

where the a_{ij} term represents the anisotropy tensor which was defined as the LHS of equation 3.6- 4. When isotropic turbulence is assumed, then the mean velocity is zero and no uniform mean velocity gradient is imposed. Then the turbulent kinetic energy only decays by the isotropic decay rate. The conservation equation for this quantity can be derived similar to the turbulent kinetic energy, by manipulating the Navier-Stokes equation. By taking the gradient of the Navier-Stokes and then multiplying by the gradient of the fluctuation velocity, we obtain,

$$\frac{\partial \epsilon}{\partial t} + \bar{U}_J \frac{\partial \epsilon}{\partial x_j} = G_\epsilon^1 + G_\epsilon^2 + G_\epsilon^3 + G_\epsilon^4 + \Pi_\epsilon + T_\epsilon + D_\epsilon - \Upsilon_\epsilon \qquad (3.7\text{-}10)$$

Where the LHS describes the accumulation of the energy dissipation rate and the RHS involves various gradient terms. Some physical meaning is lost in these RHS terms and so they are abbreviated as such. In order, the first four terms on the RHS describe different generation terms, the fifth term describes pressure diffusion, the sixth is a transport term, the seventh describes viscous diffusion, and the final term describes the sink term of the turbulent energy dissipation rate [5].

Modeling the conservation equation for turbulent kinetic energy involves two main assumptions: 1. The Boussinesq approximation is substituted into the turbulent kinetic energy production rate to replace the anisotropy tensor,

$$G_k = -a_{ij}\bar{S}_{ij} = 2\nu_t \bar{S}_{ij}\bar{S}_{ij} \qquad (3.7\text{-}11)$$

and 2. The transport of turbulent kinetic energy by velocity and pressure fluctuations give a flux of turbulent kinetic energy by the *gradient-diffusion hypothesis* [4],

$$T_j = -\frac{\nu_t}{\sigma_k}\frac{\partial k}{\partial x_j} \qquad (3.7\text{-}12)$$

where σ_k is a modeling constant which acts as a viscosity ratio. The turbulent energy dissipation rate model equation does not stem from equation 3.7-10, but instead the simplified form of this equation by assuming homogeneous turbulence [4],

$$\frac{d\epsilon}{dt} = C_{1\epsilon}\frac{\epsilon}{k}G_k - C_{2\epsilon}\frac{\epsilon^2}{k} \tag{3.7-13}$$

From this simplified expression, the model equation, given by equation 3.7-15, includes a diffusion and advective term for the conservation of turbulent energy dissipation rate. Therefore, this model equation is empirical rather than exact with simplifying assumptions. The model coefficients take the values, $C_{1\epsilon}$ = 1.44, and $C_{2\epsilon}$ = 1.92.

Making the assumptions discussed above, yields modeled equations for the turbulent kinetic energy and its dissipation rate. The FLUENT theory guide [4] describes these equations as,

$$\frac{\partial k}{\partial t} + \bar{U}_j\frac{\partial k}{\partial x_j} = \frac{\partial}{\partial x_j}\left[\left(\nu + \frac{\nu_t}{\sigma_k}\right)\frac{\partial k}{\partial x_j}\right] + G_k - \epsilon + G_b - Y_M + S_k \tag{3.7-14}$$

$$\frac{\partial \epsilon}{\partial t} + \bar{U}_j\frac{\partial \epsilon}{\partial x_j} = \frac{\partial}{\partial x_j}\left[\left(\nu + \frac{\nu_t}{\sigma_\epsilon}\right)\frac{\partial \epsilon}{\partial x_j}\right] + C_{1\epsilon}\frac{\epsilon}{k}G_k - C_{2\epsilon}\frac{\epsilon^2}{k} + C'_{3\epsilon}\frac{\epsilon}{k}G_b + S_\epsilon \tag{3.7-15}$$

These equations represent the standard k-ε closure model. The LHS of both equations is as it was for the conservation equations. The viscous diffusion term on the RHS only differs from the conservation equations by the additional turbulent eddy viscosity term, which is "converted" by a viscosity ratio. These viscosity ratios take the values, σ_k = 1.0 and σ_ϵ = 1.3. For turbulent kinetic energy this additional diffusion term was included by modeling the energy flux by gradient diffusion. For the energy dissipation rate, both diffusion terms were included to the homogeneous turbulence case in equation 3.7-13. Proceeding the diffusion terms, are the turbulent source and sink terms which exist in homogeneous turbulence. The remaining terms on the RHS are included to account for buoyancy effects and any other source. These terms are included in the FLUENT

code, but are neglected in this work. The Y_M term in the k equation represents the contribution of fluctuating dilation which can be neglected for incompressible flow.

Improvements have been made to this standard k-ε closure. In this work, the realizable k-ε closure model is used. This closure model is of similar form to the standard model, but uses a C_μ value that varies with the mean velocity gradient, and incorporates vorticity fluctuation in the dissipation rate equation. These modifications have been shown to provide more reliable results in a range of turbulent flows [2].

3.8 RANS Near-Wall Modeling

Modeling discussed in the previous section assumes isotropic turbulence, where mean turbulence properties are independent of position and directional preference. This assumption is not valid near the wall and as a consequence the closure equations derived previously cannot be applied in these regions. Additionally the no-slip boundary condition still applies and, as a result, the velocity and turbulent kinetic energy at the wall must be zero. Understanding the transition from turbulent core to the no-slip condition that occurs within the near-wall region is necessary to model turbulent flow properties near the wall.

The near-wall region is commonly subdivided into various layers. Each layer represents different physics that occur close to the wall. These divisions are arbitrary, however a variety of experiments indicate that the near wall region is divided into three layers. The location of these layers is dependent on a parameter which takes the form of a Reynolds number, the *y-plus* value,

$$y^+ = \frac{U_\tau y}{\nu} \qquad U_\tau = \sqrt{\frac{\tau_w}{\rho}} \qquad \tau_w = \mu \frac{\partial \bar{U}_x}{\partial y}(y = 0) \tag{3.8-1}$$

where the friction velocity, U_τ, is defined by the wall stress, τ_w. For simplicity, in equation 3.8-1, the y-direction is normal to the wall and the x-direction is direction of flow. Starting from the wall,

the first layer is the viscous sublayer $(0 \leq y^+ < 5)$, then the buffer layer $(5 \leq y^+ < 60)$, and fully turbulent region $(60 \leq y^+)$. Outside these three inner layers is the turbulent core which is dependent on the traditional Reynolds number [2].

There are two approaches to be considered when modeling this near-wall region. The first is the use of *wall functions*. Wall functions are semi-empirical formulas that are separate from the turbulence models and develop the near-wall velocity profile based on the y-plus value. This approach does not require a refined mesh but it may lessen the accuracy of the solution. The second approach is termed *near-wall modeling*, where the mesh is refined close to the wall and the turbulence models are modified with the intent of describing the physics near the wall.

In this work enhanced wall treatment is utilized. This is a near-wall modeling method with the use of enhanced wall functions. If the mesh density is sufficiently fine near the wall, then the enhanced wall treatment is identical to a near-wall model. If the mesh density is not sufficiently fine near the wall, then the near-wall model is used with wall functions [2]. This is accomplished by subdividing the near-wall region into a viscosity affected and fully turbulent region. In the fully turbulent region, the turbulence closure model is used, and in the viscosity affected region, the following enhanced wall function is used,

$$\nu_t = C_\mu l_\mu \sqrt{k} \qquad l_\mu = C_\alpha C_\mu^{-\frac{3}{4}} y \left[1 - \exp\left(-\frac{Re_y}{C_\mu}\right)\right] \qquad Re_y = \frac{y\sqrt{k}}{\nu} \qquad (3.8\text{-}2)$$

where the turbulent eddy viscosity is modified by the turbulent kinetic energy and an exponential decaying length scale. The constants in this enhanced wall function are as follows, $C_\mu = 0.09$, $C_\mu = 70$, and $C_\alpha = 0.4187$.

3.9 The Energy Cascade and the Scales of Turbulence

Turbulence is a multi-scale problem. Eddies or vortices of some given length and time scale carry energy. This energy moves to smaller and possibly larger eddies or vortices. This concept is termed the *energy cascade.* The energy cascade describes the spectrum of eddy sizes and the energy associated with those eddies. It is common to write the energy cascade in terms of wave number, κ, which is proportional to the inverse of the length,

$$\kappa \sim \frac{1}{L} \tag{3.9-1}$$

Therefore a low wave number on the energy cascade corresponds to large eddies. The largest eddies contribute to most of the energy in the system and as these eddies break, energy is dissipated. This can be expressed mathematically as,

$$k = \int_0^\infty E(\kappa)\, d\kappa \tag{3.9-2}$$

$$\epsilon = \nu \int_0^\infty \kappa^2 E(\kappa)\, d\kappa \tag{3.9-3}$$

where $E(\kappa)$ represents the energy spectrum and can be derived by taking the Fourier transform of the correlation tensor [5]. Equation 3.9-2 suggests that the turbulent kinetic energy, the intensity of the turbulence, is captured by integrating across the energy spectrum. Equation 3.9-3 suggests that the turbulent energy dissipation rate is dependent on a shifted energy spectrum in which larger wave numbers (smaller eddies) are more significant.

Quantifying this distribution of length scales is difficult and so scaling arguments are used to describe eddies of similar size to the integral and Kolmogorov length scales. The smallest scales of turbulence are represented by the Kolmogorov length scale, L_K. We assume that at this scale convective and viscous forces balance. A Reynold's number can be developed from this balance if both convective and viscous terms are written with respect to the Kolmogorov scale,

$$\frac{U_j \frac{\partial U_i}{\partial x_j}}{\nu \frac{\partial^2 U_i}{\partial {x_j}^2}} \sim Re_K = \frac{U_K L_K}{\nu} = 1 \tag{3.9-4}$$

Where U_K is the velocity of the smallest eddies. The rate at which the kinetic energy of these eddies dissipates can be expressed as,

$$\epsilon \sim \frac{\nu}{t_K^2} \tag{3.9-5}$$

Where t_K is the Kolmogorov time scale. By these two expressions and scaling the Kolmogorov velocity as $U_K \sim L_K/t_K$, the Kolmogorov scales can be expressed in terms only involving the energy dissipating eddies,

$$t_K = \left(\frac{\nu}{\epsilon}\right)^{\frac{1}{2}} \qquad L_K = \frac{\nu^{\frac{3}{4}}}{\epsilon^{\frac{1}{4}}} \qquad U_K = (\nu\epsilon)^{\frac{1}{4}} \tag{3.9-6}$$

These Kolmogorov scales describe smallest scale at which mixing can occur, any scales smaller and diffusion occurs.

Similar to the Kolmogorov scales, a Reynold's number and energy dissipation rate can be written in terms of the largest scales of turbulence or the integral scales. We write these quantities in terms of the integral length scale, *L*, and velocity scale, *U*.

$$Re_L = \frac{UL}{\nu} \qquad \epsilon \sim \frac{U^3}{L} \tag{3.9-7}$$

Combining equations 3.9-4 and 3.9-5, a relationship between the Kolmogorov and macroscopic length scale can be written in terms of the bulk Reynold's number.

$$\frac{L_K}{L} \sim Re_L^{-\frac{3}{4}} \tag{3.9-8}$$

This relationship has great significance in the study of turbulent behavior. It implies that the size of eddies in which viscosity becomes important is proportional to a power of the bulk Reynolds number and a characteristic length.

We are interested in describing the turbulence and the multiple scales of mixing within a pipeline rotor-stator mixer. This requires resolving eddies of multiple scales, sizes ranging from the macroscopic to the Kolmogorov scale (if possible). The mesh size can be determined from the derived relationship above (equation 3.9-6). Since this simulation is three-dimensional, the mesh size scales by a length scale to the third power.

$$M_{cells} \sim L^3 \sim Re_L^{\frac{9}{4}} \tag{3.9-9}$$

This scaling arguments provides an approximation to the mesh size needed to resolve all eddies of size equal to or larger than the Kolmogorov length scale. By this argument, the number of cells required to resolve the Kolmogorov scales for this mixer is 8.6×10^{12} cells. A mesh of this size would require an unreasonable amount of computing time and so other methods are used to describe the turbulent behavior of the mixer within a reasonable amount of time.

3.10 Filtered Equations

The RANS technique averaged out the fluctuating velocity and pressure to provide an approximation to the mean velocity and pressure field. This model lacks the ability to describe structures in the flow by its construction. The vortices or eddies in turbulent flow provide information regarding the intensity of mixing and how energy is transferred among different scales. Instead of averaging, a different turbulence modeling technique known as large eddy simulations (LES) can be used. LES attempts to resolve the larger scales of turbulence where most of the energy is present and disregards the smaller scales which are assumed negligible.

Instead of averaging as in the RANS equations, LES filters the velocity and pressure into resolved and unresolved components [4],

$$U_i = \langle U_i \rangle + u_i' \qquad\qquad P = \langle P \rangle + p' \tag{3.10-1}$$

In this work the angle brackets will denote that that quantity is filtered and the prime denotes the unresolved quantity. This filtering operator can be mathematically expressed as,

$$\langle \phi \rangle = \Gamma * \phi = \int_{\mathbb{R}^3} \Gamma(x, y)\phi(y, t)dy \tag{3.10-2}$$

where is Γ the filter kernel which is convolved with the quantity ϕ. There are a variety of filters that can be used in LES, the filter employed by FLUENT and the one used in this work is the top hat filter. As indicated by equation 3.10-1 above, the three velocity components and the pressure are filtered across space using this filter operation (equation 3.10-2).

In LES, the mass and momentum conservation equations are filtered similar to how they were averaged to develop the RANS equations in section 3.6. When the equation of continuity is filtered, the same expression results but in terms of the resolved velocity,

$$\frac{\partial \langle U_i \rangle}{\partial x_i} = 0 \tag{3.10-3}$$

By the filter equation given by equation 3.10-2 it can be noted that this operation is linear. Additionally the equation of continuity is a linear PDE. Therefore the above result is as expected. When filtering the Navier-Stokes, we obtain,

$$\frac{\partial \langle U_i \rangle}{\partial t} + \frac{\partial \langle U_i U_j \rangle}{\partial x_j} = \nu \frac{\partial^2 \langle U_i \rangle}{\partial {x_j}^2} - \frac{1}{\rho}\frac{\partial \langle P \rangle}{\partial x_i} \tag{3.10-4}$$

where again the filtering operation can be placed within the derivatives for the linear terms of the PDE. All terms are readily computed from LES except for the second RHS term which developed

from the nonlinear convective term of the Navier-Stokes. A substitution is made in which this unknown quantity is expressed as the product of known quantities,

$$\frac{\partial\langle U_i\rangle}{\partial t} + \langle U_j\rangle\frac{\partial\langle U_i\rangle}{\partial x_j} = \nu\frac{\partial^2\langle U_i\rangle}{\partial {x_j}^2} - \frac{1}{\rho}\frac{\partial\langle P\rangle}{\partial x_i} - \rho\frac{\partial\tau_{ij}^s}{\partial x_j} \tag{3.10-5}$$

The additional term that results is known as the subgrid-scale (SGS) stress tensor, which is written as,

$$\tau_{ij}^s = \langle U_i U_j\rangle - \langle U_i\rangle\langle U_j\rangle \tag{3.10-6}$$

Similar to the Reynold's stress term in the RANS equation, the SGS stress tensor must be modeled for the LES equations to be closed [4]. Various SGS models are considered in the following section.

3.11 Subgrid-scale Stress Tensor

Another similarity between the RANS equations and LES is how the Boussinesq approximation is applied. In the RANS equations, the Reynold's stress was assumed to be proportional to the average rate of strain tensor with a proportionality constant known as the eddy viscosity. For LES, the deviatoric component of the SGS stress tensor is assumed to be proportional to the filtered rate of strain tensor with a proportionality constant known as the *subgrid-scale eddy viscosity*.

$$\tau_{ij}^s - \frac{1}{3}\tau_{kk}^s\delta_{ij} = -2\nu_t^s\langle S_{ij}\rangle \tag{3.11-1}$$

The SGS eddy viscosity is a term that is modeled by the SGS models. There are a variety of SGS models, including the Smagorinsky-Lilly, dynamic Smagorinsky-Lilly, and the Wall-Adapting Local Eddy viscosity (WALE) model. Each of these models are of the form,

$$\nu_t^s = C_m\Delta^2\langle OP\rangle(x_i, t) \tag{3.11-2}$$

where C_m is some given model constant, Δ is the filter width which is typically taken to be the grid width, and OP is an operator which is a function of space and time [5].

In the Smagorinsky-Lilly model, the operator is the magnitude of the resolved strain rate. This model was found to have several flaws, particularly near the wall. The Smagorinsky-Lilly model would incorrectly predict a nonzero SGS eddy viscosity at the wall. Additionally the SGS model does not predict the proper scaling of the eddy viscosity near the wall. To correct this error, the dynamic Smagorinsky-Lilly uses an additional filter called the test filter to dynamically alter the SGS eddy viscosity near the wall. The test filter is a high pass filter in which the test filter width is twice the grid filter width.

The WALE model differs from the standard and dynamic Smagorinsky-Lilly model by using the square of the velocity gradient tensor as the operator. This operator was chosen to fulfill four major properties useful in LES:

- The operator should be invariant to any coordinate translation or rotation
- The operator can be easily applied to any computational mesh
- The operator is a function of both strain and rotation rates
- The operator tends towards zero at the wall

This invariant was determined by Nicoud and Ducros [5]. It is expressed as,

$$\mathcal{S}_{ij} = \langle S_{ik}\rangle\langle S_{kj}\rangle + \langle \Omega_{ik}\rangle\langle \Omega_{kj}\rangle - \frac{1}{3}\delta_{ij}[\langle S_{mn}\rangle\langle S_{mn}\rangle - \langle \Omega_{mn}\rangle\langle \Omega_{mn}\rangle] \qquad (3.11\text{-}3)$$

Which can be considered as the traceless part of the square of the velocity gradient tensor. Since this tensor involves the filtered rate of strain and rotation, it can be applied to any computational mesh throughout the fluid body.

Nicoud and Ducros showed that the square of this tensor, expressed below, has a zero invariant in the case of simple shear flow. Since the energy dissipation rate is dependent on velocity

gradients, the use of this as the operator would predict zero SGS eddy viscosity at the wall as desired.

$$\mathcal{S}_{ij}\mathcal{S}_{ij} = \frac{1}{6}[S^2S^2 + \Omega^2\Omega^2] + \frac{2}{3}S^2\Omega^2 + 2IV_{S\Omega} \tag{3.11-4}$$

where $S^2 = \langle S_{ij}\rangle\langle S_{ij}\rangle$, $\Omega^2 = \langle \Omega_{ij}\rangle\langle \Omega_{ij}\rangle$, and $IV_{S\Omega} = \langle S_{ik}\rangle\langle S_{kj}\rangle\langle \Omega_{jl}\rangle\langle \Omega_{li}\rangle$. Nicoud and Ducros argued that the square of this tensor scales quadratically towards the wall. To achieve the cubic profile as expected near the wall, the operator is taken to the 3/2 power. The final operator is chosen to include this squared tensor, but also to avoid instabilities. The WALE model is expressed as,

$$\nu_t^s = (C_w\Delta)^2 \frac{\left(\mathcal{S}_{ij}\mathcal{S}_{ij}\right)^{3/2}}{\left(\langle S_{ij}\rangle\langle S_{ij}\rangle\right)^{5/2} + \left(\mathcal{S}_{ij}\mathcal{S}_{ij}\right)^{5/4}} \tag{3.11-5}$$

Where C_w is the WALE constant and is taken as 0.325 in FLUENT. The denominator term is present to avoid instabilities in the simulation. In this work, the WALE SGS model is used for all LES.

3.12 LES Near-Wall Modeling

Similar to the RANS equations, the SGS model is valid for homogeneous turbulence. Near the wall we expect mean flow properties to vary with position to fulfill the no-slip boundary condition. These mean flow properties are dependent on the filtered scales as well as the interaction with resolved and unresolved scales. To properly resolve the behavior near the wall, high mesh resolution is required. However such a mesh is computationally expensive and not affordable for flows with large Reynolds numbers. For simulations in which the inner layer is not resolved by the grid, a wall model is used. This LES wall model attempts to relate the influence from the outer layer scales to the inner layers scales [6]. FLUENT offers an equilibrium-stress wall model which assumes the near wall velocity obeys the logarithmic profile,

$$\frac{\overline{U}}{U_\tau} = \frac{1}{C_\kappa} \ln y^+ + C_B \tag{3.12-1}$$

where the constant C_B is taken to be 5.565, C_κ is the von Karman constant, and the wall y-plus $y^+$and wall velocity U_τ are expressed in equation 3.8-1. The wall model replaces the instantaneous velocity with the time-averaged wall velocity. This replacement is assumed to be valid because the time step is likely to be larger than the necessary time scales near the wall, therefore filtering in this vicinity is equivalent to time averaging. If the mesh is sufficiently refined near the wall to resolve the laminar sublayer, that is to say $0<y^+<11$, then a linear wall model is taken instead of equation 3.12-1,

$$\frac{\overline{U}}{U_\tau} = y^+ \tag{3.12-2}$$

3.13 Computing Quantities from the Filtered Velocity Field

To properly compare turbulence quantities outputted from a RANS and large eddy simulation, the underlying assumptions must be understood. Quantities of interest in this work include the mean velocity field, flow rate, torque, turbulent kinetic energy, strain rate magnitude, and turbulent energy dissipation rate. Equation 3.6-1 was substituted into the Navier-Stokes equation to model the mean velocity field. Equation 3.6-1 could also be used to compute the mean flow rate and torque. By decomposing the instantaneous velocity field into its mean and fluctuating component, the fluctuating component had to be modeled. This was done by solving modeled turbulent kinetic energy and energy dissipation rate conservation equations. These modeled equations have additional assumptions which is discussed in section 3.7.

These quantities are not readily provided by a LES and must be computed using known quantities. Equation 3.10-1 decomposed the instantaneous velocity into filtered and unfiltered components where the filtered velocity component is given by equation 3.10-5 and the unfiltered

component is modeled by the SGS stress tensor. To approximate the mean velocity field from the filtered velocity field, equation 3.10-1 is averaged,

$$\overline{U_i} = \overline{(\langle U_\iota \rangle + u_\iota')} = \overline{\langle U_\iota \rangle} + \overline{u_\iota'} \approx \overline{\langle U_\iota \rangle} \tag{3.13-1}$$

The mean velocity is the summation of the average filtered and average unfiltered velocity. Although the average of the unfiltered velocity component is generally not zero, there is nothing in the LES model that can quantify it so we assume it is negligible. As the computational mesh becomes more refined, the unfiltered velocity component becomes more negligible. Therefore the error of this assumption decreases with increasing mesh refinement.

Applying equation 3.2-1 to the mean velocity field given by the RANS equations gives an estimate of the mean throughput. Applying equation 3.2-1 to the filtered velocity field given by a LES suggests,

$$Q = \iint_A U_i dA_i = \iint_A \langle U_i \rangle dA_i + \iint_A u_i' dA_i \approx \iint_A \langle U_i \rangle dA_i \tag{3.13-2}$$

The instantaneous flow rate modeled by a LES is the flow rate of the filtered and unfiltered scales. Similar to the assumption made in equation 3.13-1, for a sufficiently refined computational mesh the flow rate of the unfiltered component is negligible. Equation 3.13-2 can be averaged to give the mean flow rate as predicted by a LES. The difference between the filtered flow rate and the averaged filtered flow rate is the resolved fluctuating flow rate.

When computing the torque from a filtered pressure distribution, the procedure is similar to the computing the filtered flow rate above. The filtered and unfiltered decomposition of the pressure field is substituted into equation 3.1-7,

$$T_i = \varepsilon_{ijk} r_j \iint_A P \, dA_k = \varepsilon_{ijk} r_j \iint_A (\langle P \rangle + p') \, dA_k \approx \varepsilon_{ijk} r_j \iint_A \langle P \rangle \, dA_k \tag{3.13-3}$$

Where ε_{ijk} is the permutation operator used to perform the cross product between the moment arm and the pressure force. To approximate the instantaneous torque with the filtered torque, we assume the torque from the unfiltered pressure distribution is negligible. This assumption is equivalent to assuming the spatial average of the unfiltered pressure force is relatively small.

To compute an approximation of the turbulent kinetic energy from a LES, we must consider the velocity fluctuations. To mathematically show this, equation 3.13-1 is substituted into equation 3.6-1.

$$u_i = U_i - \bar{U}_i = \left[\langle U_i \rangle - \overline{\langle U_i \rangle}\right] + \left[u_i' - \overline{u_i'}\right] = u_i^r + u_i^u \tag{3.13-4}$$

The true velocity fluctuation can be written in two components: the resolved and unresolved velocity fluctuations. The resolved fluctuation, the difference between the filtered and average of the filtered velocity, can be computed from a LES. The unresolved fluctuation, the difference between the unfiltered and average of the unfiltered velocity, is not provided by the model equations. Now substituting this equation into the definition of turbulent kinetic energy,

$$k = \frac{1}{2}\overline{u_i{}^2} = \frac{1}{2}\overline{(u_i^r)^2} + \overline{u_i^r u_i^u} + \frac{1}{2}\overline{(u_i^u)^2} \approx \frac{1}{2}\overline{(u_i^r)^2} \tag{3.13-5}$$

The SGS stress tensor provides no information regarding the unresolved velocity fluctuations. For this reason, the turbulent kinetic energy is approximated by the resolved velocity fluctuation product. Equation 3.9-2 suggests the turbulent kinetic energy is the integration of the energy cascade. If all significant scales in the energy cascade are filtered, then the assumption made in equation 3.13-5 is reasonable.

For a RANS simulation, the strain rate magnitude involves the square of the mean strain rate tensor. Which, as was shown in equation 3.7-5 (excluding the fluctuation terms), is the sum of the mean energy dissipated and a product of cross velocity gradients which are zero in

homogeneous turbulence. For a LES, the square of the filtered strain rate tensor includes the resolved mean and resolved fluctuating velocity gradients,

$$2\langle S_{ij}\rangle\langle S_{ij}\rangle = 2\overline{\langle S_{ij}\rangle}\,\overline{\langle S_{ij}\rangle} + 4\overline{\langle S_{ij}\rangle}s_{ij}^{r} + 2s_{ij}^{r}s_{ij}^{r} \qquad (3.13\text{-}6)$$

Where the resolved fluctuating strain rate tensor is the difference between the filtered and the average filtered strain rate tensor, similar to equation 3.13-4 for velocity. Each of the three strain rate tensor products in equation 3.13-6 result in a summation of energy dissipation terms and cross velocity gradient products. When the square of the filtered strain rate tensor is averaged, the mean strain rate tensor product approximated by a LES only involves the resolved mean velocity gradients. To find the magnitude of the filtered strain rate, the square root of equation 3.13-6 is computed.

The turbulent energy dissipation rate is the integration of the energy cascade shifted by the wave number squared, as shown in equation 3.9-3. This shift weighs the energy cascade more towards the smaller scales, the turbulent energy dissipation rate therefore requires more mesh refinement to be properly resolved. Substituting equation 3.13-4 into the definition of the turbulent energy dissipation rate gives,

$$\epsilon = \nu\overline{\left(\frac{\partial u_i}{\partial x_j}\right)^2} = \nu\overline{\left(\frac{\partial u_i^r}{\partial x_j}\right)^2} + 2\nu\overline{\left(\frac{\partial u_i^r}{\partial x_j}\frac{\partial u_i^u}{\partial x_j}\right)} + \nu\overline{\left(\frac{\partial u_i^u}{\partial x_j}\right)^2} \qquad (3.13\text{-}7)$$

If the computational mesh is refined near the Kolmogorov scale then the last two terms of equation 3.13-7, represented by the unresolved velocity fluctuation gradients, can be assumed negligible. However for many engineering flows such mesh refinement is too computationally expensive.

Although the turbulent energy dissipation rate cannot be computed directly from equation 3.13-7, the unresolved scales contribution to the turbulent energy dissipation rate can be

modeled by the SGS stress tensor. To understand how, the conservation equation for the filtered kinetic energy is derived. Taking the dot product of the filtered velocity with equation 3.10-5 gives,

$$\frac{\partial\langle q\rangle}{\partial t}+\langle U_j\rangle\frac{\partial\langle q\rangle}{\partial x_j}=\frac{\partial}{\partial x_j}\left(-\langle P\rangle\langle U_j\rangle+\nu\frac{\partial\langle q\rangle}{\partial x_j}-\tau_{ij}^{s}\langle U_i\rangle\right)-\nu\left(\frac{\partial\langle U_i\rangle}{\partial x_j}\right)^2+\tau_{ij}^{s}\langle S_{ij}\rangle \quad (3.13\text{-}8)$$

Where $\langle q\rangle=\frac{1}{2}\langle U_i\rangle^2$ represents the filtered kinetic energy. The LHS represents the advection of the filtered kinetic energy. The first term on the RHS represents the transport of this kinetic energy by pressure, diffusion, and subgrid-scales. The last two terms on the RHS represent dissipation of the filtered and subgrid-scales, respectively. By substituting the Boussinesq approximation (equation 3.11-1) into the SGS energy dissipation term, the SGS turbulent energy dissipation rate can be computed,

$$\epsilon_{SGS}=-\tau_{ij}^{s}\langle S_{ij}\rangle=2\nu_t^{s}\langle S_{ij}\rangle\langle S_{ij}\rangle \quad (3.13\text{-}9)$$

As the other dissipation term in equation 3.13-8 indicates, the total turbulent energy dissipation rate is the sum of the resolved and SGS components [7],

$$\epsilon\approx\bar{\epsilon_r}+\overline{\epsilon_{SGS}}=2\overline{(\nu+\nu_t^{s})\langle S_{\iota J}\rangle\langle S_{\iota J}\rangle} \quad (3.13\text{-}10)$$

Where the contribution from the resolved scales is given by the kinematic viscosity, not the SGS eddy viscosity. It should be noted that if the Smagorinsky-Lilly SGS model is used, which assumes the SGS eddy viscosity is proportional to the magnitude of the resolved strain rate tensor, then the SGS energy dissipation rate will be proportional to the cube of the filtered strain rate magnitude. As where the resolved energy dissipation rate is proportional to the filtered strain rate magnitude squared.

3.14 Finite Volume Equations

A variety of methods are used to solve the Navier-Stokes equations and other relevant transport equations. The finite difference method converts the governing differential equations into

algebraic form which can then be solved as a linear system of equations. This method discretizes the governing equations using truncated Taylor series expansions which readily provides a truncation error. Instead of using powers as the basis function as with the Taylor series, complex exponentials are used in a different method known as Spectral methods. Contrary to the local approach in finite differencing, spectral methods use a global approach in which the basis functions are nonzero on the entire domain. For this reason, spectral methods have relatively low error compared to finite difference methods. The error for finite difference methods decreases by some power with increasing grid refinement, while the error for spectral methods decreases exponentially.

A disadvantage to using finite differencing or spectral methods is that a structured grid is required. Since engineering flows, such as in this thesis, have complicated geometry; another discretization approach is required. FLUENT uses the finite volume method which considers a cell as a control volume and computes the flux in and out of the cell. The orientation of the cell volume and its faces are readily considered by the finite volume equations and so an unstructured grid can be used. For a general flow variable ϕ, in incompressible flow, the discrete conservation equation is expressed as,

$$\frac{\partial \phi}{\partial t} V + \sum_{f}^{M} \phi_f \boldsymbol{u}_f \cdot \boldsymbol{A}_f = \sum_{f}^{M} D_\phi \nabla \phi_f \cdot \boldsymbol{A}_f - \mathrm{S}_\phi V \qquad (3.14\text{-}1)$$

Note that traditional vector notation is used instead of Einsteinian notation to avoid confusion with the summation term where properties at each face f are summed. Properties of the cell are considered using the cell volume V, and the total number of faces M. The remaining terms are properties of the flow variable, D_ϕ is the diffusion coefficient, and S_ϕ is a source term. The form of this expression is similar to other conservations equations derived earlier. The LHS describes

accumulation of the flow variable, the first term on the RHS describes diffusion and the last term describes generation or consumption of the flow variable.

In this work equation 3.14-1 is applied to the RANS k-ϵ turbulence model as well as the filtered equations of a LES. Performing this mathematical manipulation discretizes these governing equations. Discretization in time, space, gradients, and pressure are required to numerically solve these governing equations. The discretization technique used for both RANS and LES are discussed in the following section. Pressure-velocity coupling is also discussed as an additional solution method.

3.15 Solution Methods and Discretization Technique

The advective and diffusive terms in the conservation equations require spatial discretization. The finite volume method in FLUENT readily stores the cell center value ϕ. The face values ϕ_f are interpolated from neighboring cell center values. The diffusion terms are discretized using the *central-difference scheme* which is second order accurate [2],

$$\phi_f = \frac{1}{2}(\phi_0 + \phi_1) + \frac{1}{2}(\nabla\phi_0 \cdot \boldsymbol{r}_0 + \nabla\phi_1 \cdot \boldsymbol{r}_1) \tag{3.15-1}$$

where the indices 0 and 1 refer to cells that share the face f. The average of the two cell center values are used as well as the gradients directed towards the face centroid to predict the face value. Advective terms are discretized in a different manner, using the direction of the flow to bias the scheme. This procedure is known as an upwind scheme, and the second order upwind scheme is used [2],

$$\phi_f = \phi + \nabla\phi \cdot \boldsymbol{r} \tag{3.15-2}$$

where the cell center and gradient value from the upstream cell are used to predict the face value. For the RANS simulations in this work, the second order upwind scheme is utilized to discretize each momentum component, the turbulent kinetic energy, and the turbulent energy dissipation rate.

For LES in this work, the bounded central differencing scheme is used to discretize the momentum components. This scheme is the preferred choice for LES in FLUENT since low SGS diffusivities result in unphysical oscillations for the central differencing scheme. The bounded central differencing scheme uses aspects of the central differencing, second order upwind, and a first order upwind scheme.

Moving the solution forward in time requires discretizing the partial time derivative in the governing equations. This is done by considering the remaining terms of the conservation equation as a function of the solution at some time step. Then the time derivative may use the solution data from nearby time steps to advance the solution in time. For this work, time was discretized using a second order accurate scheme provided in equation 3.15-3 [2].

$$\frac{\partial \phi}{\partial t} \approx \frac{3\phi^{(n+1)} - 4\phi^{(n)} + \phi^{(n-1)}}{2\Delta t} = F(\phi^{(n+1)}) \qquad (3.15\text{-}3)$$

Solution data from time steps $n-1$, n, and $n+1$ are used in this temporal discretization scheme. The amount one time step influences the next is dependent on the weight or coefficient in the scheme. The function $F(\phi^{(n+1)})$ in equation 3.15-3 denotes the other spatial discretization terms. This function is evaluated at time step $n+1$, implicit time integration is being considered in this project. Both sides of equation 3.15-3 involve the unknown quantity, $\phi^{(n+1)}$, which cannot be explicitly expressed. It is therefore solved by iteration. If the function was evaluated at time step n instead, then the time integration would be explicit and would not require iteration. Although the implicit time scheme is computationally expensive, it is stable for larger time step sizes where the explicit time integration would be unstable.

Equations 3.15-1 and 3.15-2 use gradients, $\nabla\phi$ to discretize the diffusion and convection terms respectively. Therefore the gradient in a cell must be evaluated using information from nearby cells. FLUENT provides various methods to evaluate cell gradients, including the

application of the Gauss theorem. The theorem states that the surface integral of the flow variable ϕ is equal to the volume integral of the gradient of the flow variable. Applying this to a discrete volume such as a cell in FLUENT [2],

$$\nabla\phi = \frac{1}{V}\sum_{f}^{M} \phi_f \boldsymbol{A}_f \tag{3.15-4}$$

where the summation term represents the surface integral from the Gauss theorem and is normalized by the cell volume because the gradient is assumed constant throughout the cell volume. This Gauss method is common in finite volume approaches, however the *least squares cell-based gradient evaluation* approach is used in this work. This approach approximates the gradient in one cell $(\nabla\phi)_0$ using the first order difference formula for all surrounding cells. Since all surrounding cells are being considered, the gradient in the cell center can be written in a compact matrix equation [2],

$$B(\nabla\phi)_0 = \phi_1 - \phi_0 \tag{3.15-5}$$

where the coefficient matrix B describes the distance from the center cell to surrounding cells and therefore this coefficient matrix is only a function of mesh geometry. The center cell gradient acts as the solution vector, and the RHS describes the cell center difference between surrounding cells and the center cell. More than one surrounding cell is being considered, therefore this matrix equation is over constrained. Thus the Gram-Schmidt process is used to solve the matrix equation in a least-squares sense.

All terms in the equation of continuity and Navier-Stokes can be discretized by the schemes mentioned above, except for the pressure term. In this work, the pressure term is discretized using the *standard* scheme. This scheme is the simplest provided by FLUENT and can be considered to be first-order accurate. This scheme uses linear interpolation between cell center data to find the

pressure at the faces of cells. Considering the discretization of pressure alone is not sufficient. The Navier-Stokes equations show that the pressure field is coupled with the velocity field. For this reason, a pressure-velocity coupling scheme must be implemented. The pressure-velocity coupling solution method used in this work is the SIMPLEC method. This approach uses the Navier-Stokes equation to propose an initial pressure value, this pressure value is then corrected so that the resulting face flux satisfies the equation of continuity [2].

$$J_f = J_f^* + d_f(p_0' - p_1') \tag{3.15-6}$$

where J_f is the corrected face flux, J_f^* is the proposed face flux, p' is the cell pressure correction in some cells 0 and 1. The coefficient d_f is a term from the discretized continuity equation.

The schemes used to discretize the governing equations for all simulations in this work are listed as a summary.

- Second-order upwind discretization for average momentum, turbulent kinetic energy, and turbulent energy dissipation rate equations
- Bounded central differencing for filtered momentum equations
- Second-order temporal discretization
- Least-squares cell based for gradient spatial discretization
- Standard discretization for pressure
- SIMPLEC pressure-velocity coupling

3.16 Measures of Convergence

Numerical solutions to partial differential equations are provided in this work. In numerical analysis, the consistency, stability, accuracy, and convergence of numerical solutions is of interest. To avoid confusion when discussing these terms, they are defined here as they are used throughout this work. A solution is considered *consistent* if the truncation error approaches zero as the distance

between points in space and time approach zero. The finite element discretization technique ensures that the governing equations are obtained as cell volume and time step size approach zero; this technique is therefore consistent. The *accuracy* of a discretization scheme is quantified by the number of Taylor series terms used. A solution is considered *stable* if truncation and round-off errors decay as the simulation proceeds in time. A solution is *converged* if it approaches the true solution upon spatial and temporal refinement. The measures discussed in this section are used to quantify convergence for the RANS and large eddy simulations.

One simple metric is the Courant-Friedrichs-Lewy (CFL) number. The CFL value can be used to impose time step or cell size,

$$CFL = \frac{U}{\Delta x/\Delta t} \tag{3.16-1}$$

This metric is a ratio of fluid velocity and relative "mesh speed." A CFL value below one is recommended because this would imply a fluid element travels from one cell to the next. For high shear rotor-stator mixers, maintaining a low CFL number can be difficult in the shear gap and jet regions surrounding the rotor. With high fluid velocity, high mesh refinement or small time step size must be imposed.

FLUENT uses an implicit time scheme which requires computing some set number of iterations for a given time step. Ideally, the solution at a particular time step should become more reliable with each iteration. If the predicted flow variable is exact, it must satisfy the conservation equation [2],

$$a_C \phi_C = \sum_{nb} a_{nb} \phi_{nb} + b \tag{3.16-2}$$

where the subscript *C* denotes the center value of a particular cell, subscript *nb* denotes the value from neighboring cells. The coefficients a_C and a_{nb} describe the influence of the particular cell on

the flow variable. The last term on the RHS is a constant contribution from the source term in the conservation equation. Since this expression is unlikely to be fulfilled the scaled residual is used as a metric for iteration convergence [2],

$$R^{\phi} = \frac{\sum_{cells}|\sum_{nb} a_{nb}\phi_{nb} + b - a_P\phi_P|}{\sum_{cells}|a_P\phi_P|} \tag{3.16-3}$$

The residual reported is the error of equation 3.16-2, summed across all cells, then normalized by the sum of the given conserved quantity across all cells.

Another concept, flow field convergence, is vague compared to the others previously discussed, and is dependent on the quantities being investigated. For a RANS simulation that models a time-averaged flow field, the mean of a flow variable should remain the same across all similar instances. However, since the mean flow variable is modeled, it may vary among similar instances. One possible metric that can be used to quantify how much a mean flow variable differs from one instance to the next is the absolute difference,

$$E_{abs}^{\bar{\phi}} = \left|\bar{\phi}_2 - \bar{\phi}_1\right| \tag{3.16-4}$$

In this work, we are interested in time-averaged quantities in the stator slots. These quantities should be similar from one rotor period to the next. The flow variables considered in this work include mean slot flow rate, mean rotor torque, and time-average slot velocity profiles. This is discussed in more detail in section 5.8. Another statistic that is used to quantify how much a flow variable deviates from average is the variance, which is also shown as the root mean square deviation,

$$\mathrm{var}(\phi) = \mathrm{rmsd}^2(\phi) = \frac{1}{M}\sum_{i=1}^{M}(\phi_i - \bar{\phi}_i)^2 \tag{3.16-5}$$

It should be noted that modeled mean quantities can vary even among similar instances, therefore using equation 3.16-4 and 3.16-5 for RANS simulations describes deviation instead of convergence.

Since LES models an instantaneous flow field, which contains fluctuating components, the measures of flow field convergence for RANS cannot be used for LES [8]. To compare results from RANS and LES, portions of the filtered flow field are sampled and then averaged. Therefore, when discussing flow field convergence of LES, we are interested in determining when it is appropriate to begin sampling. In this work, the outlet flow rate was monitored from the beginning of the simulation. When the outlet flow rate reached a steady value (varying within 3% of the average) the flow field was considered converged and sampling began. Just as flow field convergence of RANS was quantified by errors on quantities that should not vary, the outlet flow rate of the actual mixer or the outlet flow rate of a mixer modeled by LES should not vary significantly.

Another question that needs to be answered when using LES is when to stop sampling. Sampling for an extraneous amount of time results in a large amount of data and can be time taking to record the samples. If there are an insufficient amount of samples, then the predicted average would inaccurately predict the actual average. Since the actual average cannot be computed without an infinite amount of samples, the convergence of statistics is shown using different predicted averages. Ideally the distance between predicted averages should decrease as more samples are included. Equation 3.16- 4 is employed where both averages contain a different set of samples. Note that for RANS, the averages in equation 3.16-4 represent modeled averages from the governing equations, but for LES the averages in equation 3.16-4 represent predicted averages from samples of filtered variables. The average is a first moment statistic and so equation 3.16-4

provides information about how the first moment statistic converges. The variance involves a second moment statistic. Therefore to measure how the variance converges, we use equation 3.16- 6,

$$E_{abs}^{\mathrm{var}} = |\mathrm{var}(\phi_2) - \mathrm{var}(\phi_1)| \tag{3.16-6}$$

Again, when equation 3.16-6 is employed for LES, each variance term includes a different set of samples. Thirty samples (or realizations) were taken from each LES with differing mesh level and operating condition. This is discussed in more detail in section 6.6.

More refined meshes are expected to give more accurate results but are more computationally expensive. For this reason, determining the appropriate mesh to use is a major concern in CFD. In particular, the evaluation of gradients is dependent on local number of cells. In the context of rotor-stator mixers, the number of cells across the shear gap is a metric to describe how well the derivatives are resolved. Mesh convergence for RANS simulations can be accomplished by further refining the mesh until the desired results (such as shear gap velocity profile) are consistent between successive meshes. A comparison between the coarse hex 4.2M and refined hex 20M computational mesh for RANS is provided in section 5.7.

Mesh convergence for LES is directly dependent on the influence of the resolved scales. Therefore, the equations in section 3.9 can be used to approximate which scales of turbulence are resolved. When modeling scales below the grid resolution, which assumes homogeneity in its derivation of the SGS tensor, a significant error can occur if the mesh cannot resolve the inhomogeneous scales with. This error can be quantified by the SGS eddy viscosity, as mesh resolution increases, the ratio of SGS eddy viscosity and fluid viscosity approaches zero suggesting the mesh has resolved the inhomogeneous turbulence. The SGS eddy viscosity for the refined

hex 20M LES are discussed in section 6.4 and 6.5, respectively for the coarse hex 4.2M simulations.

4 Literature Review

In this chapter, current simulation methodologies and their experimental validation for turbulent flow in mixing devices is summarized. Flow behavior in stirred tanks has been widely studied and available literature is summarized in the first part of this chapter. Experimental techniques have been used to validate results from RANS and LES, including distribution of turbulent kinetic energy and energy dissipation rate. Knowledge from stirred tanks can be extended to rotor-stator mixers. Although less understood than stirred tanks, the mean flow within certain rotor-stator mixers has been studied within a RANS perspective.

4.1 Stirred Tanks Simulations

Fox and coworkers [9] studied turbulent flow in a baffled stirred tank equipped with a 45 degree pitched blade turbine. The Renormalization Group (RNG) k-ε model and Reynolds Stress Model (RSM) were used to close the RANS equations. A fixed frame method was used to conduct the simulations for one symmetrical quarter of the tank. To impose the influence from the blades, experimental PIV data was prescribed as the boundary condition. The mean velocity field, flow pattern, and turbulence quantities from RANS were compared to results from the PIV. It was concluded that the RNG k-ε model did not accurately predict the mean velocity in high shear regions. Turbulence quantities were well predicted in the impeller region. However, the turbulent kinetic energy and energy dissipation rate were under predicted in regions where the local isotropic assumption is no longer valid, such as the flow discharge region.

Numerical issues arising from the RANS equations in their application to stirred tanks has been extensively studied [10]. The RANS k-ε model was applied to a baffled stirred tank with a Rushton turbine impeller. Four meshes were considered with increasing refinement. Different discretization schemes were studied including first order upwind, second order upwind, and higher

order QUICK schemes. The effect of mesh and discretization scheme were considered on global parameters, including power number and flow number, as well as mean velocity, turbulent kinetic energy, energy dissipation rate, and velocity covariance's. Numerical error decreased with increasing grid refinement. However, the RANS model did not adequately describe energy dissipation in regions where turbulent properties are anisotropic.

Results from RANS and LES for a baffled stirred tank with a Rushton turbine were assessed using LDA [11]. The impeller Reynolds number was relatively low, although in the turbulent regime, and so LES may be considered a Direct Numerical Simulation (DNS). For this reason, two SGS models were utilized. The classic Smagorinsky-Lilly model with a wall damping function and the Voke SGS model. The Voke model is the Smagorinsky-Lilly model with the modification that the SGS eddy viscosity goes to zero in well resolved regions. It was concluded that the turbulent kinetic energy was accurately predicted by LES, while RANS under predicted the turbulent kinetic energy, especially in the impeller discharge region. Additionally, RANS predicted higher turbulent energy dissipation rate than LES, however the smaller spreading gradient of energy dissipation rate was smaller for RANS than for LES.

A relatively new turbulence model, termed Detached Eddy Simulation (DES), uses LES in regions which require low resolution and transitions to RANS where higher resolution is required, such as at the walls. The DES model was applied to a baffled stirred tank with a Rushton impeller, and results were then compared to purely RANS and LES models [8]. The Spalart-Allmaras (SA) RANS model, which was the RANS closure used in the DES, with a grid size of one million hexahedral cells, provided sufficient wall y-plus values for the DES. It was shown that DES sufficiently predicted the trailing vortex behind the blade, as well as the turbulent kinetic energy and power number. However, the chosen turbulent viscosity model under predicted the energy

dissipation rate. It was concluded that DES worked well for a relatively coarse grid with a wall y-plus value of 20.

4.2 Rotor-Stator Mixer Simulations

The power draw of a Greerco 1 ½ HR high-shear homogenizer has been studied in the laminar, transitional, and turbulent regimes experimentally [12]. It was shown that the relationship between power number and Reynolds number for this high-shear mixer was similar to that of stirred tanks. It was concluded that the power draw was highly influenced by the pumping mode, the down-pumping mode required 40% higher power draw than the up-pumping mode.

The periodic flow pattern and turbulent energy dissipation rate in a batch rotor-stator mixer has also been studied [13]. The RANS k-ε equations for the L4R-T Silverson high-shear mixer were solved using FLUENT. The mesh employed both tetrahedral and hexahedral cells consisting of 1 million cells total. It was shown that the periodicity in the mixer is related to blade position which effects the jet velocity, flow rate, torque, and energy dissipation rates. The turbulent energy dissipation rate peaks at the edge of the stator holes. However, only 7.6% of the energy dissipated is accounted for in this region. Instead, the rotor swept volume accounts for 48.5%, the jet region accounts for 20.7%, and the rest of the tank accounts for 23.1% of the energy dissipated by the working fluid.

The study of flow pattern and energy dissipation in the Silverson L4R-T rotor-stator mixer was continued, but with the emphasis on studying the effect of stator geometry [14]. Three different stator heads were investigated: the disintegrating head, slotted head, and square hole head. Again, the turbulent model used in FLUENT was the standard k-ε model. The mesh density was similar for each stator geometry, with 25 hexahedral cells across the disintegrating head openings, and 8 hexahedral cells across the slotted head and square hole head openings. With each

stator geometry, 5 hexahedral cells spanned the shear gap. The flow pattern in the stator slots was similar for each geometry. However, the extent to which the jet protruded from the opening was proportional to stator slot cross-sectional area. It was concluded that the square hole head dissipated the most energy, compared to the slotted head and disintegrating head.

Flow patterns and power draw have also been studied in a Silverson mixer with disintegrating and square hole heads, and in a Ytron Z unit [15]. The Silverson mixer contained two radial flow rotor-stator stages, and the Ytron Z unit has three stages. The mesh contained 3 million tetrahedral and hexahedral cells, with majority of the cells located in the mixer head region. The selected turbulence model was the realizable k-ε model. The Silverson mixing heads showed emerging jets from the stator holes, the Ytron Z unit did not show this behavior due to the different rotor geometry. Additionally, the Silverson mixing heads showed higher energy dissipation rate in the rotor swept volume and jet region, the Ytron Z unit showed relatively uniform distribution of energy dissipation. The Ytron Z unit velocity field shows no recirculation, zones while the Silverson mixing heads do not.

To the author's knowledge, the only published work showing LES results for an in-line high-shear mixer is from Xu and coworkers [16]. The studied unit was the pilot-scale FLUKO, FDXI in-line high-shear mixer. The mixer has two rows of ultrafine teeth and the fluid body was discretized into two meshes: one with 2 million cells and the other with 3.6 million cells. The standard RANS k-ε model and LES turbulence model with the Smagorinsky-Lilly SGS eddy viscosity model were compared to LDA experimental data. Compared to a Silverson mixer with a fine screen head, this ultrafine (teeth) high-shear mixer consumed 60% more power while operating at the same flow number. The instantaneous results from LES were angularly averaged across one revolution, with thirty periods per revolution. It was concluded that the predicted power

draw from LES agreed with experimental data. It was also concluded that LES predicted flow patterns well in regions of high vorticity and anisotropy.

5 RANS Simulation Results

This section discusses the RANS results, including flow rate at various planes within the mixer, power requirements to spin the rotors and shaft, and a description of the fluid deformation within the shear gap. Turbulent kinetic energy and energy dissipation rate predicted from the realizable RANS k-ε model are also discussed. Unless otherwise noted, all results presented in this section are from the hex 20M mesh and 7-psi backpressure operating scenario. Results with different mesh refinement and operating scenarios are also compared. This chapter concludes by quantifying the level of convergence of the flow field in these simulations as ascertained.

5.1 Mean Velocity Field in Stator Slots

Several planes located in various regions throughout the Greerco pipeline mixer are used to investigate the flow field. These data planes are shown in figure 5.1 below. The x = 0 mm plane (shown in gray) is the center plane of the mixer and is used to investigate flow through the stator slots. The z = 0 mm plane is shown in figure 5.1 (in green) to indicate where the origin is however no flow field information is presented from this data plane. The z = 40 mm and z = 80 mm data planes (shown in red) show information from the primary and secondary rotor respectively. The z = 60 mm and z = 100 mm data planes (shown in blue) are used to investigate flow through the stator slots from a different perspective compared to the x = 0 mm plane.

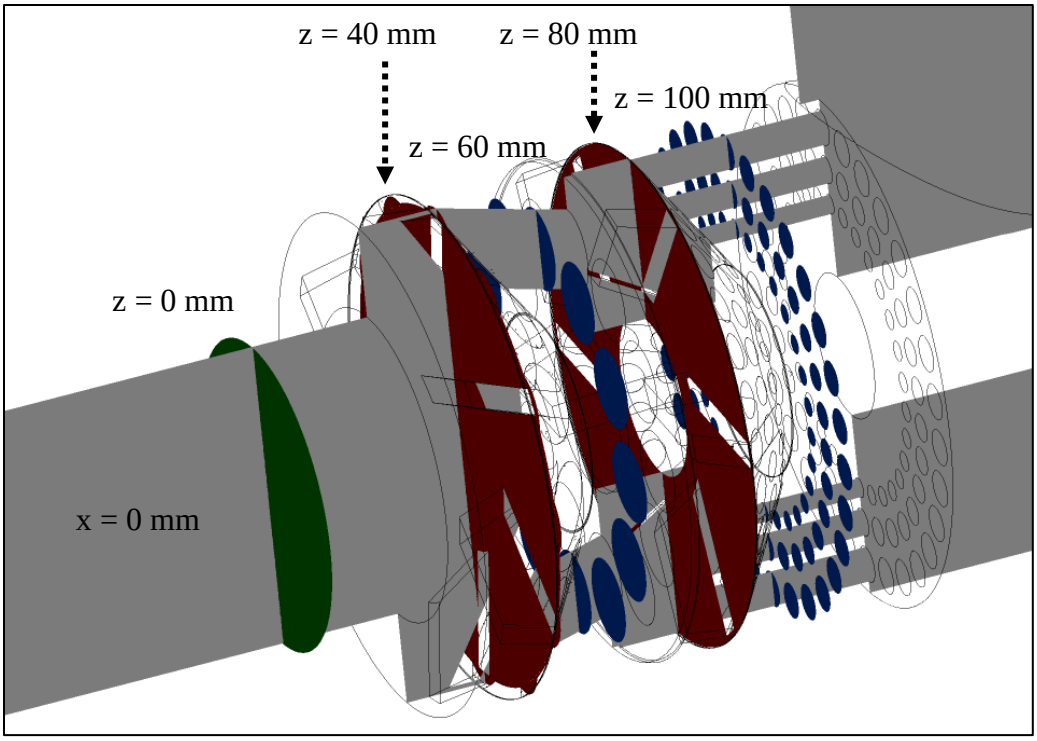

Figure 5.1 – Data planes and their locations in the Greerco pipeline mixer. Inlet, volute, and outlet regions extend beyond figure boundaries.

To understand the flow within the stator slots, the behavior of the flow within the rotor region must first be explained. The average plug flow velocity profile is introduced into the rotor region from the inlet pipe as a boundary condition. The six rotor blades force the fluid to move in a tangential direction. Shown in figure 5.2 below is the velocity field in this region. Note that the blades are pitched and are therefore shown as slanted white shapes in this figure. The relative blade speed increases with rotor radius and as a result, the fluid velocity increases further away from the centerline of the inlet pipe. This behavior implies that higher fluid velocity is expected on the outer edge of the stator slots. It should be noted that the rotor is conical in shape and so the maximum tip speed of the rotor blade decreases along the axial direction. As indicated by equation 3.1-3 this tip speed is a function of rotor speed (N) and maximum rotor diameter (D), these two parameters are used to normalize flow variables below. All figures presented in this section have the same

rotor position as shown in figure 2.7. In this rotor position, a primary rotor blade is in front of primary slot 6 and a secondary rotor blade covers secondary slot column 18.

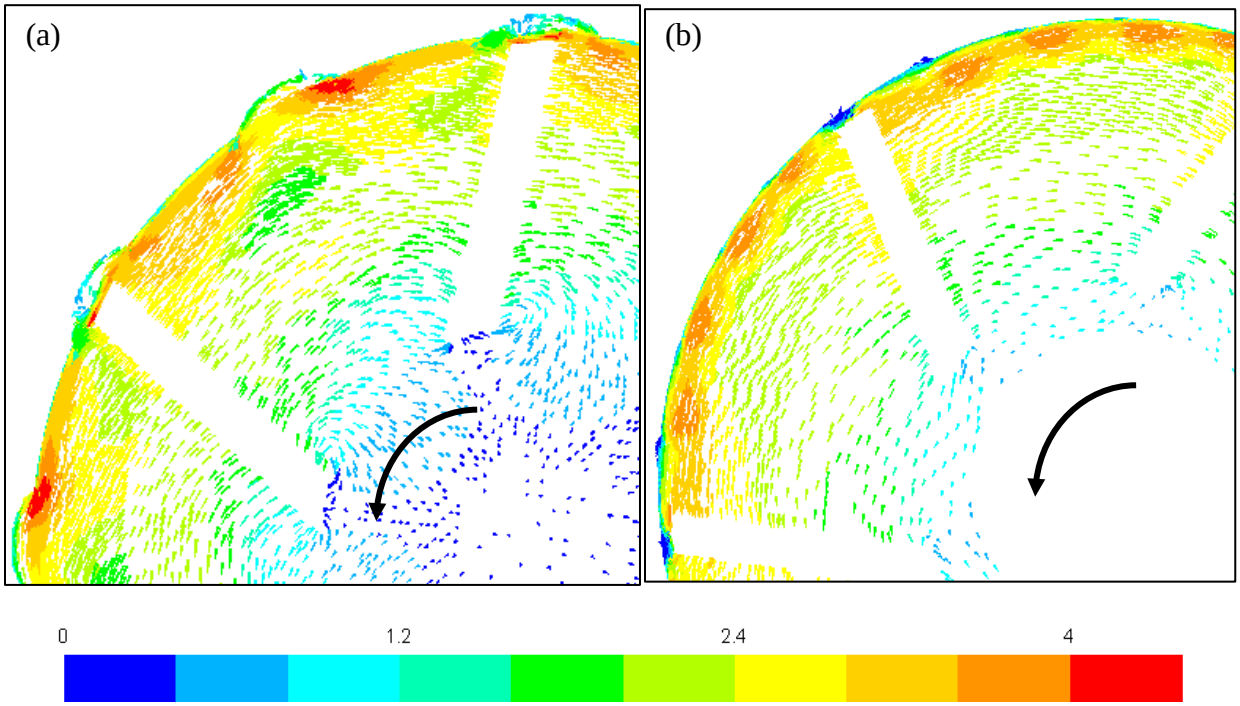

Figure 5.2 – Mean velocity field colored by velocity magnitude in the (a) primary rotor, z = 40 mm, and (b) secondary rotor, z = 80 mm, regions. Showing top left quadrant of rotor stages. Color legend scaled by (ND) = 5.8 m/s. Skipped every two arrows. ΔP = 7 psi, hex 20M.

Another flow property to consider in the rotor region is the static pressure distribution, provided in figure 5.3. As the rotor blade sweeps the flow, a pressure distribution varying between the blades develops. For this reason the static pressure contour is scaled by the inertial scaling of pressure using the fluid density, rotor speed, and maximum rotor diameter. In front of the blade a higher pressure region develops, conversely behind the blade a lower pressure region develops. This pressure distribution explains the periodic behavior observed in the throughput in the stator slots. As the blade approaches a slot, the higher pressure region momentarily increases the throughput in that slot. After the blade passes the slot the throughput lowers to a minimum. This behavior is explained in further detail in section 5.3.

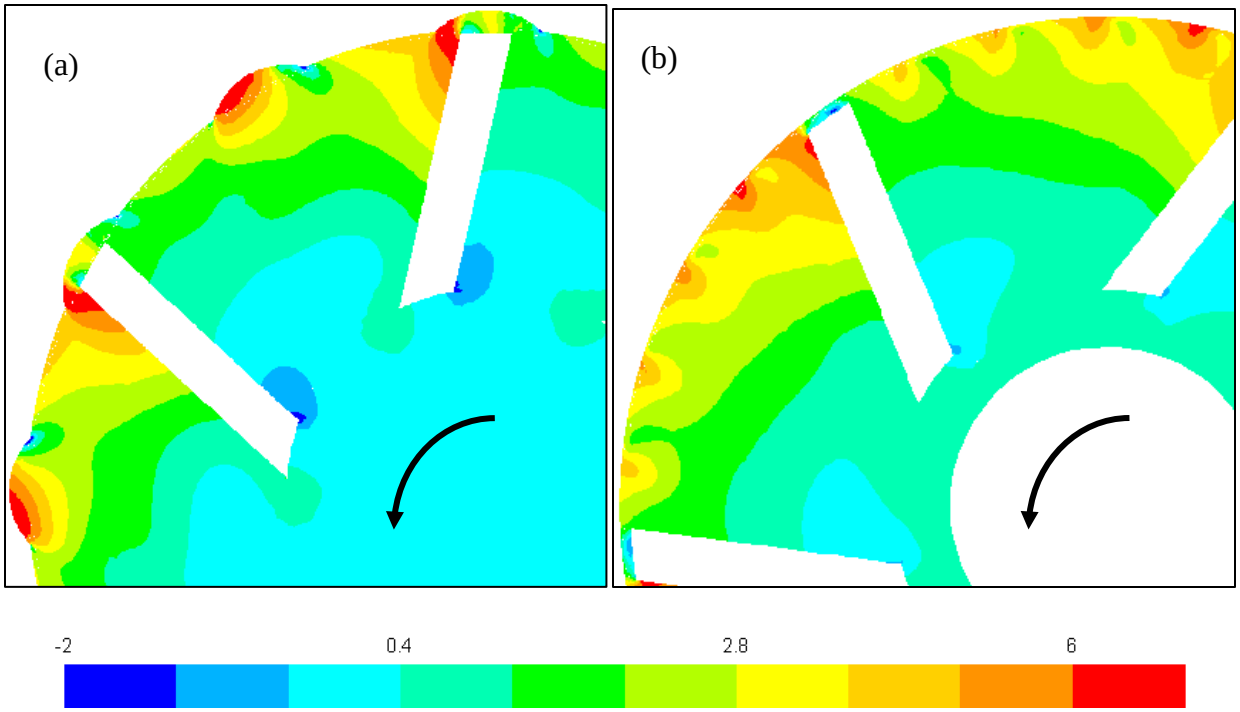

Figure 5.3 – Mean static pressure distribution in the (a) primary rotor, z = 40 mm, and (b) secondary rotor, z = 80 mm, regions. Showing top left quadrant of rotor stages. Color legend scaled by $\rho(ND)^2$ = 33.64 kPa. ΔP = 7 psi, hex 20M.

As explained in section 2.1, the rotor blades are pitched to ensure high axial throughput in the stator slots. The configuration of the stator slots also force the fluid to flow in an axial direction. Shown in figure 5.4 below is the velocity field in the primary and secondary stator slots. This figure also depicts the higher velocity occurring on the outer edge of the stator slots. All slots show a recirculation region on the inner edge of the stator slots. This recirculation is a result of the obtuse geometrical angle between the slot and the conical rotor region. Between the high axial velocity on the outer edge and the recirculation on the inner edge, a time-averaged vortex is developed. The size of this vortex is of similar size to the smallest local length size which is the diameter of the slot. Two other time-averaged vortices are observed downstream in the middle and inner secondary stator slots. These vortices are not a result of the geometry, but the imposed backpressure and will be discussed in detail in section 5.6.

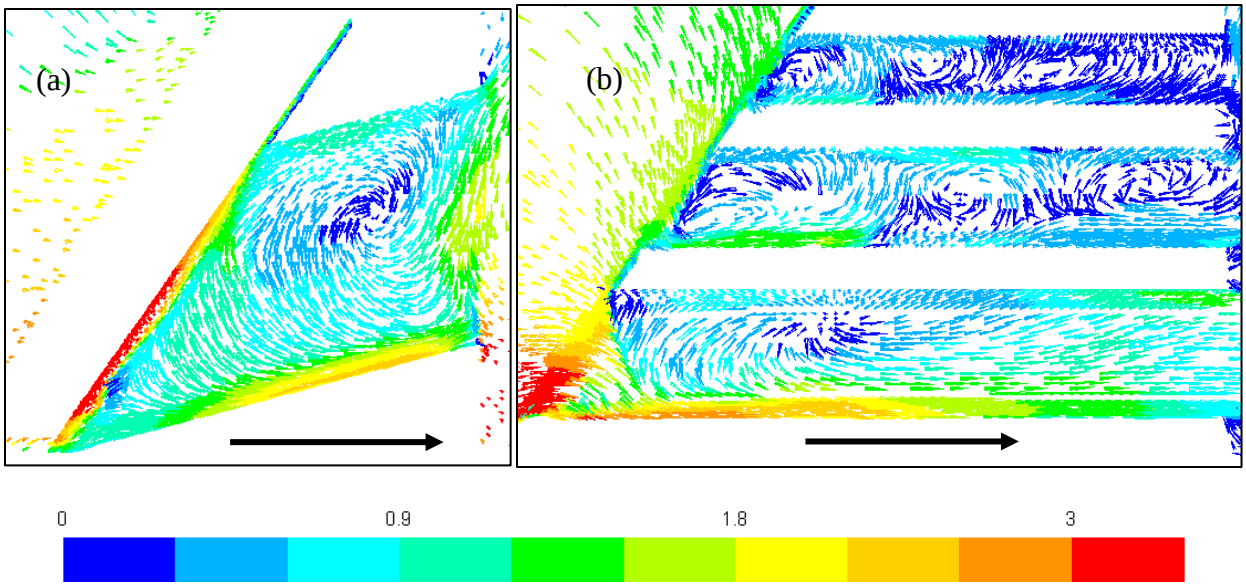

Figure 5.4 – Mean velocity field colored by velocity magnitude in the center plane, x = 0 mm, for the (a) primary stage and (b) secondary stage. Showing bottom half of the center plane. Color legend scaled by (ND) = 5.8 m/s. Skipped every three arrows. ΔP = 7 psi, hex 20M.

Provided in figure 5.5 is a different perspective of the time-averaged vortex at the slot tips. The vortices spin in the clockwise direction. It should be noted that the velocity profile within the slots changes slightly with rotor position. In figure 5.5, the primary rotor blade is over primary slot 6 and the secondary rotor blade covers secondary slot column 18 (see figure 2.7). As the blade covers the slot, the lower pressure region causes the recirculation region to increase in size and the vortex shifts closer towards the center of the slot. The velocity profile is different among the secondary stator slots as indicated in figure 5.4 and figure 5.5. The outer secondary slot shows higher axial velocity than the secondary inner and middle. This is a manifestation of the relative high tip speed of the conical rotor blade. We expect the throughput in the outer secondary slots to be significantly higher than the throughput in the inner and middle secondary stator slots.

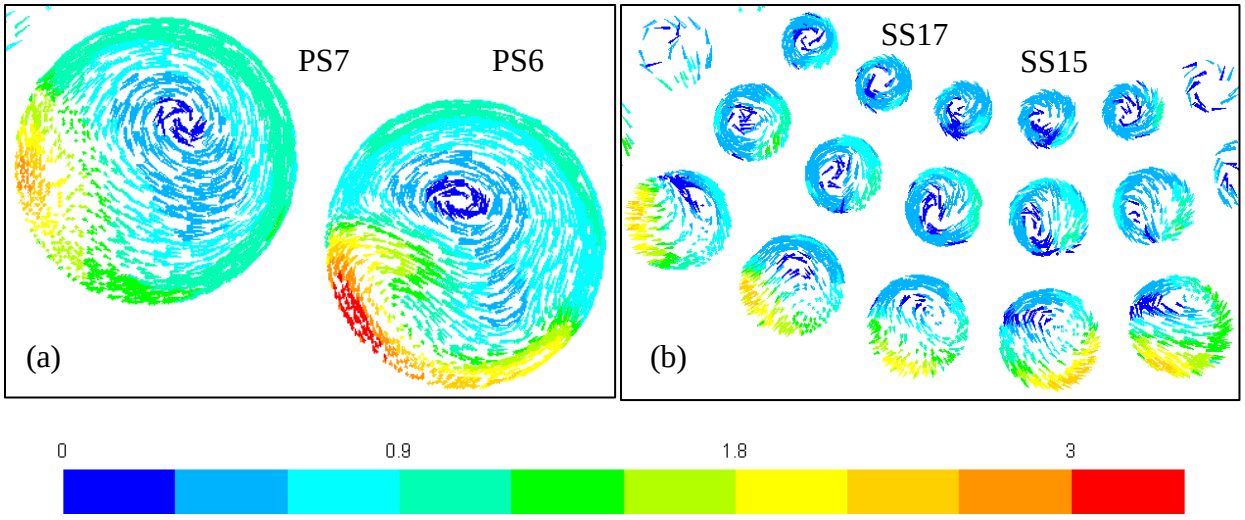

Figure 5.5 – Mean velocity field colored by velocity magnitude in the (a) primary stator, z = 60 mm, and (b) secondary stator, z = 100 mm, regions looking upstream. Showing one rotor period of stator slots. Color legend scaled by (ND) = 5.8 m/s. Skipped every three arrows. ΔP = 7 psi, hex 20M.

5.2 Mean Velocity Field in Shear Gap

The mean velocity in the gap between the rotor blade and stator wall will be predominantly tangential. To satisfy the no-slip boundary conditions at the rotor and stator walls, a large velocity gradient forms in the shear gap region. In high-shear mixers, high strain rates are found in the shear gap ranging from 2×10^4 s^{-1} to 1×10^5 s^{-1} [1]. In this section, the velocity field and corresponding strain rate magnitude contour is described as the blade passes over a primary stator slot. Time-averaged structures in this region such as the tip vortex and mixing layer are discussed.

First the velocity field in this region is shown. Shown in figure 5.6 is the velocity field as the blade passes over primary slot 6. Since the blade is conical in shape and decreases in radius farther down the centerline, the relative tip speed is dependent on axial location. The max rotor radius is 48.3 mm with a tip speed of 18.2 m/s. For the given axial position, the rotor radius is 43.5 mm with a tip speed of 16.4 m/s, which is used to scale the velocity field in these figures. As the blade passes over the slot, flow is driven towards the outer edge in agreeance with the previous

section. On the other edge, recirculation develops from the passing rotor blade. Contrary to the time-averaged vortices in the previous section which size were on the order of the diameter of the slot, this time-averaged vortex is closer in size to the width of the rotor blade.

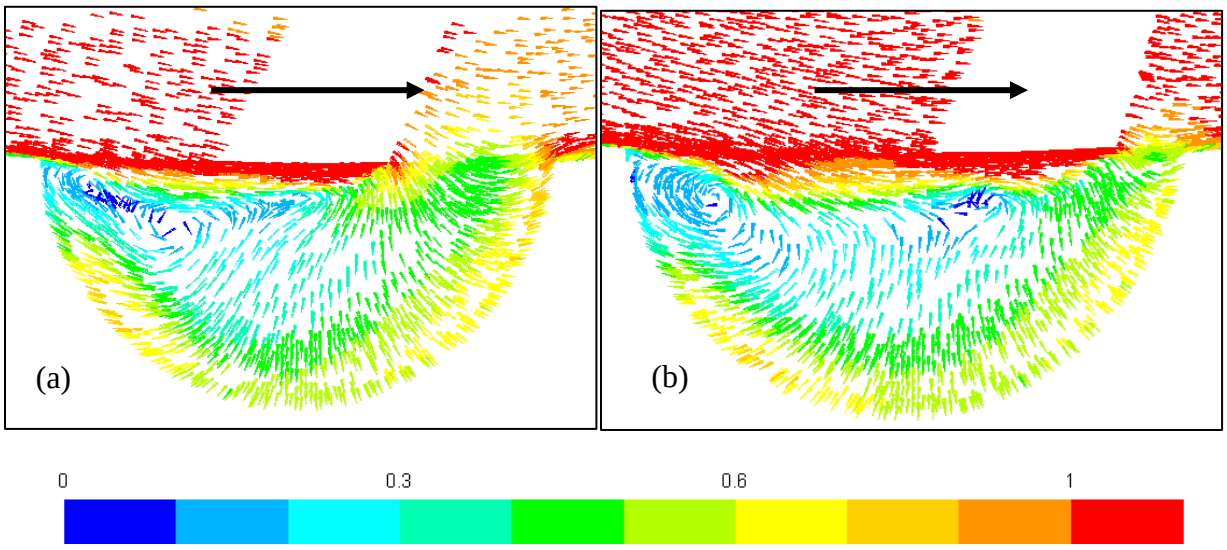

Figure 5.6 – Mean velocity field colored by velocity magnitude and scaled by relative tip speed of 16.4 m/s in the primary shear gap region when (a) the blade is near the center of slot and when (b) the blade is leaving slot. The view is of primary slot 6, normal to shear gap. Skipped every 2 arrows. ΔP = 7 psi, hex 20M.

This vortex, shown in figure 5.6a, stretches as the blade begins to pass over the slot. A large change in velocity develops between the blade tip and center of the vortex. This relatively large velocity gradient describes a mixing layer where deformation rates are high. Then once the blade has nearly passed over the slot, as in figure 5.6b, flow is pushed against the outer slot wall contributing to the stator jet. With the high velocity at the outer stator edge and low pressure region behind the blade, the time-averaged vortex remains at the other edge of the stator slot. When the next blade approaches the slot, the time-averaged vortex stretches and then decreases in size but never diminishes.

The large velocity gradients predicted in figure 5.6 can be shown in a different perspective using strain rate magnitude contours. Using equation 3.4-4 for the mean strain rate tensor,

figure 5.7 was developed. The rotor position shown in this figure is equivalent to the one shown in figure 5.6. With a relative tip speed of 16.4 m/s and a shear gap width of 0.25 mm, equation 3.4- 5 was used to compute a nominal shear rate of 6.56×10^4 s^{-1}. This was used to scale the color legend for this strain rate magnitude contour.

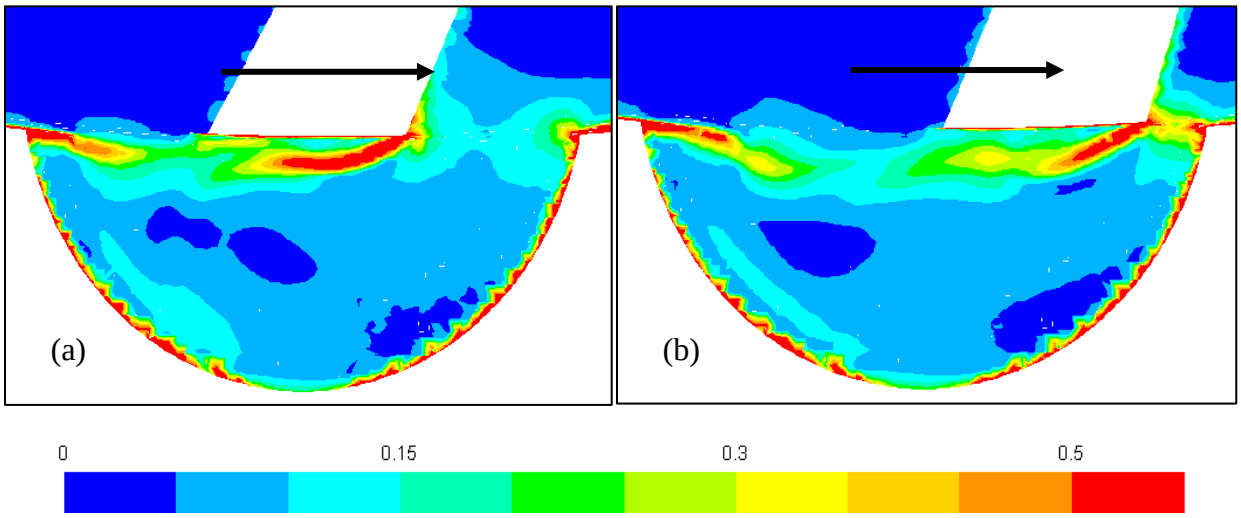

Figure 5.7 – Mean strain rate magnitude contour scaled by the nominal strain rate magnitude of 6.56×10^4 s^{-1} in the primary shear gap region when (a) the blade is near the center of slot and when (b) the blade is leaving slot. The view is of primary slot 6, normal to shear gap. $\Delta P = 7$ psi, hex 20M.

The high mean strain rate magnitude at the blade tip agrees with the change in velocity observed in figure 5.6. Two other regions in the stator slot opening show high strain rates. The outer edge of the stator slot where the flow is pushed to contribute to the stator jet shows a region of high strain rate magnitude. This large velocity gradient occurs because the stator jet velocity is high in comparison to the no-slip boundary nearby. The other region of high strain rate is the other edge of the stator slot. This region is developed from the time-averaged vortex that persists even as the blade has passed.

Data planes spanning the primary and secondary shear gap at varying angular values were used to quantify the mean strain rate magnitude in this region. These planes were drawn at the

center of the shear gap, in degrees this is ±15° for primary and ±6° for secondary, at the center of the slot corresponding to 0°, and between these locations. The 0° position is shown in figure 2.2. To show how the deformation rates vary with time or rotor position, an average strain rate magnitude was computed across each plane. Similar to the strain rate magnitude contours above, these data were normalized by the maximum nominal strain rate of 7.3×10^4 s^{-1}, and is shown in figure 5.8 below.

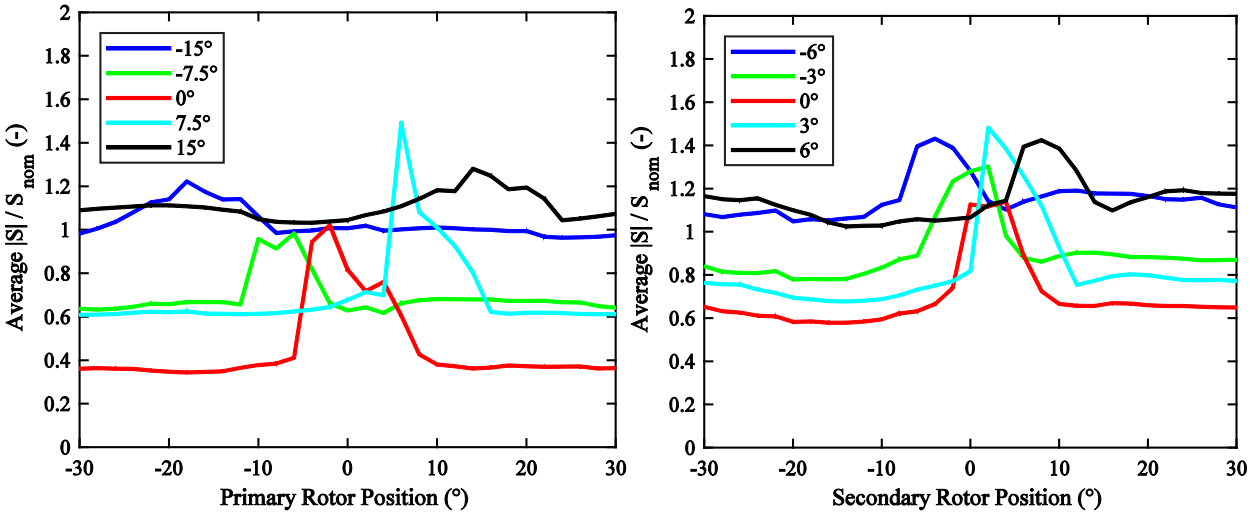

Figure 5.8 – Spatially averaged strain rate magnitude for the (a) primary and (b) secondary shear gaps. ΔP = 7 psi, hex 20M.

From figure 5.8 it is clear that the strain rate magnitude across a plane reaches its maximum value when the blade passes by that particular region. The maximum values attained in the shear gap, before and after the slot is similar. However, the average strain rate reaches a different maximum across the data planes that are placed in the slot opening. For both the primary and secondary stages, the strain rate maximum is larger for the data plane placed at 7.5° and 3° degrees respectively. Another noteworthy difference between the data planes at the center of the shear gap and at the center of the slot is that a higher strain rate magnitude is observed when the blade is not present for the planes at the center of the shear gap. Comparing the primary stage to the secondary,

higher normalized averaged strain rates are observed in the secondary. However since more stator slots are present in the secondary, the length of the shear gap between slots is less and so the maximum strain rate value is not maintained longer than for the primary.

5.3 Throughput and the Flow Number

For a pipeline mixer, the flow rate within the inlet, outlet, and stator slots are of interest to industry and those who use this Greerco pipeline mixer. The flow rate within these regions is expected to vary depending on operating scenario, i.e. different pressure requirements. In addition, since the rotor blades cover certain stator slots at a given time, the flow rate in these slots will vary with rotor position. FLUENT can output velocity field data across a given plane. From this, the axial velocity component can be determined and used to compute the throughput. This was completed for the inlet (z = 0 mm), the primary slots (z = 60 mm), and secondary stator slots (z = 100 mm). Using this approach, it was found that the flow rate across the inlet plane does not vary significantly with rotor position.

As discussed in section 5.1, the flow within the primary and secondary stator slots are strongly influenced by the flow in the rotor region, causing the throughput to vary with rotor position. This is shown in figure 5.9 below. By collecting flow rate data across one rotor period, an angularly averaged flow rate can be computed. This value is represented by $Q_{average}$ and as a flow number in the caption of figure 5.9. Since this angularly average flow rate is constant with rotor period by construction, deviations from this average show the extent and the behavior of throughput as a function of rotor position. Additionally, these angularly resolved flow rate deviations rate can be nondimensionalized by normalizing the quantity with the angularly averaged value. Normalizing the flow rate in this manner shows what percentage of the average is deviating

at any given rotor position. It should be noted that since these results are from a RANS simulation, these so-called *angularly resolved deviations* are deviations from the overall converged flow rate.

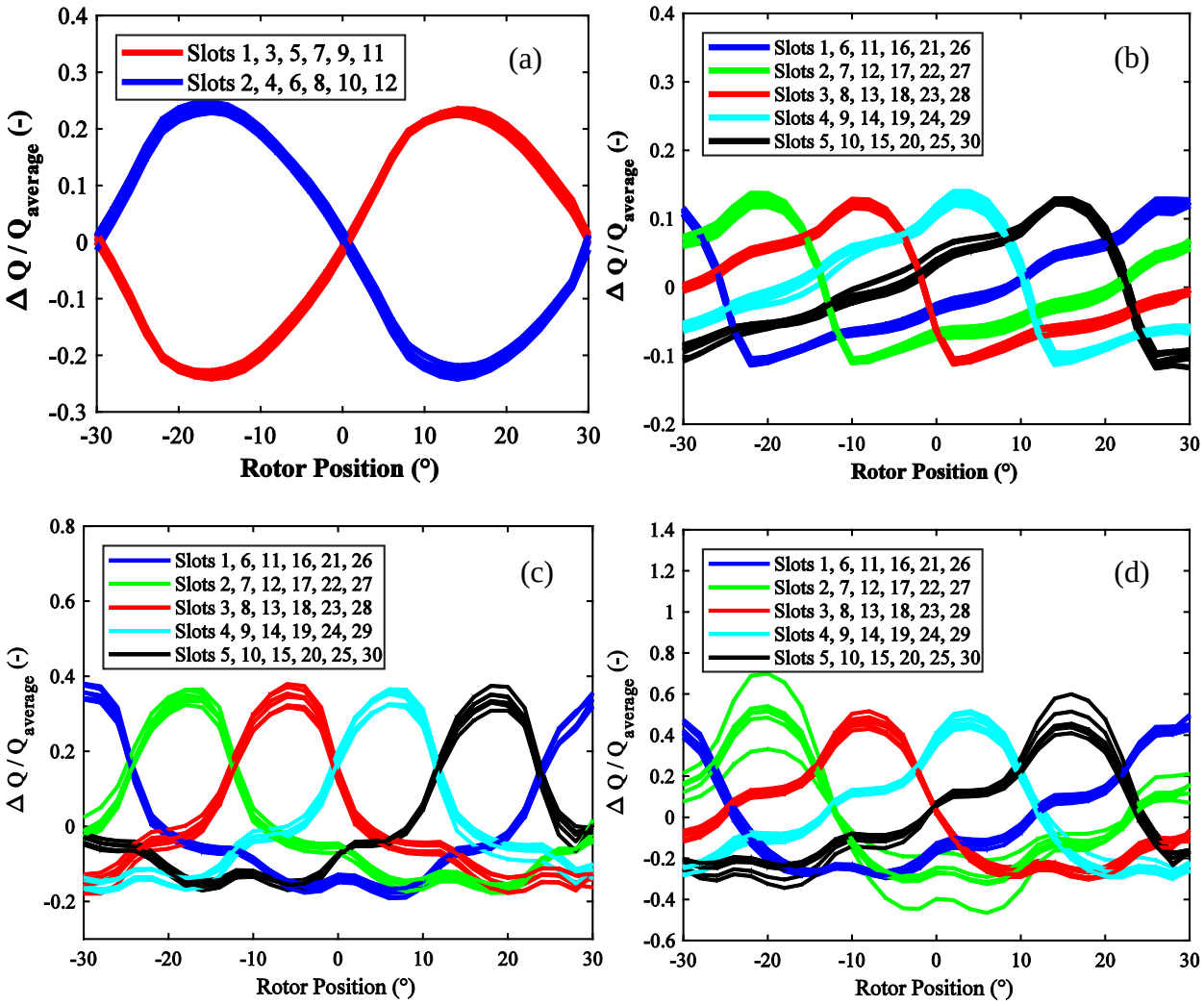

Figure 5.9 – Dimensionless flow rate versus rotor position in: (a) primary stator $Q_{average} = 6.0 \times 10^{-4}$ m^3/s (N_Q = 0.0111) (b) secondary outer slots $Q_{average} = 2.0 \times 10^{-4}$ m^3/s (N_Q = 0.0037), (c) secondary middle slots $Q_{average} = 3.0 \times 10^{-5}$ m^3/s (N_Q = 0.0006) and (d) secondary inner slots $Q_{average} = 8.2 \times 10^{-6}$ m^3/s (N_Q = 0.0002). ΔP = 7 psi, hex 20M.

Different color curves are shown in figure 5.9. These curves are grouped according to the provided legend. The number of types of curves is equivalent to the number of slots per number of blades. For example, the primary stage has twelve slots and six blades, therefore two different types of curves. The secondary stator is similar, however each row must be considered individually

(a row of secondary stator slots consists of one outer, one middle, and one inner slot all at the same angular position). It should be noted that the average flow number in the secondary inner and middle slots is significantly lower than the outer slot. This result is expected given the discussion in section 5.1.

To explain the shape of these flow rate curves, the position of the blade relative to a given slot must be considered. It was shown in figure 5.3 that there is higher static pressure in front of the blade, which would imply high throughput as the blade approaches a slot. Conversely, low static pressure behind the blade would imply low throughput once the blade has passed a slot. As an example take figure 5.6a. At the rotor position of 15 degrees the blade is approaching primary slot 1 and passing primary slot 12. Indeed a maximum in the flow rate is observed in slot 1 (~25% above the average) and a flow rate minimum in slot 12 (~25% below the average). The angularly resolved flow rate deviations in the primary slots closely compare to a sinusoidal curve. However the angularly resolved flow rate deviations in the secondary slots resemble a different shape. As shown in figure 5.8b less time is required to obtain the minimum throughput than the maximum. This implies that the flow rate in a given slot only decreases as the blade moves to the next adjacent slot, and once the blade moves past the adjacent slot the flow rate in the given slot begins to increase.

Ideally each flow rate curve in a given set would have the same value at a given rotor position. However, the flow rate curves of a given color in figure 5.9 may vary at the same rotor position. These differences occur due to the different distances each slot in a given set may have from the outlet pipe. The outlet pipe, which is perpendicular to the centerline of the mixer, is closest to slots 28, 29, 30, 1, and 2, by the slot naming convention discussed in section 2.1. Some flow rate curves show higher deviations from the others in a given set, in particular the green flow

rate curves in figure 5.9d of the secondary inner slots. These larger deviations imply the flow rate from these slots has not converged. This is discussed in more detail in section 5.8.

5.4 Power Draw Requirements

The power required to operate the motor which turns the shaft and rotor within the mixer is of interest to industry and to those who use rotor-stator mixers. This power draw is a measure of the small scale mixing capability in rotor-stator mixers. For this reason, the CFD simulations considered in this study are used to provide power draw predictions for the Greerco mixer. By Newton's second law, the torque to operate the motor is equal and opposite of the torque to move the necessary components within the mixer. As a multi-stage mixer, the power draw will be reported for the primary rotor and the secondary rotor. The power draw to move the shaft is relatively small and is neglected. A summation of the power to rotate all these moving parts gives the total power to operate the motor.

Power is computed from the torque using equation 3.1-6. Since the power and power number are proportional to the torque, the torque for each stage of this rotor-stator mixer are shown at varying rotor position. Similar to the angularly resolved flow rate deviations shown in the previous section, dimensionless angularly resolved torque deviations can be computed relative to the angularly averaged torque. This angularly averaged torque is represented as $T_{average}$ and as a power number in the caption of figure 5.10. The angularly resolved torque deviations are shown in figure 5.10 below.

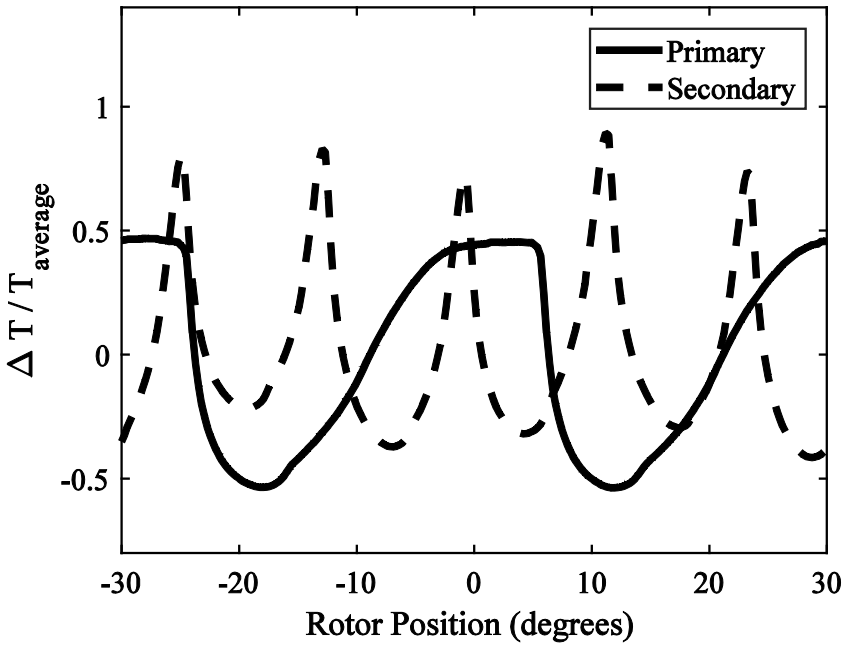

Figure 5.10 - Dimensionless primary (solid) and secondary (dashed) rotor torque versus rotor position. For the primary rotor, average torque is 4.51 Nm (N_{Po} = 0.932) and for the secondary rotor it is 4.71 Nm (N_{Po} = 0.973). ΔP = 7 psi, hex 20M.

As flow rate in a slot is dependent on rotor position, so is the torque for each stage. The number of oscillations in torque for a given stage is the number of slots per number of blades. This was also observed for the different sets of flow curves. The torque reaches its maximum value (~50% of the average for the primary and ~75% for the secondary) when the rotor blade covers the slot. Two peaks are observed for the primary stage torque since the six blades can cover a set of six slots for two instances in a rotor period. This is similar for the secondary stage, but with five peaks instead. A minimum in the torque occurs when the blade is not covering any portion of the slots, allowing for axial flow in all slots. The location of these maximum and minimum torque values relative to the rotor position imply that torque is dependent on amount of fluid being displaced.

It is obvious from figure 5.10 that the torque fluctuations for each stage take different shaped curves. Since the geometry of the rotor blades does not change with each stage, this

difference in torque fluctuations must be a result from the difference in stator geometry. The primary stator slots are larger in diameter compared to the width of a rotor blade. The opposite is true for the secondary stator slots. The maximum in the primary torque is sustained because the entire rotor blade width is used to cover a portion of the primary stator slots for several rotor positions. The maximum in the secondary torque occurs only for an instant because the rotor blades cover 18 secondary stator slots at 5 different rotor positions. This reasoning implies that the duration of the maximum in torque oscillations depends on the width of the rotor blade relative to the diameter of the adjacent stator slot. Since the maximum torque in the primary stage is sustained longer, the time-averaged torque is larger than the torque in the secondary stage.

Another characteristic in the primary stage torque fluctuations is that one oscillation, represented by half a rotor period, is similar to the next. This is not true for the secondary stage torque fluctuations. The local maximum/minimum varies from one oscillation to the next, where a single wave in the secondary stage torque is represented by one fifth of a rotor period. This change in secondary stage oscillations represents the influence the primary stage has on the secondary. The secondary stage torque at any given rotor position is dependent on the primary stage torque at that position.

5.5 Turbulent Kinetic Energy and Energy Dissipation Rate

As explained in section 3.7, the turbulent kinetic energy represents the energy associated with velocity fluctuations. Turbulent kinetic energy is therefore a measure of mixing intensity. The rate at which the turbulent kinetic energy dissipates is also of interest in mixing. As shown in section 3.9, the turbulent energy dissipation rate and kinematic viscosity together represent the scales in which inertial and viscous forces balance. These scales describe the smallest scales in which mixing occurs and where particles are most likely to break and coalesce.

In this section the turbulent kinetic energy and the energy dissipation rate are quantified in the rotor and stator regions of the Greerco mixer. The same rotor position is used for all figures in this section, this rotor position is depicted in figure 2.7. The results below are from a RANS k-ε model in which both turbulent kinetic energy and the energy dissipation rate model equations are solved to close the RANS equations. Aside from numerical error, the results shown are as valid as the assumptions made to develop these model equations. The assumptions made to develop the RANS k-ε model are summarized in section 3.7. Contours of the turbulent kinetic energy and its isotropic dissipation rate are explained in terms of mixing.

First, turbulent kinetic energy contours are quantified. The turbulent kinetic energy in the primary and secondary rotor regions are shown in figure 5.11 and then for the primary and secondary center plane views in figure 5.12. The turbulent kinetic energy depends on velocity fluctuations. We expect these fluctuations to vary in magnitude with the time-averaged velocity. It is reasonable to scale the turbulent kinetic energy as the blade tip squared or with $(ND)^2$ where D is the maximum rotor diameter.

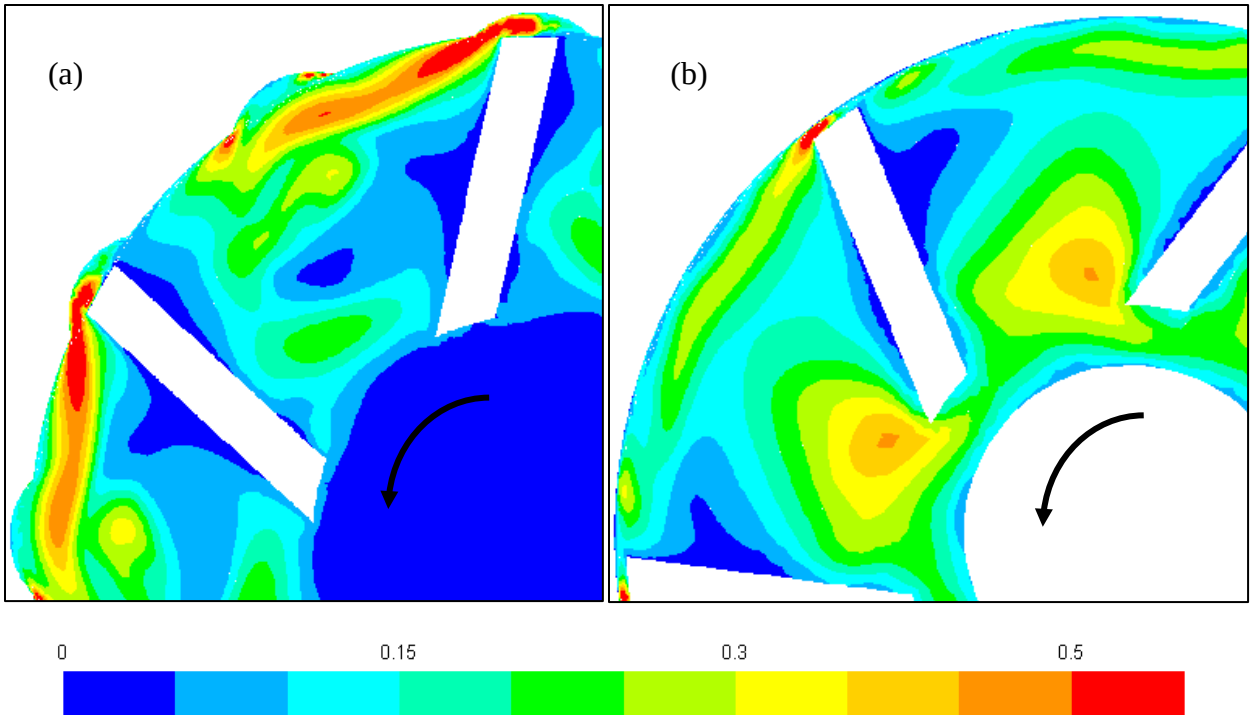

Figure 5.11 - Turbulent kinetic energy contour scaled by $(ND)^2$ = 33.64 m^2/s^2 in the (a) primary rotor, z = 40 mm, and (b) secondary rotor, z = 80 mm, regions. Showing top left quadrant of rotor stages. ΔP = 7 psi, hex 20M.

Both primary and secondary rotor regions show high turbulent kinetic energy at the blade tip, although a higher magnitude and spread of turbulent kinetic energy is observed for the primary stage. The spread protruding from the blade tip occurs because eddies travel tangentially with blade rotation and dissipate farther from the blade. At the outer edge of the stator slots, higher velocity fluctuations are observed as the flow is directed axially by the stator slots and directed tangentially by the movement of the rotor blade. High turbulent kinetic energy is shown in figure 5.11b between the secondary rotor blades close to the centerline. This phenomena does not occur due to the low relative blade velocity but instead from the exit of the primary stator slots.

From the center plane view show in figure 5.12, velocity fluctuations are higher in magnitude along the outer edge of the stator slots compared to the inner recirculation region. For the primary stator, the turbulent kinetic energy peaks at the exit. This region peaks in turbulent

kinetic energy since the flow is influenced by the movement of the secondary rotor. There is no peak in turbulent kinetic energy at the exit of the secondary stator since the flow is introduced into the volute and not another rotor stage. The two most inner secondary stator slots show low turbulent kinetic energy compared to the outer secondary slot. This occurs because the axial velocity in the inner and middle slots is significantly lower than in the outer slot, as observed in section 5.1.

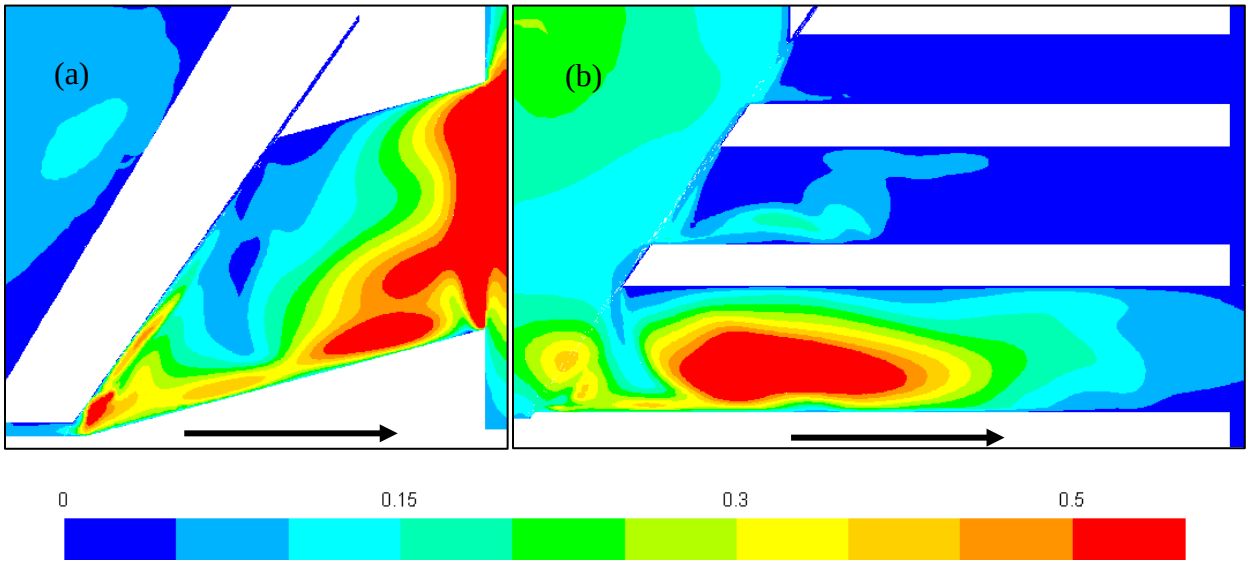

Figure 5.12 - Turbulent kinetic energy contour scaled by $(ND)^2$ = 33.64 m^2/s^2 in the center plane, x = 0 mm, for the (a) primary stage and (b) secondary stage. Showing bottom half of the center plane. ΔP = 7 psi, hex 20M.

Contours of the turbulence energy dissipation rate are shown in the rotor regions in figure 5.13 and in the center plane view in figure 5.14 below. The turbulent energy dissipation rate is scaled by N^3D^2 in these figures. As indicated by equation 3.7-6, turbulent energy dissipation rate

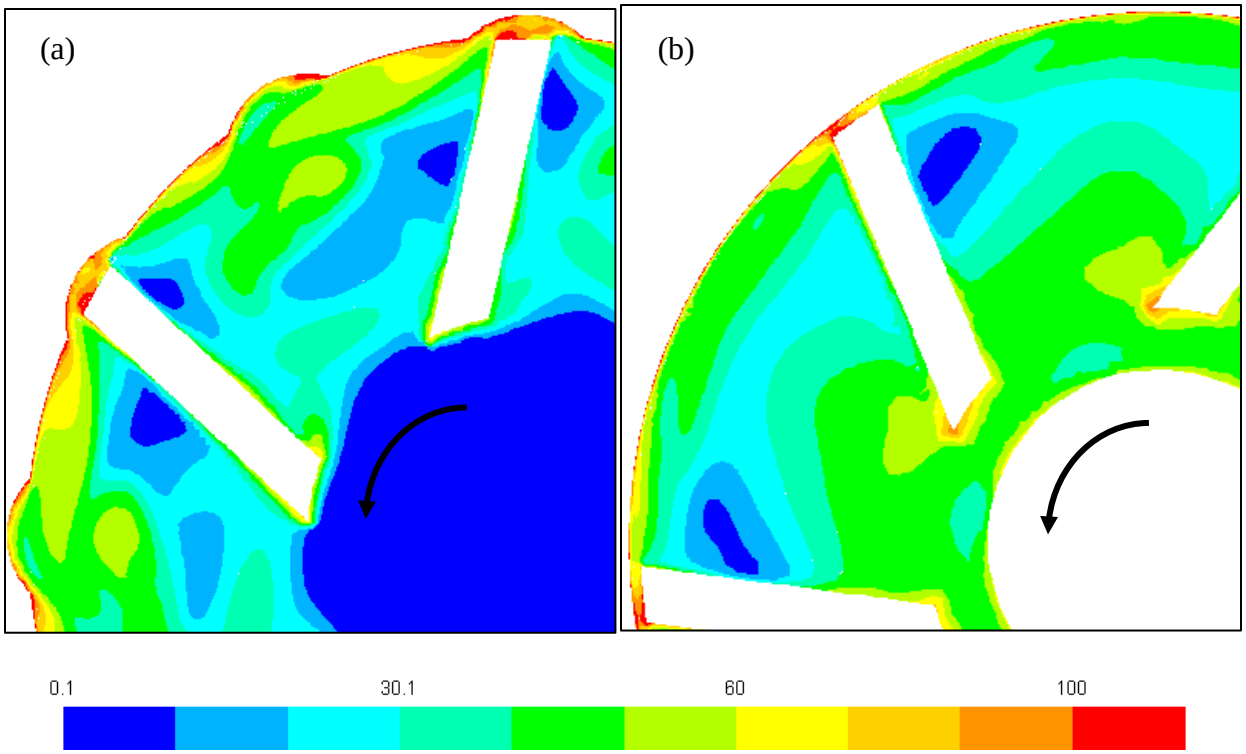

Figure 5.13 - Turbulent energy dissipation rate contour scaled by N^3D^2 = 2018.4 m^2/s^3 in the (a) primary rotor, z = 40 mm, and (b) secondary rotor, z = 80 mm, regions. Color legend is log scale. Showing top left quadrant of rotor stages. ΔP = 7 psi, hex 20M.

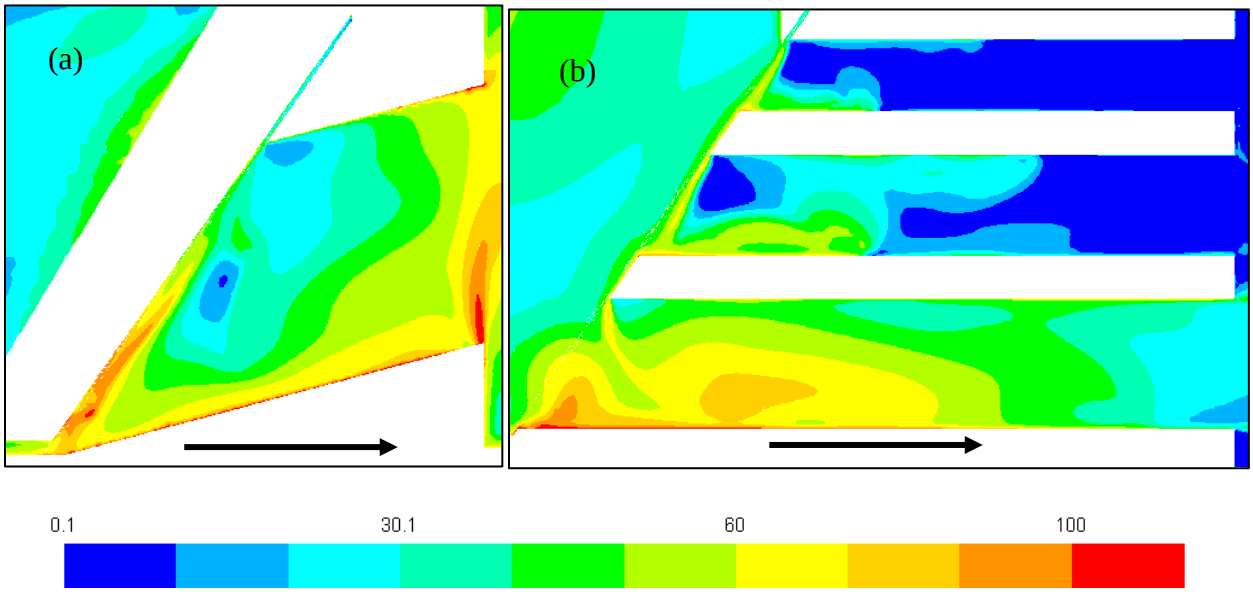

Figure 5.14 - Turbulent energy dissipation rate contour scaled by N^3D^2 = 2018.4 m^2/s^3 in the center plane, x = 0 mm, for the (a) primary stage and (b) secondary stage. Color legend is log scale. Showing bottom half of the center plane. ΔP = 7 psi, hex 20M.

is dependent on the fluctuating velocity gradient. We expect such a quantity to be high near the wall where the fluid must obey the no-slip boundary condition. This is observed at the stator wall in the rotor swept volume due to stagnation of the fluid from the movement of the rotor blades. Comparing the two stages, higher turbulent energy dissipation rate is observed for the secondary stage, particularly near the centerline.

Similar to the turbulent kinetic energy contours shown in figure 5.11, higher turbulent energy dissipation rate is observed at the outer stator slot edge compared to the inner recirculation region of the slot. This is another implication from fluid stagnation as the stator slots direct the flow from a tangential to an axial direction. At the exit of the primary stator slots, high turbulent energy dissipation rates are also observed as the fluid redirects from the axial to the tangential direction from the movement of the secondary rotor. Comparing the slots of the secondary stator, the outer slot shows higher energy dissipation rate than the middle and inner slots.

From the turbulent kinetic energy and energy dissipation rate contours provided by the RANS k-ε model, we can estimate the magnitude and regions of mixing intensity. The rotor speed determines the level of mixing intensity in the rotor swept volume and stator slots. The diameter of the rotor determines the level of mixing intensity at the blade tip where turbulent kinetic energy peaks. The outer edge of the slots, where the stator jet is located, contributes the most to mixing intensity and is the region in which particle dispersion is most likely to occur. Among the secondary stator slots, it is unlikely particles will be highly deformed in the inner and middle slots. The primary slots and outer secondary stator slots show similar energy dissipation rates.

5.6 Backpressure Influence on Mean Properties

In this section, results from the hex 20M mesh with the RANS k-ε model are presented and compared for the 0- and 7-psi backpressure operating scenarios. The influence this change in

backpressure has on the mean velocity field in the stator slots is shown. This resulting velocity field and the influence it has on the throughput and power draw is also discussed. The throughput of the secondary stator slots is presented as a distribution for a given rotor position. The flow distribution in the secondary stator slots is shown for the two backpressures. This section concludes by discussing the mean and turbulent energy dissipated throughout the primary and secondary stages as a function of backpressure.

The velocity field shown in figure 5.4 is reproduced and compared to the velocity field developed from the 0-psi backpressure scenario. This comparison for the primary stage is presented in figure 5.15 and for the secondary stage in figure 5.16. By lowering the backpressure imposed across the mixer, we expect the throughput to increase. This change should be evident in the area-averaged velocity profile in the stator slots. For reasons explained in section 5.1, a time-

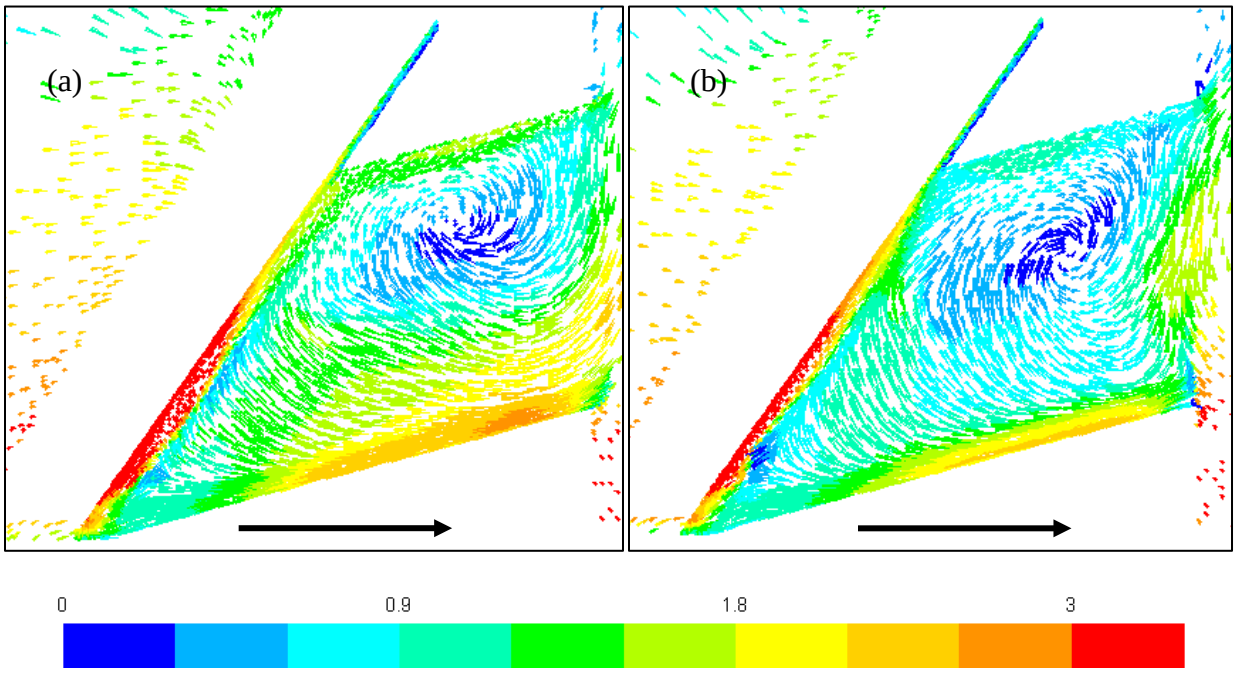

Figure 5.15 – Mean velocity field colored by velocity magnitude in the center plane, x = 0 mm, for the primary stage at the (a) 0-psi and (b) 7-psi backpressure operating scenarios. Showing bottom half of the center plane. Color legend scaled by (ND) = 5.8 m/s. Skipped every three arrows. Hex 20M.

averaged vortex is apparent in the primary slot for both the 0-psi and 7-psi backpressures. A noticeable difference in the velocity fields however is that the center of the time-averaged vortex in the 0-psi scenario is closer to the inner edge of the stator slot.

As this recirculation region changes in size and location, the stator jet region observed in the 0-psi scenario is larger than the 7-psi scenario. Then as the flow changes from the axial direction and moves radially inwards, a more gradual change is made for the 0-psi case as where the 7-psi case shows a steeper turn. By considering the cross-sectional plane across this primary stator slot, and computing the flow rate using equation 3.2-1, we would expect the throughput to increase since the axial stator jet region is larger in volume. A similar behavior is observed in the secondary outer slots, however less noticeable.

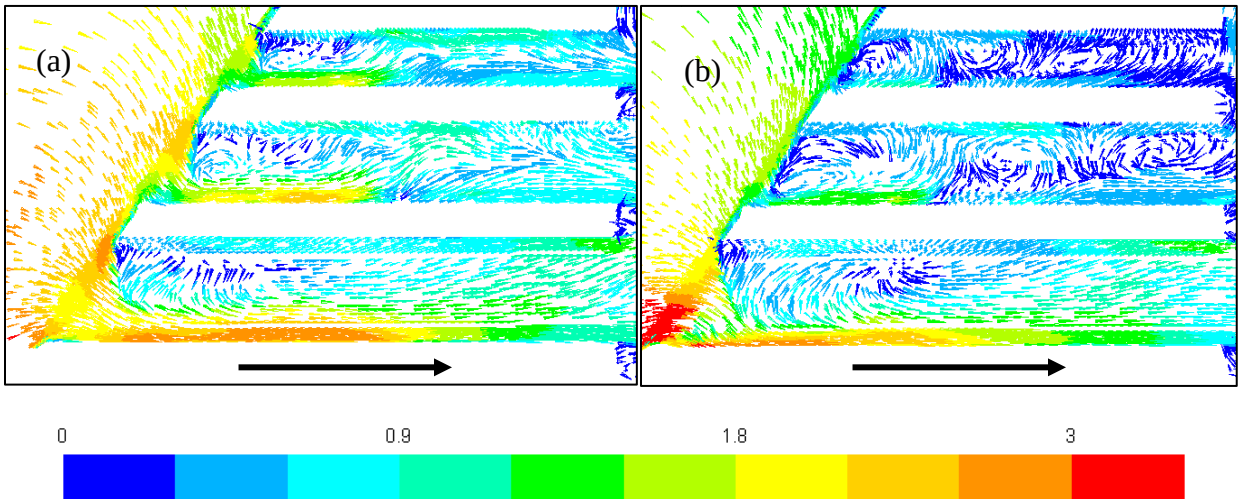

Figure 5.16 – Mean velocity field colored by velocity magnitude in the center plane, x = 0 mm, for the secondary stage at the (a) 0-psi and (b) 7-psi backpressure operating scenarios. Showing bottom half of the center plane. Color legend scaled by (ND) = 5.8 m/s. Skipped every three arrows. Hex 20M.

There is a significant change in the velocity field of the inner and middle secondary stator slots by changing the backpressure. With lower backpressure, the axial stator jet velocity is higher. An initial time-averaged vortex still develops near the entrance of the secondary inner and middle

slots for the 0-psi scenario, however the other two time-averaged vortices observed in the 7-psi scenario are not apparent in the 0-psi scenario. This suggests that the time-averaged vortex near the entrance of the stator slots is present due to the movement of the rotor blade and the configuration of the stator slot. Any other time-averaged vortices observed throughout the slot are present due to the imposed backpressure. If we again consider the cross-sectional plane spanning these stator slots, we would expect higher throughput. We would also expect the inner and middle secondary stator slots contributing more to the overall throughput for lower backpressures.

The significant change in the velocity field of the inner and middle secondary stator slots suggests quantifying a flow rate distribution for different backpressures. Shown in figure 5.17 is the amount of the flow through the secondary stator slots at a given rotor position and backpressure. The backpressures considered are 0-psi and 7-psi respectively. The values presented are percentages in which when summed will total to 100% for a single figure. The percentage in one slot is the amount of flow in that slot divided by the total flow from all slots in the given rotor period. Totals are also provided for each row of secondary stator slots.

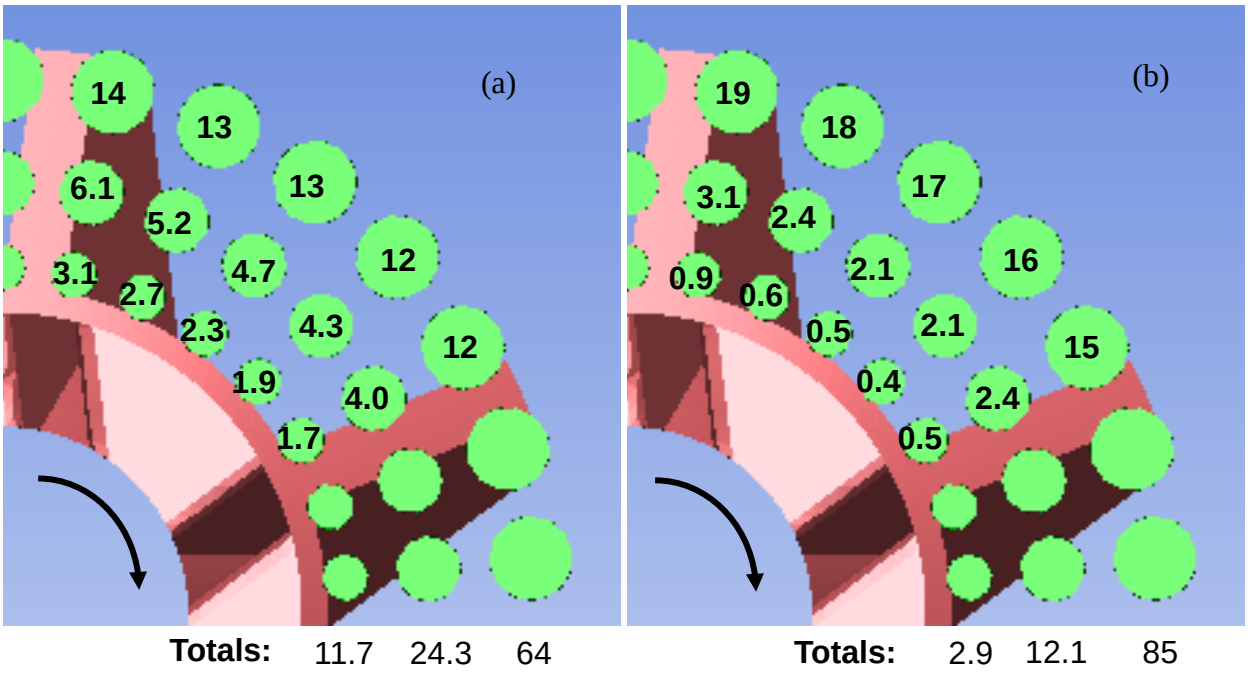

Figure 5.17 - Flow rate as a slot percentage in period of secondary stator slots for an instant in time for the (a) 0-psi backpressure and (b) 7-psi backpressure. Values shown are relative percentages. Hex 20M.

As discussed in sections 5.1 and 5.3, higher flow rate is observed in the outer slots compared to the inner and middle slots for any given backpressure. It was also noted that as the blade approaches a slot, the throughput increases and then decreases once the blade has passed. This phenomena is also observed by the larger values close to the approaching blade. As the secondary stator velocity field comparison suggests, the middle and inner slots contribute more to the throughput for lower backpressures. As backpressure increases, there is higher recirculation in the middle and inner slots causing less flow from those slots.

Angularly resolved flow rate deviations in all stator slots were shown varying with rotor position in figure 5.9 for the 7-psi backpressure. These deviations from the angularly averaged mean are reproduced in figure 5.18 to be compared to analogous deviations from the 0-psi backpressure simulation with the same hex 20M computational mesh. Flow rate trends are similar

among stator slots, as shown in figure 5.9. Therefore the flow rate in one slot from the primary stator (PS6) and in one secondary stator column (SS15) is shown. Vertical dashed lines are shown to indicate when the corresponding rotor blade is centered over the given slot. The angularly averaged value which these deviations center around vary significantly with backpressure, as indicated in figure 5.20 of the next section. In the primary slot, the flow rate varies less with decreasing backpressure. The maximum/minimum flow rate achieved at the 0-psi backpressure occurs at a different rotor position than the 7-psi backpressure. The flow rate deviations in the secondary outer slot are similar among each backpressure. However, the flow rate deviations in the secondary middle and inner slots changes with backpressure. This change is the result of differing velocity fields in these slots observed in figure 5.16. For the 0-psi backpressure, the flow rate deviates from the angularly averaged value less than the 7-psi backpressure. Also, the secondary middle and inner slot flow rate deviations from the 0-psi backpressure show a similar profile to the secondary outer flow rate deviation. This suggests that this profile occurs when the only time-averaged vortex occurs at the slot opening.

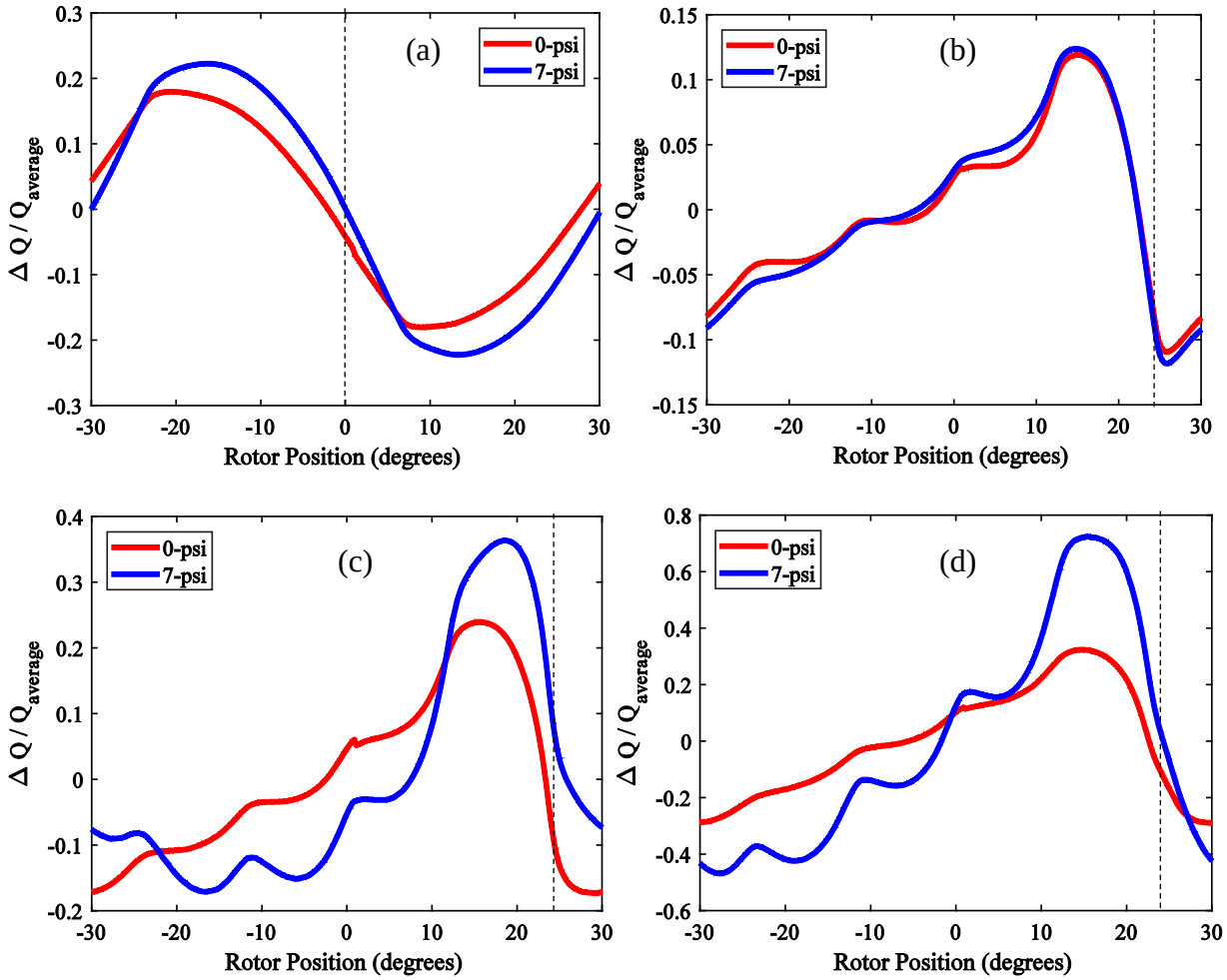

Figure 5.18 – Dimensionless flow rate versus rotor position for the 0-psi (red) and 7-psi (blue) backpressures in (a) primary slot 6, (b) secondary outer slot 15, (c) secondary middle slot 15, and (d) secondary inner slot 15. Hex 20M.

The magnitude and length of the axial stator jet increases with decreasing backpressure. With this increase in mean velocity we expect the fluctuations, and therefore turbulent kinetic energy, to increase as well. The rate in which this kinetic energy dissipates would also increase, both in terms of the mean and turbulent component. By integrating the strain rate magnitude and energy dissipation rate across a fluid volume, the energy dissipated in that region can be computed using equation 3.7-7. The energy dissipated by mean and turbulent velocity gradients were time-

averaged for one rotor revolution for the two backpressures. These values are shown in tables 5.1 and 5.2 below.

Table 5.1 – Turbulent energy dissipated in various regions for different backpressures.

	Primary Stage			Secondary Stage			
Backpressure	Rotor (W)	Gap (W)	Stator (W)	Rotor (W)	Gap (W)	Stator (W)	Total (W)
0-psi	284.2	70.68	682.5	984.2	102.1	844.0	2968
7-psi	273.6	63.96	651.4	659.2	66.17	610.9	2325

Table 5.2 – Mean energy dissipated in various regions for different backpressures.

	Primary Stage			Secondary Stage			
Backpressure	Rotor (W)	Gap (W)	Stator (W)	Rotor (W)	Gap (W)	Stator (W)	Total (W)
0-psi	1.03	9.95	2.11	1.02	15.75	3.19	33.05
7-psi	0.89	9.23	1.86	0.80	12.13	2.28	27.19

It should be noted that the energy dissipated by the turbulent component is two orders of magnitude larger than the mean component. This is a result of the high Reynolds number provided by the movement of the rotor. Comparing backpressures for both tables 5.1 and 5.2, more mean and turbulent energy is dissipated for the 0-psi scenario across all rotor regions. As mentioned previously, this is a result from the higher axial velocity in the stator jet. The fluid region with the most significant difference between backpressures is the turbulent energy dissipated in the secondary stage.

As shown in tables 5.1 and 5.2, more energy is dissipated in the primary stator region than the primary rotor region. However, higher turbulent energy dissipation is predicted for the secondary rotor compared to the stator. This is a result from the flow exiting the primary stator and entering the secondary stage. Comparing the shear gap regions, more energy is dissipated in the secondary gap than the primary gap. Since the secondary stator slots have smaller cross-sectional area on a per slot basis, this is an expected result.

Torque deviations for the 7-psi backpressure are shown in figure 5.9. Similar to flow rate deviations in figure 5.18, torque deviations can be compared for different backpressures, as is done in figure 5.19. The angularly averaged value which these torque deviations center around varies significantly with backpressure, as indicated by the change in power numbers in figure 5.21. Torque deviation time profiles vary less with backpressure then the flow rate deviation time profiles. Larger maximum and minimum primary rotor torque deviations are observed for the 0-psi backpressure. The maximum and minimum values reached in the secondary rotor vary with each rotor position, however the torque deviations of both backpressures show similar trends.

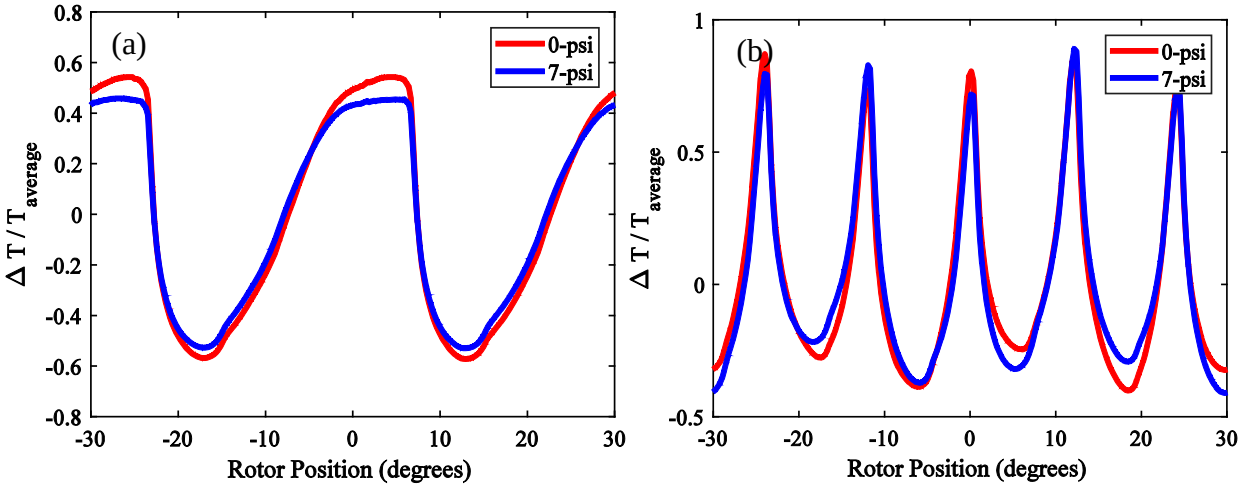

Figure 5.19 – Dimensionless torque versus rotor position for the 0-psi (red) and 7-psi backpressures from the (a) primary rotor and (b) secondary rotor. Hex 20M.

5.7 Mesh Comparison

The mathematical discussion in sections 3.14 and 3.15 indicates mesh quality strongly influences the accuracy of the numerical solution. These finite volume equations, which all results in this work are computed from, approach an accurate and reliable answer as the cell volume approaches zero. For this reason, we expect a more refined mesh to provide a more accurate and reliable answer. However a larger more refined mesh can be computationally expensive, it is

therefore worthwhile to compare the results of different levels of mesh refinement. In doing so, the appropriate mesh can be developed and used for a given task. In this section, the computational meshes explained in section 2.5 are compared. The level of mesh refinement on flow rate and torque are first discussed. Then a given mesh's ability to resolve mean velocity gradients is quantified by measuring strain-rate magnitude as a function of rotor position. The section concludes by comparing predicted mean and turbulent energy dissipated among the different meshes.

The flow number for the entire mixer, as computed by equation 3.1-4, is shown varying with backpressure in figure 5.20. The original tet mesh was used to study flow rate across several different backpressures. The more resolved hex meshes were only used for the 0- and 7- psi backpressures. All meshes and their respective flow numbers are shown in this figure. The flow rate decreases with increasing backpressure, which is shown in figure 5.20 and is demonstrated in the above velocity field comparisons in section 5.6.

At the 0-psi backpressure, the hex 4.2M and hex 20M meshes predict a higher flow number compared to the relatively coarse tet mesh. These flow numbers differ less than 5%. As discussed in sections 2.4 and 2.5, the length of the inlet pipe was 23.9 mm for the tet mesh and 307.6 mm for the hex 4.2M and hex 20M meshes, the length of the outlet pipe was 127.7 mm for the tet mesh and 283.5 mm for the hex 4.2M and hex 20M meshes. As pipe length increases we would expect throughput to decrease due to wall friction. However this change in pipe length does not significantly influence throughput and is therefore not considered in figure 5.20. Since the hex 4.2M and hex 20M meshes predict higher throughput with a longer pipe length compared to the coarse tet mesh, throughput is dependent on level of mesh refinement and cell type. The dependence throughput has on mesh refinement is not observed between the hex 4.2M and hex

20M meshes since both meshes predict similar flow numbers with less than 1% difference at either backpressure.

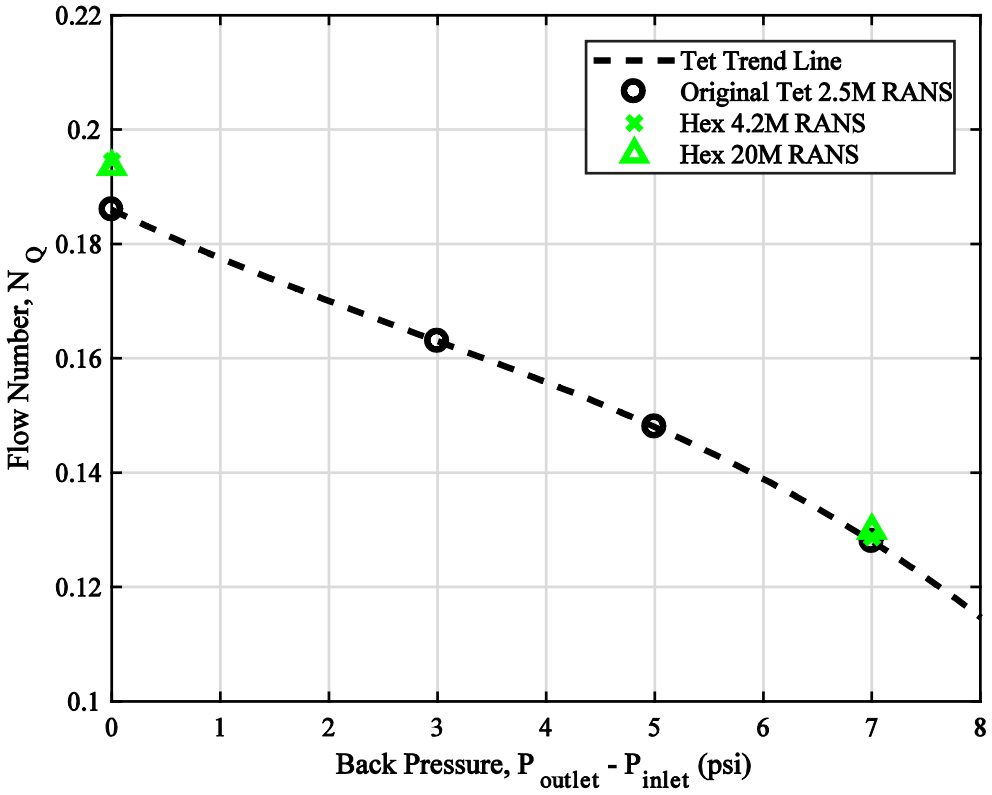

Figure 5.20 - Flow number for each RANS simulation. The dashed trend line was developed from four points using the original tet mesh which does not have extended inlet and outlet pipes.

Similar to figure 5.20, the power number can be computed for both rotor stages at different backpressures using equation 3.1-5. This is shown for different meshes in figure 5.21 below. Comparing the power number in this manner, power draw decreases with backpressure just as throughput did. The power required to move and accelerate the fluid across the mixer, as given by equations 3.2-2 and 3.2-3, is relatively small compared to the power dissipated by the rotors. Although the flow work and work to accelerate the fluid increases with increasing backpressure, these work terms are not larger than the energy dissipated by the 0-psi scenario compared to the

7-psi case (see tables 5.1 and 5.2). For this reason, a higher power number is observed for smaller backpressures.

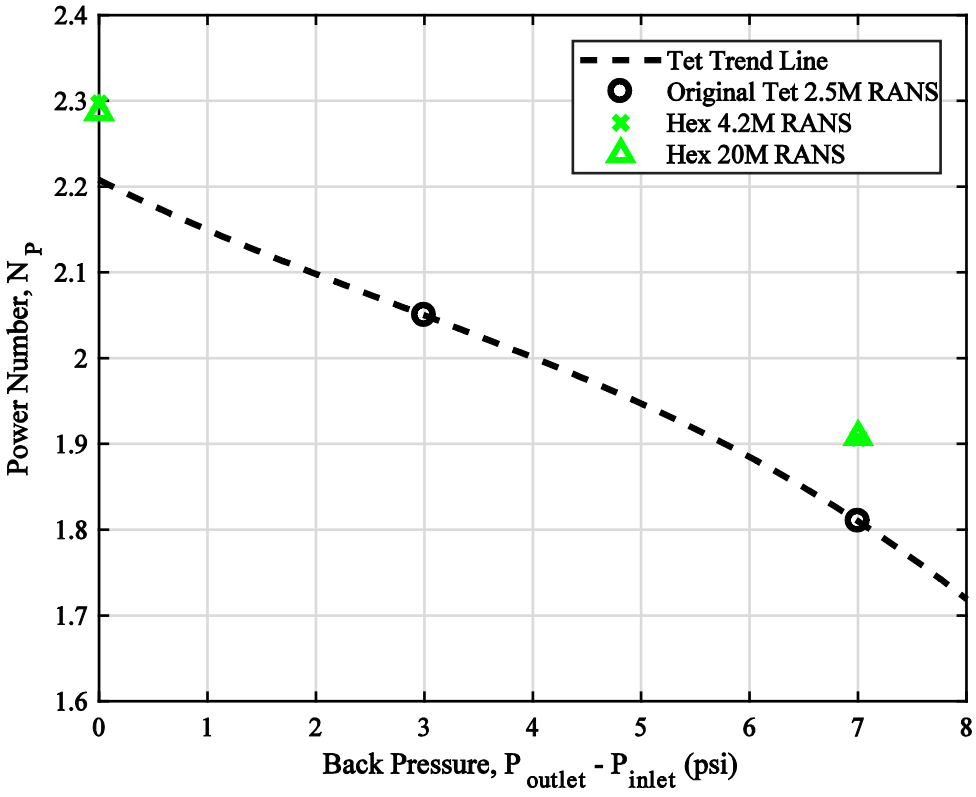

Figure 5.21 – Power number for each RANS simulation. The dashed trend line is developed from linear interpolation of the flow number curve developed from the original tet mesh which does not have extended inlet and outlet pipes.

The coarse tet mesh predicts a power number lower than 5% the power numbers predicted by the hex 4.2M and hex 20M meshes at the 7-psi backpressure. The power number predicted by the hex 4.2M and hex 20M meshes is also higher than the power predicted by the tet mesh trend line at the 0-psi backpressure. This difference in power number among meshes is due to the level of mesh refinement where velocity gradients are high, particularly in the shear gap. As indicated by equation 3.7-7, power is dissipated by mean and turbulent velocity gradients. With more mesh refinement, velocity gradients are better resolved, and therefore higher power number is predicted.

This is investigated more in the remainder of this section in figure5.22 and tables 5.4 and 5.5 below.

The trends observed in the flow rate and torque curves with varying rotor position are observed for all meshes. However the angularly averaged value which these flow rate and torque deviations center around may differ among computational meshes. These angularly averaged values are presented as flow and power numbers in figures 5.20 and 5.21, as well as table 5.3 below. To quantify and compare the amount to which the quantities deviate from average, the root mean square deviation is also provided and is nondimensionalized in a similar manner to the average nondimensionalization. As the mesh size increases, the average and deviations of the flow rate and power numbers also increase. However this change is relatively small, within 1%.

Table 5.3 – Flow and power numbers for different meshes.

	Angular Average		Angularly Resolved RMSD	
Mesh	N_Q	N_P	N_Q'	N_P'
Hex 4.2M	0.1287	1.9073	4.9×10^{-4}	0.4507
Hex 20M	0.1299	1.9205	5.6×10^{-4}	0.4549

In section 5.2, the spatial-averaged strain rate magnitude across data planes in the gap between the rotor and stator at varying rotor position was given. Since this quantity is a representation of the highest velocity gradients observed in the mixer, comparing it among different mesh levels will describe mesh convergence. Shown in figure 5.22 is the average strain-rate magnitude for the hex 4.2M mesh at a backpressure of 7-psi for both the primary and secondary stages. This is to be compared to figure 5.8, where the spatial-average strain rate magnitude was reported for the hex 20M mesh at the same backpressure.

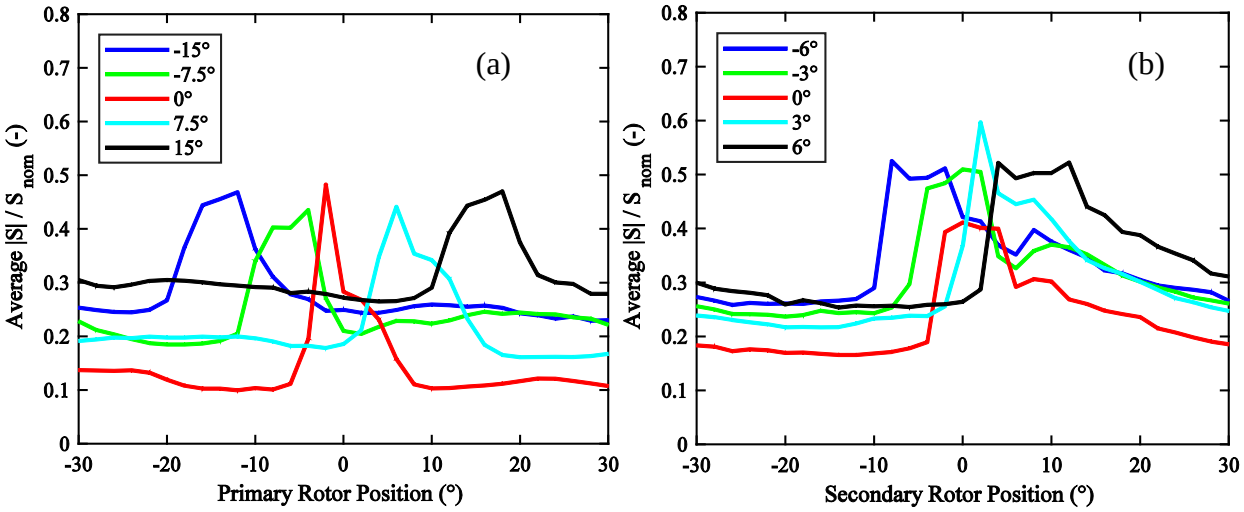

Figure 5.22 – Spatial-averaged strain rate magnitude for the (a) primary and (b) secondary shear gaps. ΔP = 7 psi, hex 4.2M.

The hex 4.2M mesh has six uniform cells across the shear gap, and the hex 20M mesh has fourteen cells across the shear gap. We would expect this increase in mesh refinement to resolve larger velocity gradients and therefore have a larger strain rate magnitude. Comparing the average strain rate magnitude in figure 5.8 to figure 5.22, a different y-axis range was used since the predicted average strain rate magnitude is less for the hex 4.2M mesh. The maximum value of the average strain rate magnitude increased by ~66% for the primary shear gap and ~60% for the secondary shear gap from the hex 4.2M to the hex 20M mesh.

Another quantity that can be compared among different mesh levels is the energy dissipated throughout the mixer. Tables 5.4 and 5.5 show the turbulent and mean energy dissipated throughout the mixer for the 5 and 20 million cell meshes. These tables are analogous to tables 5.1 and 5.2 where backpressure was compared instead. The hex 20M simulation predicted a higher power number than the hex 4.2M simulation. From this we would expect a higher predicted amount of energy dissipated in the larger mesh.

Table 5.4 – Turbulent energy dissipated in various regions for different meshes.							
	Primary Stage			Secondary Stage			
Mesh	Rotor (W)	Gap (W)	Stator (W)	Rotor (W)	Gap (W)	Stator (W)	Total (W)
Hex 4.2M	269.2	60.85	603.7	645.3	62.00	555.6	2197
Hex 20M	273.6	63.96	651.4	659.2	66.17	610.9	2325

Table 5.5 – Mean energy dissipated in various regions for different meshes.							
	Primary Stage			Secondary Stage			
Mesh	Rotor (W)	Gap (W)	Stator (W)	Rotor (W)	Gap (W)	Stator (W)	Total (W)
Hex 4.2M	0.76	1.78	1.48	0.75	2.31	1.78	8.86
Hex 20M	0.89	9.23	1.86	0.80	12.13	2.28	27.19

Indeed the larger mesh predicts a larger amount of turbulent and mean energy dissipated in every region of the mixer. The largest increase in turbulent energy dissipated between the two meshes occurs in both the stator regions. Overall, the hex 20M simulation predicts 5.5% more turbulent energy is dissipated than the hex 4.2M simulation. Regarding the mean energy dissipated, the largest increase occurred in the gaps of both stages. The total predicted mean energy dissipated in the mixer is 67% larger for the hex 20M than for the hex 4.2M simulation.

5.8 Mean Flow Field Convergence

Applied in this section are the various measures of convergence as discussed in section 3.16. First the residuals reported by FLUENT and the number of iterations per time step to reach time step convergence will be discussed for each RANS simulation. Then convergence of flow rate and torque profiles will be quantified across all rotor positions. Finally, flow field convergence will be described by quantifying the differences between various flow field variables in the stator slots. The values reported in this section describe convergence, but can also be thought to describe the amount to which the given flow field variable varies from one rotor period to the next.

The first convergence criteria checked for RANS was the amount to which the outlet flow rate varied. If the outlet flow rate varied within 3% of the average value, then other convergence criteria were checked. The hex 4.2M 7-psi simulation was initialized from an interpolated data file from the tet simulation discussed in section 2.4. Initializing a new simulation from a different mesh is discussed in section 2.4. The old and new simulation shared the same rotor position. After this simulation was run for ~10 revolutions, the flow field was used to initialize the 0- psi simulation with the same computational mesh. The hex 20M simulations were initialized using the coarse hex 4.2M mesh with the corresponding backpressure. Since the hex 20M flow field was initialized from a simulation with similar operating conditions that had been run for ~10 revolutions, we expect the results to be reliable for the hex 20M simulation even though it was only run for 2 revolutions. Results are reported one rotor period after the simulation was considered converged.

FLUENT reports residual values given by equation 3.16-3 for every flow variable at each iteration. As these residual values approach zero the governing conservation equation for that flow variable, given by equation 3.16-2, becomes satisfied. The RANS k-ϵ model involves six governing equations, therefore the residual values of six flow variables are reported with each iteration. These flow variables are: continuity, the time-averaged x-, y-, and z-velocities, turbulent kinetic energy, and the turbulent energy dissipation rate. The residual values reached and the number of iterations required to reach those values are reported in table 5.6 below for all RANS simulations.

Table 5.6 – Iteration convergence for all RANS simulations.						
Simulation Parameters		Residuals (-)				
Mesh	Backpressure	Continuity	$\bar{U}_i$	k	ϵ	M_{iter}
Hex 4.2M	0-psi	10^{-4}	10^{-7}	10^{-7}	5×10^{-6}	40
	7-psi	10^{-4}	10^{-7}	10^{-7}	5×10^{-6}	40
Hex 20M	0-psi	10^{-4}	10^{-6}	10^{-6}	5×10^{-6}	45
	7-psi	10^{-4}	10^{-6}	10^{-6}	5×10^{-6}	50

The continuity residual is the limiting factor for all RANS simulations. The residual of this particular flow variable would slowly plateau near the end of each time step. For this reason, the number of iterations were limited to those described in table 5.6. It was found that more iterations were required to reach iteration convergence for the larger computational meshes. The residual values achieved for the mean velocity components and the turbulent kinetic energy were lower for the smaller computational meshes, however the continuity and turbulent energy dissipation rate residuals achieved for all computational meshes were quantitatively similar.

From the discussion in sections 5.3 and 5.4, we know that flow rate and torque is highly dependent on rotor position. The flow rate and torque were recorded for every time step across one rotor revolution. Since there are six identical rotor blades, there are six instances in a rotor revolution which are qualitatively similar in a time-averaged sense. By comparing these six instances at every rotor position, the level to which the flow rate and torque vary from one rotor period to the next can be quantified. Regarding flow rate, only one slot from each stator is considered since the flow rate from all rotor positions is used. Primary slot 6 and the inner, middle, and outer slots of row 15 in the secondary stator were considered.

Shown in figure 5.23 and 5.24 is the flow rate and torque profiles of all six rotor periods respectively. The average and the root mean square deviation from this average is also given. In this context, the average of all profiles represents the flow rate and torque value likely to be taken at the given rotor position. Ideally the flow rate and torque reported from a perfectly converged

simulation should be equivalent to this average for every rotor period. Therefore any deviation from this average is a measure of convergence. In this work, the deviation is presented as the root mean square. As was done in sections 5.3 and 5.4, the flow rate and torque profiles can be presented as dimensionless fluctuations. In this discussion, the average used is the overall average of all rotor periods across all rotor positions. The root mean square deviations of these profiles is presented as bounding the average.

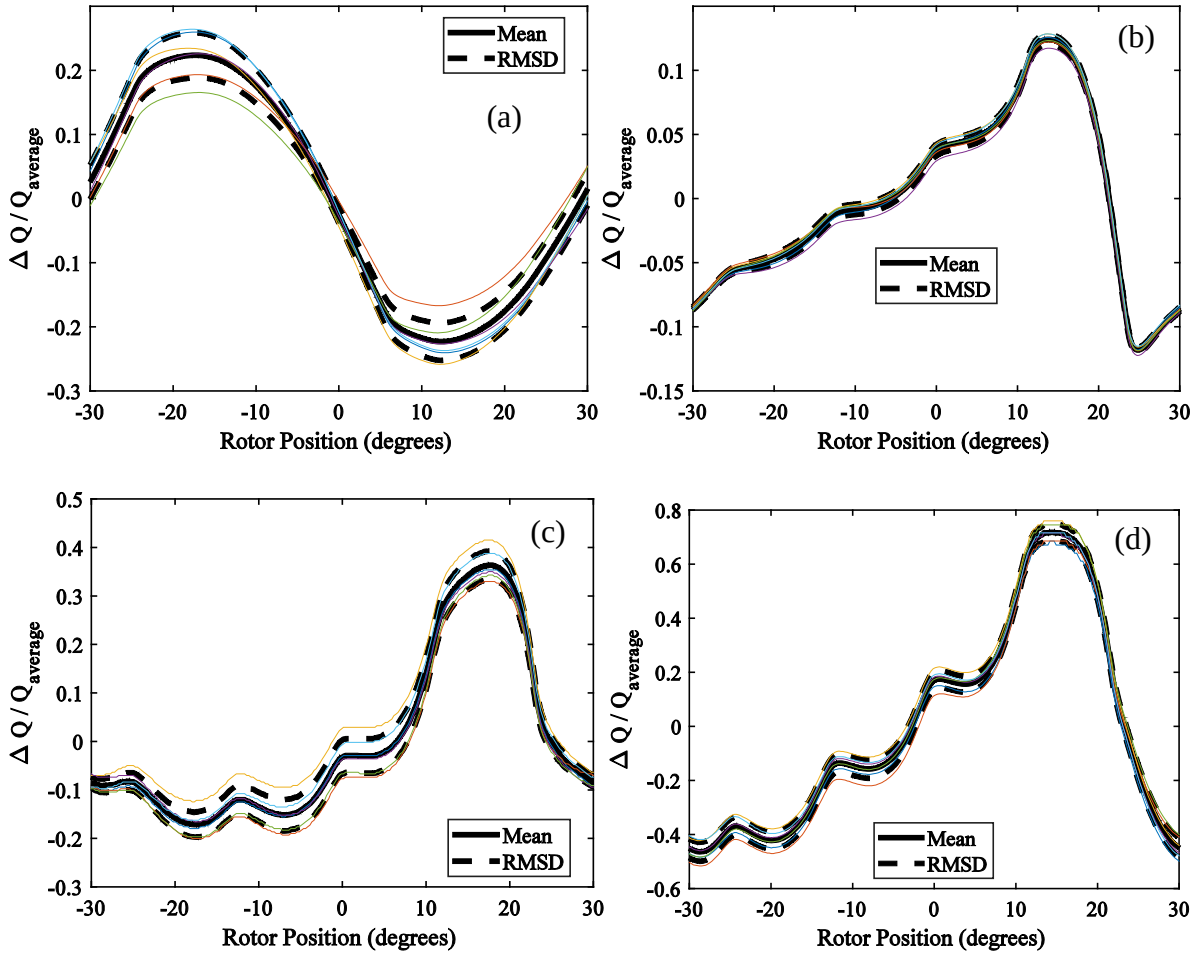

Figure 5.23 – Six instances, the angular average, and the root mean square deviation of the flow rate through (a) primary slot 6, secondary (b) outer, (c) middle, and (d) inner slots 15. ΔP = 7 psi, hex 20M.

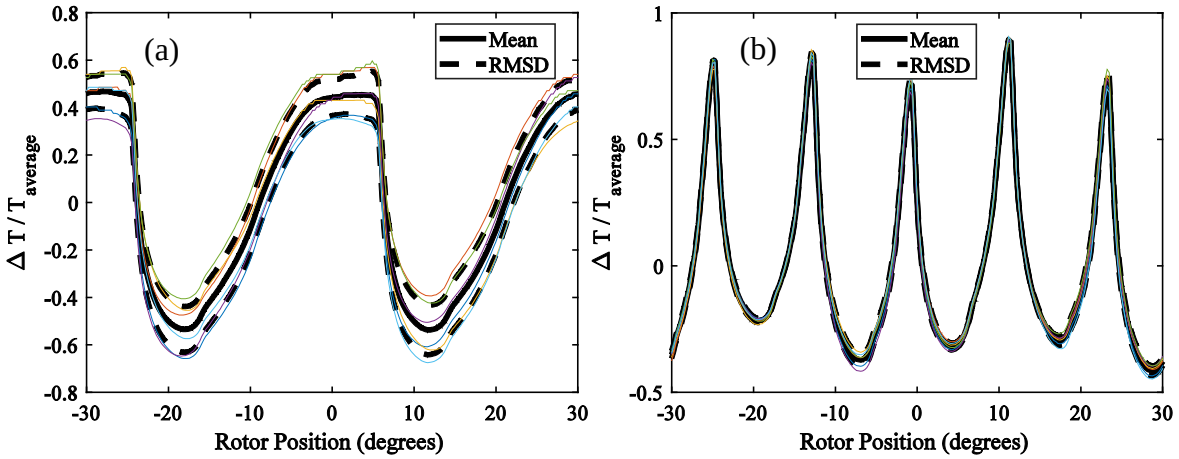

Figure 5.24 – Six instances, the angular average, and the root mean square deviation of the torque from the (a) primary rotor and (b) secondary rotor. ΔP = 7 psi, hex 20M.

The smallest flow rate deviations from average in all slots considered occurs after the maximum flow rate is reached. The secondary outer slot has the smallest root mean square deviation across all rotor positions compared to the other stator slots as shown in figure 5.23b. For the primary slot the largest root mean square deviation normalized by the overall time average is 3.17%, for the secondary outer 0.47%, for the secondary middle 3.63%, and for the secondary inner 3.70%. These maximum deviations occur when the flow rate is at a maximum.

The primary torque shows similar deviations from average as those shown by the flow rate deviations. The smallest deviation of torque for the primary rotor occurs after the maximum torque is reached. The maximum torque deviation for the primary rotor normalized by the overall time average is 11.5% and occurs when the torque reaches a maximum. The torque from the secondary rotor shows noticeable smaller deviation than the primary across all rotor positions. The maximum torque deviation for the secondary rotor normalized by the overall time average is 2.87% and occurs at one of the local minimums.

The flow rate and torque trends in the above discussion were assumed to depend on a period of one rotor blade pass. Indeed this frequency is the most significant, however other frequencies

may be inherent in the flow of this rotor-stator mixer. If the time-averaged flow rate and torque are dependent on other frequencies than deviations from this one rotor period ensemble average would be expected. Therefore, the root mean square deviation curves bounding the ensemble average curve exist due to frequencies inherent in the system that have yet to be accounted for, and/or numerical error. The frequencies that influence the time-averaged flow rate and torque is quantitatively described in section 7.1.

Flow rate can be thought of as a spatial average of axial velocity. Therefore convergence of flow rate does not depict flow field convergence of axial velocity at different points in space. To quantify the amount in which a flow variable varies between rotor periods, equation 3.16-4 was applied at every cell center in the stator slots. The center plane and cross-sectional planes in the stator slots was considered. Rotor position was kept constant and so the comparison was made across a period worth of stator slots. The position of the rotor is shown in figure 2.7. However for brevity, the slot with the largest time-averaged velocity magnitude changes at the given rotor position is reported for both the primary and secondary stators. Flow variables considered consist of velocity magnitude, strain-rate magnitude, turbulent kinetic energy, and turbulent energy dissipation rate.

Since one revolution of data was taken, six instances can be compared. We expect each of these instances to be quantitatively similar, and so all can be compared to one another. From these six instances, there are 15 different possible comparisons that can be made. A distribution of error values develops from the 15 comparisons at every cell center in a given plane. The value reported from this distribution, given in table 5.7, is the value of the flow variable in which 95% of these comparisons is under.

Table 5.7 – Flow field values in which 95% of cells vary across six instances.					
Planes		Flow Variables			
Slot	Location	$\|\|\bar{U}_i\|\|$ (m/s)	$\|\|\bar{S}_{ij}\|\|$ (1/s)	k (m/s)^2	ϵ m^2/s^3
PS7	x0	2.53	4510	4.46	10600
	z060	2.43	2600	4.01	5810
SOS14	x0	0.652	910	0.646	1990
	z100	0.606	853	0.692	1810
SMS14	x0	0.477	1270	0.341	881
	z100	0.936	2020	0.457	1240
SIS14	x0	0.141	583	0.0727	316
	z100	0.200	550	0.0847	216

It was shown in figure 5.23 that the largest flow rate deviation from average occurred when the flow rate reached its maximum value. Similarly, the largest velocity magnitude deviation occurs when the blade is approaching the given slot, which is when the flow rate reaches its maximum value. Among the stator slots, the largest changes in flow variables can be expected to occur in the primary stator. Excluding the middle and inner secondary slots, the cross-sectional planes (z = 60 and 100 mm) show smaller changes in the flow variables compared to the center plane (x = 0 mm). Just as the flow variables scale with slot diameter and relative blade speed, the changes in all flow variables scale in a similar manner.

5.9 Summary of RANS Simulation Results

The mean velocity field, turbulent kinetic energy, and energy dissipation rate predicted by the RANS realizable k-ε model were shown. The flow field in the rotor, stator, and shear gap regions were investigated. The trends observed in the stator slot flow rate and rotor torque were found to be related to number of blades and stator slots. These flow pattern and power characteristics showed periodic behavior dependent on rotor position. Results from simulations with different backpressures and computational meshes were compared.

High axial velocity is observed along the outer edge of the stator slots. A recirculation region develops across the entirety of the stator slots. High intensity velocity fluctuations are

observed at the rotor tip and along the outer edge of the stator slots. As the flow impinges on the stator slot outer edge, high turbulence energy dissipation rate is predicted. As the rotor blade approaches a slot, throughput in the slot increases and torque decreases. At the tip of the rotor, high mean strain rate magnitude is observed within the time-averaged vortex that develops.

The outer secondary slot show high axial velocity and energy dissipation rate at the outer edge similar to the primary slots. The primary slot shows high turbulent kinetic energy and energy dissipation rate at the exit due to the close proximity of the secondary rotor. The middle and inner secondary slots contribute little to the throughput and energy dissipated in the secondary stator. The secondary stage contributes more to the total energy dissipated by both rotor stages. The presence of more stator slots in a rotor period, as in the secondary stator compared to the primary stator, increases the amount of time to reach maximum slot flow rate, increases number of torque oscillations, and decreases the amount of time the maximum torque is maintained.

As backpressure increases, throughput and power requirement decrease. Although flow work increases for higher backpressure, energy dissipated by the rotor is higher for lower backpressures. The shape of the time-averaged vortex in the primary stator slot changes and fewer recirculation vortices are observed in the secondary stator slots as backpressure decreases. The secondary middle and inner slots contribute more to secondary stator throughput as a result.

The coarse tet mesh and refined hex meshes predicted different flow and power numbers as a result of cell type and mesh refinement. However, all meshes predicted similar trends in the stator slot flow rate and rotor torque. Higher mean strain rate magnitude and turbulent energy dissipation rates were predicted in the hex 20M compared to the hex 4.2M mesh as a result of better resolved velocity gradients.

6 Large Eddy Simulation Results

Discussed in this section are the LES results, including the filtered velocity field in the stator slots and near the shear gap, flow rate through the stator slots, and torque requirements to move the rotor. The SGS eddy viscosity is presented to show how much the SGS contribute to the turbulent energy dissipation rate estimation. The velocity field and SGS eddy viscosity results are provided by the hex 20M, 7-psi simulation, and the flow rate and torque profiles are provided by the hex 4.2M 7-psi simulation. A comparison between the hex 4.2M and hex 20M mesh is made, in which the contributions of smaller scales are noted. The influence of backpressure is discussed by comparing results of a LES with 0-psi and 7-psi backpressures. This section concludes by quantifying the convergence of a velocity field with a fluctuating component.

6.1 Filtered Velocity Field in Stator Slots

The mean velocity field in the stator slots as predicted by RANS was shown in section 5.1. The slot velocity field predicted by the hex 20M LES is shown and discussed in this section. From the definition of resolved fluctuations in equation 3.13-3, the LES velocity field contains a mean filtered component and a resolved fluctuating component. By modeling a velocity field with a fluctuating component, results will vary significantly from one period to the next as compared to the RANS velocity field. This section discusses the filtered velocity field in the stators slots using figures from one rotor period. Since the RANS mean velocity field was presented in section 5.1, the influence of the resolved fluctuating component is the focus of this section.

Shown in figure 6.1 is the filtered velocity field of the outer edge of primary slot 6. For convenience rotor positions in the following figures are described by the same notation used when discussing throughput and torque in section 5.3 and 5.4. Therefore a rotor position of 0° corresponds to a rotor blade covering primary slot 6 and secondary slots 18, as shown in figure 2.7.

Rotor positions of ±30° corresponds to primary slot 7 being covered and a secondary rotor blade between secondary slots 15 and 16. When the blade covers a majority of the slot, as in figure 6.1a, the velocity field at the slot opening drastically changes. The speed of the blade and the velocity from the already-existing turbulent structures in the slot both contribute to the velocity of the resulting eddies and vortices which are now present at the slot opening. Once the blade has passed, a large eddy enters the outer edge of the slot (figure 6.1b). This large eddy contributes to the maximum in the flow rate, however a minimum in the flow rate is realized after the blade has passed as it takes time for this eddy to reach the plane where the flow rate is recorded. As time progresses, the influence of this eddy on the filtered velocity field is shown in figure 6.1c. Some portion of this eddy's momentum diminishes from change in geometry and from the slower moving fluid introduced from the inner edge of the slot. Occasional vortices develop from this local change in momentum. The remaining momentum from this large eddy moves in the axial direction along the outer edge stator wall. This momentum of this filtered stator jet later diminishes due to wall effects (figure 6.1d). The presence of the mean stator jet observed in figure 5.4a is observed in figure 6.1 but with turbulent structures and fluctuations.

To understand the recirculation region observed in figure 5.4a, the filtered velocity field at the inner edge of the primary slot is shown in figure 6.2. It should be noted that the velocity field shown in figure 6.2 does not occur at the same time as the field in figure 6.1. The stator jet in figure 6.1 moves across the slot from the outer edge to the inner edge due to the movement of the secondary rotor near the exit of the primary slot. A large eddy moving across the slot, shown in figure 6.2a, is prevented from exiting the slot as flow is introduced from the tip of the secondary rotor blade (figure 6.2b). As this fast moving eddy encounters the inner stator edge, shown in figure

6.2c, the flow is forced to move either back into the slot or exit it. For the portion remaining in the slot, vortices shed and the eddy's momentum diminishes due to wall effects (figure 6.2d).

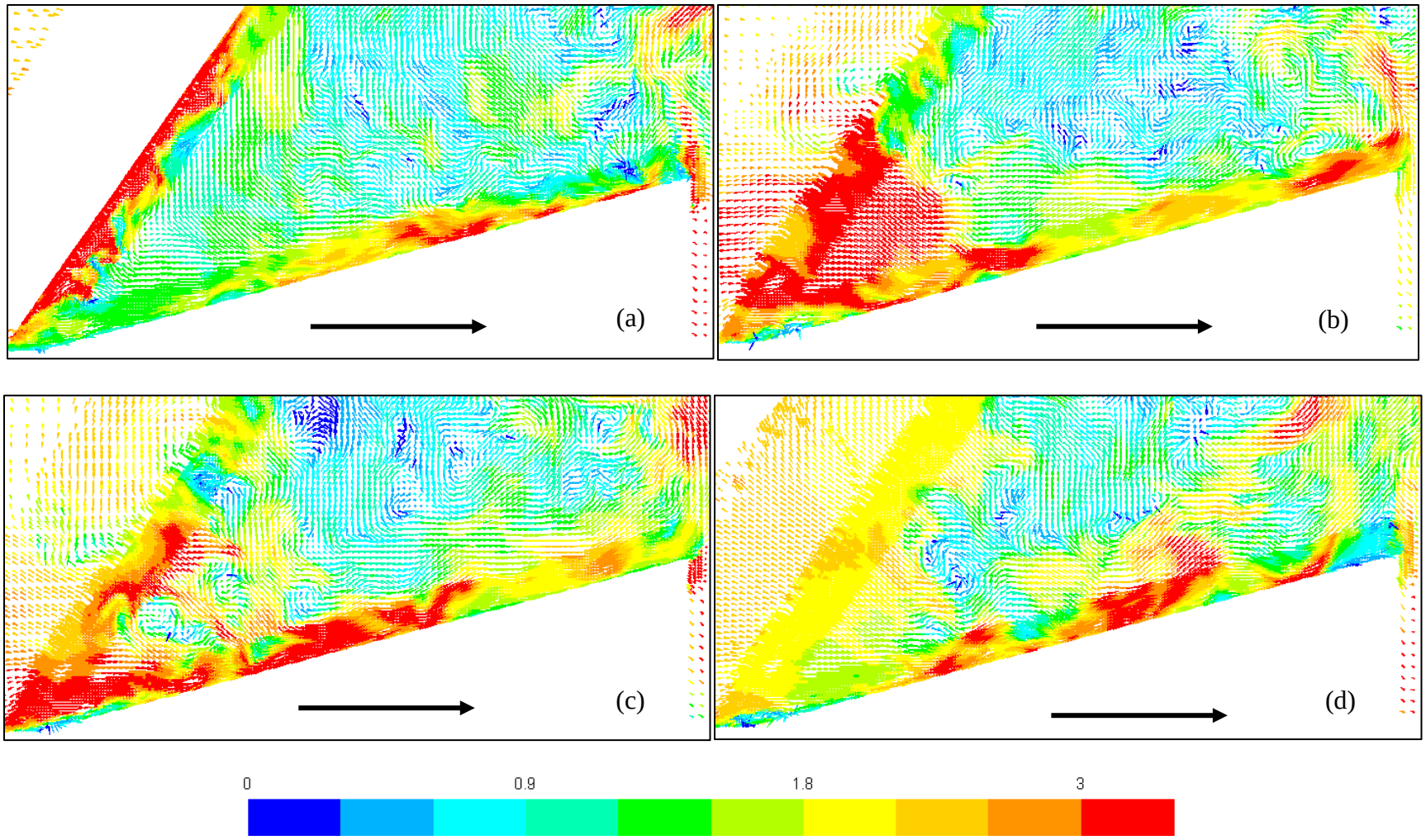

Figure 6.1 – Filtered velocity field colored by velocity magnitude in the center plane, x = 0 mm, for the outer edge of primary slot 6. Images arranged in chronological order at rotor positions of: (a) 0° (b) 20° (c) -28° and (d) -8°. Color legend scaled by (ND) = 5.8 m/s. ΔP = 7 psi, hex 20M.

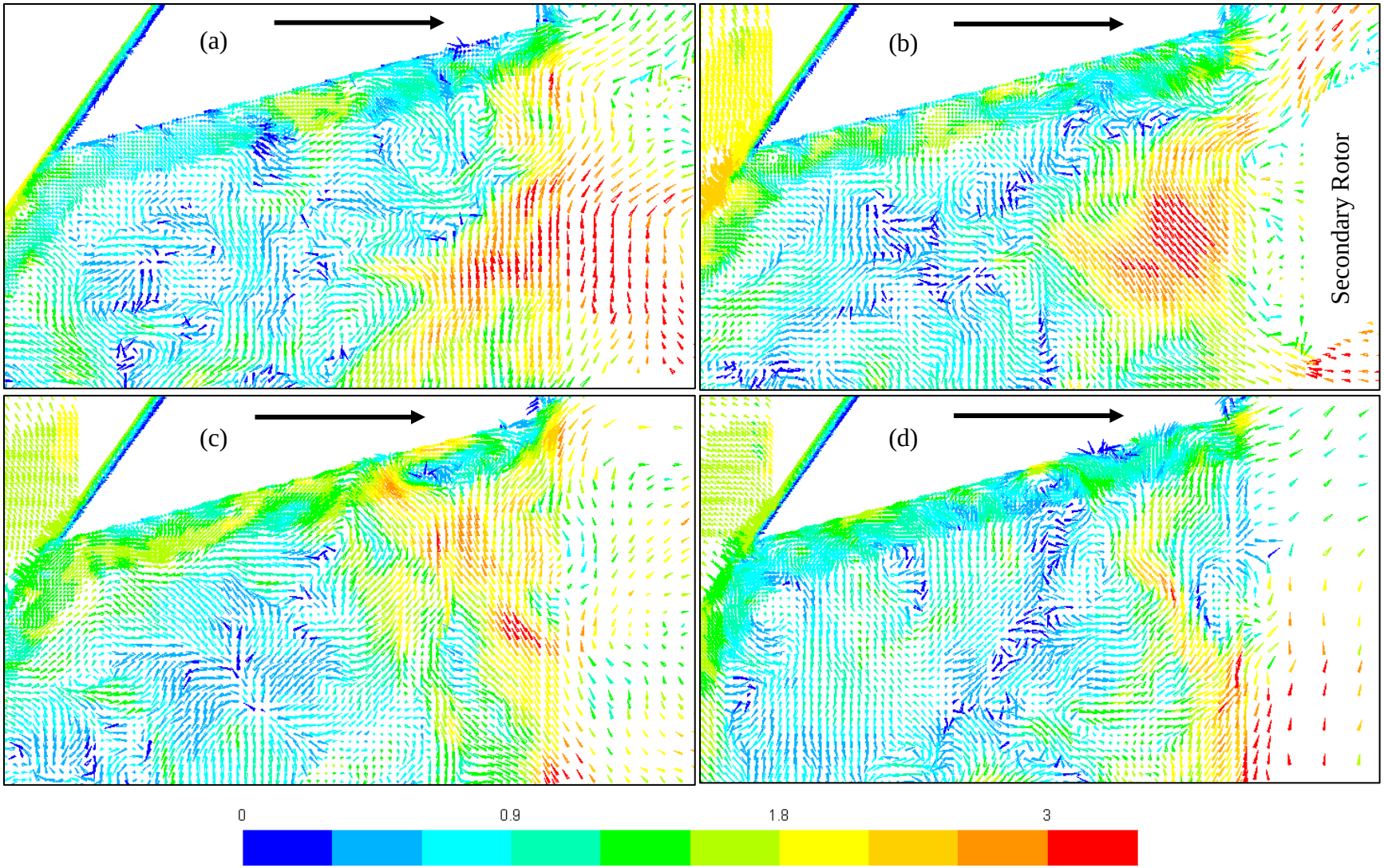

Figure 6.2 – Filtered velocity field colored by velocity magnitude in the center plane, x = 0 mm, for the inner edge of primary slot 6. Images arranged in chronological order at rotor positions of: (a) -2° (b) 8° (c) 22° and (d) -16°. Color legend scaled by (ND) = 5.8 m/s. ΔP = 7 psi, hex 20M.

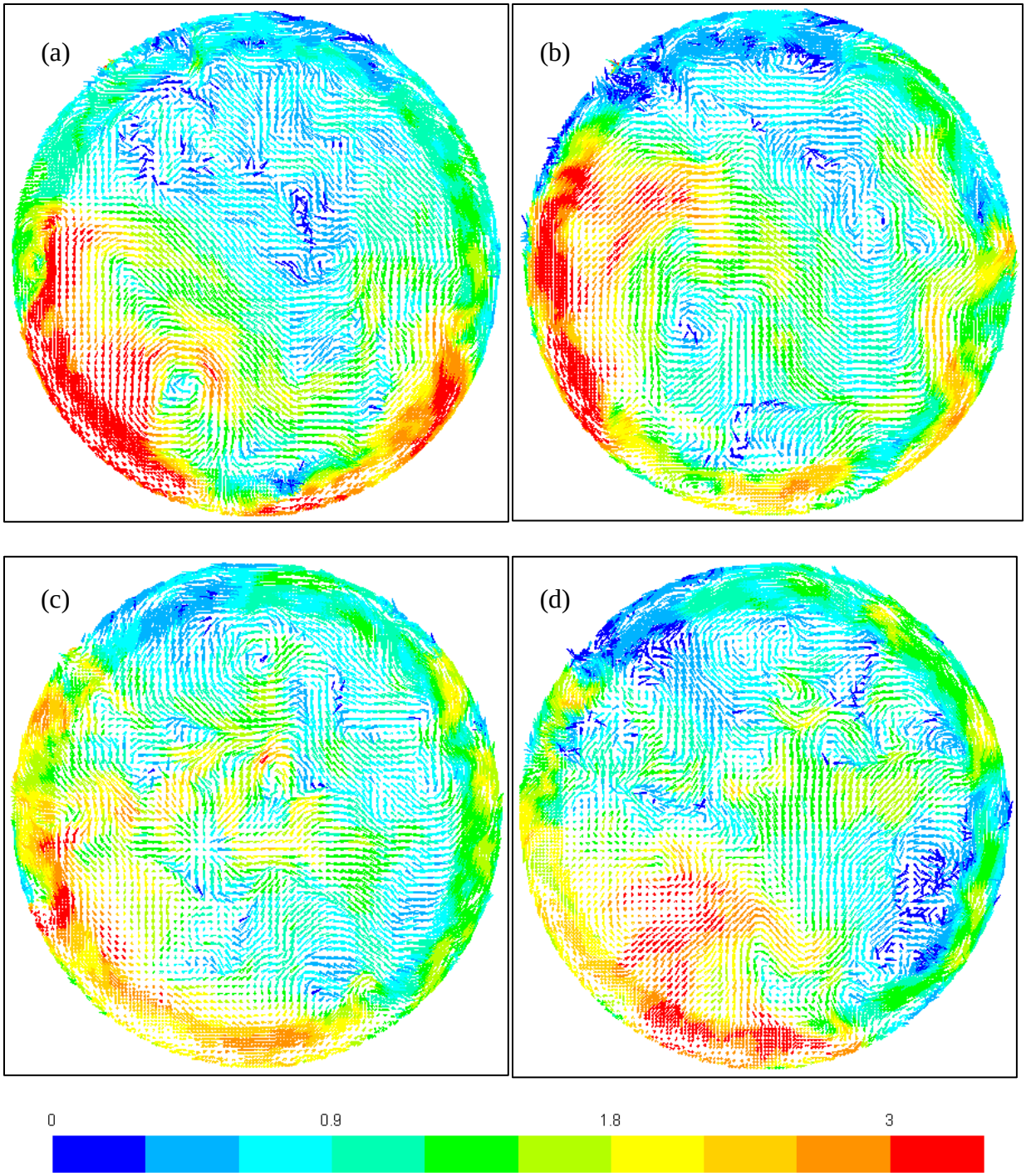

Figure 6.3 – Filtered velocity field in primary stator slot 6 at z = 60 mm looking upstream. Images shown in chronological order at rotor positions of: (a) 0° (b) 14° (c) 28° and (d) -18°. Color legend scaled by (ND) = 5.8 m/s. ΔP = 7 psi, hex 20M.

Another perspective of the primary stator slot time-averaged vortex was shown in figure 5.5a. The same perspective, but of primary slot 6 only, is shown in figure 6.3. With the primary rotor blade present over the slot opening, as in figures 6.3a and 6.3b, the axial stator jet shifts to the left. The influence of the secondary rotor blade movement is evident on the right outer edge, as the flow moves across the slot. This phenomena is shown in figure 6.2b as well as figure 6.3b. This flow continues to move in counter-clockwise direction around the slot. The velocity magnitude diminishes at the inner edge of the stator slot. The axial velocity of the stator jet also diminishes as the primary rotor blade rotates (figure 6.3c). This process repeats as the next primary rotor blade approaches the slot, as shown in figure 6.3d. Throughout this rotor period, a range of vortices and other turbulent structures appear in the region between the stator jet and the mean recirculation vortex.

Similar analyses can be made for the velocity field in the secondary stator. However, the configuration and size of the secondary stator slots result in a somewhat different velocity field. With smaller diameter slots, the turbulent Reynolds number decreases and so the range of eddy sizes and lifetimes decrease. The velocity field at the entrance of a secondary outer slot is shown in figure 6.4. Another perspective of this slot is shown in figure 6.5. A “plug flow like” profile is observed at the exit of the secondary outer slots and is not shown in this section. Only the filtered velocity field of the outer slot in the secondary stator is shown here. The velocity fields in the middle and inner slots are similar and comparable to figure 5.4b. The velocity fields at the exit of the middle and inner slots show vortices traveling down the length of the slot. The opening of the secondary outer slot is similar to the primary when the rotor blade is covering the slot as shown in figure 6.4a. The flow moves radially outwards from the movement of the blade then hits the outer edge of the stator slot. Due to the configuration of the secondary slots relative to the conical blade

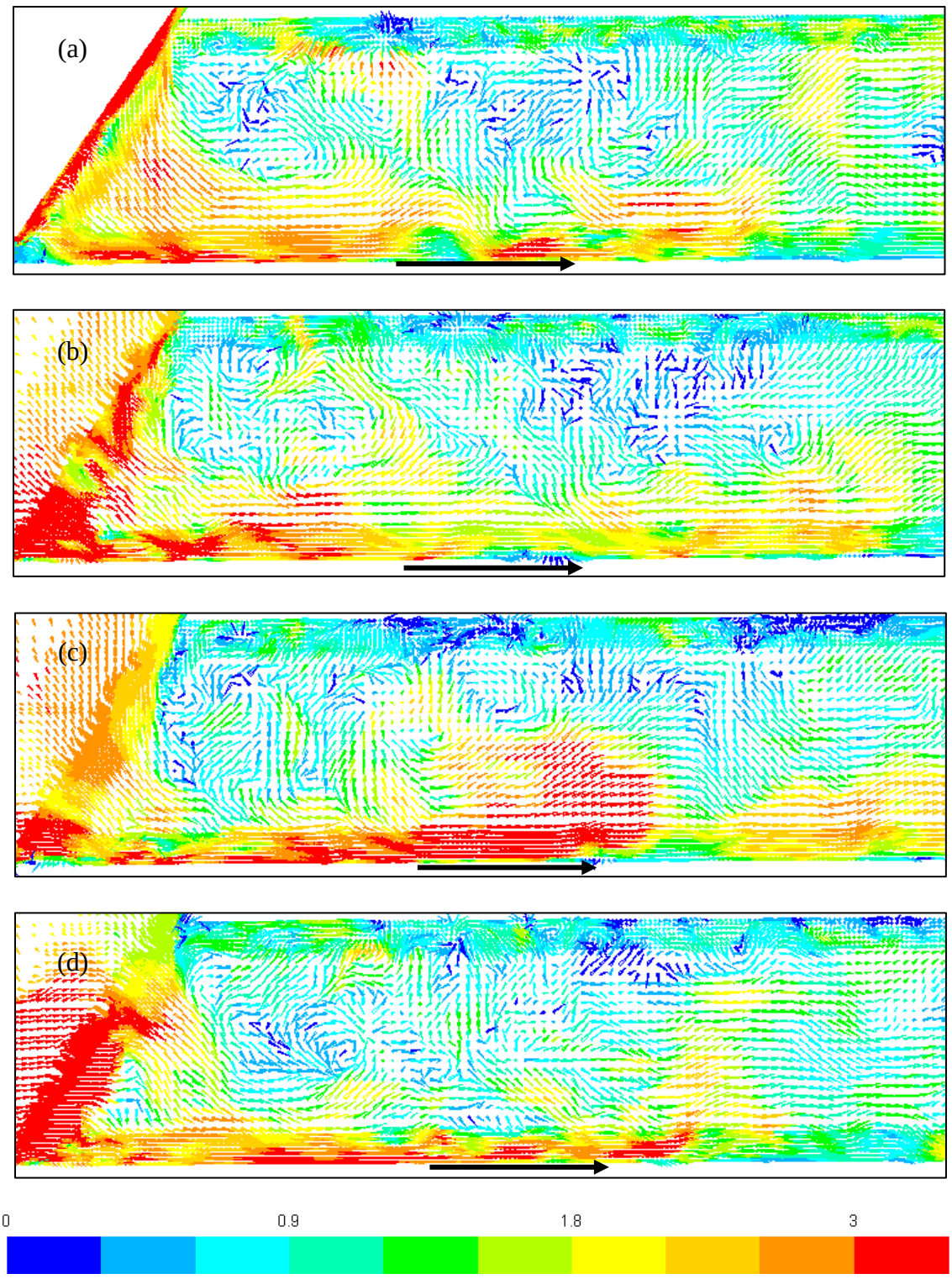

Figure 6.4 – Filtered velocity field colored by velocity magnitude in the center plane, x = 0 mm, for the entrance of secondary outer slot 15. Images arranged in chronological order at rotor positions of: (a) 22° (b) -28° (c) -16° and (d) -2°. Color legend scaled by (ND) = 5.8 m/s. ΔP = 7 psi, hex 20M.

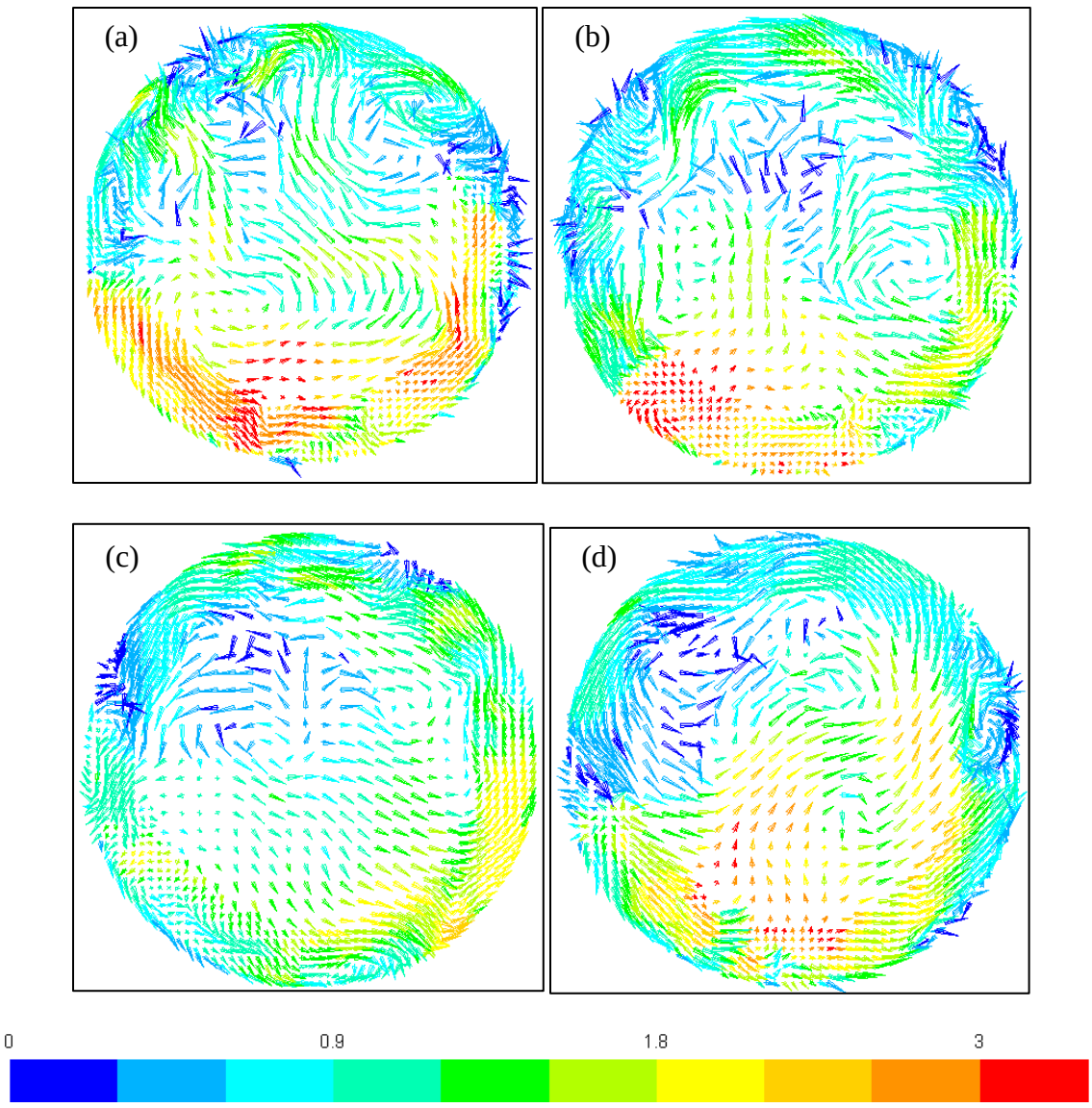

Figure 6.5 – Filtered velocity field colored by velocity magnitude in secondary outer slot 15 at z = 100 mm looking upstream. Images shown in chronological order at rotor positions of: (a) 22° (b) -28° (c) -16° and (d) -2°. Color legend scaled by 5.8 m/s. ΔP = 7 psi, hex 20M.

shape, a recirculation region is observed at the inner edge of the stator slot. Once the blade has passed, an eddy of similar size to the slot diameter enters as shown in figure 6.4b. The velocity magnitude and length of the stator jet is dependent on wall effects and vortices from the inner edge of the stator slot (figure 6.4c). The time-averaged vortex observed at the entrance of the secondary slot in figure 5.4b is the size of the diameter of the slot because that is the size of the largest eddy

that enters the slot. Contrary to the primary slot where one large eddy entered with each blade pass, several eddies may be observed with each blade pass in the secondary stator. Each of these eddies contribute to the different local maximum flow rates observed in the flow rate. The filtered flow rate profiles as predicted by this LES are shown in section 6.3.

Another perspective of the filtered velocity in secondary outer slot 15 is shown in figure 6.5. This velocity field is qualitatively similar to the primary slot which is shown in figure 6.3. The velocity magnitude of the stator jet is shown to shift with the change in rotor position, as shown in figures 6.5a and 6.5b. The recirculation region is observed at the inner edge of the slot, similar to the primary, however fewer filtered vortices are observed in this region. The magnitude of the stator jet velocity is shown to diminish significantly in figure 6.5c.

6.2 Filtered Velocity Field near Shear Gap

The mean velocity field near the shear gap was discussed in section 5.2. This section discusses the filtered velocity field in the hex 20M computational mesh near the shear gap. The filtered velocity field can be thought of as having a mean and fluctuating component. As mentioned in section 6.1, this fluctuating component significantly changes the velocity field from one period to the next. Strain rate magnitude contours were also shown in section 5.2 and are shown as well in this section. RANS predicts mean strain rates and LES predicts filtered strain rates. The filtered strain rate magnitude predicted by LES was shown to have three components from equation 3.13- 6. Because strain rate magnitude involves the square of the strain rate tensor, the product of the resolved mean and fluctuating strain rates contribute to the total magnitude. This section discusses these filtered flow variables as the blade passes a primary slot.

The filtered velocity field is shown in figure 6.6 below. To make this velocity field comparable to the mean velocity field shown in figure 5.6, the same color legend is used where

the maximum is the relative blade tip speed. As the blade approaches, as in figure 6.6a, some flow enters and is pushed against the outer edge of the slot. Recirculating vortices are apparent at the edge closest to the rotor blade. Once time-averaged, these vortices develop the recirculation region shown in figure 5.6.

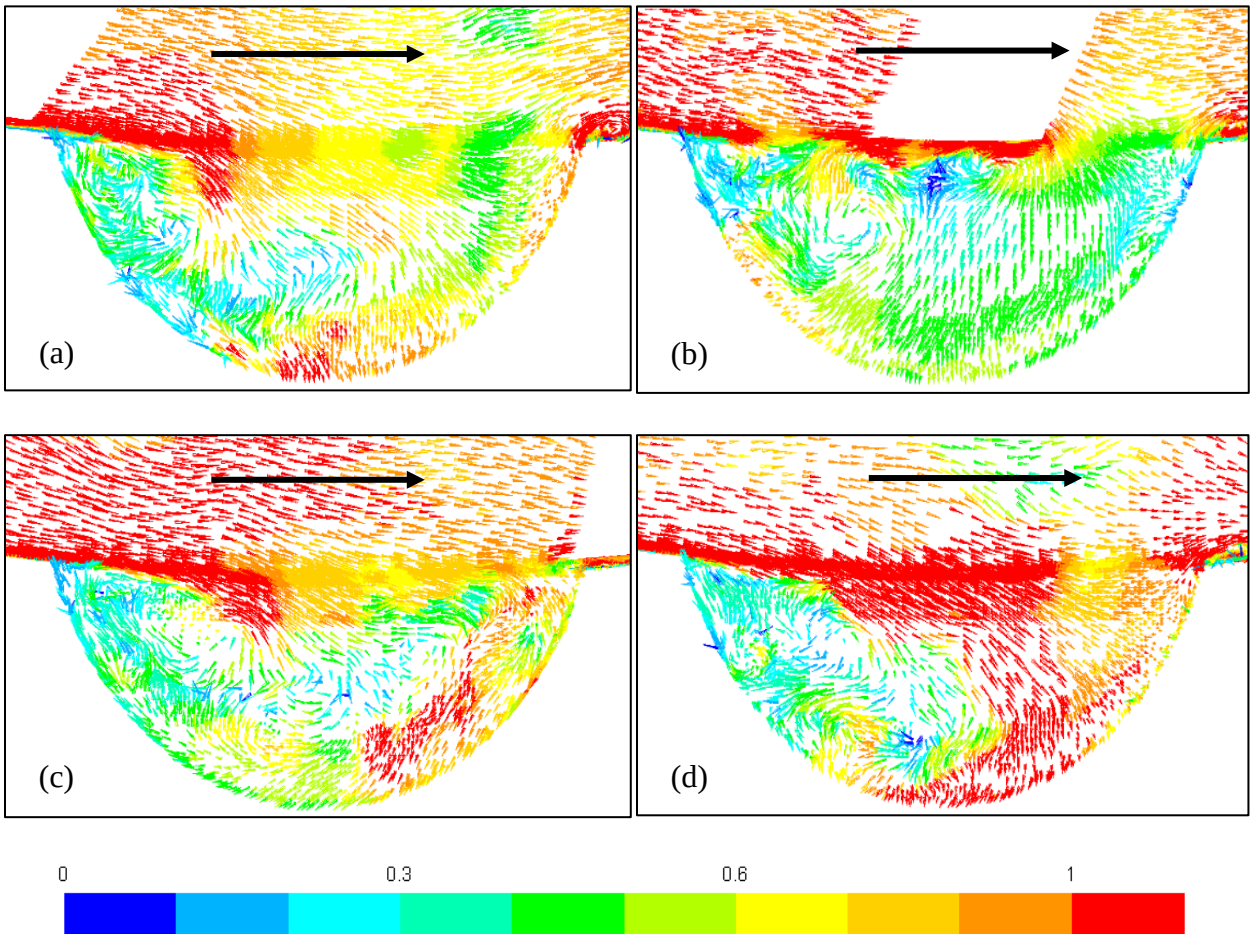

Figure 6.6 – Filtered velocity field colored by velocity magnitude and scaled by relative tip speed of 16.4 m/s in the primary shear gap region at rotor positions of: (a) -14° (b) 0° (c) 12° and (d) - 28°. The view is of primary slot 6, normal to the shear gap. Skipped every 1 arrow. ΔP = 7 psi, hex 20M.

When the blade tip covers a portion of the slot opening, as in figure 6.6b, the velocity magnitude in the slot decreases. A vortex forms at the tip which is not observed in the mean velocity field shown in figure 5.6. As the blade passes the slot, as in figure 6.6c, a high velocity

magnitude radial jet is observed along the stator wall behind the blade. After some time (figure 6.6d) a large eddy enters the slot opening and impinges on the outer edge of the slot. The vortices in the recirculation region interact with this relatively fast moving eddy.

Strain rate magnitude contours of the velocity fields shown above are provided in figure 6.7 below. Compared to figure 5.7, it is evident that the filtered strain rate magnitude is higher than the mean strain rate magnitude because of the fluctuating component. As the blade approaches the slot, as in figure 6.7a, the highest strain rates are observed in the recirculation region where high

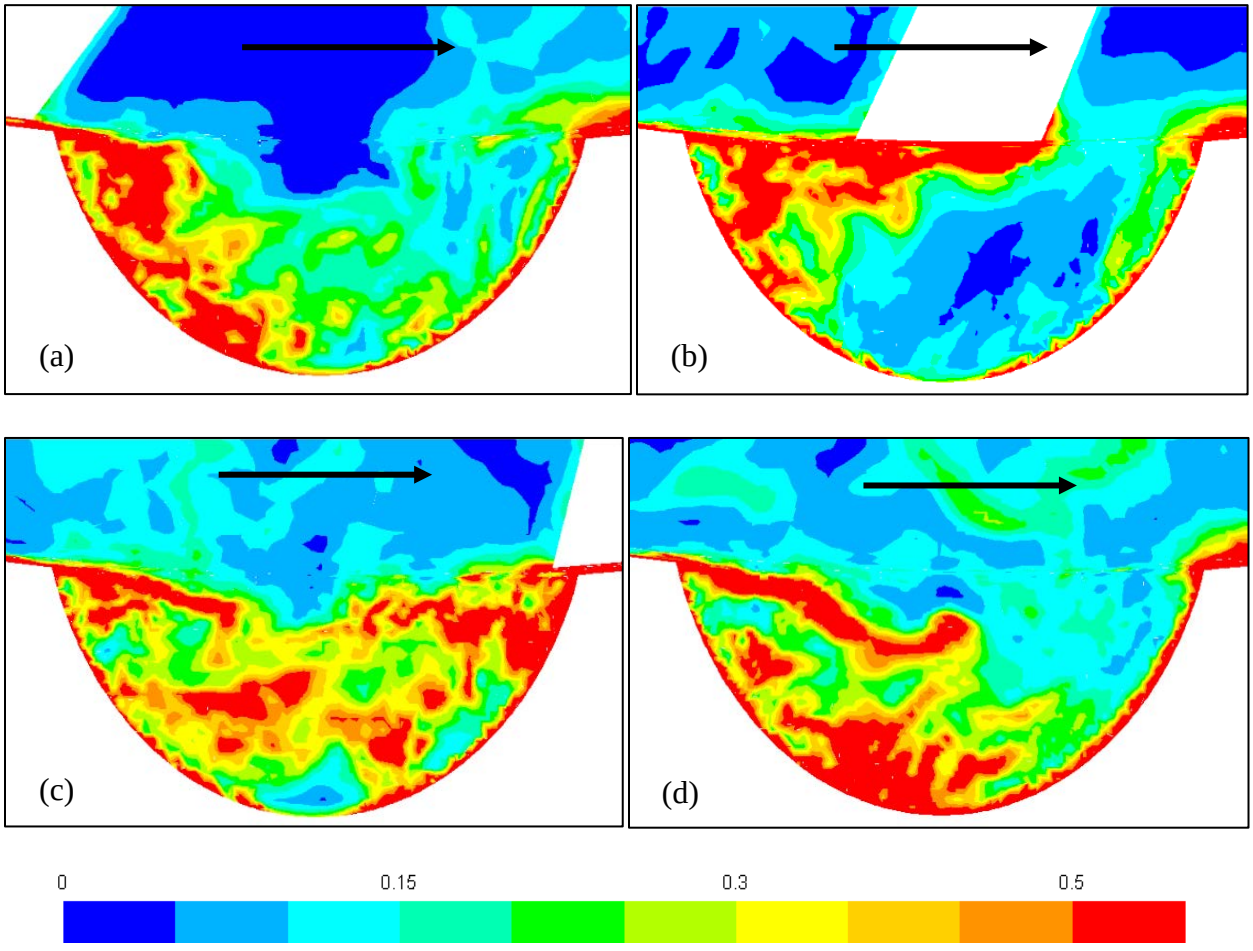

Figure 6.7 – Filtered strain rate magnitude contour scaled by the nominal strain rate magnitude of 6.56×10^4 s^{-1} in the primary shear gap region at rotor positions of: (a) -14° (b) 0° (c) 12° and (d) - 28°. The view is of primary slot 6, normal to the shear gap. ΔP = 7 psi, hex 20M.

velocity fluid enters the slot and interacts with the recirculation region. When the blade covers a portion of the slot, as in figure 6.7b, the highest strain rate magnitude is observed at the blade tip and the region the blade has passed.

Compared to figure 5.7a, the mean strain rate component contributes to the mixing layer, but the fluctuating component contributes to the vortices in the recirculation region where the blade has passed. After the blade has passed, as in figure 6.7c, high strain rate magnitude is observed throughout the slot opening. These high strain rates occur due to the fluctuations as the radial jet interacts with the vortices present in the slot. Compared to figure 5.7b, the mean strain rate component contributes to the high strain rate at the edge of the stator wall where the recirculation region is present. The fluctuating component of the strain rate product extends the region and intensity of this high strain rate region. After some time as the large eddy enters the slot, high strain rates are observed where the eddy interacts with the vortices in the recirculation region.

6.3 Filtered Flow Rate and Torque

The flow rate and torque can be computed from a LES similar to a RANS simulation, which was discussed in section 5.3 and section 5.4. However as indicated in section 6.1, we expect the flow rate in the stator slots from the filtered Navier-Stokes equations to provide different results than flow rate from the RANS equations. With a velocity field varying from one rotor period to the next, the flow rate in the stator slots and the torque from the rotors for the hex 4.2M LES are presented across several revolutions. In this section, the filtered flow rate in one primary slot (PS6) and one secondary stator column (SS15) is shown varying across one rotor period (60°). Ensemble averaging at each rotor position is performed to show the angular average and angularly resolved root mean square deviation as predicted by LES. Since we expect the filtered flow rate to vary from one rotor period to the next, more realizations are preferred. For this reason, results from the

computationally less expensive hex 4.2M mesh is presented instead of the hex 20M mesh. It was concluded in section 5.7 that the hex 4.2M and hex 20M mesh predict similar slot flow rate and rotor torque trends in a Reynolds-averaged sense.

The angularly resolved flow rate and root mean square deviation across all rotor positions was shown in figure 5.23 of section 5.8. These statistics were computed from a RANS simulation which describes the time-averaged flow. Reproducing these figures and statistics from a LES would describe the ensemble average and deviations of the filtered flow rate. Contrary to the flow rate provided by a RANS simulation, the filtered flow rate (equation 3.13-2) has a fluctuating velocity component. The root mean square deviation therefore quantifies how much the fluctuating flow rate influences the flow within the stator slots of the mixer. The flow rate from the hex 4.2M 7-psi LES was recorded for five revolutions. Again, the dependence on the current rotor period is assumed to be the most significant. Therefore, thirty realizations can be shown from these five revolutions. These thirty realizations and corresponding statistics for the flow rate are shown in figure 6.8 below. The thirty realizations are shown by the different colored curves in figure 6.8. The solid black curve represents the ensemble average of these thirty realizations. The dashed black curve represents one root mean square deviation above and below the ensemble average curve.

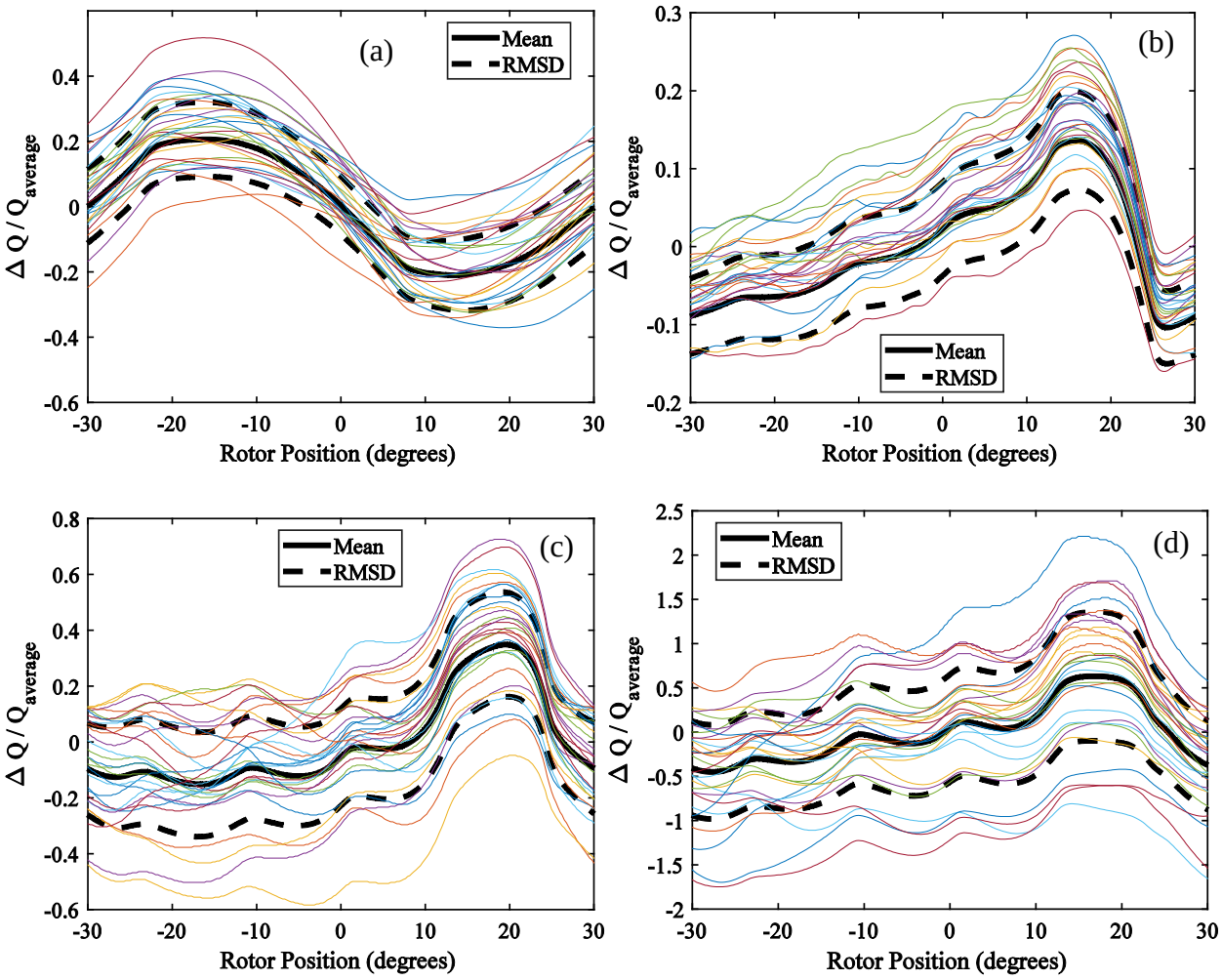

Figure 6.8 – Instantaneous and ensemble average angularly resolved flow rate bounded by root mean square deviation for thirty realizations for (a) primary slot 6 $Q_{average}$ = 6.1 × 10^{-4} m^3/s (N_Q = 0.0113), secondary (b) outer $Q_{average}$ = 2.1 × 10^{-4} m^3/s (N_Q = 0.0039), (c) middle $Q_{average}$ = 3.0 × 10^{-5} m^3/s (N_Q = 0.0006), and (d) inner slots 15 $Q_{average}$ = 5.4 × 10^{-6} m^3/s (N_Q = 0.0001). ΔP = 7 psi, hex 4.2M.

As expected, the filtered flow rate curves in figure 6.8 are noticeably different than the time-averaged flow rate curves in figure 5.23. The root mean square deviation has increased as a result of the fluctuating flow rate component modeled by LES. The secondary inner slot shows the largest root mean square deviation, where one of the given realizations reaches twice the overall time-averaged flow rate. The secondary outer slot shows the smallest root mean square deviation compared to all other slots. For all slots the root mean square deviation is highest when the

maximum flow rate is reached, and the root mean square deviation is lowest when the minimum flow rate is reached. Similar to what was done in section 5.8, the root mean square deviation can be normalized by the overall time-average flow rate for that slot. The maximum and minimum RMSD normalized by the overall time-average are reported in table 6.1 below. The overall time-average flow rate is also reported, but as a dimensionless flow number. Slot notation used in table 6.1 is shown in figure 2.2.

Table 6.1 – RMSD of slot flow rate in hex 4.2M 7-psi simulation.

		Normalized RMSD	
Slot	N_Q	Minimum (%)	Maximum (%)
PS6	0.0109	17.69	24.75
SOS15	0.0039	3.47	5.23
SMS15	0.00055	13.91	18.70
SIS15	0.00010	52.47	76.96

As discussed in section 3.3, the discrete Fourier transform can be applied to a wave to determine the significant frequencies. The one-sided spectrum of the flow rate fluctuations is shown in figure 6.9 below. Since the discrete Fourier transform operates in the frequency domain, the flow rate fluctuations are shown varying in units of inverse rotor periods. The frequency with the largest amplitude in the primary slot (1 inverse rotor period) corresponds to the oscillation observed in figure 6.8a (from -30° to 30°, which corresponds to one rotor period). All secondary slots show this frequency to be significant, as well as for 2, 3, and 4 inverse rotor periods. These frequencies correspond to a half, third, and quarter of rotor period dependence, respectively. Secondary slots 15 show this smaller rotor period (larger frequency) dependence due to the presence of four other neighboring slot rows in one rotor blade passage period.

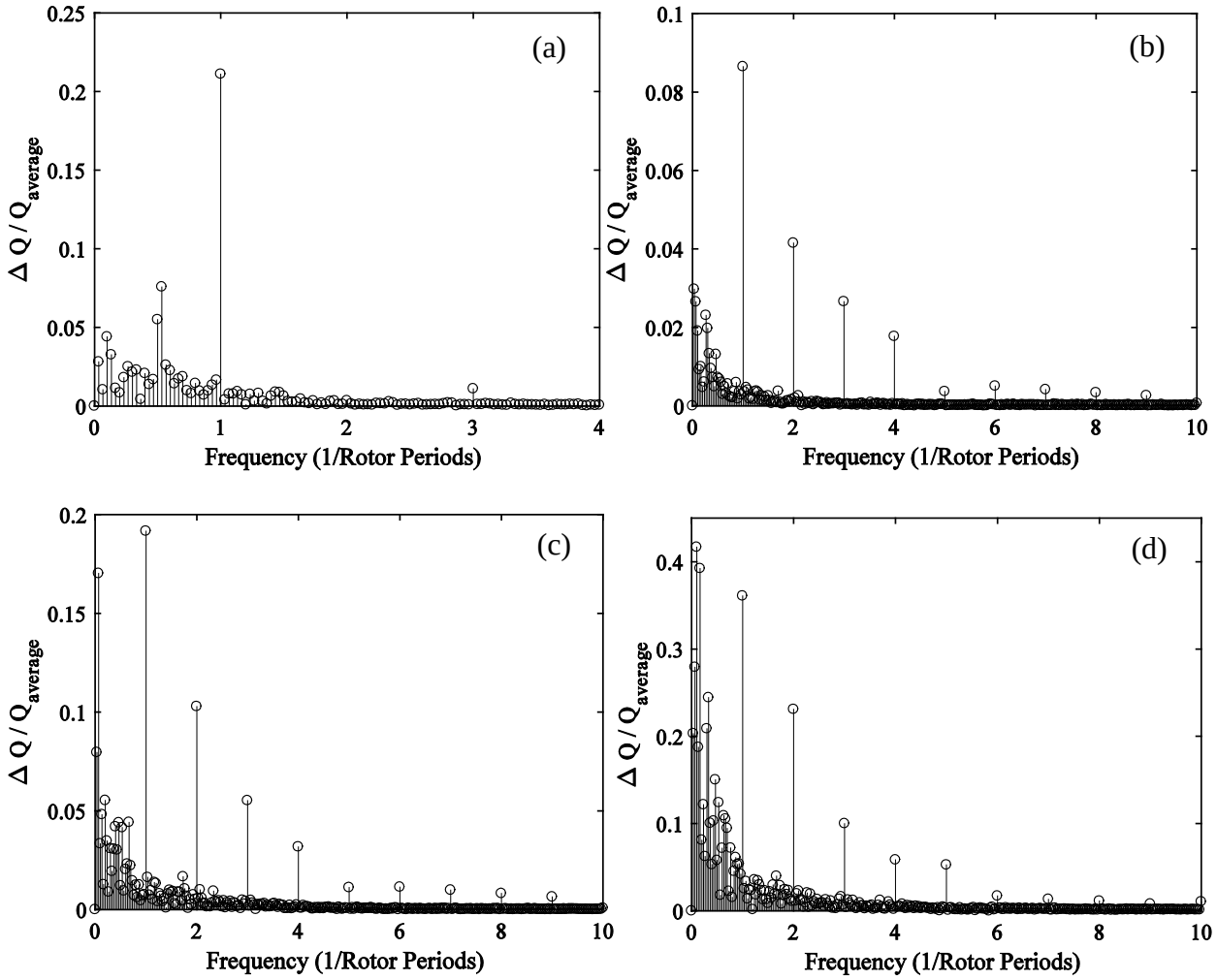

Figure 6.9 –Dimensionless flow rate fluctuations shown in the frequency domain for the (a) primary slot 6, secondary (b) outer, (c) middle, (d) inner slots 15. ΔP = 7 psi, hex 4.2M.

The relatively large amplitudes occurring at integer frequencies form the shape of the flow rate fluctuation curves shown in figure 6.8. Other large amplitude values are shown below a frequency of 1 inverse rotor period. These large rotor periods (small frequencies) correspond to the dependence that flow rate fluctuations have on two, three, or more blade passes. As the thirty flow rate realizations show in figure 6.8, the flow rate fluctuations maintain this shape but vary relative to the angularly averaged value. From outer, middle, to inner secondary slots, the

amplitude of the larger rotor periods has more influence. The amplitude from the larger rotor periods is greater than the amplitude of the single rotor period for the secondary inner slot.

Similar to the filtered flow rate, the filtered torque (given by equation 3.13-3) has an average and a fluctuating component. However, the angularly resolved torque profiles in figure 6.10 show less variance than the flow rate profiles. This is because flow rate is reported across a single stator slot. While torque is reported across all six rotor blades for a given stage. The largest variances in the torque profiles occur when the rate of change of torque is low. This occurs when the primary rotor torque reaches a maximum and minimum, and when the secondary rotor torque reaches a minimum. The torque on the primary rotor shows higher variance then on the secondary rotor. The maximum root mean square deviation normalized by the overall average is 8.11% for the primary rotor and 7.50% for the secondary rotor.

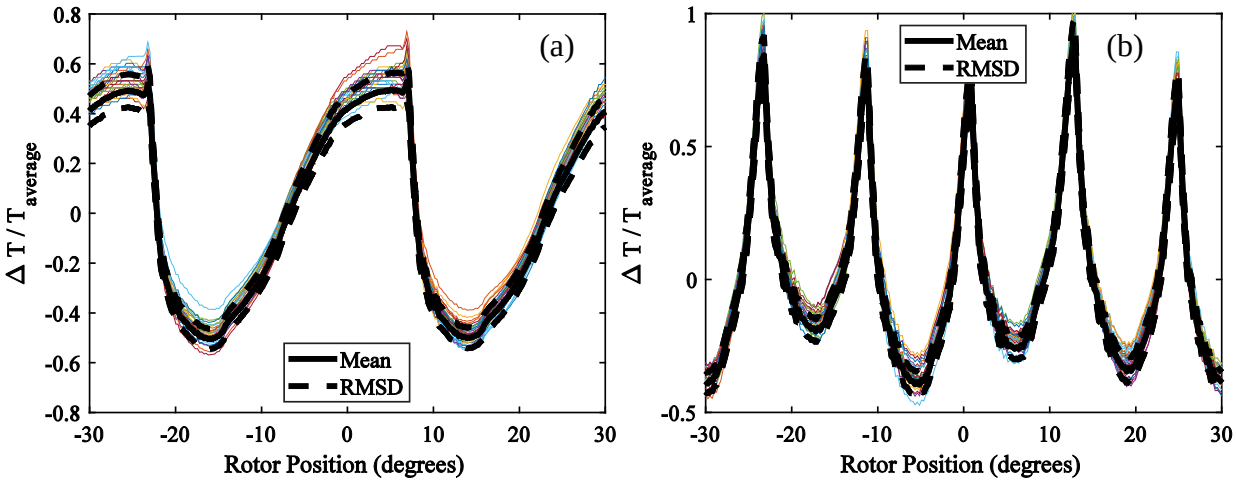

Figure 6.10 – Ensemble average torque bounded by root mean square deviation with thirty realizations for the (a) primary rotor with average torque 4.51 Nm (N_{Po} = 0.933) and (b) secondary rotor with average torque 4.74 Nm (N_{Po} = 0.980). ΔP = 7 psi, hex 4.2M.

The discrete Fourier transform can be applied to the torque fluctuations observed in figure 6.10. The one-sided spectrum of the torque fluctuations is shown in figure 6.11 below. The frequency with the largest amplitude contributing to the primary rotor torque occurs every 2

inverse rotor periods. The amplitudes of these frequencies decrease in magnitude as the frequency increases. The largest amplitude, corresponding to one half rotor period (2 inverse rotor periods) is observed in figure 6.10a. Two oscillations in one rotor period are observed in the primary rotor torque fluctuation curves indicating a half rotor period dependence. Five oscillations in one rotor period are observed in the secondary rotor torque, this corresponds to the largest amplitude (at five inverse rotor periods). The next largest amplitudes contributing to the secondary rotor torque occur at every 5 inverse rotor periods.

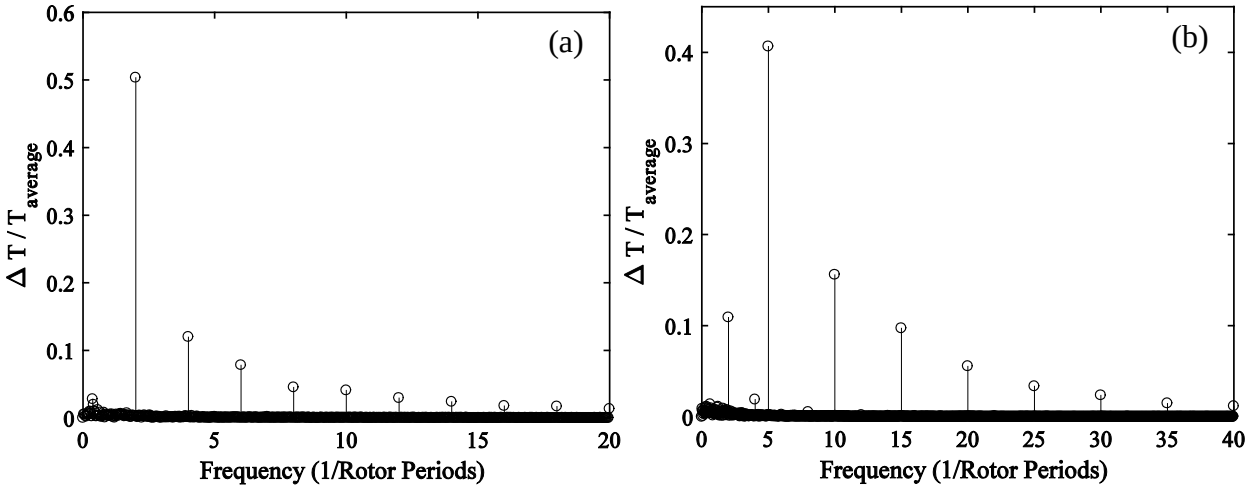

Figure 6.11 – Dimensionless torque fluctuations in the frequency domain for the (a) primary and (b) secondary rotor. ΔP = 7 psi, hex 4.2M.

The amplitude values of the frequency multiplies, two inverse rotor periods for the primary rotor torque and five inverse rotor periods for the secondary rotor torque, form the shape of the torque fluctuation curves. This is similar to what was observed for the flow rate fluctuations in the frequency domain in figure 6.9. The one-sided spectrum of the secondary rotor torque also shows dependence on the two and four inverse rotor periods. This dependence is observed in the change in the local minimum/maximum value in figure 6.10 and is the result of the primary rotor's influence on the secondary rotor. Compared to the flow rate fluctuations, the torque fluctuations

show less dependence on small frequencies. This is observed in figure 6.10 by the relatively small torque RMSD values at all rotor positions.

6.4 Subgrid-scale Eddy Viscosity

The SGS eddy viscosity is the proportionality constant used to relate the SGS stress tensor to the filtered strain rate tensor, as shown in equation 3.11-1. The general expression of the SGS eddy viscosity (equation 3.11-2) shows it is dependent on the filter length given by the grid and some known operator. In this work the WALE SGS model was used; the operator was shown to depend on the magnitude of the strain rate and vorticity tensor in equation 3.11-5. The significance of the SGS eddy viscosity is apparent when approximating the turbulent energy dissipation rate of the subgrid-scales, shown in equation 3.13-9.

In this section, contours of the SGS eddy viscosity are shown for the hex 20M 7-psi simulation. These contours are shown across a region of stator slots as a snapshot with a given rotor position (figure 2.7). The magnitude of the SGS eddy viscosity is compared to the kinematic viscosity. By comparing the viscosities, the turbulent energy dissipation rate of the resolved and subgrid-scales are also compared. This will therefore highlight the regions with insufficient mesh refinement. Contours of the SGS eddy viscosity divided by kinematic viscosity are shown in figure 6.12 below.

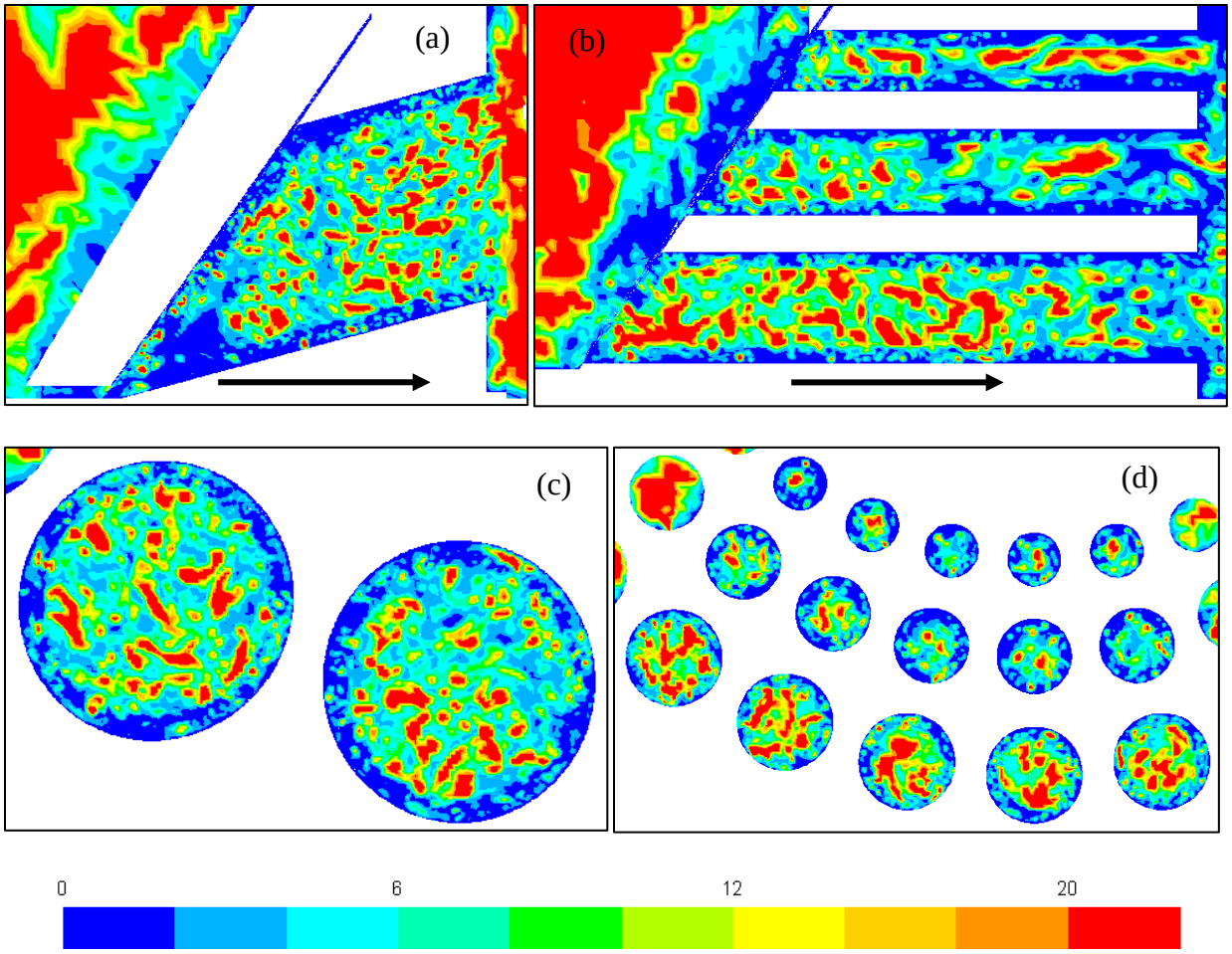

Figure 6.12 – Subgrid-scale eddy viscosity ratio contours in the (a) primary stage, x = 0 mm, (b) secondary stage, x = 0 mm, (c) primary stator slots 6 and 7, z = 60 mm, and (d) secondary stator slots 14-18, z = 100 mm. ΔP = 7 psi, hex 20M.

The SGS eddy viscosity is shown to be less at the outer edge of the stator slots compared to the inner portion. This trend occurs because the filter length is less in these locations. The computational mesh (figure 2.6) shows refinement in these areas so there is smaller local filter length. The SGS eddy viscosity in the inner portion of the slots is shown to vary from ~6 to ~20 times larger than the kinematic viscosity. The filter length is uniform in this region; therefore this variance in SGS eddy viscosity occurs because of the magnitude of the strain and vorticity tensors. Since these contours display an instant of the SGS eddy viscosity, the value of the strain rate and vorticity magnitude and the value of this model constant will change at another instant. It should

also be noted that a higher viscosity ratio is predicted in the primary and secondary outer slots compared to the secondary middle and inner slots. This implies that higher strain rate and vorticity magnitude are predicted in the larger slots. As a result, the turbulent energy dissipation rate is modeled more heavily in the larger stator slots.

6.5 Influence of Backpressure and Mesh Resolution on Filtered Properties

As section 5.6 described the influence of backpressure on mean properties predicted by RANS, this section describes the influence of backpressure on filtered properties predicted by LES. The backpressures considered in this comparison are the 0- and 7-psi operating conditions. The influence a change on backpressure has on flow and power number is discussed.

Flow numbers computed from different RANS simulations were provided in figure 5.20. These values were computed using the outlet throughput and normalized using the outer rotor diameter. This procedure can be repeated for each LES. The flow numbers for these LES have been included in figure 5.20 and reproduced in figure 6.13 below. As the velocity field comparison above demonstrated, flow rate, and therefore flow number, decreases with increasing backpressure.

Similar to the RANS flow numbers, the LES flow numbers are larger than the flow number predicted by the coarse tet RANS simulation. At the 0-psi backpressure, the flow number predicted by the hex 4.2M LES is 4% larger than the flow number predicted by the hex 20M LES. However, at the 7-psi backpressure, the flow number predicted by the hex 20M LES is 6% larger than the hex 4.2M LES flow number. Comparing all meshes and turbulence models, the largest flow number difference is between the coarse tet mesh and the hex 20M LES at the 7-psi backpressure. These flow numbers differ by 10%. The flow number predicted by each simulation differs slightly, implying flow number is weakly influenced by mesh resolution and turbulence model.

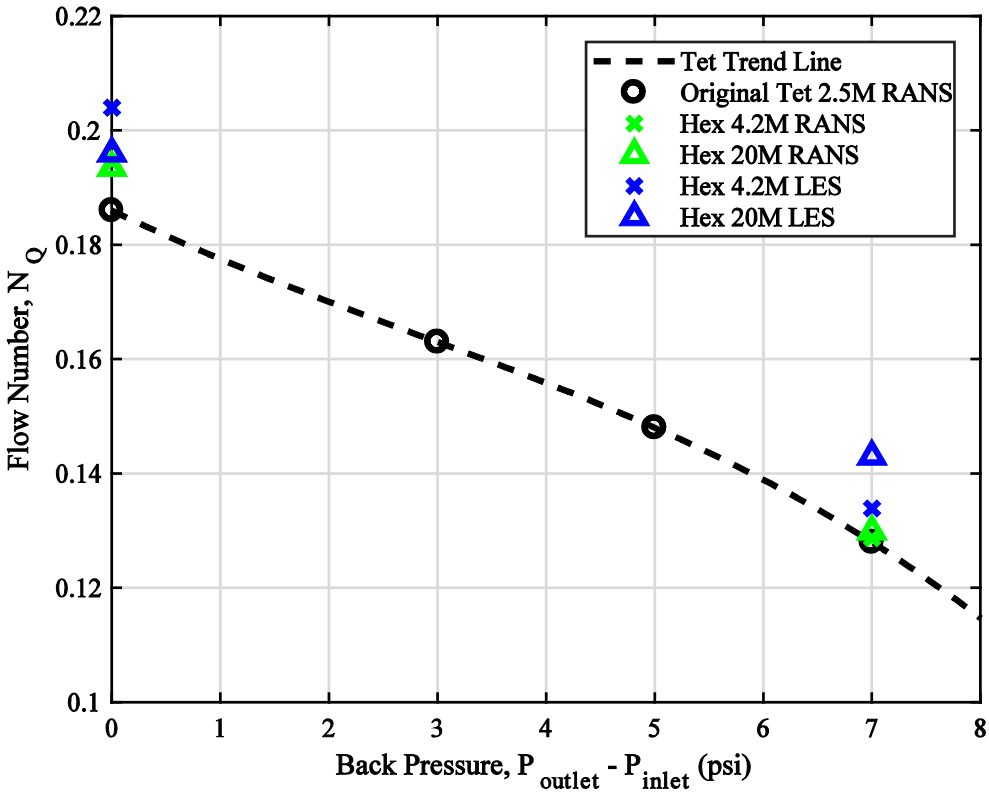

Figure 6.13 – Flow number for all simulations. The dashed trend line was developed from four points using the original tet mesh which does not have extended inlet and outlet pipes.

As flow numbers from the LES were added to figure 5.20, power numbers from the LES can be added to figure 5.21. The power number from a LES is computed in a similar manner as was done for the RANS simulations. Again, power across both rotor stages is normalized by the fluid density, rotor speed, and outer rotor diameter. The power numbers for each LES are provided in figure 6.14 below. Since throughput between RANS and large eddy simulations was comparable, we expect power to be relatively close. This is confirmed in figure 6.14 below, as backpressure increases the power reported by LES decreases.

Similar to the flow numbers in figure 6.14, the LES power numbers are larger than the power numbers predicted by the coarse tet RANS simulation. At the 0-psi backpressure, the hex 4.2M and hex 20M LES predict power numbers within 1% of each other. At the 7-psi

backpressure, the hex 4.2M and hex 20M LES predict power numbers within 3% of each other. This implies that the power number is not strongly influenced by mesh resolution for LES. The largest difference among reported power numbers is between the coarse tet mesh and the hex 4.2M LES. The hex 4.2M LES predicts a power number 6% larger than the power number predicted by the tet mesh. Therefore the conclusion reached for flow numbers applies to power numbers, power numbers are weakly influenced by mesh resolution and turbulence model.

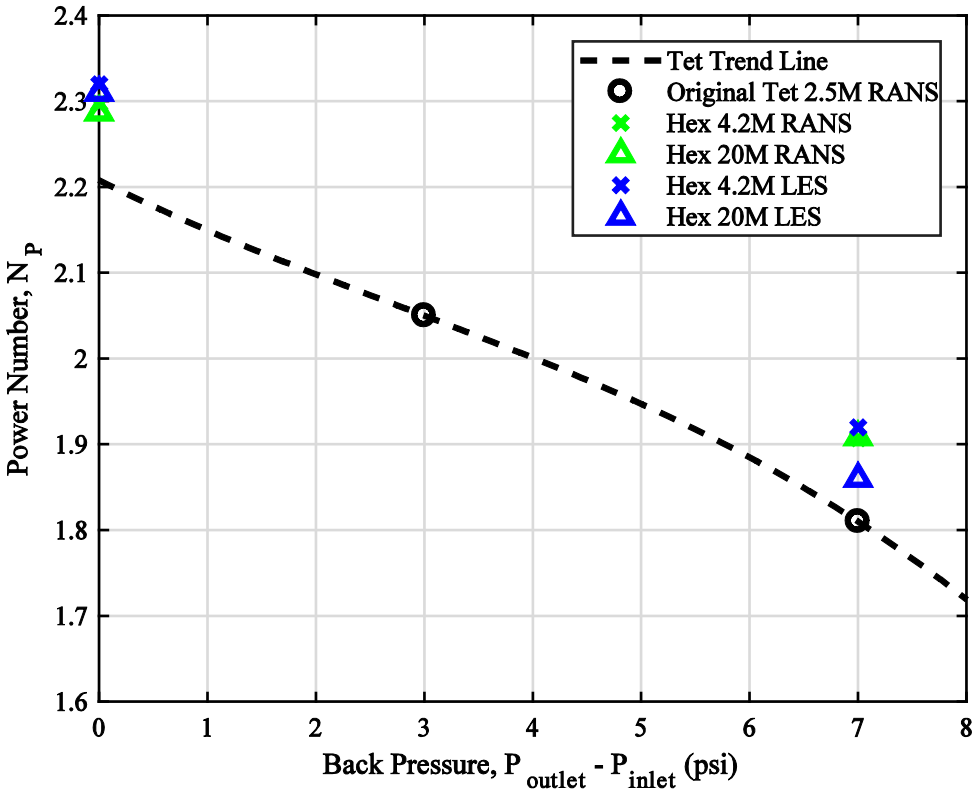

Figure 6.14 – Power number for all simulations. The dashed trend line is developed from linear interpolation of the flow number curve developed from the original tet mesh which does not have extended inlet and outlet pipes.

The smaller vortices observed in the hex 20M simulations of sections 6.1 and 6.2 would be absent in a coarser mesh such as the hex 4.2M mesh. For this reason, the filtered velocity field simulated by the hex 4.2M computational mesh is shown as a snapshot in figure 6.15. In section 6.4 the viscosity ratio showed the regions in which the modeled SGS energy dissipation rate was

larger than the resolved. We expect the SGS eddy viscosity to increase with filter length, this is shown using contours from the hex 4.2M simulation. Since computational expense increases with mesh refinement, this section discusses how much is gained by resolving more scales.

The filtered velocity field in the primary and secondary stage from the hex 4.2M simulation at the 7-psi backpressure operating scenario is shown in figure 6.15. The filtered velocity field and filtered strain rate magnitude contour near the primary shear gap for this simulation are also shown in figure 6.16. Both of these figures share the same rotor position which was shown in figure 2.7. These figures are meant to be compared to analogous figures for the hex 20M simulation shown in sections 6.1 and 6.2. The color legend used is equivalent to the legends used in sections 6.1 and 6.2.

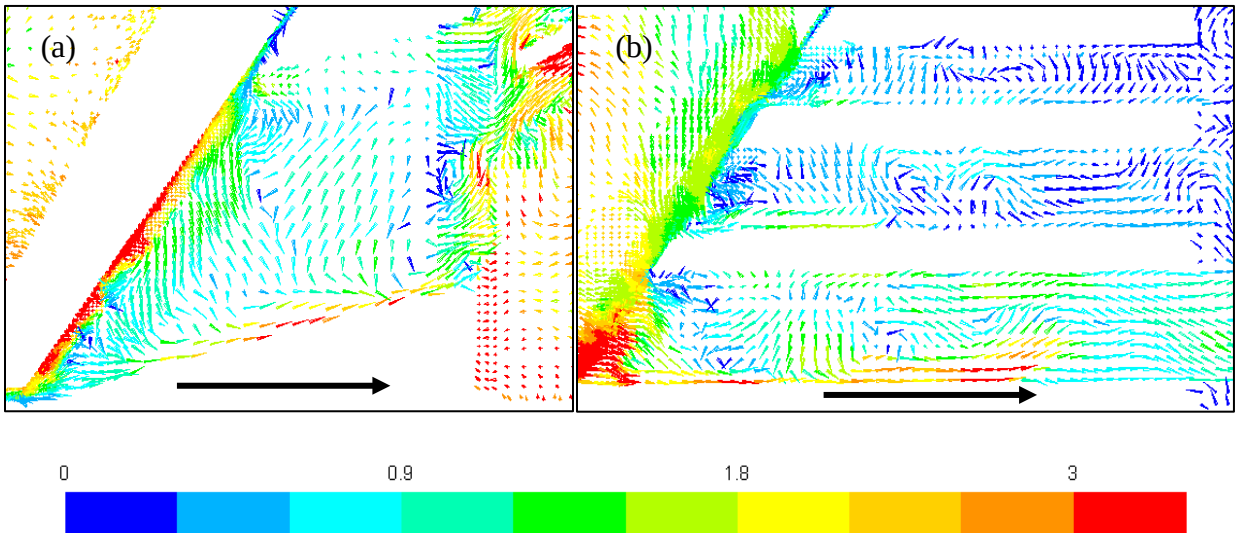

Figure 6.15 – Filtered velocity field colored by velocity magnitude in the center plane, x = 0 mm, for the (a) primary stage, and (b) secondary stage. Color legend scaled by (ND) = 5.8 m/s. ΔP = 7 psi, hex 4.2M.

Both the primary stator outer edge and secondary outer slot show the axial stator jet that was observed in figures 6.1 and 6.4 respectively. Since the axial stator jet is a large scale phenomenon, a relatively coarse mesh such as the hex 4.2M will still resolve the phenomenon.

However, for the particular instance shown, no vortices are observed in the recirculation regions in figure 6.16. The flow is shown moving in the negative axial direction at the inner edge of the stator slots, however no vortices are shown. This phenomenon is not observed in the hex 4.2M simulation because the grid is too coarse to resolve it. As a result, any interaction the recirculating vortices have with the axial stator jet is not resolved in the hex 4.2M simulation. We would therefore expect the hex 4.2M simulation to under-predict the turbulent kinetic energy and the turbulent energy dissipation rate relative to the hex 20M simulation.

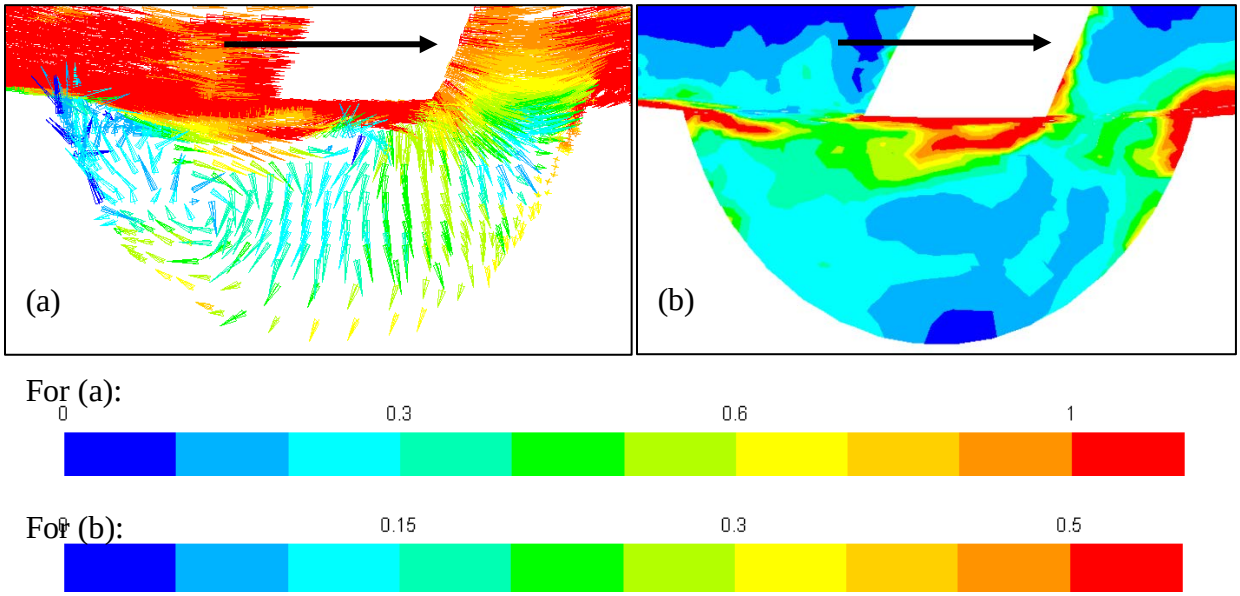

Figure 6.16 – (a) Filtered velocity field colored by velocity magnitude and scaled by relative tip speed of 16.4 m/s. (b) Filtered strain rate magnitude contour scaled by the nominal strain rate magnitude of 6.56×10^4 s^{-1} in primary slot 6, normal to the shear gap. ΔP = 7 psi, hex 4.2M.

The filtered velocity field near the primary shear gap for the coarse hex 4.2M computational mesh shows a vortex at the rotor tip and at the right edge of the slot in figure 6.16a. These phenomena were both observed for the hex 20M mesh in figure 6.6b. However the recirculation region at the right edge of the slot showed several vortices, which are not observed at the given instant in the hex 4.2M simulation. The corresponding filtered strain rate magnitude

contour in figure 6.16b shows high strain rates at the rotor tip and at the edges of the shear gap opening. The filtered strain rate magnitude contour from the hex 20M simulation, in figure 6.7b, showed high strain rates throughout the recirculation region due to the interactions between the large scale eddies and the small recirculation vortices. Since the small recirculation vortices are not resolved in the hex 4.2M simulation, strain rates are under-predicted in the recirculation region.

The scales necessary to resolve the turbulent energy dissipation rate were discussed in section 6.4. To support this discussion, SGS eddy viscosity ratio contours for the hex 20M simulation were shown in figure 6.12. As previously discussed, the SGS eddy viscosity is dependent on filter length. Since filter length increases with a coarser mesh, we would expect this quantity to be larger for the hex 4.2M compared to the hex 20M simulation. The SGS eddy viscosity ratio for the hex 4.2M simulation is shown in figure 6.19 below. Note the color scale used to quantify the SGS eddy viscosity in the hex 4.2M simulation is four times larger than the color scale used for

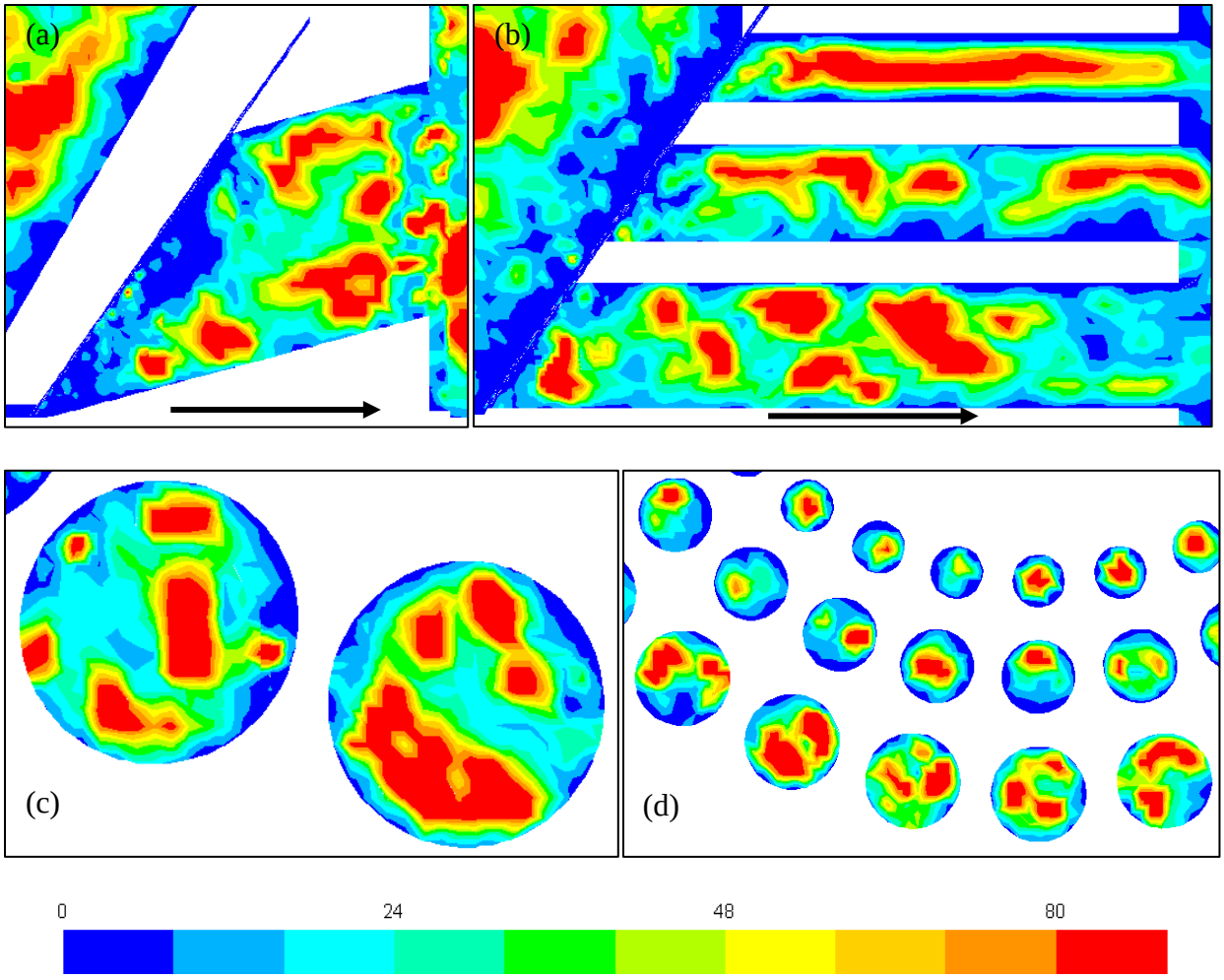

Figure 6.17 – Subgrid-scale eddy viscosity ratio contours in the (a) primary stage, x = 0 mm, (b) secondary stage, x = 0 mm, (c) primary stator slots 6 and 7, z = 60 mm, and (d) secondary stator slots 14-18, z = 100 mm. ΔP = 7 psi, hex 4.2M.

the hex 20M simulation. This suggests that if the hex 4.2M simulation was to be used to predict the turbulent energy dissipation rate, the approximated value would be modeled significantly more than the value predicted by the hex 20M simulation.

6.6 Filtered Flow Field Convergence

Similar to section 5.8, the measures of convergence discussed in section 3.16, are applied to LES instead of RANS. First the level of flow field convergence of the LES is discussed. Residual

values reported by FLUENT at the end of time steps are quantified. The number of iterations required to reach these residual values is also mentioned.

As explained in section 3.16, the LES flow field presented in this work were considered converged when the outlet flow rate varied within 3% of the average value. The LES from each computational mesh and operating scenario reached this state. Samples from these LES were not taken until after this convergence state was reached. Samples of the stator slot velocity field, flow rate, and torque were taken for 5 revolutions for the hex 4.2M simulation. Samples of the stator slot velocity field for the hex 20M simulation were taken for 5 revolutions, and 1 revolution for the flow rate and torque. The LES runs were initialized in a similar manner as discussed in section 5.8. The hex 4.2M 7-psi LES was initialized from the hex 4.2M 7-psi RANS simulation. Then the hex 4.2M 0-psi LES was initialized from the 7-psi LES. The hex 20M simulations were initialized from an interpolated flow field of their corresponding hex 4.2M simulation.

It should be noted that the LES results presented in this thesis have not reached grid convergence. As discussed in section 6.5, the SGS eddy viscosity was altered significantly from the hex 4.2M to the hex 20M mesh. With no further refined mesh to compare to, it cannot be concluded that the hex 20M mesh has reached grid convergence. As a result, quantities such as the turbulent energy dissipation rate, which is discussed in section 7.3, may not be adequately quantified.

The residual values reported by FLUENT at each iteration using equation 3.16-3 for RANS are given in table 5.6. A similar table was developed for all LES, shown below as table 6.2. The LES model involves four governing equations, therefore the residual values of four flow variables are reported with each iteration. These flow variables are: continuity, and the filtered x-, y-, and z-velocities. It should be noted that on an iteration basis, a LES is less computationally expensive

than a RANS k-ε simulation because four governing equations are solved instead of six. Similar to RANS, continuity is the largest residual value for the LES. Another similarity, is the number of iterations required for the coarse hex 4.2M simulation compared to the hex 20M simulation.

Table 6.2 – Iteration convergence for all large eddy simulations.

Simulation Parameters		Residuals (-)		
Mesh	Backpressure	Continuity	$\langle U_i \rangle$	M_{iter}
Hex 4.2M	0-psi	10^{-4}	5×10^{-7}	40
	7-psi	10^{-4}	5×10^{-7}	40
Hex 20M	0-psi	10^{-4}	10^{-7}	45
	7-psi	10^{-4}	10^{-7}	60

Thirty samples from these converged flow fields are used to predict the ensemble flow rate and torque (see section 6.3), and various turbulence quantities (see chapter 7). The slots considered in chapter 7 include primary slot 6 and secondary slot column 15. Turbulence quantities, or various velocity statistics, are computed across the center plane (x = 0 mm) of these slots. To show how these statistics converge with additional realizations, equations 3.16-4 and 3.16-6 are used. With each new realization, the maximum absolute difference between the previous and new statistical value is computed. Since thirty realizations are used in this thesis, there are twenty nine differences. These differences are shown in figure 6.18 below. The statistics computed from the velocity field across the various stator slot center planes is considered in figure 6.18. The average flow variable substituted into equation 3.16-4 is the magnitude of the average velocity, $\|\overline{U}_i\| = \sqrt{\overline{U}_i \overline{U}_i}$, which is shown by the red points. The variance term substituted into equation 3.16-6 is the square root of the sum of variances, which is also proportional to the turbulent kinetic energy, $\sqrt{2k} = \sqrt{\overline{u_i u_i}}$, and is shown by the blue points.

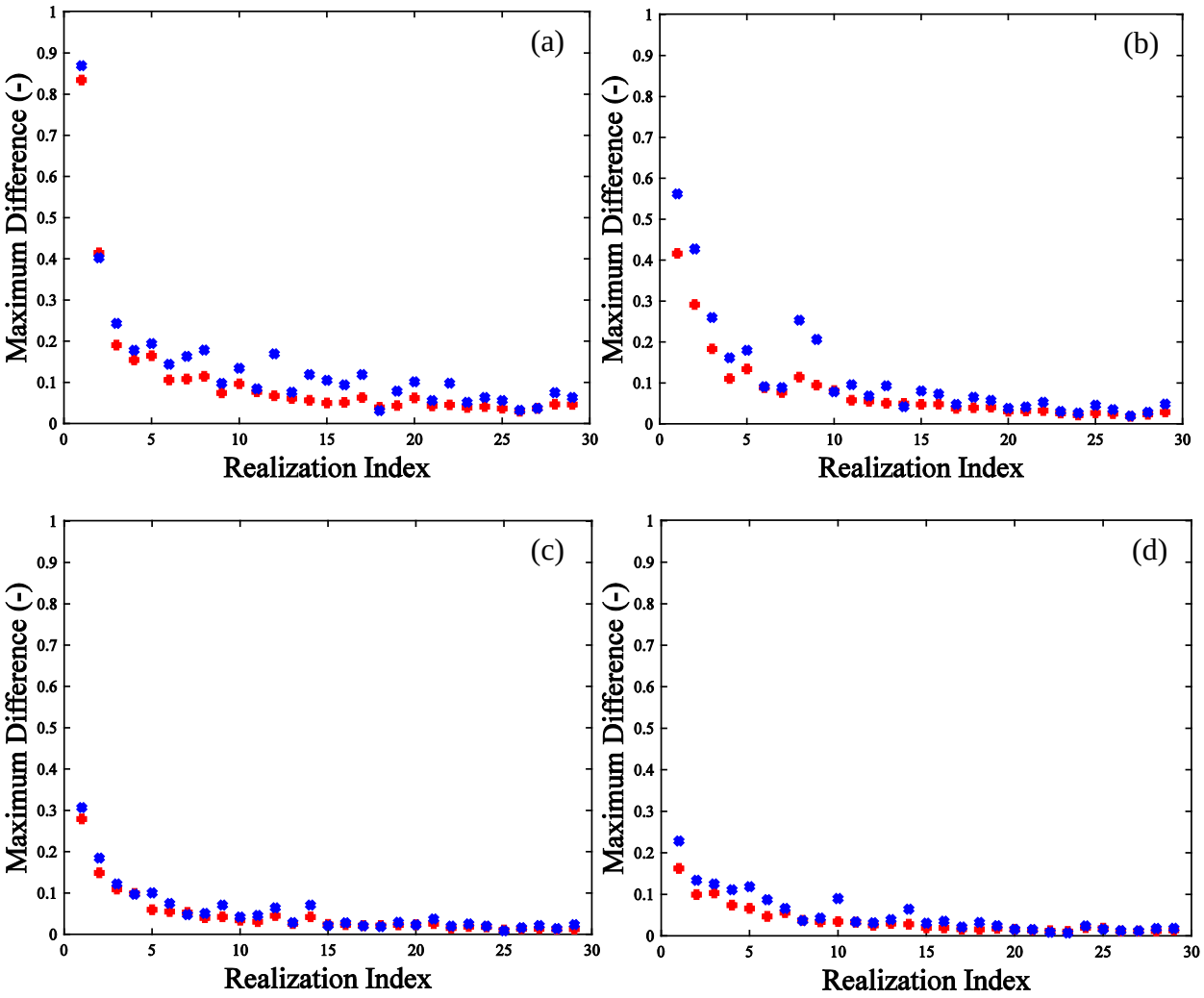

Figure 6.18 – Convergence of the first moment statistic, $\|\overline{U_i}\| = \sqrt{\overline{U_i}\overline{U_i}}$, (red) and the variance, $\sqrt{2k} = \sqrt{\overline{u_i u_i}}$, (blue) of velocity in (a) primary slot 6, secondary (b) outer, (c) middle, and (d) inner slot 15. Velocity normalized by maximum tip speed, 18.2 m/s. ΔP = 7 psi, hex 20M.

The maximum absolute difference between these statistics is normalized by the maximum tip speed of 18.2 m/s. As more realizations are added, the maximum absolute difference of both statistics approach zero for all planes. The change in the first moment statistic, represented by the change in the magnitude of the average velocity, is below the change in the turbulent kinetic energy for majority of the realization indices. This implies that statistics involving the variance, or the second moment, would take more realizations to converge than statistics involving the average of

the first moment. Comparing the convergence profiles for the different slots, primary slot 6 and secondary outer slot 15 converge at a slower rate than secondary middle and inner slots 15. This is expected since the relative blade speed and intensity of the turbulence is smaller by comparison in the middle and inner secondary slots.

Convergence of statistics other than velocity are of interest. The convergence of velocity gradients, more specifically deformation rates, are considered in figure 6.19. This figure is produced using the same method to produce figure 6.18, except the flow variable considered has been altered. To consider the convergence of the first moment statistics involving deformation rates, the magnitude of the average strain rate tensor is considered, $\|\bar{S}_{ij}\| = \sqrt{2\bar{S}_{ij}\bar{S}_{ij}}$, which is shown in red. To consider the convergence of the variance involving deformation rates, the square root of the sum of strain rate tensor variances is used, $\sqrt{2\overline{s_{ij}s_{ij}}}$, which is shown in blue. Where s_{ij} is the fluctuating component of the instantaneous strain rate tensor. It should be noted that this term includes the turbulent energy dissipation rate given by equation 3.7-6. The maximum absolute difference of these quantities is normalized by the maximum nominal strain rate of 7.3×10^4 s^{-1}.

Similar to figure 6.18, all convergence profiles approach zero as more realizations are included. The change in the average strain rate magnitude is smaller than the change in the sum of strain rate tensor variances for most realization indices. The scale used in figure 6.19 is five times larger than that used in figure 6.18, suggesting that statistics involving deformation rates require more realizations to converge. The convergence profiles in the primary slot and secondary outer slot take longer to converge compared to the secondary middle and inner slots. This is due to the relative strain rate magnitude decreasing with rotor diameter.

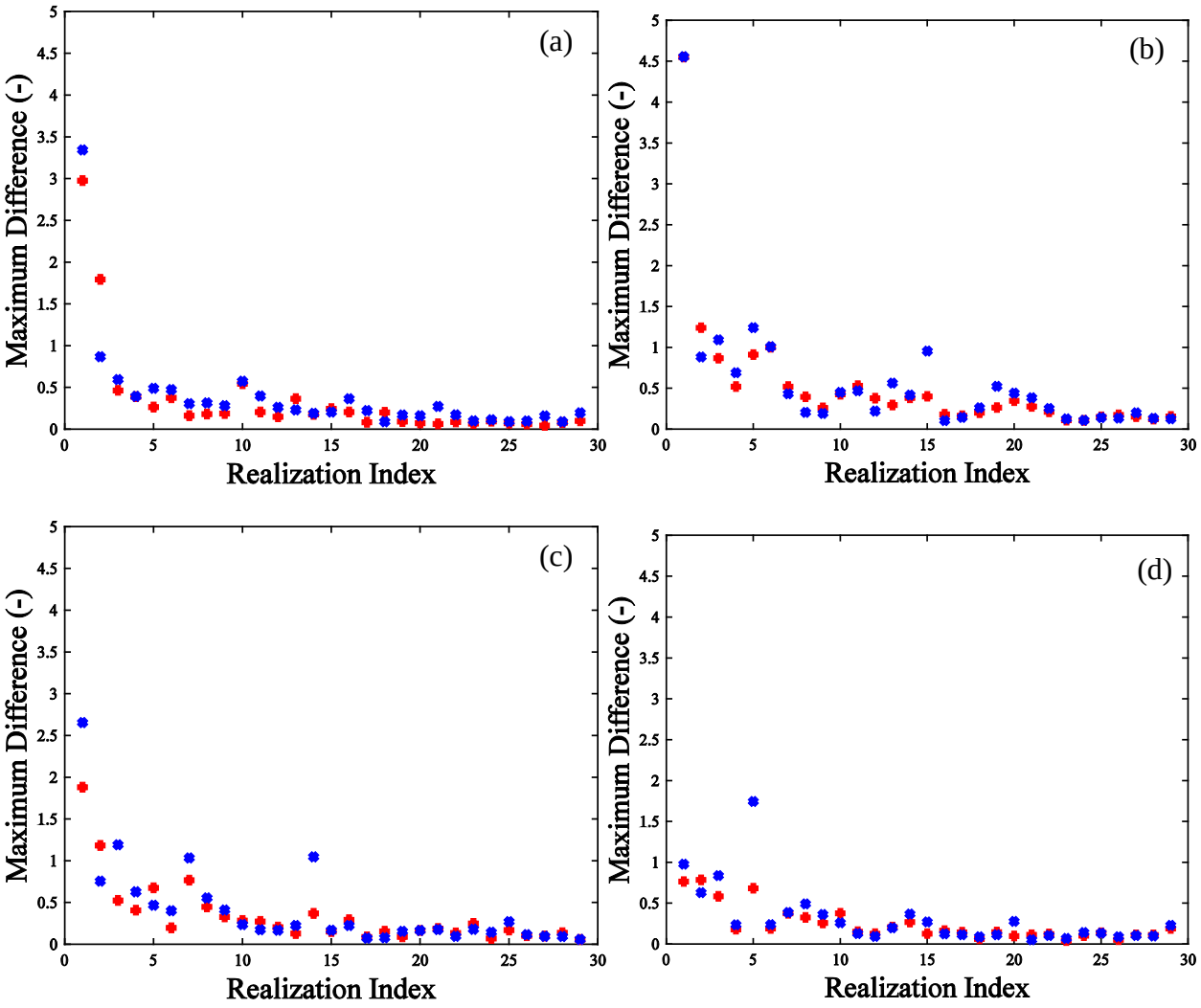

Figure 6.19 – Convergence of the first moment statistic, $\|\bar{S}_{ij}\| = \sqrt{2\bar{S}_{ij}\bar{S}_{ij}}$, (red) and the variance, $\sqrt{2\overline{s_{ij}s_{ij}}}$, (blue) of deformation rates in (a) primary slot 6, secondary (b) outer, (c) middle, and (d) inner slot 15. Deformation rates normalized by maximum nominal strain rate, 7.3×10^4 s^{-1}. ΔP = 7 psi, hex 20M.

6.7 Summary of Large Eddy Simulation Results

The phenomena observed in the filtered velocity field in stator slots and near the shear gap was presented. By qualitatively comparing LES results to RANS, the influence of the fluctuating component was discussed. Filtered strain rate magnitude contours were presented near the shear gap as the rotor blade passes a primary stator slot. Although filtered results change from one rotor

period to the next, qualitative conclusions on the resolved eddies and flow features in this mixer were made. The filtered stator slot flow rate and rotor torque was analyzed in the time and frequency domain. Results from the hex 4.2M and hex 20M meshes were compared using the SGS eddy viscosity.

Large eddies enter the stator slots between a blade passage. The intensity and size of these eddies diminish as it penetrates further into the stator slot and is influenced by wall effects and recirculating vortices already present in the slot. These eddies travel along the outer edge stator wall, acting as a stator jet, and thereby contributing to the filtered stator slot flow rate. Vortices make up the recirculation region. The trajectory of these vortices collide with the inner edge stator wall and interfere with incoming larger eddies to shape the stator jet.

In the primary stator, roughly one large eddy enters with each blade passage. In the secondary stator, several large eddies may enter with each blade passage resulting in different flow rate curves. The largest eddies that may enter a stator slot are the diameter of that slot. The diameter of the secondary stator slots is less than the primary stator slots. Therefore, the turbulent Reynolds number is less and so is the eddy intensity and lifetime. The recirculation region in the primary stator forms due to the movement of the secondary rotor blade near the exit of the primary stator. The recirculation region in the secondary stator forms due to slot configuration.

In the shear gap region, recirculating vortices travel near the rotor blade tip and interact with the time-averaged mixing layer. After the blade passes a stator slot, a radial jet forms and either diminishes at the stator wall or contributes to slot throughput. Between each blade passage, a large eddy enters the shear gap region. This eddy interacts with recirculating vortices present in the time-average recirculation region. These vortices and their interactions with the mixing layer,

radial jet, and large eddies entering the slot, contribute to the resolved strain rate magnitude in the shear gap region.

The filtered stator slot flow rate was dependent on the flow features present in the slot, particularly the stator jet. Since the intensity and size of the stator jet varied due to resolved fluctuations, the filtered flow rate showed a fluctuating component. The root mean square of this fluctuating component is highest when the ensemble averaged flow rate reaches a maximum. The filtered secondary inner stator slot flow rate was particularly influenced by this fluctuating component. Fourier analysis revealed that these fluctuations contribute at smaller frequencies which shape the filtered flow rate signal. The fluctuating component of the rotor torque is negligible.

Turbulent structures and vortices, seen in the hex 20M LES, were not resolved in the hex 4.2M LES. The absence of these structures influence turbulence quantities such as turbulent kinetic energy, the production and dissipation rates of the turbulent kinetic energy, and the strain rate tensor. The SGS eddy viscosity ratio showed the influence of the SGS is higher for a less resolved mesh. Local refinements made near the stator wall of the hex 20M mesh strongly influenced the SGS eddy viscosity ratio. SGS scales unaccounted for in the hex 4.2M LES did not significantly influence macroscopic properties such as stator slot flow rate and rotor torque. That is, the predicted values for all coarse mesh simulations compared favorably with the hex 20M results.

7 Comparison between RANS and Large Eddy Simulations

This chapter compares results provided by RANS and LES. To accomplish this, filtered quantities provided by LES are ensemble-averaged. In this first section of this chapter, flow rate and torque profiles are compared in the time and frequency domain. Then quantities directly provided by RANS are compared to averages LES quantities, including the mean velocity, turbulent kinetic energy, and the turbulent energy dissipation rate. Modeling assumptions made by the RANS k-ε closure are validated by comparing quantities such as the eddy viscosity, production and transport of turbulent kinetic energy using LES. Anisotropic regions in the stator slots are presented in the remainder of this chapter. Unless otherwise mentioned, all results in this chapter are from simulations operating at the 7-psi backpressure.

7.1 Flow Rate and Torque

Stator slot flow rate and rotor torque time profiles have been shown for RANS and LES in chapters 5 and 6, respectively. In this section, the time and frequency profiles from these two simulations are directly compared. Since filtered flow rate and torque information was recorded longer for the hex 4.2M computational mesh, the flow rate and torque from the hex 4.2M mesh will be compared. It was shown that the hex 20M mesh did not provide greater accuracy for flow rate and torque. To make this comparison, the ensemble average from the filtered flow rate and torque are shown. Flow rate and torque fluctuations from these ensemble averages are shown as one RMSD above and below the average. When comparing flow rate and torque from these two simulations in the frequency domain, no ensemble averaging is performed. Therefore, any flow rate and torque deviation predicted by the two models in the frequency domain describes differences between the RANS modeled average and the filtered flow rate and torque from LES.

Dimensionless flow rate fluctuations in primary slot 6 and all secondary slots of column 15 as predicted by RANS and LES are shown in figure 7.1. The overall time-average which these fluctuations center around differ between RANS and LES. These overall time-average values are shown in table 7.1 in scientific units and in terms of the flow number. The overall time-average slot flow rates predicted by RANS and LES are within 5% of each other, excluding the secondary inner slot. This discrepancy is due to the different secondary inner stator slot mean velocity fields predicted by RANS and LES. The mean velocity fields are compared in section 7.2.

Table 7.1 – Overall time-average stator slot flow rates.

	RANS		LES	
Slot	$Q_{average}$ (m^3/s)	N_Q (-)	$Q_{average}$ (m^3/s)	N_Q (-)
PS6	6.0×10^{-4}	0.0111	6.1×10^{-4}	0.0113
SOS15	2.0×10^{-4}	0.0037	2.1×10^{-4}	0.0039
SMS15	3.0×10^{-5}	0.0006	3.0×10^{-5}	0.0006
SIS15	8.2×10^{-6}	0.0002	5.4×10^{-6}	0.0001

Flow rate fluctuations from LES and angularly resolved deviations from RANS shown in figure 7.1 share similar trends. As the diameter of the slot decreases, the magnitude of the fluctuations grow larger, and so do the difference in flow rate fluctuations predicted by RANS and LES. The largest differences in the secondary middle and inner slots occurs as the flow rate increases to its ultimate maximum. The magnitude of the largest difference in the secondary inner slot is 0.11 and 0.044 in the secondary middle slot. The largest difference in the primary slot occurs when the rotor blade is between slots, the magnitude of this difference is 0.017.

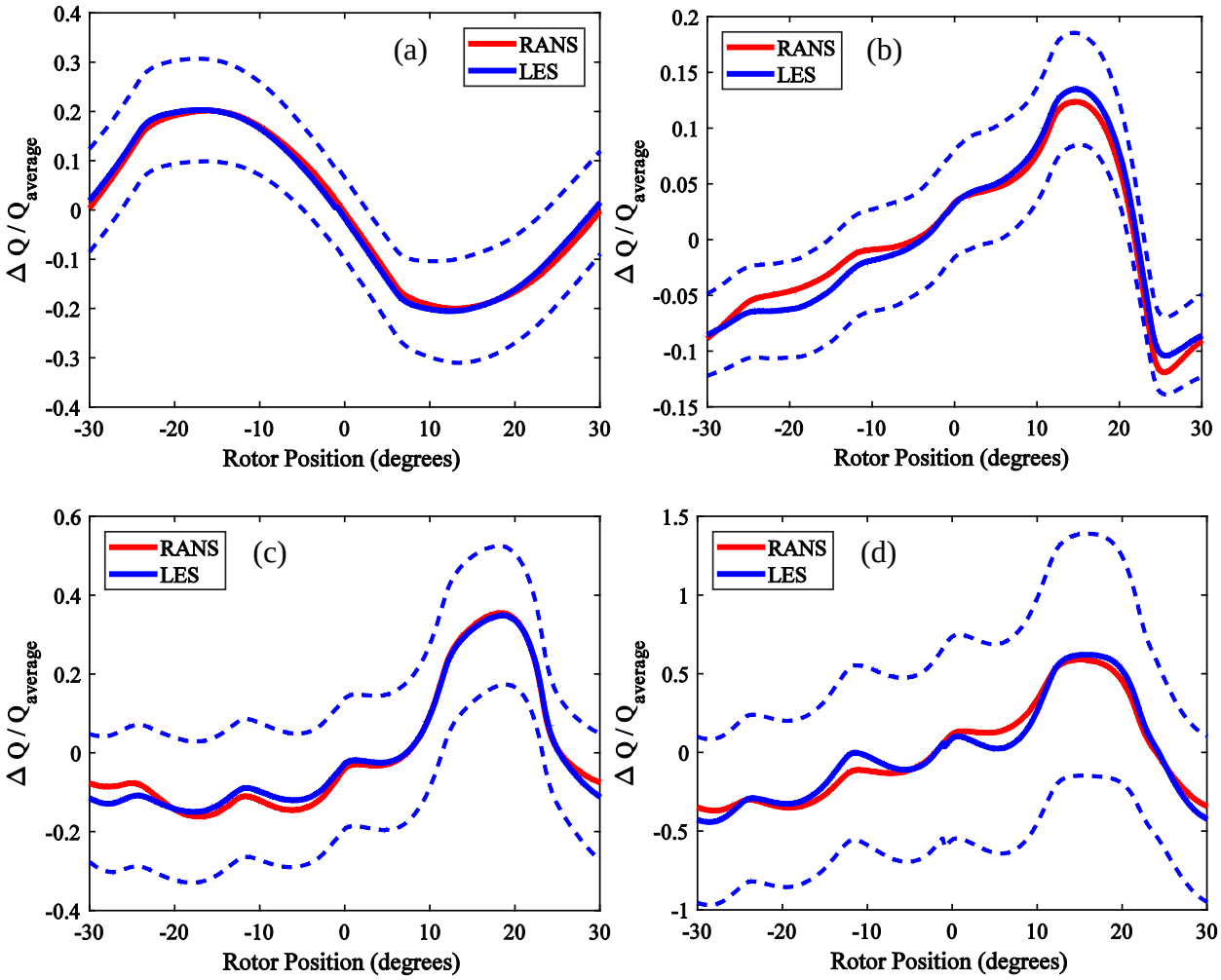

Figure 7.1 – Comparison of mean flow rate varying with rotor position from RANS (red) and LES (blue) in (a) primary slot 6, (b) secondary outer slot 15, (c) secondary middle slot 15, and (d) secondary inner slot 15. Blue dashed lines show one RMSD above and below the mean flow rate predicted by LES. ΔP = 7 psi, hex 4.2M.

Comparing frequency profiles from RANS and LES shown in figure 7.2, both simulations predict similar amplitudes occurring at a frequency of 1 inverse rotor period for the primary slot and at integer frequencies for the secondary slots. As discussed in section 6.3, these frequencies contribute to the shape of the flow rate time profiles. The amplitude predicted by LES at a frequency of 1 inverse rotor period is 0.0025 and 0.0095 larger for the primary and secondary outer slots, respectively. However for the secondary middle and inner slots, RANS predicts amplitudes

that are larger than LES by 0.0086 and 0.03 respectively. Another notable difference is the amplitude values at frequencies lower than 1 inverse rotor period. LES predicts higher amplitudes at these low frequencies. This results from the fluctuating flow rate component which RANS does not model.

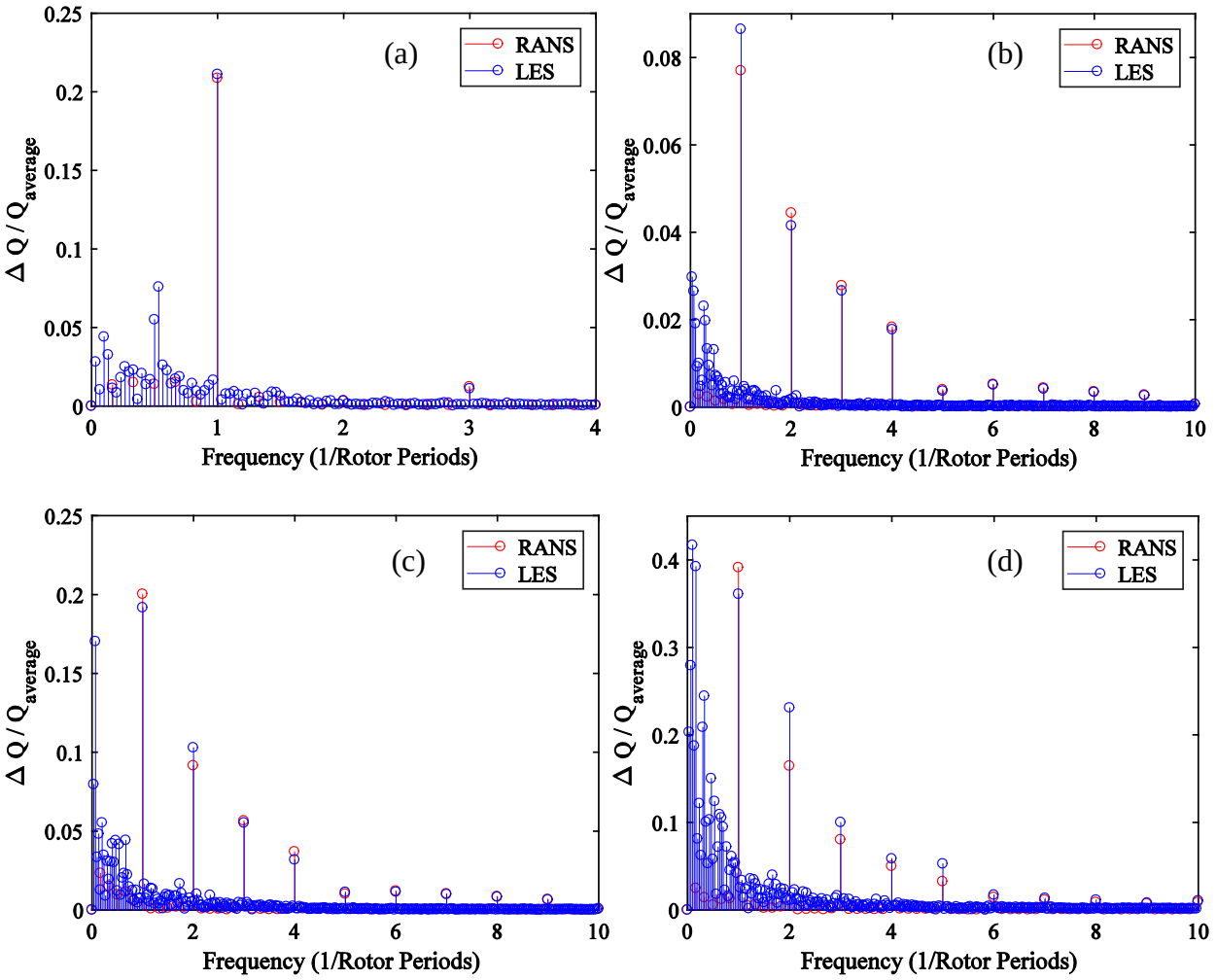

Figure 7.2 – Comparison of mean flow rate from RANS (red) and filtered flow rate from LES (blue) varying with frequency in (a) primary slot 6, (b) secondary outer slot 15, (c) secondary middle slot 15, (d) secondary inner slot 15. ΔP = 7 psi, hex 4.2M.

The angularly averaged torques from RANS and LES are provided in table 7.2. Similar to table 7.1, these values are reported with units and in terms of the respective dimensionless number. The power numbers predicted by RANS and LES are within 1% of each other for both the primary

and secondary rotors. RANS and LES predict similar torque fluctuation trends as shown in figure 7.3. The corresponding frequency profiles for the torque comparisons is shown in figure 7.4. The largest differences for torque fluctuations between RANS and LES occur when the torque reaches its maximum value. The largest difference in the primary rotor is 0.07 for the secondary rotor is 0.1.

Table 7.2 – Overall time-average rotor torque.

	RANS		LES	
Rotor	$T_{average}$ (Nm)	N_{Po} (-)	$T_{average}$ (Nm)	N_{Po} (-)
Primary	4.51	0.932	4.51	0.933
Secondary	4.71	0.973	4.74	0.980

Similar to the flow rate fluctuations, both RANS and LES predict similar amplitudes at the frequencies that contribute to the shape of the torque fluctuations. RANS predicts an amplitude that is 0.0042 larger than that predicted by LES at a frequency of 2 inverse rotor periods for the primary rotor, and 0.0077 larger at a frequency of 5 inverse rotor periods for the secondary rotor. Below a frequency of 2 inverse rotor periods, RANS predicts a high amplitude which LES does not predict. This high amplitude is attributed to convergence error which was discussed in section 5.8.

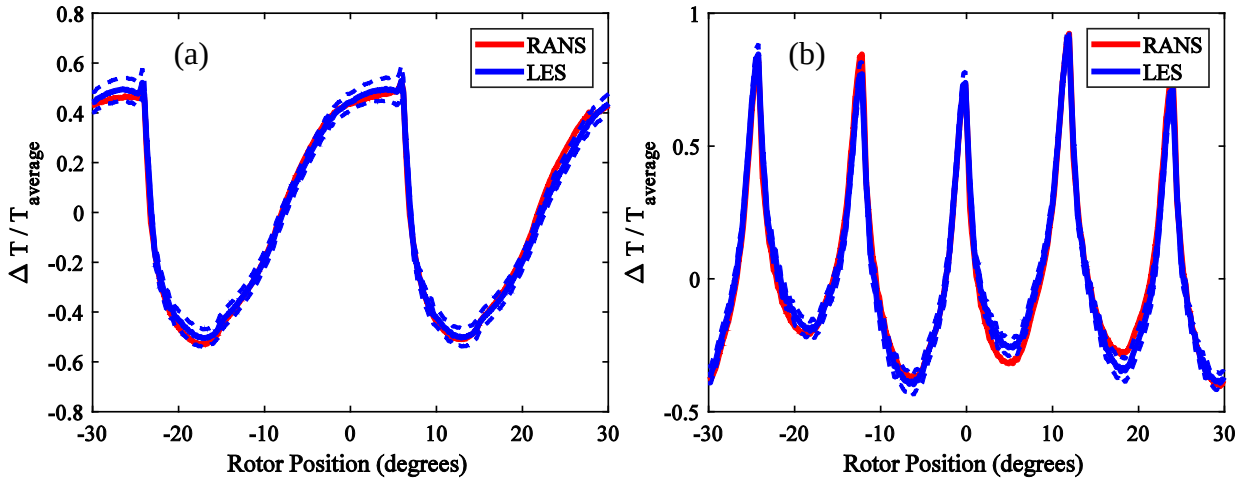

Figure 7.3 – Comparison of mean torque varying with rotor position from RANS (red) and LES (blue) from the (a) primary and (b) secondary rotor. Blue dashed lines show one RMSD above and below the mean flow rate predicted by LES. ΔP = 7 psi, hex 4.2M.

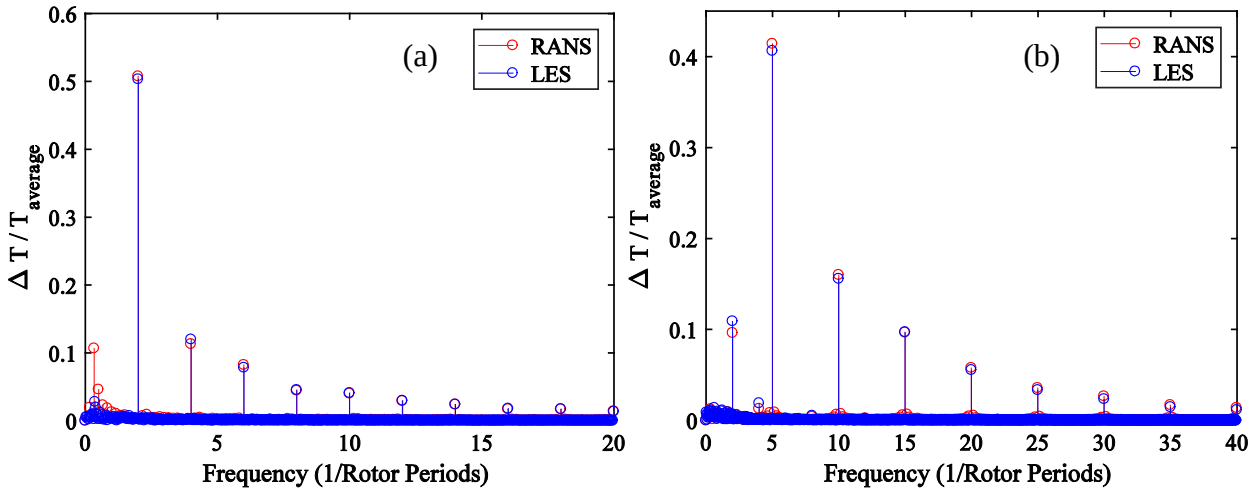

Figure 7.4 – Comparison of mean torque from RANS (red) and filtered torque from LES (blue) varying with frequency from the (a) primary and (b) secondary rotor. ΔP = 7 psi, hex 4.2M.

7.2 Mean Velocity

Mean velocity profiles in the stator slots from RANS were shown in section 5.1. The filtered velocity field at one instant from the LES was shown in section 6.1. By ensemble-averaging thirty realizations at the same rotor position, the angularly resolved mean velocity can be approximated (equation 3.13-1). The computed mean velocity profile from a LES can be

compared to the modeled mean velocity from a RANS simulation. The assumptions made by the RANS equations to model the mean velocity are discussed in sections 3.6 and 3.7. In this section, mean velocity profiles from both simulations, at the same 7-psi backpressure, mesh level, and rotor position are compared.

The mean velocity profiles in the primary stator at planes x = 0 mm and z = 60 mm are shown in figures 7.5 and 7.6 respectively. The RANS and averaged LES profiles predict similar mean flow features, such as the high velocity at the stator opening, the stator jet, influence from the secondary rotor at the stator exit, and the recirculating vortex. However the regions occupied by these features are slightly different. The penetration distance of the high velocity from the primary rotor blade into the slot is larger for RANS. The axial length of the stator jet into the slot predicted by RANS is less than the ensemble averaged LES profile, but the height (distance from the wall) is larger. The penetration distance of the relatively high velocity feature (from the secondary rotor) at the primary stator exit is larger for RANS. In the z = 60 mm view, RANS predicts higher velocities in the cells closest to the wall.

Similar to the primary stator mean velocity comparison, the RANS and ensemble averaged LES profiles predict similar flow features in the secondary outer slots but the shape of these features differs. The mean velocity profiles in the secondary outer stator slot at planes x = 0 mm and z = 100 mm are shown in figures 7.7 and 7.8 respectively. The speed of the stator jet near the opening is smaller for RANS; however its penetration along the outer edge is longer for RANS. As a result, the location where the flow begins to recirculate at the inner edge is further downstream in the slot. In the z = 100 mm view, the shape of the mean vortex is more circular for the averaged LES profile. The magnitude of the velocity near this recirculating vortex is smaller for RANS.

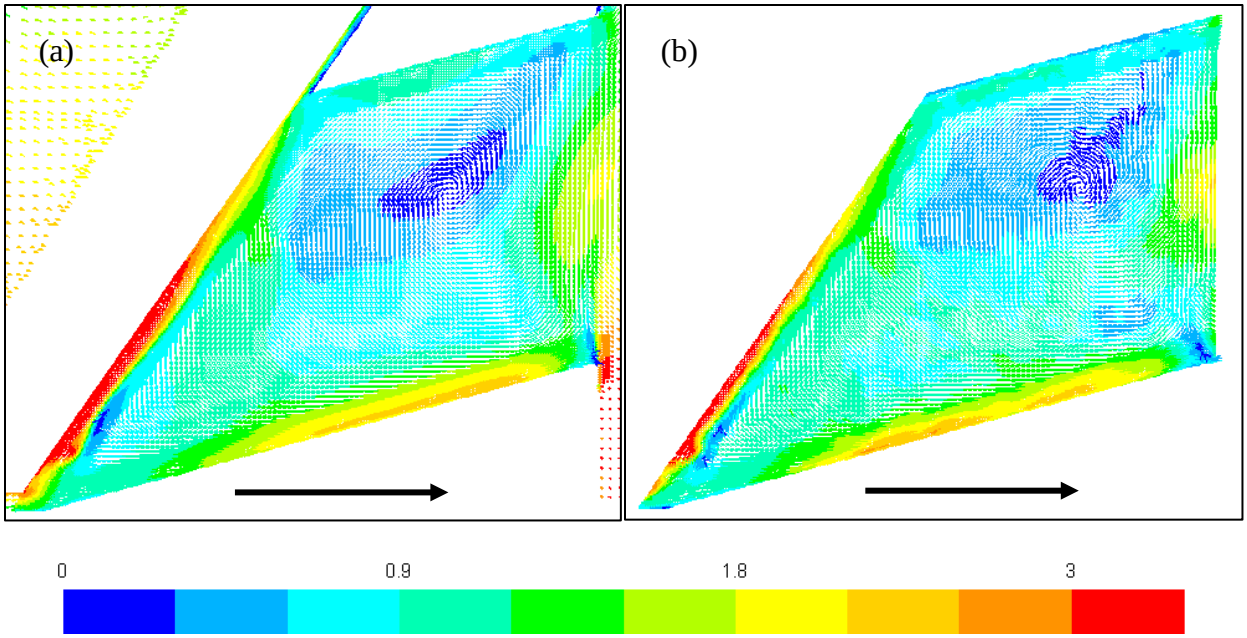

Figure 7.5 – Primary stator slot 6 mean velocity field colored by velocity magnitude in the center plane, x = 0 mm, from (a) RANS and (b) LES. Color legend scaled by (ND) = 5.8 m/s. ΔP = 7 psi, hex 20M.

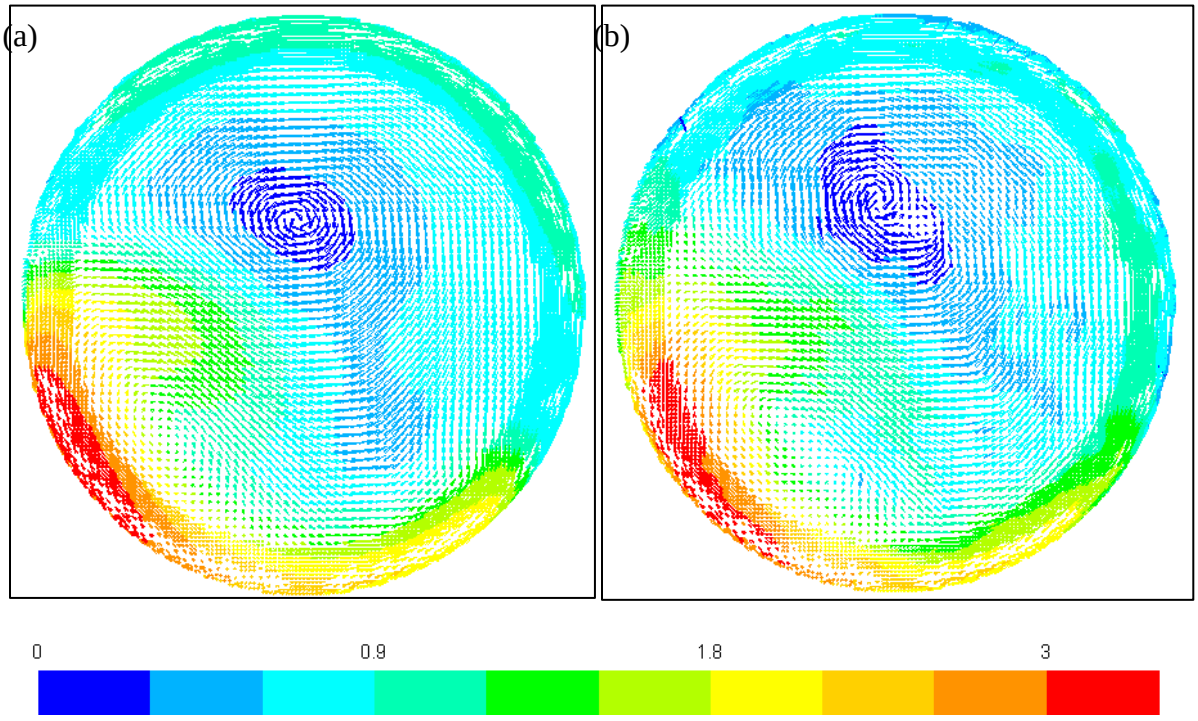

Figure 7.6 – Primary stator slot 6 mean velocity field colored by velocity magnitude in the z = 60 mm plane looking upstream from (a) RANS and (b) LES. Color legend scaled by (ND) = 5.8 m/s. ΔP = 7 psi, hex 20M.

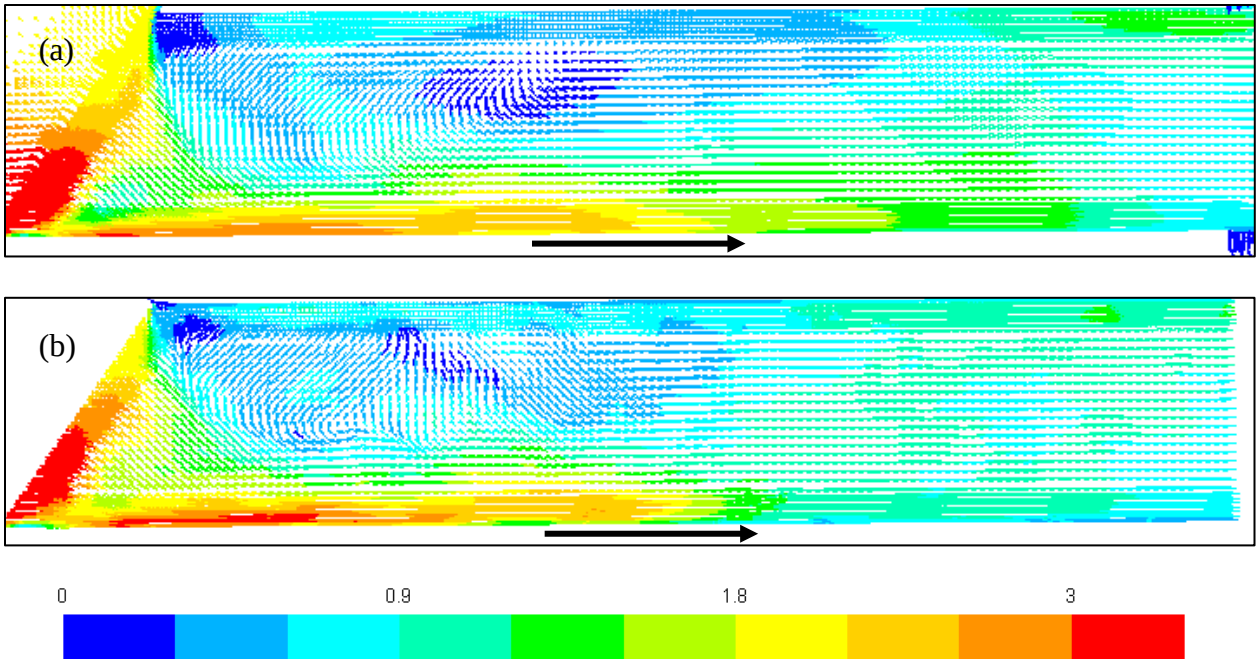

Figure 7.7 – Secondary outer slot 15 mean velocity field colored by velocity magnitude in the center plane, x = 0 mm, from (a) RANS and (b) LES. Color legend scaled by (ND) = 5.8 m/s. ΔP = 7 psi, hex 20M.

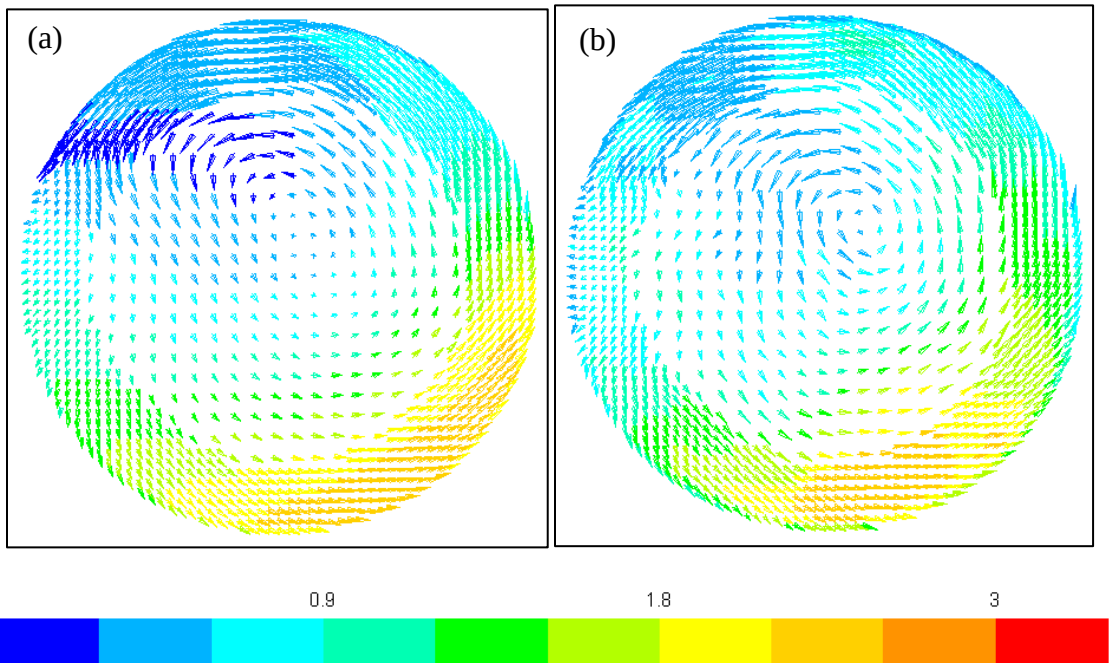

Figure 7.8 – Secondary outer slot 15 mean velocity field colored by velocity magnitude in the z = 100 mm plane looking upstream from (a) RANS and (b) LES. Color legend scaled by (ND) = 5.8 m/s. ΔP = 7 psi, hex 20M.

The mean velocity profiles from RANS and LES in the secondary middle and inner slots at views x = 0 mm and z = 100 mm are shown in figures 7.9 and 7.10, respectively. In these figures, the color legend of a given slot is scaled using the relative rotor diameter. Both simulations predict three mean recirculation vortices in the secondary middle and inner slots. However, the location of last vortex (vortex closest to the stator exit) differs. In both the secondary middle and inner slots, the RANS mean velocity profile predicts the location of the last vortex to be closer to the middle vortex. The predicted length of the stator jet is similar for both simulations; however RANS predicts a stator jet with higher speed. The speed close to the inner wall near the middle vortex is also larger for RANS. In the z = 100 mm view, the shape of the recirculating vortex in the middle slot is noticeably different between the two simulations. Higher velocity magnitude is observed in the secondary inner slot from the averaged LES profiles.

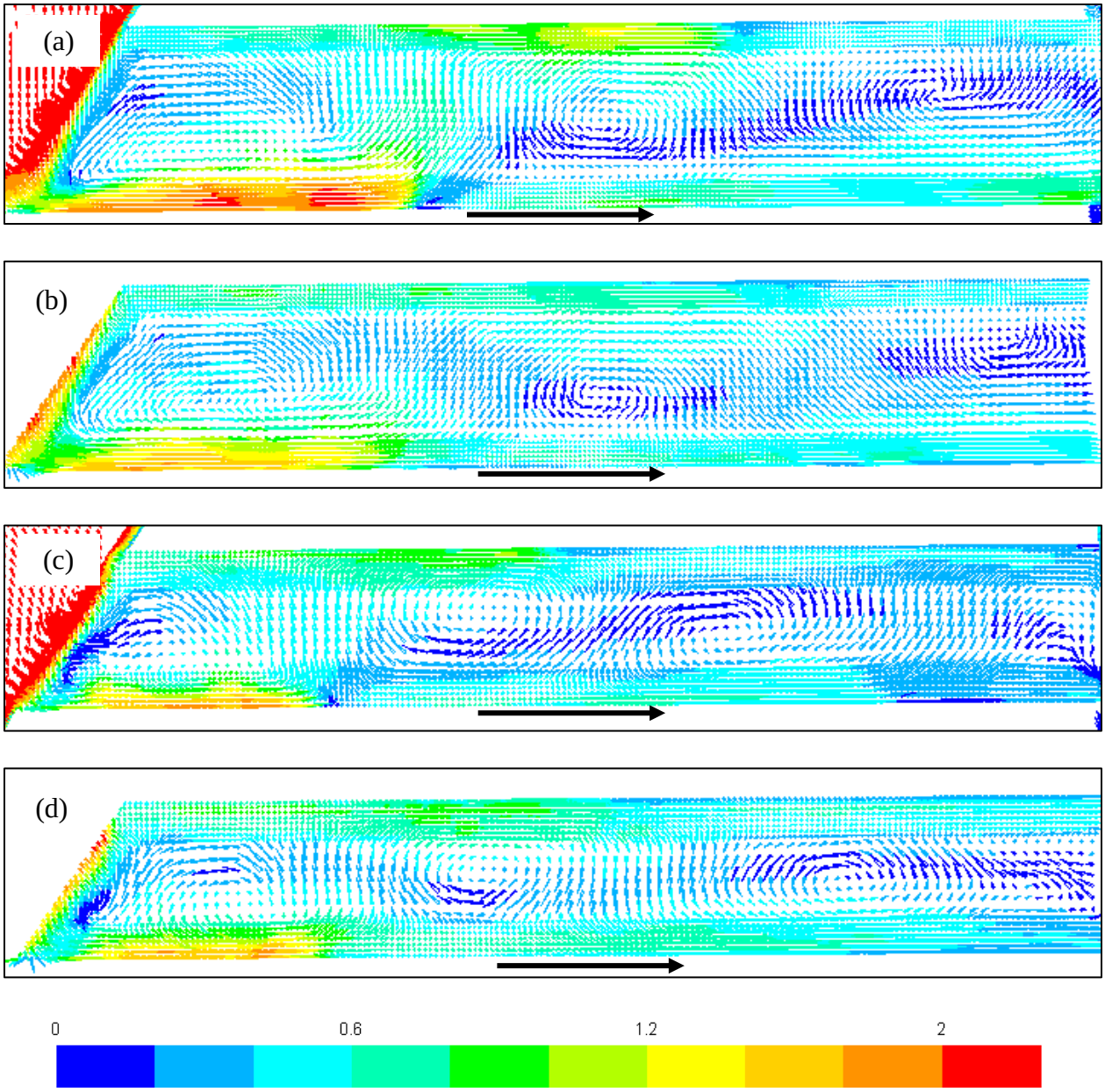

Figure 7.9 – Mean velocity fields colored by velocity magnitude in the center plane, x = 0 mm, from the (a) RANS secondary middle, (b) LES secondary middle, (c) RANS secondary inner, and (d) LES secondary inner slots of column 15. Color legend scaled by (ND) = 4.65 m/s for the secondary middle and (ND) = 3.7 m/s for the secondary inner slot. ΔP = 7 psi, hex 20M.

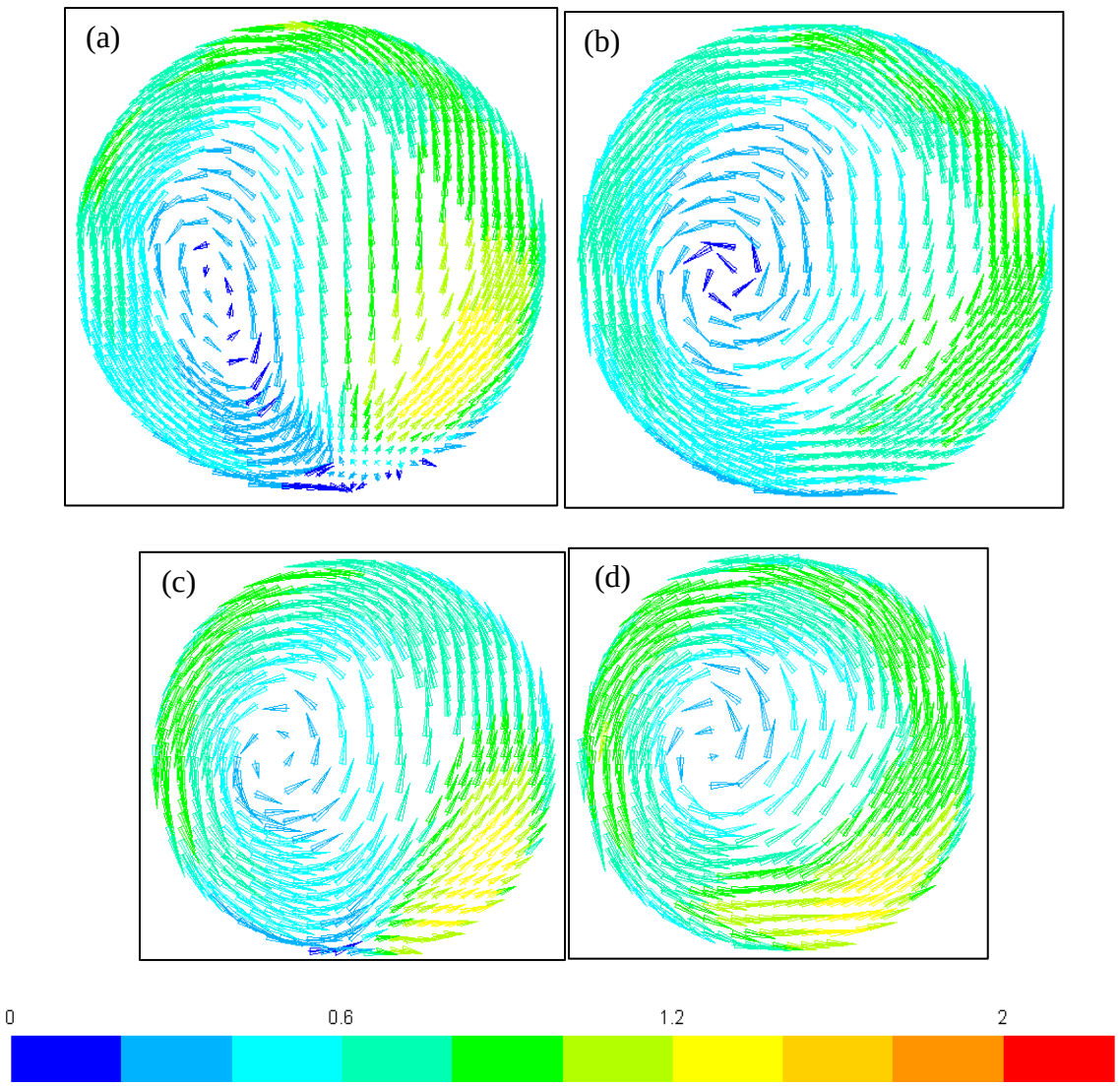

Figure 7.10 – Mean velocity fields colored by velocity magnitude in the z = 100 mm plane looking upstream from the (a) RANS secondary middle, (b) LES secondary middle, (c) RANS secondary inner, and (d) LES secondary inner slots of column 15. Color legend scaled by (ND) = 4.65 m/s for the secondary middle and (ND) = 3.7 m/s for the secondary inner slot. ΔP = 7 psi, hex 20M.

To provide a more quantitative comparison of the mean velocity field predicted by both simulations, the mean velocity magnitude from RANS is subtracted from the ensemble averaged velocity magnitude from LES on a cell basis. Statistics regarding this pointwise comparison distribution are reported in table 7.3, below. These statistics simplify the pointwise comparisons to a single value, and therefore the spatial influence is removed. Information regarding time-

averaged structures is lost. Statistics considered include the spatial average, root mean square deviation from this average, as well as the minimum, and maximum values. Since the average is influenced by outliers, the median is also reported. Since the pointwise comparison distribution is the difference between the RANS flow variable and the LES flow variable, if the pointwise comparison is positive, then the RANS flow variable at that point is larger than the LES flow variable. Conversely, if the pointwise comparison is negative, then the LES flow variable is larger than the RANS flow variable at that point. By this construction, statistics (excluding the root mean square deviation) can be negative. For example, if the mean flow variable comparison value is negative than on average LES predicts a higher value for that flow variable compared to RANS.

Table 7.3 – Time-averaged velocity magnitude comparison in the stator slots.

Location		$\|\|\bar{U}_i\|\|^{(RANS)} - \|\|\bar{U}_i\|\|^{(LES)}$ (m/s)				
Slot	Plane	Mean	RMSD	Minimum	Median	Maximum
PS6	x = 0 mm	0.035	1.57	-7.27	-0.012	7.68
	z = 60 mm	0.061	1.08	-3.25	0.191	5.93
SOS15	x = 0 mm	0.093	1.25	-2.52	-0.025	4.69
	z = 100 mm	0.230	1.52	-2.30	-0.050	6.52
SMS15	x = 0 mm	0.456	0.88	-2.13	0.273	4.44
	z = 100 mm	0.319	0.87	-2.11	0.165	2.81
SIS15	x = 0 mm	-0.013	0.78	-3.32	-0.200	2.79
	z = 100 mm	-0.327	0.75	-3.13	-0.287	1.33

In all planes excluding the secondary inner slot, on average RANS predicts larger velocity magnitudes than LES. In the secondary stator, as the diameter of the slot decreases, the root mean square deviation decreases. This implies that the pointwise difference between these two models decreases with lower time-averaged velocity magnitude. The cell with the largest difference in velocity magnitude between RANS and LES is located in the primary slot, across the plane x = 0 mm. This large difference is about one third of the tip speed and is located in the stator jet region.

7.3 Turbulent Kinetic Energy and Energy Dissipation Rate

In this section, contours of turbulent kinetic energy and turbulent energy dissipation rate predicted from RANS and LES in the stator slots are compared. Similar to the comparisons made in section 7.2, results are shown from the 7-psi backpressure, hex 20M computational mesh, and at the rotor position indicated on figure 2.7. In the RANS realizable k-ε model, a modeled form of the turbulent kinetic energy conservation equation was used. To solve for the turbulent energy dissipation rate, the RANS realizable k-ε model uses an empirical expression based on a simplified form of the conservation equation which assumed homogeneous turbulence. For LES, the predicted turbulent kinetic energy is dependent on the energy of the resolved velocity fluctuations (equation 3.13-5). In addition, the predicted turbulent energy dissipation rate uses the SGS model to add the influence from unfiltered scales (equation 3.13-10).

Turbulent kinetic energy contours in the primary stator slot 6 in the x = 0 mm and z = 60 mm view are shown in figures 7.11 and 7.12 respectively. LES predicts higher turbulent kinetic energy at the stator opening where the primary rotor is present and in the recirculation region at the inner edge of the stator slot. A larger spread of turbulent kinetic energy is predicted by LES at the stator exit (close to the secondary rotor) and along the outer edge where the stator jet is present. RANS predicts a higher turbulent kinetic energy at the outer most tip of the primary stator. In the z = 100 mm view, LES predicts a larger spread of turbulent kinetic energy.

Similar to the primary stator slot, LES predicts a higher distribution of turbulent kinetic energy in the secondary outer slot. Turbulent kinetic energy contours in this slot are shown in the x = 0 mm and z = 100 mm view in figures 7.13 and 7.14, respectively. Both RANS and LES predict high turbulent kinetic energy between the stator jet and recirculation region, however LES predicts high turbulent kinetic energy at the stator opening as well.

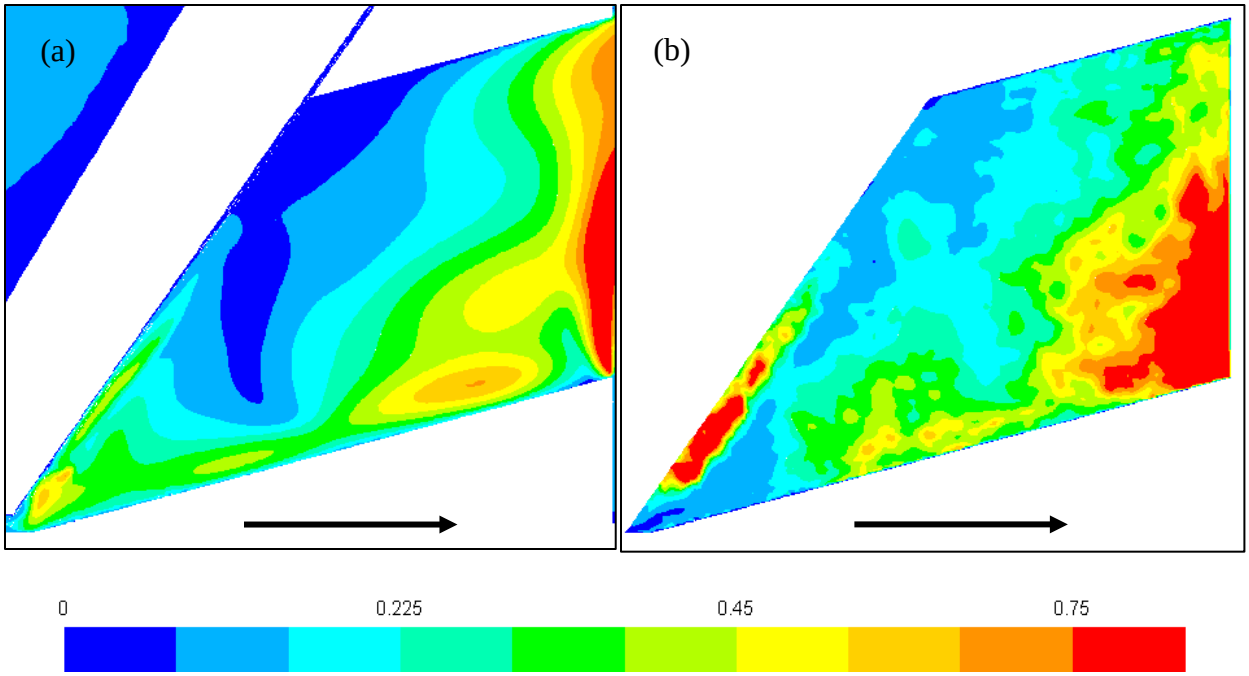

Figure 7.11 – Primary slot 6 turbulent kinetic energy in the x = 0 mm plane from (a) RANS and (b) LES. Color legend scaled by $(ND)^2 = 33.64\ m^2/s^2$. $\Delta P = 7$ psi, hex 20M.

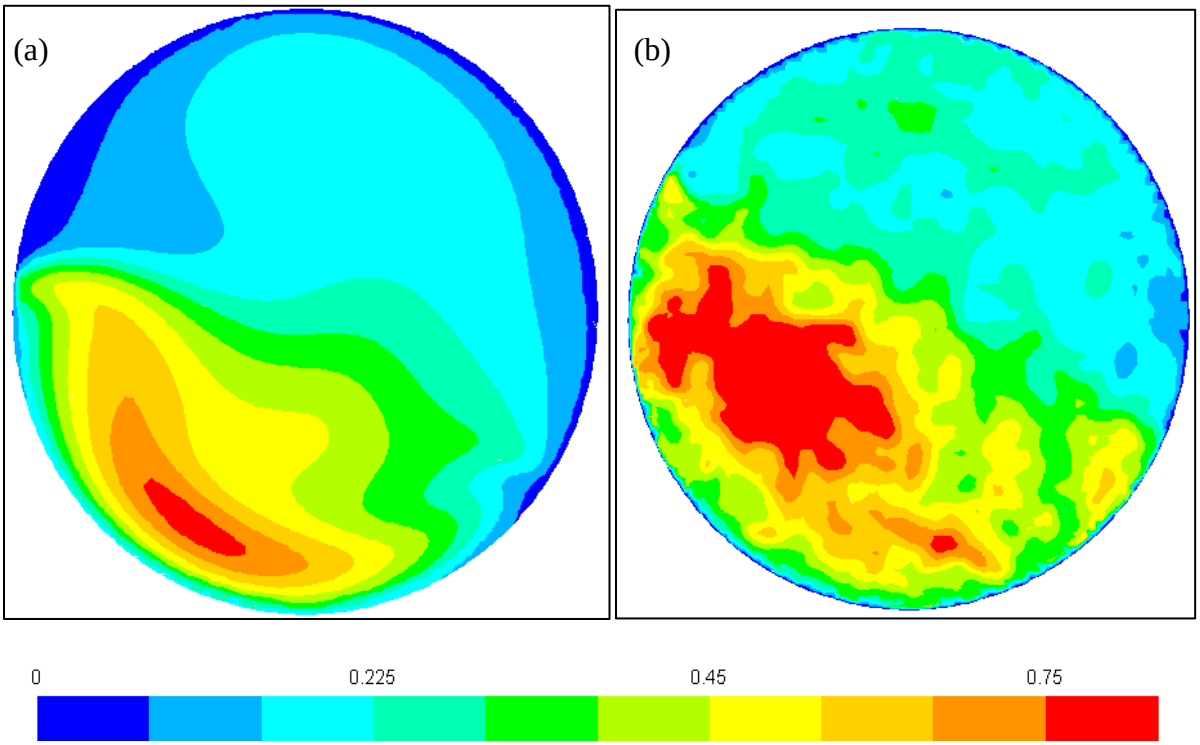

Figure 7.12 – Primary slot 6 turbulent kinetic energy in the z = 60 mm plane looking upstream from (a) RANS and (b) LES. Color legend scaled by $(ND)^2 = 33.64\ m^2/s^2$. $\Delta P = 7$ psi, hex 20M.

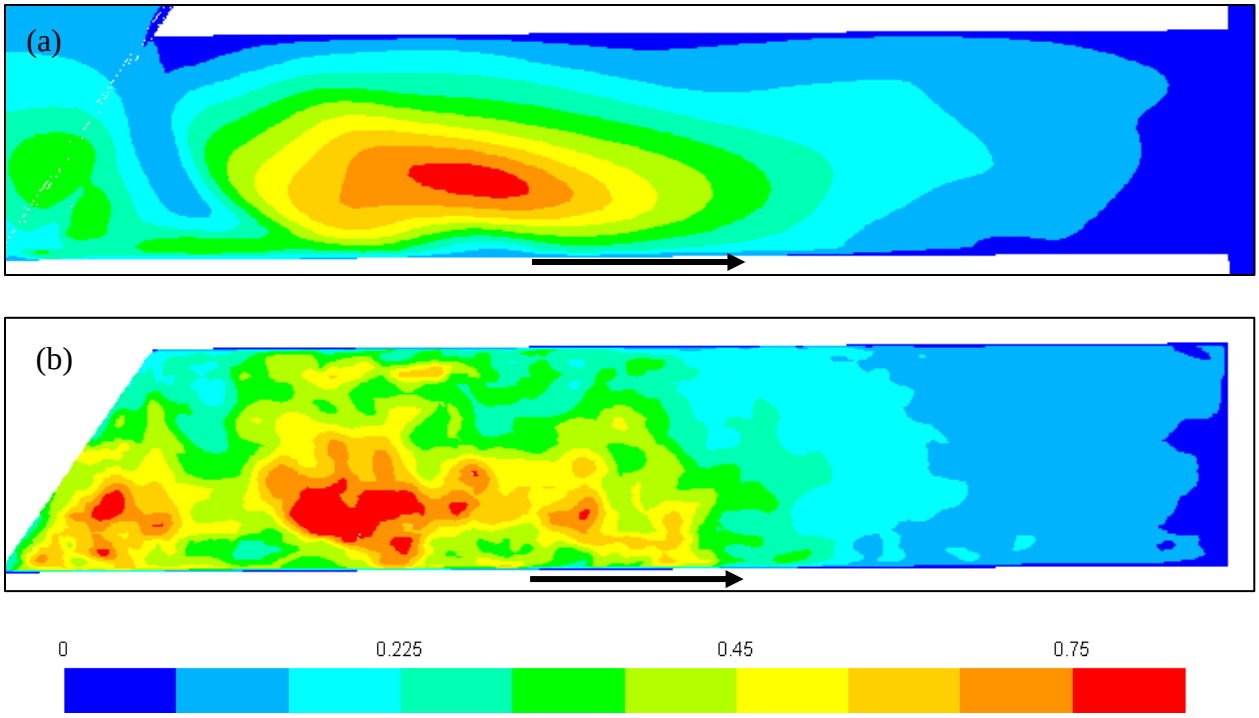

Figure 7.13 – Secondary outer slot 15 turbulent kinetic energy in the x = 0 mm plane from (a) RANS and (b) LES. Color legend scaled by $(ND)^2 = 33.64\ m^2/s^2$. $\Delta P = 7$ psi, hex 20M.

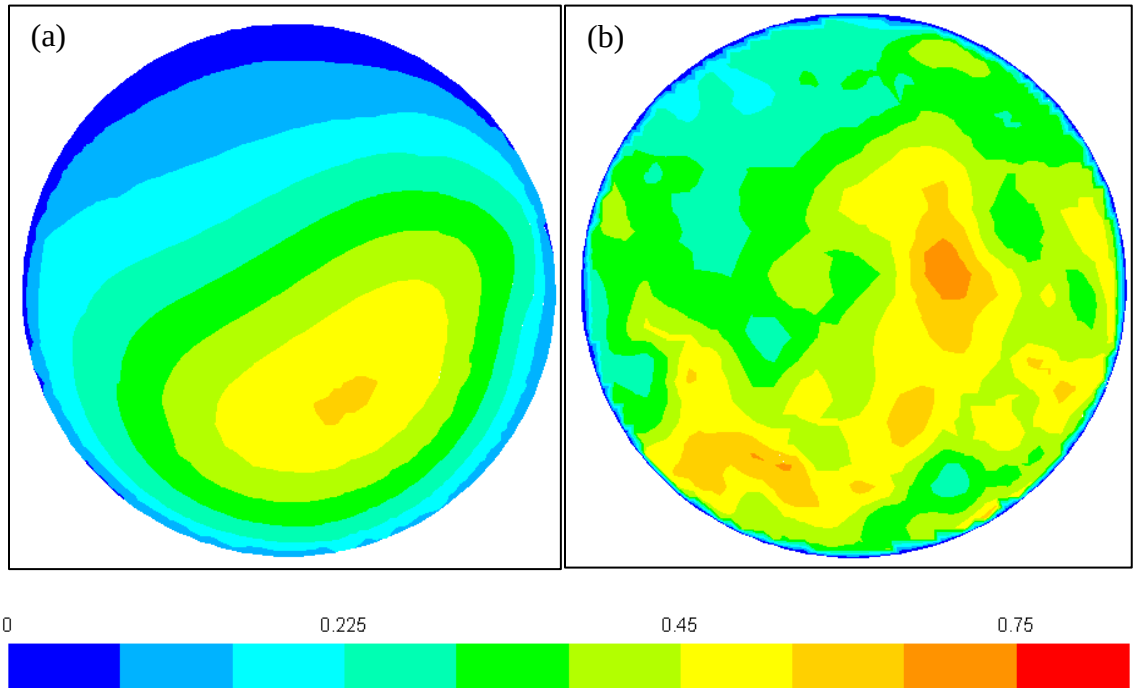

Figure 7.14 – Secondary outer slot 15 turbulent kinetic energy in the z = 100 mm plane looking upstream from (a) RANS and (b) LES. Color legend scaled by $(ND)^2 = 33.64\ m^2/s^2$. $\Delta P = 7$ psi, hex 20M.

A pointwise comparison between RANS and LES can be made for the turbulent kinetic energy. Spatial statistics, similar to those produced for the time-averaged velocity magnitude in table 7.3, can be computed for the turbulent kinetic energy comparison, as shown in table 7.4. As the above turbulent kinetic energy contours show, LES predicts higher turbulent kinetic energy than RANS for all stator slots considered in table 7.4. Similar to the time-averaged velocity magnitude comparison, as the diameter of the stator slot decreases, the variance of the pointwise difference distribution decreases. The cell with the largest difference in turbulent kinetic energy occurs in the x = 0 mm plane of the primary slot. In this particular cell, LES predicts a turbulent kinetic energy value 1.75 times larger than $(ND)^2 = 33.64\ (m/s)^2$.

Table 7.4 – Turbulent kinetic energy comparison in the stator slots.

Location		$k^{(RANS)} - k^{(LES)}$ $(m/s)^2$				
Slot	Plane	Mean	RMSD	Minimum	Median	Maximum
PS6	x = 0 mm	-2.84	6.61	-58.9	-2.12	14.0
	z = 60 mm	-3.45	4.35	-20.4	-2.81	9.39
SOS15	x = 0 mm	-2.98	3.57	-17.6	-1.89	10.2
	z = 100 mm	-5.15	3.33	-15.1	-5.40	5.10
SMS15	x = 0 mm	-1.00	1.42	-8.9	0.48	1.56
	z = 100 mm	-1.06	1.08	-4.3	-0.79	1.15
SIS15	x = 0 mm	-0.63	1.04	-7.9	-0.29	0.58
	z = 100 mm	-1.10	1.05	-4.2	-0.83	0.24

Turbulent energy dissipation rate contours in the primary stator slot at view x = 0 mm and z = 60 mm are shown in figures 7.15 and 7.16, respectively. Analogous contours for the secondary outer slot at views x = 0 mm and z = 100 mm are shown in figures 7.17 and 7.18, respectively. In all stator slots, the RANS predicts a higher turbulent energy dissipation throughout majority of the slot. For the primary slot, high turbulent energy dissipation rate is predicted by both models along the outer edge, at the stator opening, and at the inner edge of the slot near the

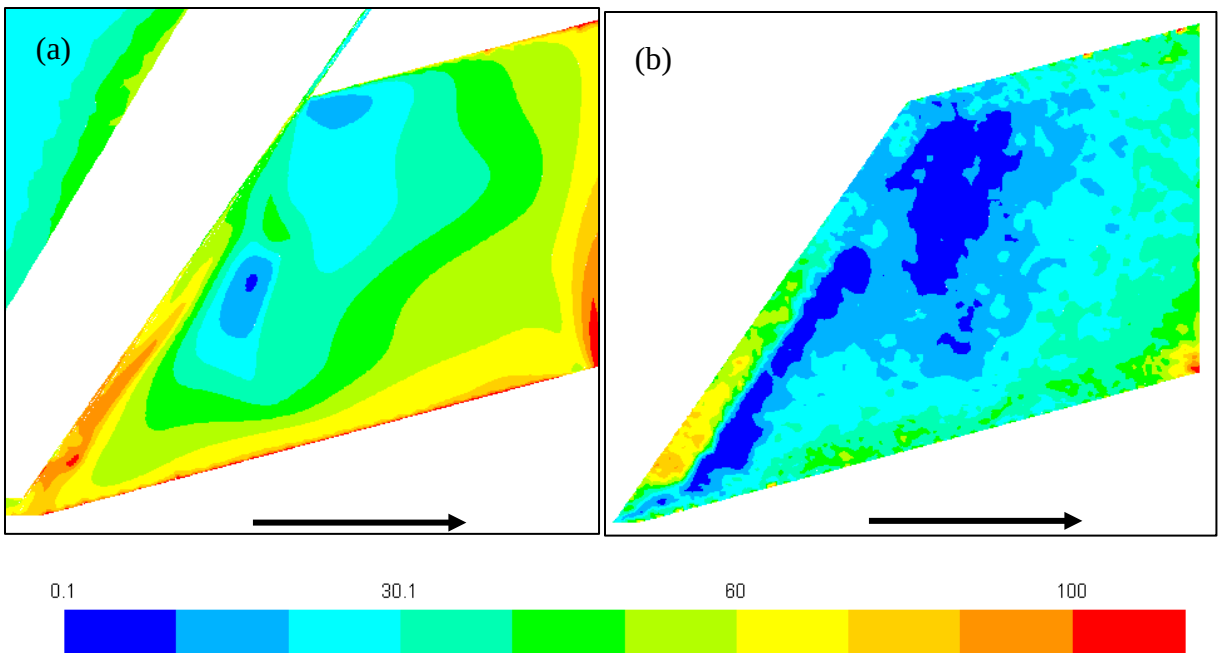

Figure 7.15 – Primary slot 6 turbulent energy dissipation rate in the x = 0 mm plane from (a) RANS and (b) LES. Color legend is logarithmic and scaled by N^3D^2 = 2018.4 m^2/s^3. ΔP = 7 psi, hex 20M.

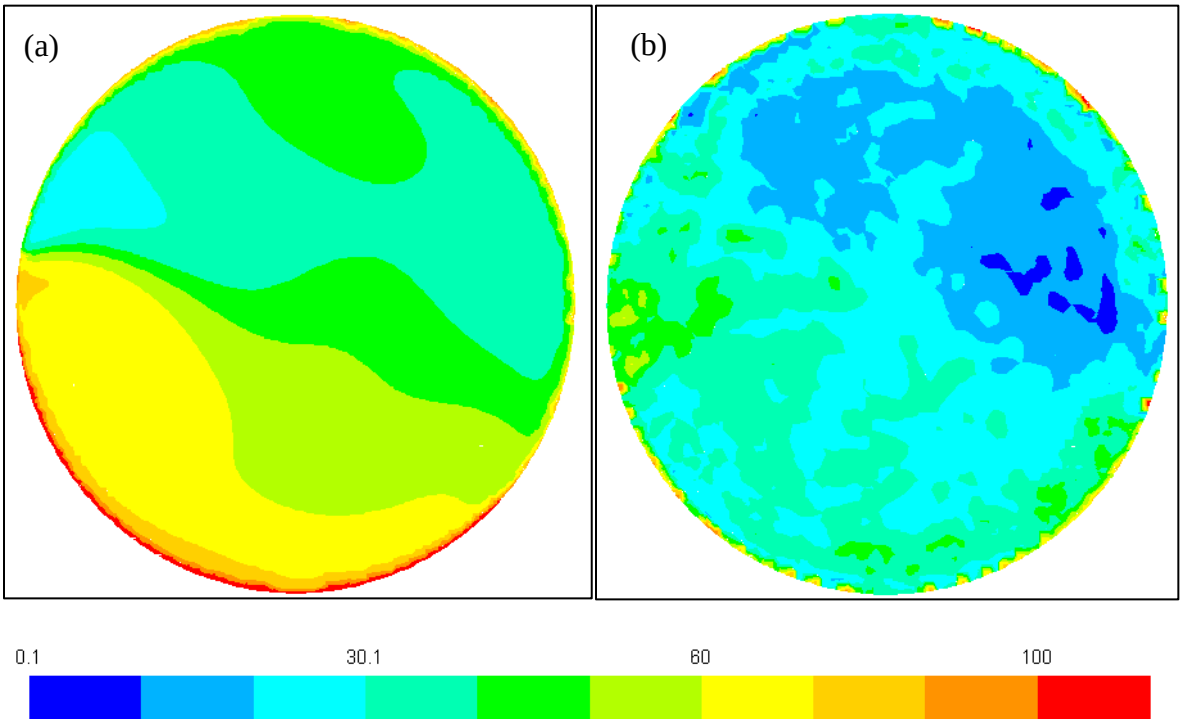

Figure 7.16 – Primary slot 6 turbulent energy dissipation rate in the z = 60 mm plane looking upstream from (a) RANS and (b) LES. Color legend is logarithmic and scaled by N^3D^2 = 2018.4 m^2/s^3. ΔP = 7 psi, hex 20M.

exit. Relatively low turbulent energy dissipation rates are predicted by both simulations in the recirculation region of the primary slot. The largest difference between the predicted turbulent energy dissipation rate from these simulations occurs between the regions of maximum and minimum turbulent energy dissipation rate. RANS predicts a smaller spreading gradient than the LES.

A smaller spreading gradient of the turbulent energy dissipation rate is also observed in the secondary outer slots from RANS compared to LES. Regardless of the discrepancy in the spread of the turbulent energy dissipation rate, both RANS and LES predict high turbulent energy dissipation in the stator jet along the outer edge of the slot. Relatively high turbulent energy dissipation rates are also observed along the inner edge of the slot for both simulations.

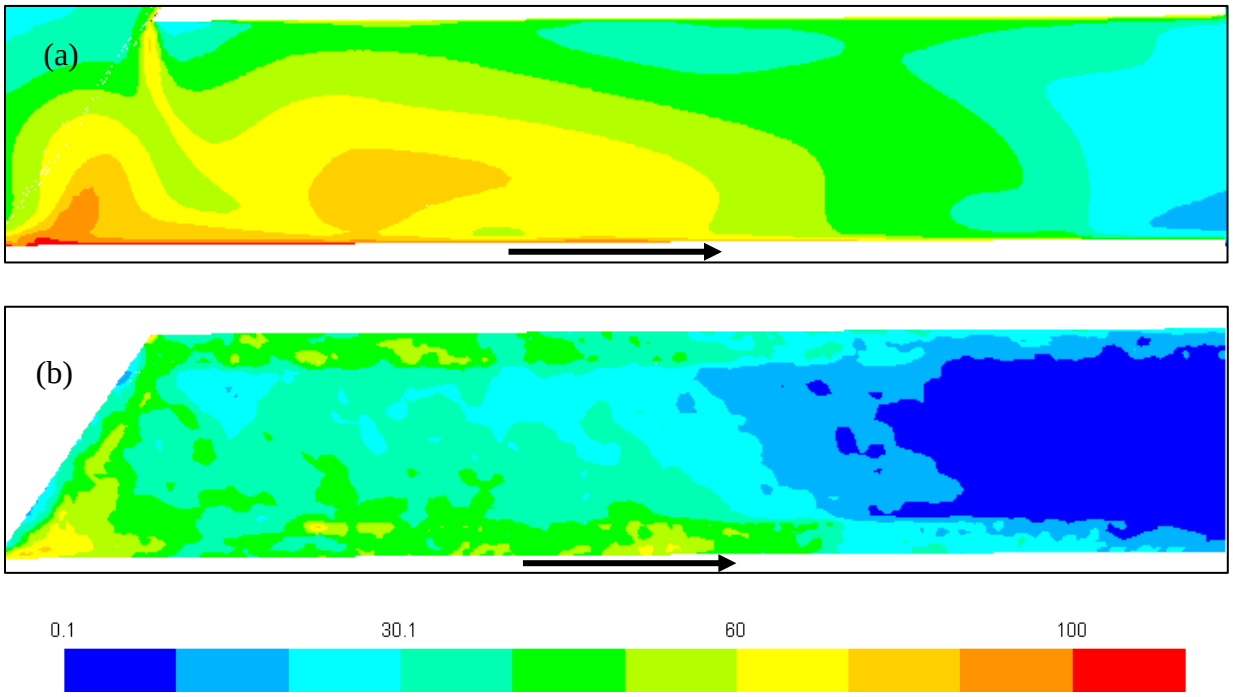

Figure 7.17 – Secondary outer slot 15 turbulent energy dissipation rate in the x = 0 mm plane from (a) RANS and (b) LES. Color legend is logarithmic and scaled by N^3D^2 = 2018.4 m^2/s^3. ΔP = 7 psi, hex 20M.

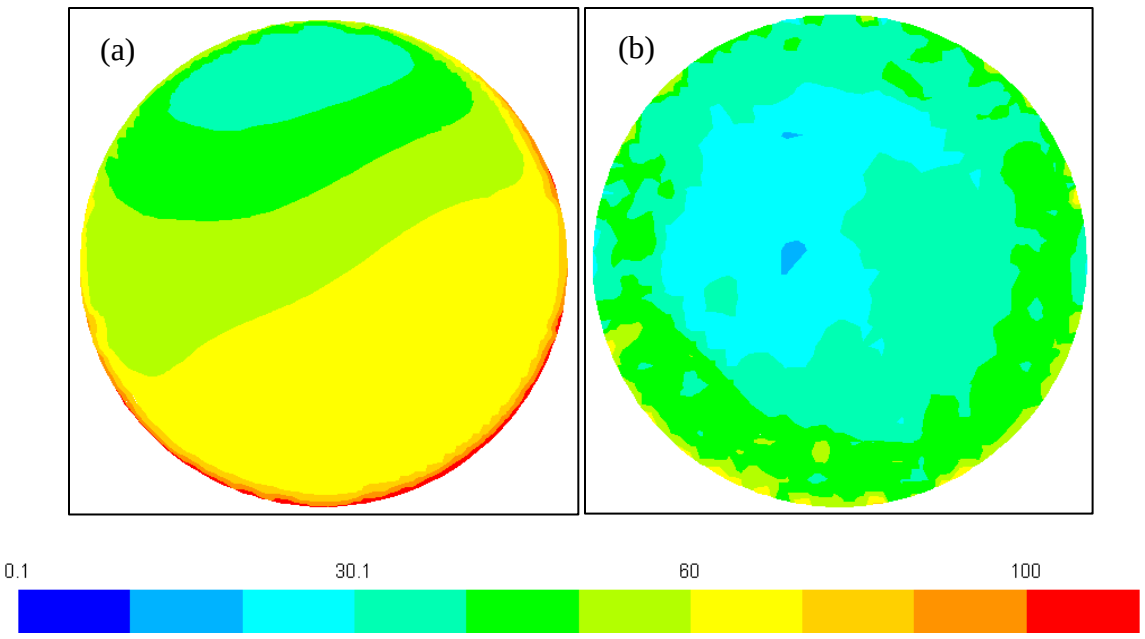

Figure 7.18 – Secondary outer slot 15 turbulent energy dissipation rate in the z = 100 mm plane looking upstream from (a) RANS and (b) LES. Color legend is logarithmic and scaled by N^3D^2 = 2018.4 m^2/s^3. ΔP = 7 psi, hex 20M.

The turbulent energy dissipation rate contours predicted from LES show a relatively steep change in a region near the wall. This phenomena occurs due to the mesh adaption layer imposed in this region. This change in mesh refinement can be observed in figure 2.6. As discussed in section 6.4, the SGS eddy viscosity is dependent on filter width which is determined by the mesh size. The SGS eddy viscosity was shown to decrease in this region of high mesh refinement in figure 6.12 as a result of equation 3.11-5. Although the SGS eddy viscosity decreased, higher turbulent energy dissipation rates are observed in this region. According to equation 3.13-10, this is because the resolved strain rate tensor product is higher. This implies that the computational mesh needs to be further refined to capture smaller scales necessary for the turbulent energy dissipation rate, or that the SGS eddy viscosity is not modeling the captured scales properly.

Spatially averaged statistics for the turbulent energy dissipation rate pointwise comparison are provided in table 7.5, below. As the turbulent energy dissipation rate contours demonstrate,

RANS predicts a higher turbulent energy dissipation rate on average for all stator slots considered in table 7.5. However the magnitude of the minimum value is larger than the maximum value for all x = 0 mm planes. This implies that at least one cell has higher turbulent energy dissipation rate for LES compared to RANS. Although the peak turbulent energy dissipation rate is higher in the x = 0 mm planes for LES, RANS predicts higher turbulent energy dissipation rate away from this peak value.

Table 7.5 – Turbulent energy dissipation rate comparison in the stator slots.

Location		$\epsilon^{(RANS)} - \epsilon^{(LES)}$ (10^3 m^2/s^3)				
Slot	Plane	Mean	RMSD	Minimum	Median	Maximum
PS6	x = 0 mm	11.5	23.2	-2020	6.63	235
	z = 60 mm	8.62	21.3	-658	3.77	275
SOS15	x = 0 mm	6.93	20.8	-1000	3.24	116
	z = 100 mm	10.5	12.0	-10.9	9.73	122
SMS15	x = 0 mm	1.05	6.49	-221	0.39	28
	z = 100 mm	1.26	1.20	-3.72	1.01	9.66
SIS15	x = 0 mm	0.47	3.08	-69.4	0.06	25.6
	z = 100 mm	0.34	0.83	-7.52	0.35	6.89

7.4 Eddy Viscosity and the Boussinesq Approximation

As discussed in section 3.6 and 3.7, the RANS realizable k-ε closure model is an eddy viscosity model which assumes that the anisotropy tensor is proportional to the mean rate of strain (equation 3.6- 4). The eddy viscosity in this Boussinesq approximation is modeled using the turbulent kinetic energy and energy dissipation rate in the form of equation 3.7-1. The C_μ term in this equation for the realizable k-ε model is a function of the mean strain and rotation rates. This modeled eddy viscosity from the RANS model can be compared to a computed eddy viscosity using LES. Both the resolved anisotropy and rate of strain tensor can be computed from LES. The eddy viscosity, which is the unknown scalar coefficient equating these second order tensors by the Boussinesq approximation, is the coefficient that minimizes the least squares error. When

comparing the eddy viscosities predicted by both simulations, the Boussinesq approximation is assumed to hold true.

Primary stator slot 6 contours of the modeled eddy viscosity from RANS and the eddy viscosity which minimizes the least squares error from LES are shown in figures 7.19 and 7.20. Both simulations predict a high eddy viscosity near the exit of the slot. However, RANS predicts higher eddy viscosity closer to the inner edge. The reason the RANS eddy viscosity is high near the inner edge and low near the outer edge is because it is inversely proportional to the turbulent energy dissipation rate. The eddy viscosity from LES is highest at the outer edge near the exit, where the turbulent energy dissipation rate was also shown to be high. The RANS model also predicts high eddy viscosity at the outer most tip of the primary stator opening which is not observed in LES. The reason for this high RANS eddy viscosity is most likely because the turbulent kinetic energy was predicted to be high in that region.

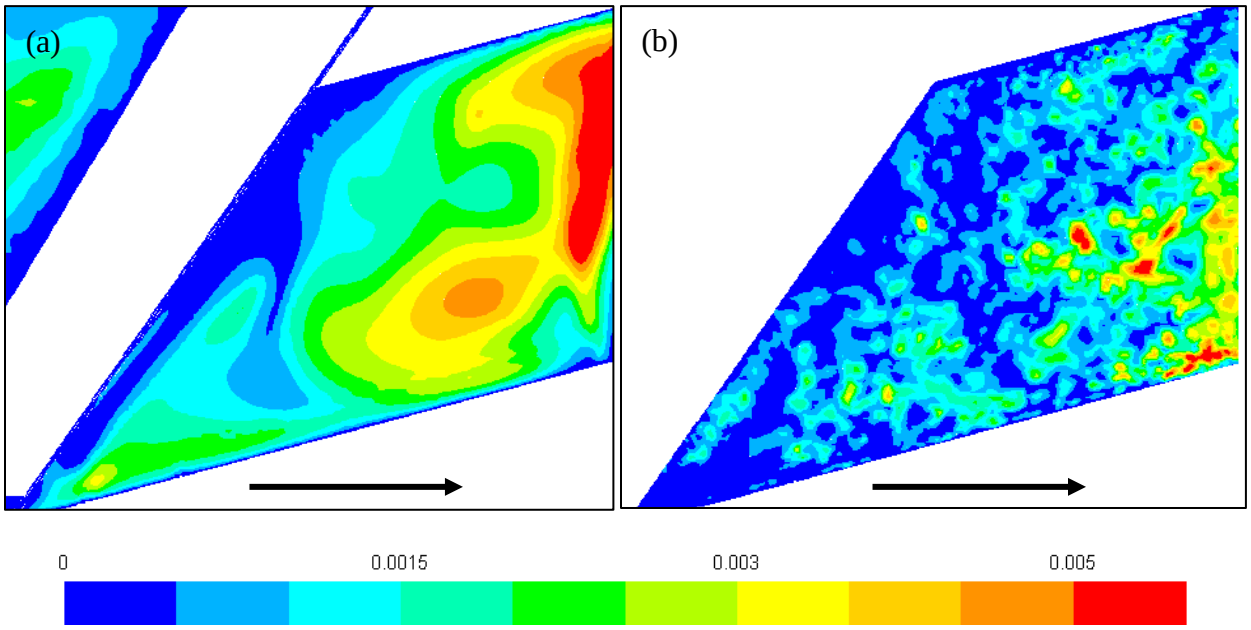

Figure 7.19 – Primary slot 6 eddy viscosity in the x = 0 mm plane from (a) RANS and (b) LES. Color legend is scaled by ND^2 = 0.56 m^2/s. ΔP = 7 psi, hex 20M.

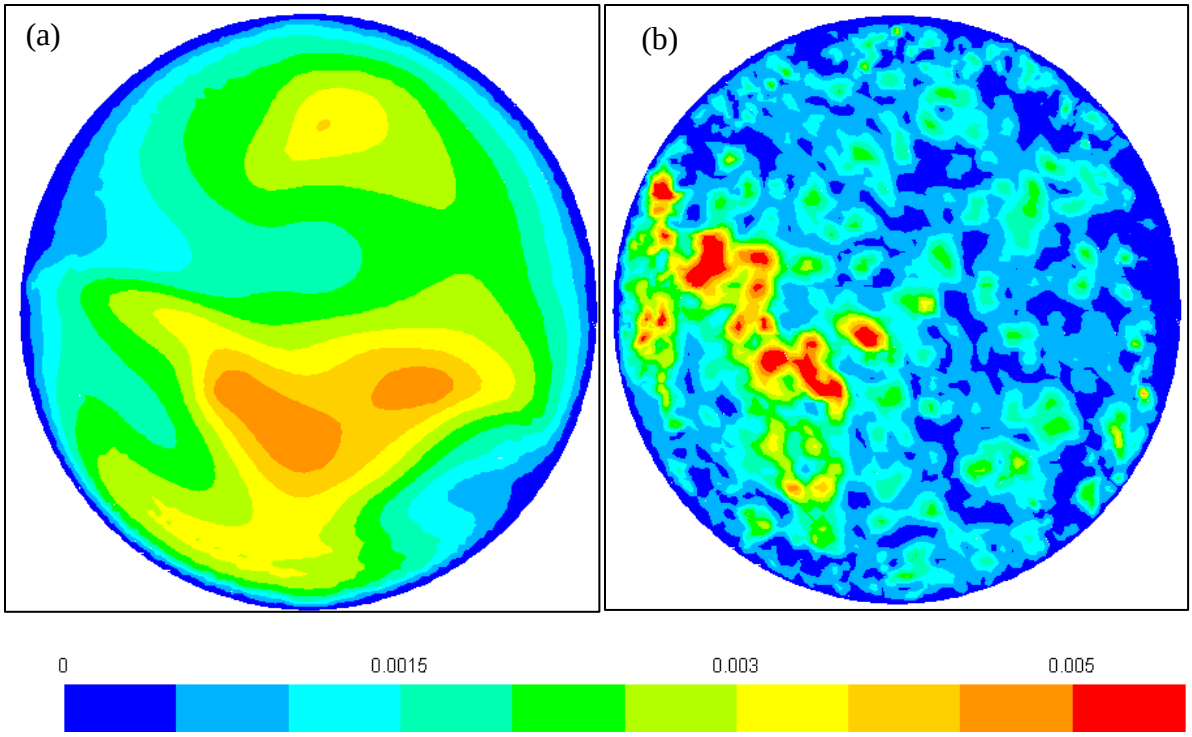

Figure 7.20 – Primary slot 6 eddy viscosity in the z = 60 mm plane looking upstream from (a) RANS and (b) LES. Color legend scaled by ND^2 = 0.56 m^2/s. ΔP = 7 psi, hex 20M.

Similar eddy viscosity contours are shown for the secondary outer slots in figures 7.21 and 7.22. The RANS model predicts lower eddy viscosity compared to the primary slot, although the eddy viscosity from LES is as high as in the secondary outer slot as it was in the primary slot. Both simulations predict the eddy viscosity to be highest between the stator jet and recirculation region. The RANS model predicts a low eddy viscosity near the stator opening, yet the eddy viscosity from LES is relatively high in that region. The RANS model could be predicting this phenomena because the turbulent kinetic energy is high and the turbulent energy dissipation rate is low in this region.

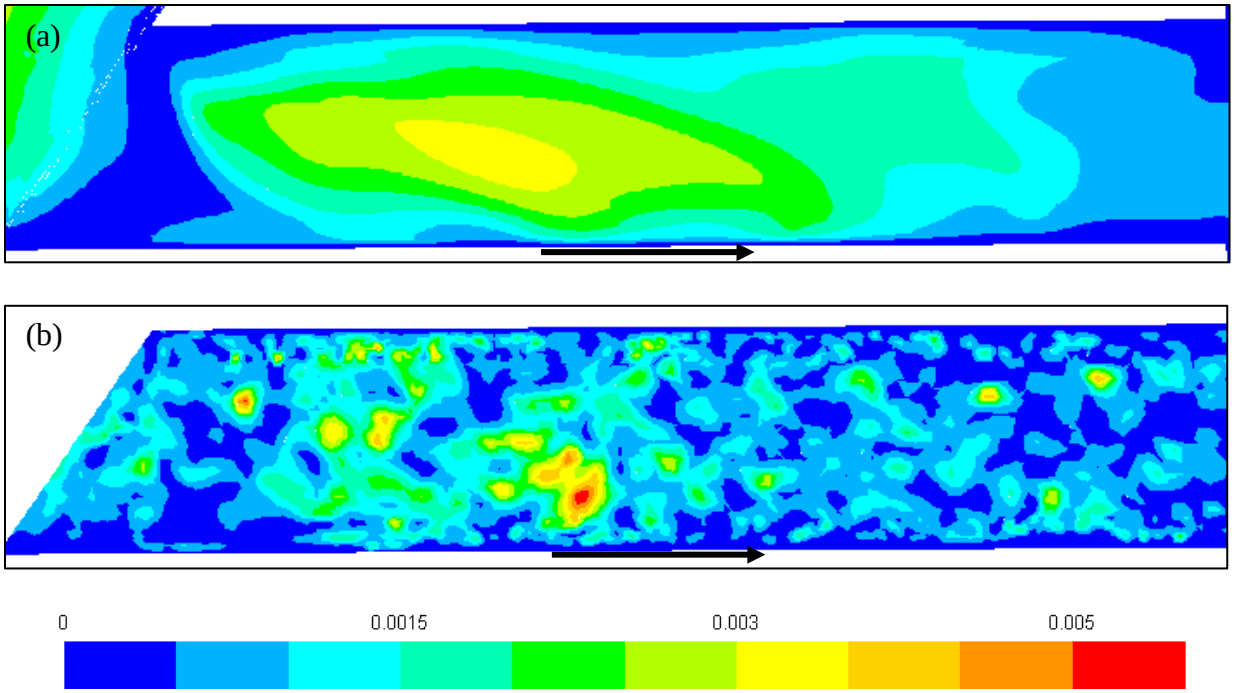

Figure 7.21 – Secondary outer slot 15 eddy viscosity in the x = 0 mm plane from (a) RANS and (b) LES. Color legend scaled by ND^2 = 0.56 m^2/s. ΔP = 7 psi, hex 20M.

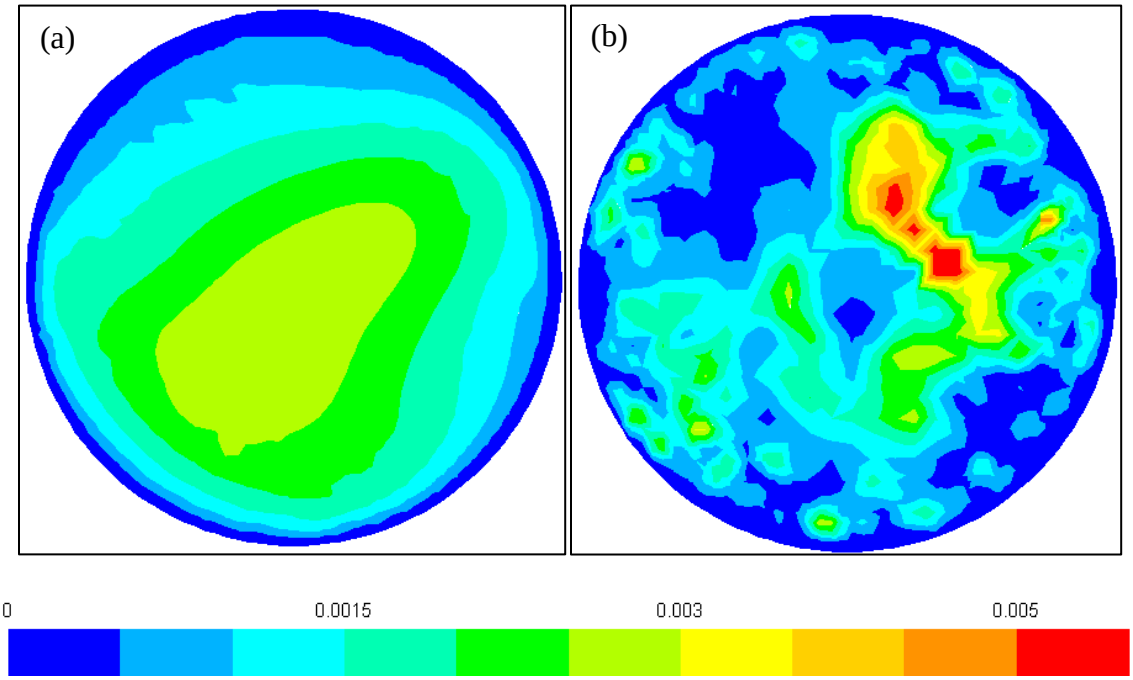

Figure 7.22 – Secondary outer slot 15 eddy viscosity in the z = 100 mm plane looking upstream from (a) RANS and (b) LES. Color legend scaled by ND^2 = 0.56 m^2/s. ΔP = 7 psi, hex 20M.

To further compare the turbulent eddy viscosities predicted by RANS and LES, spatial statistics from the pointwise difference distribution are shown in table 7.6. Although LES predicts a higher maximum eddy viscosity as shown in the above eddy viscosity contours, RANS predicts a higher eddy viscosity throughout the primary and secondary outer slots, on average. As was shown in pointwise comparisons for other flow variables, as the diameter of the slot decreases, the variance of the eddy viscosity pointwise difference distribution decreases.

Table 7.6 – Eddy viscosity comparison in the stator slots.

Location		$\nu_t^{(RANS)} - \nu_t^{(LES)}$ (10^{-3} m^2/s)				
Slot	Plane	Mean	RMSD	Minimum	Median	Maximum
PS6	x = 0 mm	0.39	0.75	-4.95	0.23	4.18
	z = 60 mm	0.44	0.79	-5.00	0.49	2.39
SOS15	x = 0 mm	0.14	0.45	-3.81	0.07	1.81
	z = 100 mm	0.21	0.62	-8.56	0.21	1.52
SMS15	x = 0 mm	-0.02	0.18	-1.58	0.0001	0.74
	z = 100 mm	-0.05	0.24	-1.6	-0.0004	0.34
SIS15	x = 0 mm	0.01	0.17	-0.96	0.00003	0.89
	z = 100 mm	-0.06	0.14	-0.78	-0.01	0.13

7.5 Production and Transport of Turbulent Kinetic Energy

The rate of production of turbulent kinetic energy, given by equation 3.7-6, is the source term in the turbulent kinetic energy budget. In the RANS realizable k-ε model, this production term was approximated by substituting the Boussinesq approximation into the anisotropy tensor. Modeling the production term in this manner, it takes the form of a mean energy dissipation rate with the eddy viscosity replacing the kinematic viscosity. In this section, the modeled production from RANS (equation 3.7-11) is compared to the production computed from the definition (equation 3.7-9) using filtered quantities from LES.

The rate of turbulent kinetic energy production predicted from RANS and LES in the primary stator slot is shown in figures 7.23 and 7.24. Since the turbulent energy dissipation rate

was the sink term in the turbulent conservation equation, the source term, the rate of turbulent kinetic energy production will be scaled in a similar manner. The use of a logarithmic color scale precludes negative values which are observed in some regions near the stator walls and in the recirculation region for LES. RANS, which assumes the Boussinesq approximation, cannot predict negative production. The negative production rate predicted by LES represents energy transferred from the small to the large scales.

Both simulations predict high turbulent kinetic energy production rates at the stator entrance and exit where the primary and secondary rotors act respectively. However, LES predicts that a larger area is occupied by these high production rates. In the stator jet at the outer edge wall, the simulations predict a similar magnitude of production rate, but RANS predicts a larger spread. In the recirculation region, both simulations predict low production rates.

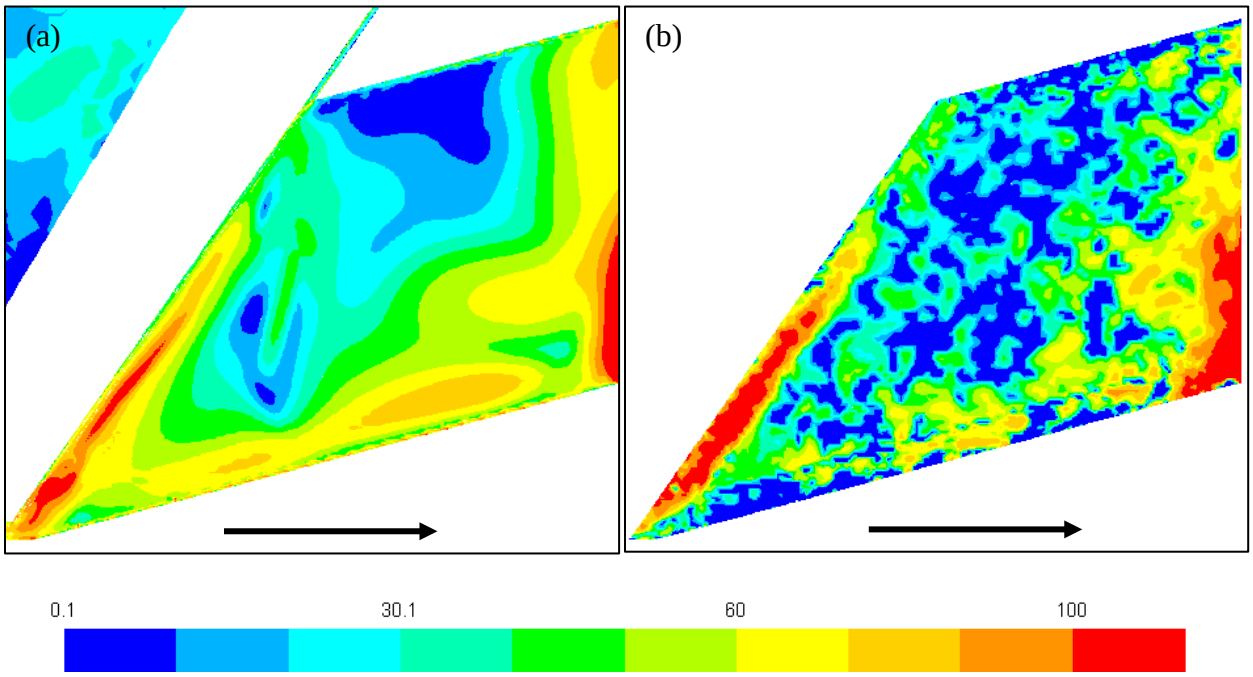

Figure 7.23 – Primary slot 6 turbulent kinetic energy production rate in the x = 0 mm plane from (a) RANS and (b) LES. Color legend is logarithmic and scaled by N^3D^2 = 2018.4 m^2/s^3. ΔP = 7 psi, hex 20M.

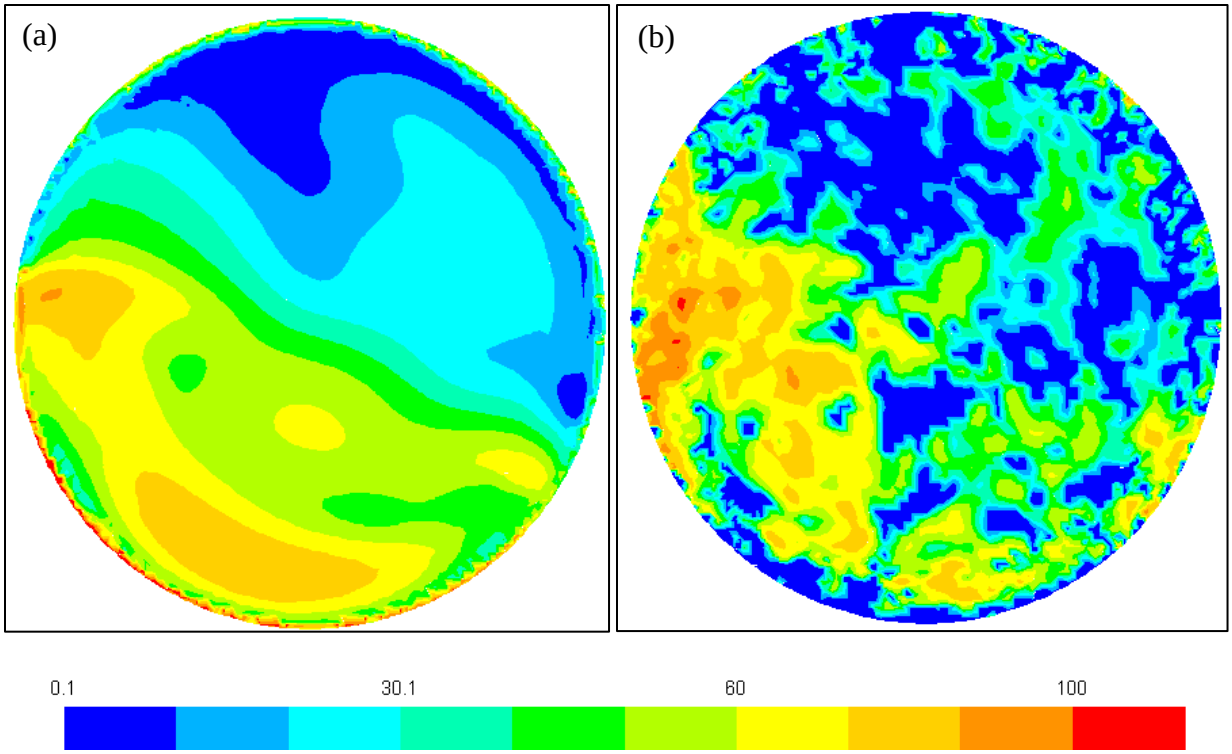

Figure 7.24 – Primary slot 6 turbulent kinetic energy production rate in the z = 60 mm plane looking upstream from (a) RANS and (b) LES. Color legend is logarithmic and scaled by N^3D^2 = 2018.4 m^2/s^3. ΔP = 7 psi, hex 20M.

Similar contours of the rate of turbulent kinetic energy production are shown for the secondary outer slot in figures 7.25 and 7.26. Again, RANS predicts higher production rates at the outer edge of the slot compared to those predicted by LES. Turbulent kinetic energy production rates are highest in the stator jet region. Both simulations predict this and the area occupied by these high production rates in these simulations is similar. Near the exit of the slot, RANS predicts a higher rate of turbulent kinetic energy production than LES. RANS predicts a relatively high eddy viscosity in this region. Both simulations show low production in the recirculation region, but RANS predicts slightly higher production in this region.

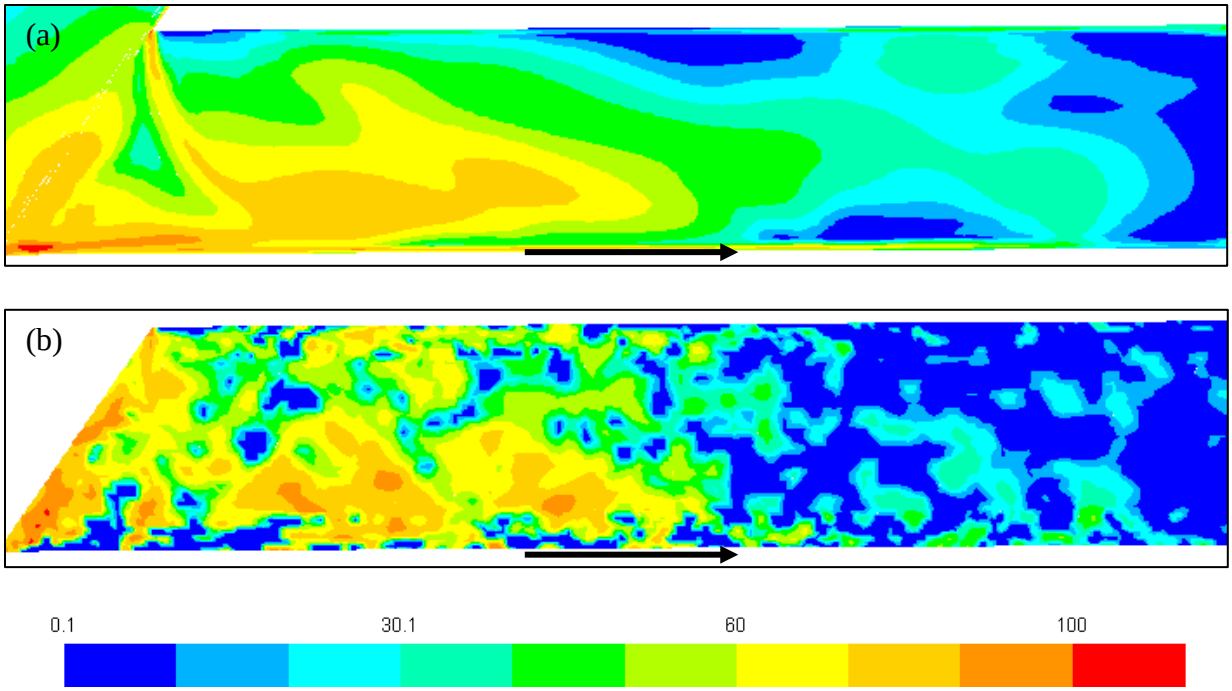

Figure 7.25 – Secondary outer slot 15 turbulent kinetic energy production rate in the x = 0 mm plane from (a) RANS and (b) LES. Color legend is logarithmic and scaled by N^3D^2 = 2018.4 m^2/s^3. ΔP = 7 psi, hex 20M.

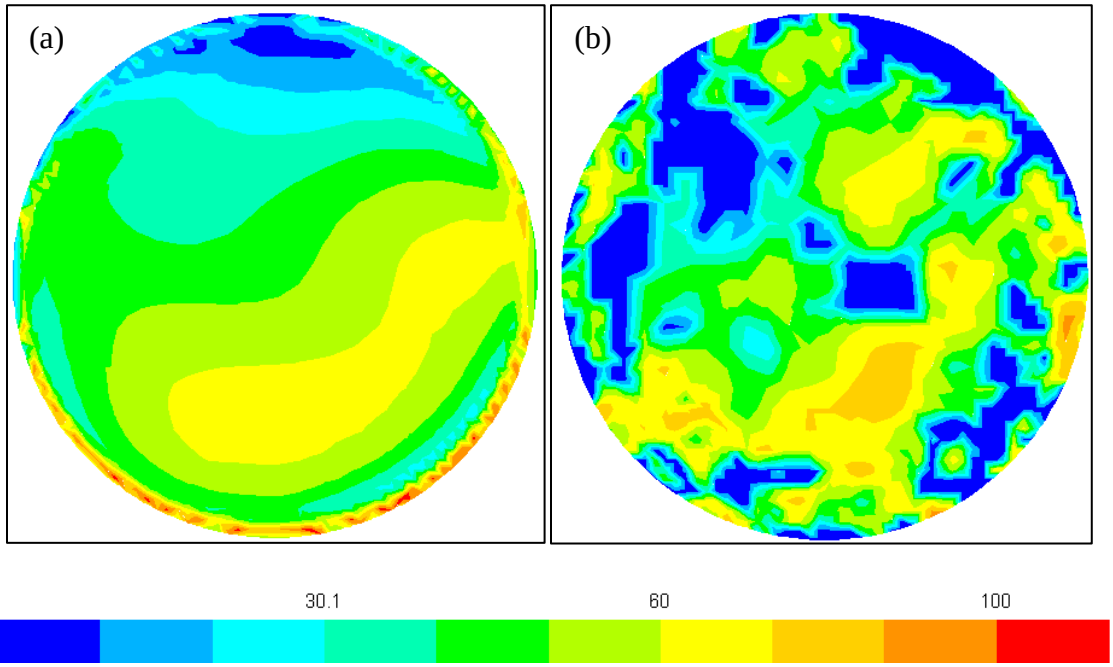

Figure 7.26 – Secondary outer slot 15 turbulent kinetic energy production rate in the z = 100 mm plane looking upstream from (a) RANS and (b) LES. Color legend is logarithmic and scaled by N^3D^2 = 2018.4 m^2/s^3. ΔP = 7 psi, hex 20M.

The spatially averaged statistics from the pointwise difference distribution shown in table 7.7 imply that, on average, higher turbulent kinetic energy production rates are observed in LES. Similar to the turbulent energy dissipation rate pointwise comparison, the magnitude of the minimum difference is significantly larger than the maximum value in the primary slot x = 0 mm plane. This is due to the high turbulent kinetic energy production rates predicted by LES at the exit of the stator compared to RANS. The median value is smaller in magnitude compared to the magnitude of the mean value. This suggests that the reported mean value is heavily influenced by the peak turbulent kinetic energy production rate observed in LES.

Table 7.7 – Turbulent kinetic energy production rate comparison in the stator slots.

Location		$G_k^{(RANS)} - G_k^{(LES)}$ (10^3 m^2/s^3)				
Slot	Plane	Mean	RMSD	Minimum	Median	Maximum
PS6	x = 0 mm	-25.7	73.1	-3040	-3.76	548
	z = 60 mm	-7.47	21.9	-220	-2.60	299
SOS15	x = 0 mm	-8.01	22.8	-257	-1.62	372
	z = 100 mm	-5.36	14.2	-93.2	-4.37	58.6
SMS15	x = 0 mm	-1.98	6.85	-83.4	-0.13	78.8
	z = 100 mm	-1.01	2.49	-18.7	-0.50	11.2
SIS15	x = 0 mm	-1.35	5.38	-80.0	-0.09	92.5
	z = 100 mm	-1.60	3.43	-18.3	-0.35	8.0

Another term in the turbulent kinetic energy conservation equation, given by equation 3.7- 4, is the transport of turbulent kinetic energy. This term includes the transport by velocity and pressure fluctuations. These terms were modeled so that the turbulent kinetic energy conservation equation could be closed. The RANS realizable k-ε model assumes the gradient-diffusion hypothesis, given by equation 3.7-12. For the remainder of this section, the transport of turbulent kinetic energy from the gradient-diffusion hypothesis and from the definition are compared.

In the previous sections, the turbulence quantity predicted from RANS was shown on the left as figure (a) and the quantity predicted from LES was shown on the right as figure (b). To continue this trend, the transport of turbulent kinetic energy as computed from the gradient-diffusion hypothesis (the assumption made in the RANS model) will be shown on the left as figure (a). The transport of turbulent kinetic energy as computed from the definition will be shown on the right as figure (b). The divergence of these terms is shown as contours in figures 7.27 and 7.28 for primary slot 6. In these and later contours, the transport of turbulent kinetic energy from the definition is given by LES. Also since gradient of turbulent kinetic energy is not readily available in FLUENT, the gradient-diffusion hypothesis as computed from the LES will be shown instead of from RANS.

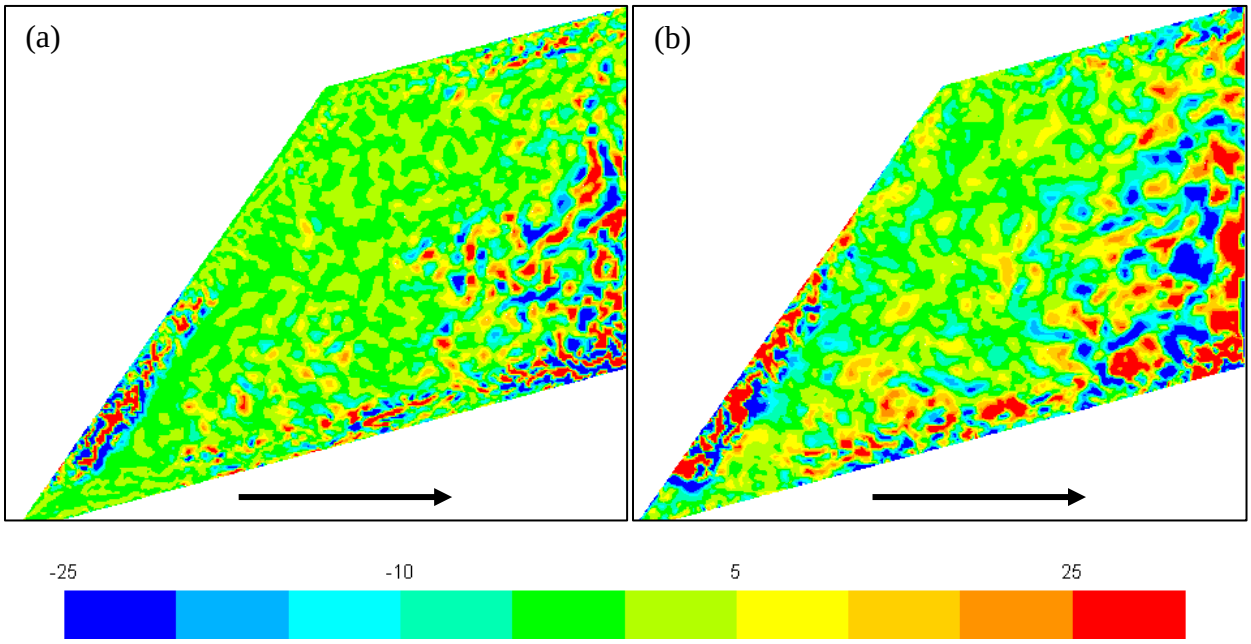

Figure 7.27 – Primary slot 6 transport of turbulent kinetic energy in the x = 0 mm plane from the (a) gradient-diffusion hypothesis and the (b) definition. Color legend is scaled by N^3D^2 = 2018.4 m^2/s^3. ΔP = 7 psi, hex 20M.

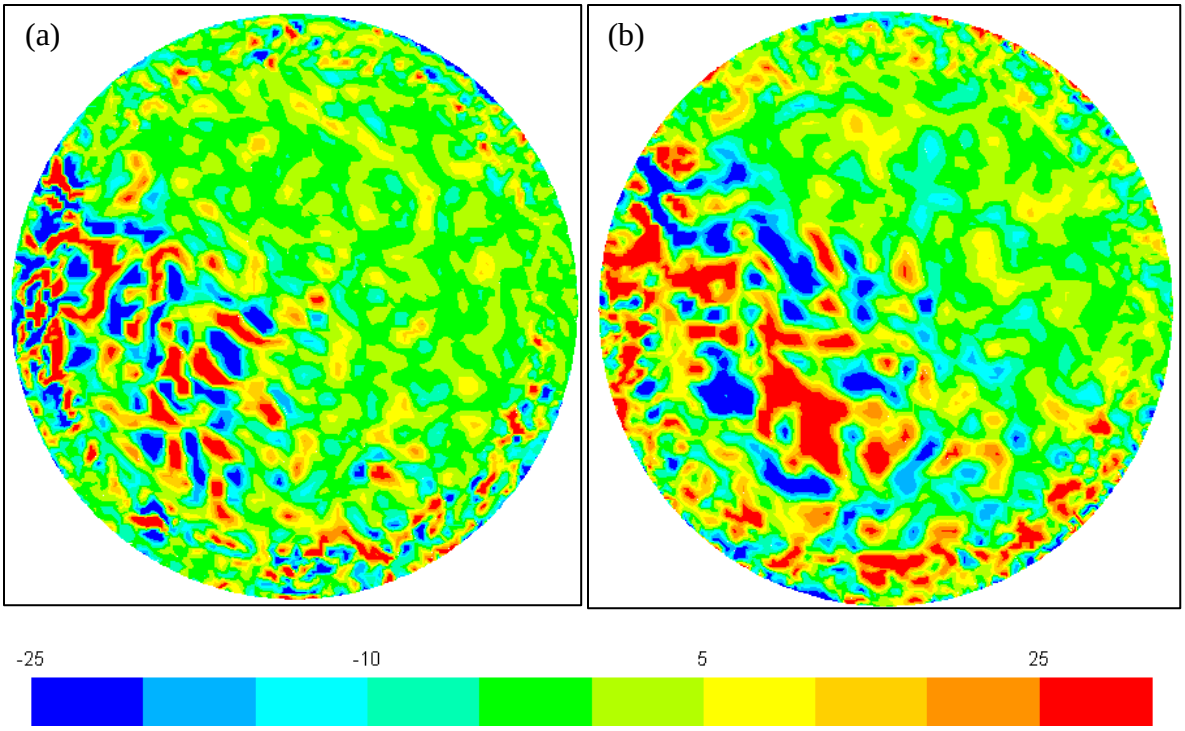

Figure 7.28 – Primary slot 6 transport of turbulent kinetic energy in the z = 60 mm plane looking upstream from the (a) gradient-diffusion hypothesis and the (b) definition. Color legend is scaled by N^3D^2 = 2018.4 m^2/s^3. ΔP = 7 psi, hex 20M.

The divergence of the turbulent kinetic energy transport term can take positive and negative values. If it takes a positive value, then turbulent kinetic energy is transported outwards. Conversely, if negative then it is transported inwards. The magnitude of the turbulent kinetic energy transport term given by the gradient-diffusion hypothesis (figure 7.27a) and by the definition (figure 7.27b) is high at the entrance of the slot, in the stator slot, and at the exit of the slot. The transport of turbulent kinetic energy computed from the definition has a larger spread in these regions. Although the magnitude of the turbulent kinetic energy transport term given by the gradient-diffusion hypothesis and the definition is relatively high in the same regions, the gradient-diffusion hypothesis predicts negative turbulent kinetic energy transport when the definition predicts positive transport, and vice-versa. Both the transport of turbulent kinetic energy from the gradient-diffusion hypothesis and the definition is low in the recirculation region.

Similar contour comparisons for the secondary outer slot are shown in figures 7.29 and 7.30. These contours show similar results as the primary slot contours. The magnitude of the turbulent kinetic energy transport from the definition is relatively high in the recirculation region and at the entrance of the stator. This phenomenon is not accounted for by the gradient-diffusion hypothesis. However, the magnitude of the turbulent kinetic energy transport term as predicted by the gradient-diffusion hypothesis and the definition are high in the stator jet.

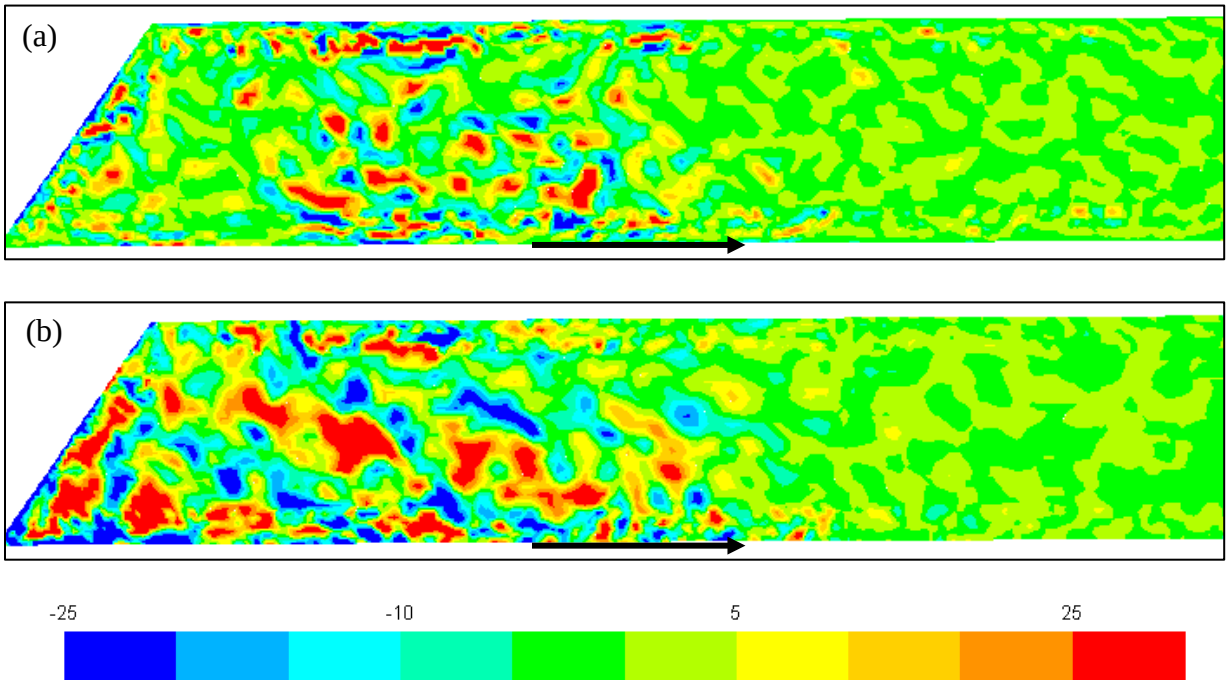

Figure 7.29 – Secondary outer slot 15 transport of turbulent kinetic energy in the x = 0 mm plane from the (a) gradient-diffusion hypothesis and the (b) definition. Color legend scaled by N^3D^2 = 2018.4 m^2/s^3. ΔP = 7 psi, hex 20M.

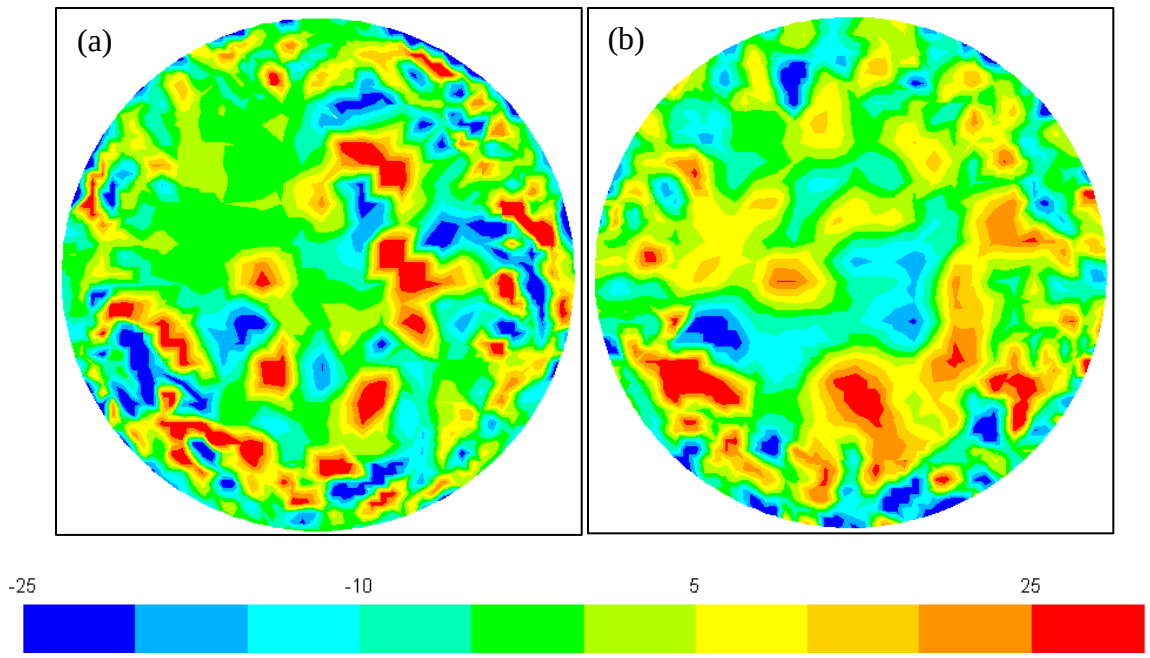

Figure 7.30 – Secondary outer slot 15 transport of turbulent kinetic energy in the z = 100 mm plane looking upstream from the (a) gradient-diffusion hypothesis and the (b) definition. Color legend scaled by N^3D^2 = 2018.4 m^2/s^3. ΔP = 7 psi, hex 20M.

A steep change in the transport and production or turbulent kinetic energy is observed away from the outer edge or from the stator opening. This phenomena is similar to that observed in the turbulent energy dissipation rate contours. This steep change is due to the change in mesh refinement. This implies that the transport and production of turbulent kinetic energy are dependent on the resolved scales. However this steep change is less noticeable than that observed in the turbulent energy dissipation rate contours, suggesting that the transport and production of turbulent kinetic energy are not influenced as much by the smaller scales as the turbulent energy dissipation rate.

7.6 Turbulent Kinetic Energy Budget

The conservation equation of turbulent kinetic energy, shown by equation 3.7-3, can be used to verify that the turbulent energy is conserved. The energy rate not accounted for by the computed quantities in this balance is termed the *residual energy rate*. Theoretically this residual

energy rate should be zero. However due to modelling assumptions made in LES, nonzero values are predicted. The SGS was modelled by the SGS eddy viscosity and used to predict the turbulent energy dissipation rate in section 7.3. The production rate and transport of turbulent kinetic energy was computed by definition as predicted by LES in section 7.5. The only terms in the turbulent kinetic energy balance that have not be shown are the advection and the transport by diffusion terms. These terms are considered in this section to compute the residual energy rate. Contours of the residual energy rate are shown at a constant rotor position (figure 2.7). Therefore, time is held constant and the turbulent kinetic energy time derivative does not contribute to the balance.

Before contours of the residual energy rate can be presented and discussed, the advection term must be considered. The transport of turbulent kinetic energy by diffusion is small throughout the stator slots, $\sim 0.1N^3D^2$ uniformly, this is orders of magnitude smaller than other terms therefore the transport by diffusion term can be neglected. Advection of turbulent kinetic energy in primary slot 6 and secondary outer slot 15 are shown in figure 7.31 below. This term may take positive values if the mean velocity and turbulent kinetic energy gradient share the same sign or negative values if they do not. The advection of turbulent kinetic energy was found to scale similar to the transport of turbulent kinetic energy and therefore the same color legend is used.

Advection is highest in magnitude in the stator entrance and jet regions for both stator slots. At the stator entrance, advection is initially positive since the average velocity and turbulent kinetic energy gradient share the same sign. However, at some distance into the slot, the advection term becomes negative since turbulent kinetic energy decreases and so the gradient changes sign. In the stator jet, the mean axial velocity component dominates and remains positive, however the gradient of turbulent kinetic energy changes sign. The magnitude of the advection term is also high at the exit of the primary stator, due to the motion of the secondary rotor. Advection of turbulent kinetic

energy in the recirculation region is relatively small due to low velocity and weak spatial change in turbulent kinetic energy.

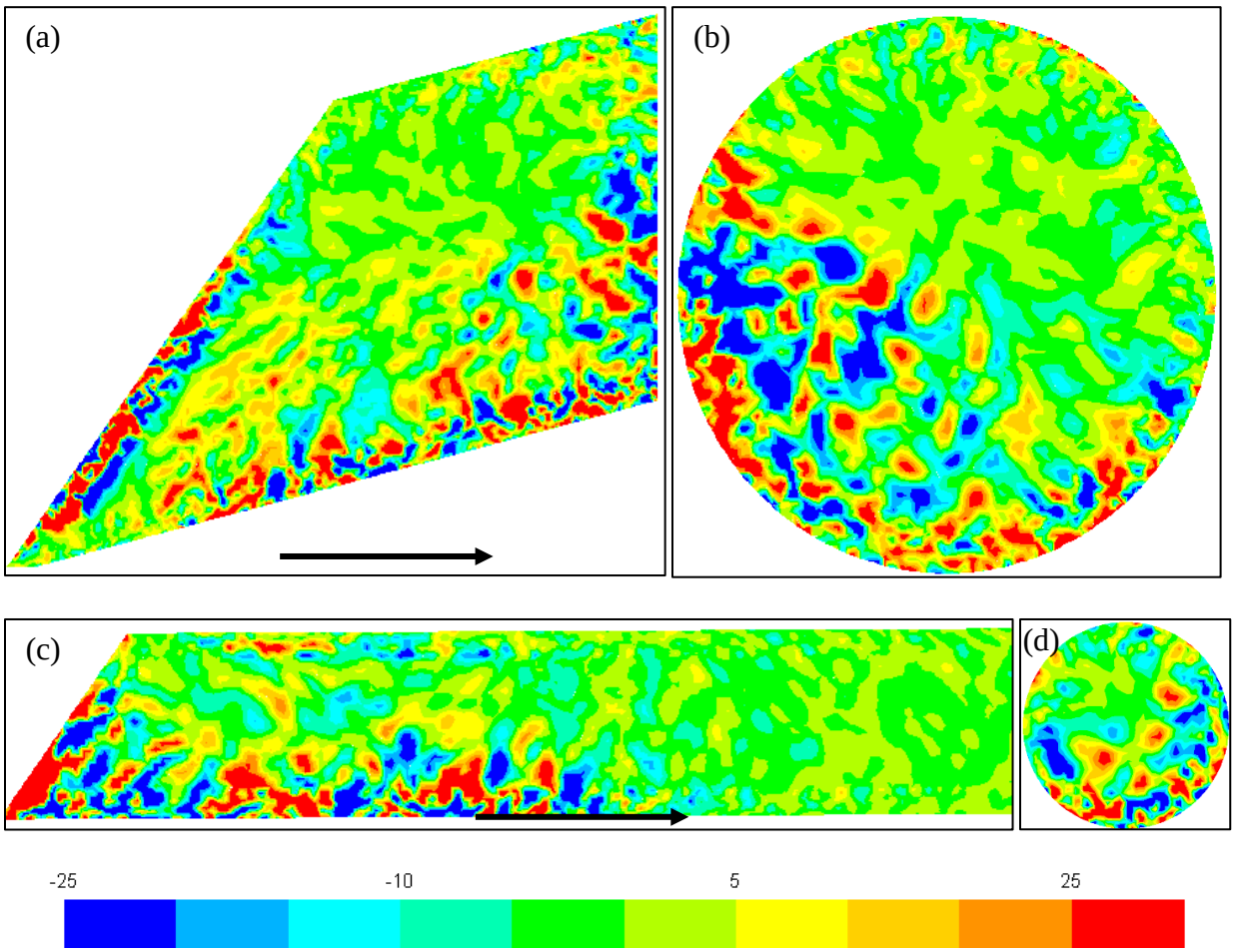

Figure 7.31 – Advection of turbulent kinetic energy in the (a) x = 0 mm and (b) z = 60 mm planes of primary slot 6, and in the (c) x = 0 mm and (d) z = 100 mm planes of secondary outer slot 15. Color legend is scaled by N^3D^2 = 2018.4 m^2/s^3. ΔP = 7 psi, hex 20M LES.

This residual energy rate is defined by rearranging equation 3.7-3 such that the RHS terms are moved to the LHS. In this thesis, the residual energy rate is expressed as,

$$r - \frac{\partial k}{\partial t} = \bar{U}_j \frac{\partial k}{\partial x_j} + \frac{\partial}{\partial x_j}\left[T_j - \nu \frac{\partial k}{\partial x_j}\right] - G_k + \epsilon \qquad (7.6\text{-}1)$$

The transient term remains on the LHS since it cannot be computed using data planes from one rotor position. According to Fox this transient term is zero [8], however this has not been confirmed

in rotor-stator mixers. The production rate removes from the residual energy rate and the dissipation rate adds to the residual energy rate. This residual energy rate is shown in primary slot 6 and secondary outer slot 15 in figure 7.32 below. Negative residual energy rate is predicted at the primary stator entrance and exit where the production rate dominates. Within the stator jet and recirculation region, advection and transport of turbulent kinetic energy are more significant than production and dissipation rates. The magnitude of the residual energy rate in the secondary stator is high at the entrance, and decreases

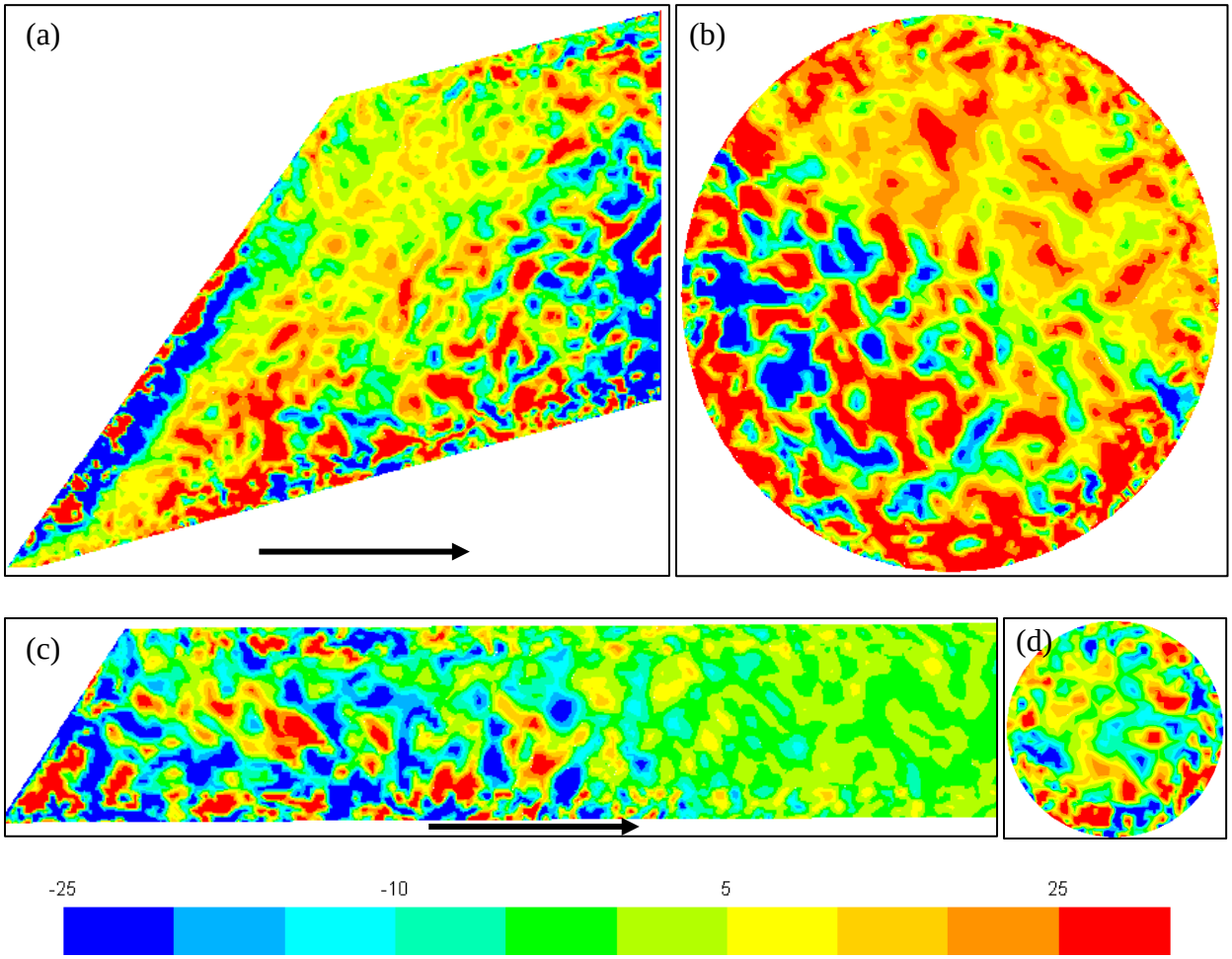

Figure 7.32 – Residual energy rate contours in the (a) x = 0 mm and (b) z = 60 mm planes for primary slot 6, and in the (c) x = 0 mm and (d) z = 100 mm planes for secondary outer slot 15. Color legend scaled by N^3D^2 = 2018.4 m^2/s^3. ΔP = 7 psi, hex 20M LES.

near the exit. The equation for conservation of turbulent kinetic energy is more balanced (the magnitude of the residual energy rate is less) in regions less affected by the rotor, such as the primary stator recirculation region or the exit of the secondary stator.

In section 7.3, the turbulent energy dissipation rate was predicted using the kinematic and SGS viscosities by equation 3.13-10. In this section the turbulent energy dissipation rate is predicted by the conservation equation of turbulent kinetic energy (equation 3.7-3) such that,

$$\epsilon = G_k - \bar{U}_j \frac{\partial k}{\partial x_j} - \frac{\partial}{\partial x_j}\left[T_j - \nu \frac{\partial k}{\partial x_j}\right] \tag{7.6-2}$$

All terms in the turbulent kinetic energy conservation equation excluding the dissipation rate involve the energy of large scales [7]. Similar to the analysis above, rotor position is constant and so the time derivative is negligible. The balance is rearranged to solve for the turbulent energy dissipation rate. Then the production rate adds to the dissipation, and the advection and transport terms remove dissipation. By construction, the residual energy rate discussed previously will be zero. By estimating the turbulent energy dissipation rate in this manner, negative dissipation can be predicted. This occurs if the advection and transport terms are larger than the production rate. As discussed in section 7.5, the production rate can be negative and therefore lower the predicted dissipation rate further.

Turbulent energy dissipation rate as predicted by the turbulent kinetic energy conservation equation is shown in figure 7.33 for primary stator slot 6 and secondary outer slot 15. Negative turbulent energy dissipation rate is observed in these regions, however the use of a color log scale precludes negative turbulent energy dissipation rate. From this method of approximating the turbulent energy dissipation rate, high dissipation is predicted where the production rate dominates, at the stator entrance and exit of the primary stator. Small or negative turbulent energy dissipation rate is predicted in the recirculation region of the primary stator and near the exit of the

secondary stator. In these regions the transport and advection rate of turbulent kinetic energy is larger than or equal to the production rate.

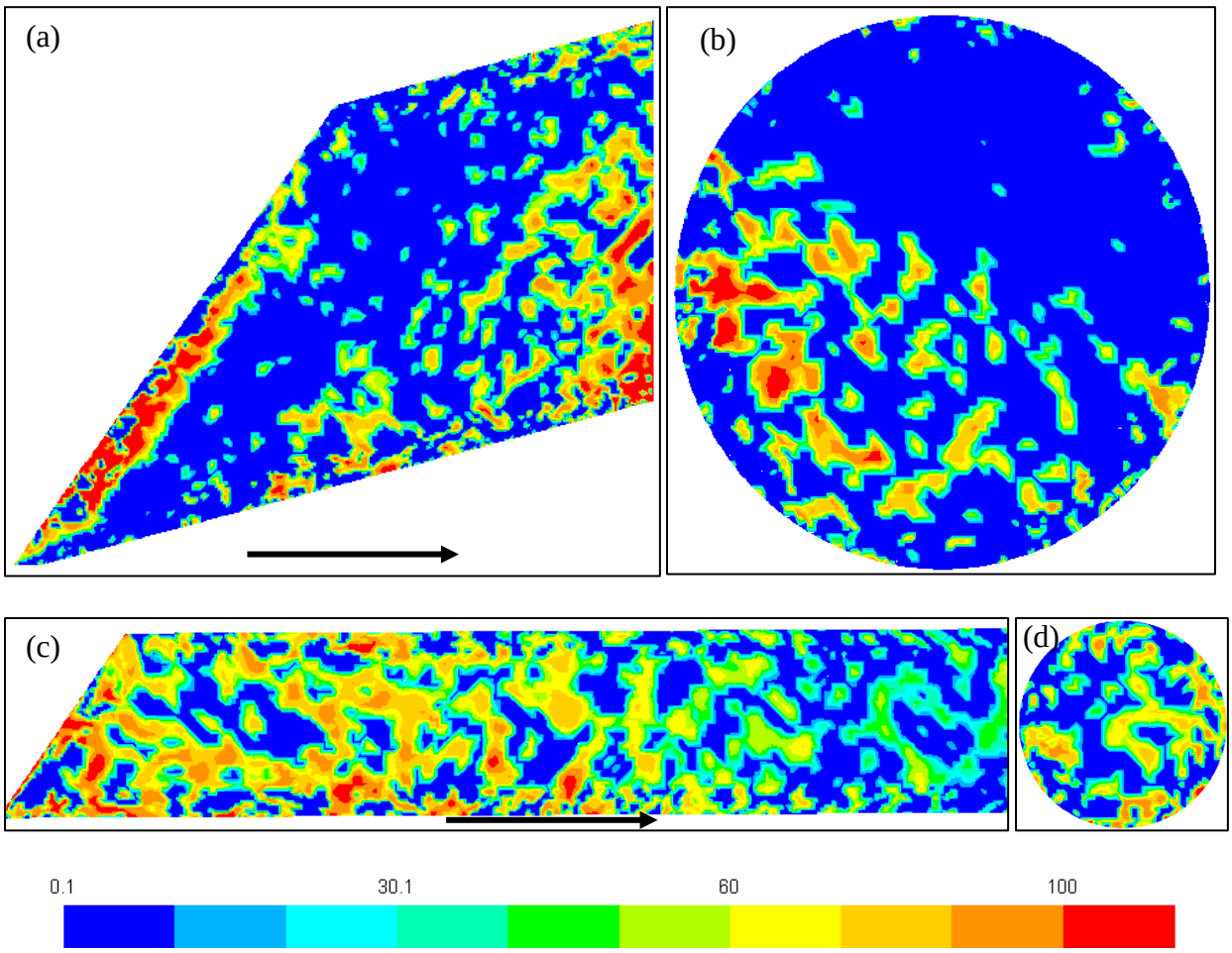

Figure 7.33 – Turbulent energy dissipation rate contours as predicted by equation 7.6-2 in the (a) x = 0 mm and (b) z = 60 mm planes in primary slot 6, and in the (c) x = 0 mm and (d) z = 100 mm planes for secondary outer slot 15. Color legend scaled by N^3D^2 = 2018.4 m^2/s^3. ΔP = 7 psi, hex 20M LES.

7.7 Turbulence Anisotropy

The empirical turbulent energy dissipation rate equation of the RANS k-ε model was built on the turbulent energy dissipation rate conservation equation simplified by the assumption of isotropic turbulence. The SGS model used for LES also assumes isotropic turbulence. It is therefore useful to quantify anisotropy and highlight the regions where it is highest. To accomplish

this, the anisotropy tensor predicted from LES is used. This anisotropy tensor was used in the Boussinesq approximation in section 7.4 and in the production of turbulent kinetic energy in section 7.5.

In this thesis, results from the anisotropy tensor will be unitless by normalizing the a_{ij} by the trace of the Reynold's stress tensor. This trace is equivalent to twice the turbulent kinetic energy by its definition. We define the normalized anisotropy tensor as,

$$b_{ij} = \frac{a_{ij}}{2k} = \frac{\overline{u_i u_j}}{\overline{u_k u_k}} - \frac{1}{3}\delta_{ij} \tag{7.7-1}$$

To show contours of anisotropy in the stator slots, the dimension of the normalized anisotropy tensor must be reduced to a scalar. To do this, the invariants of the normalized anisotropy tensor are used. The first invariant, the trace of the normalized anisotropy tensor is zero, by construction. The second and third invariants, $b_{ij}b_{ji}$ and $b_{ij}b_{jk}b_{ki}$, may be nonzero. The values in which these invariants may take are bounded by the laws of physics described by the Lumley triangle [17]. To now characterize these invariants into a single quantity, the magnitude of these invariants is shown. The magnitude of these invariants represents the distance traveled from the origin in the Lumley triangle which represents isotropic turbulence. When the second and third invariants of the anisotropy tensor are zero, or the magnitude of these invariants is zero, then there is isotropic turbulence.

Contours of the magnitude of the anisotropy tensor invariants in the primary slot are shown in figure 7.34. As expected, anisotropic turbulence is predicted at the stator walls. Other regions with anisotropic turbulence conditions are observed at the entrance and exit of the primary stator where the primary and secondary rotor act, respectively. Isotropic turbulence, as quantified by the magnitude of the invariants, is predicted at the center of the stator slot, particularly in the recirculation region. Anisotropic turbulence is predicted farther away from the outer edge of the

stator wall than from the inner edge of the stator wall. This is due to the interaction between the stator jet and wall effects.

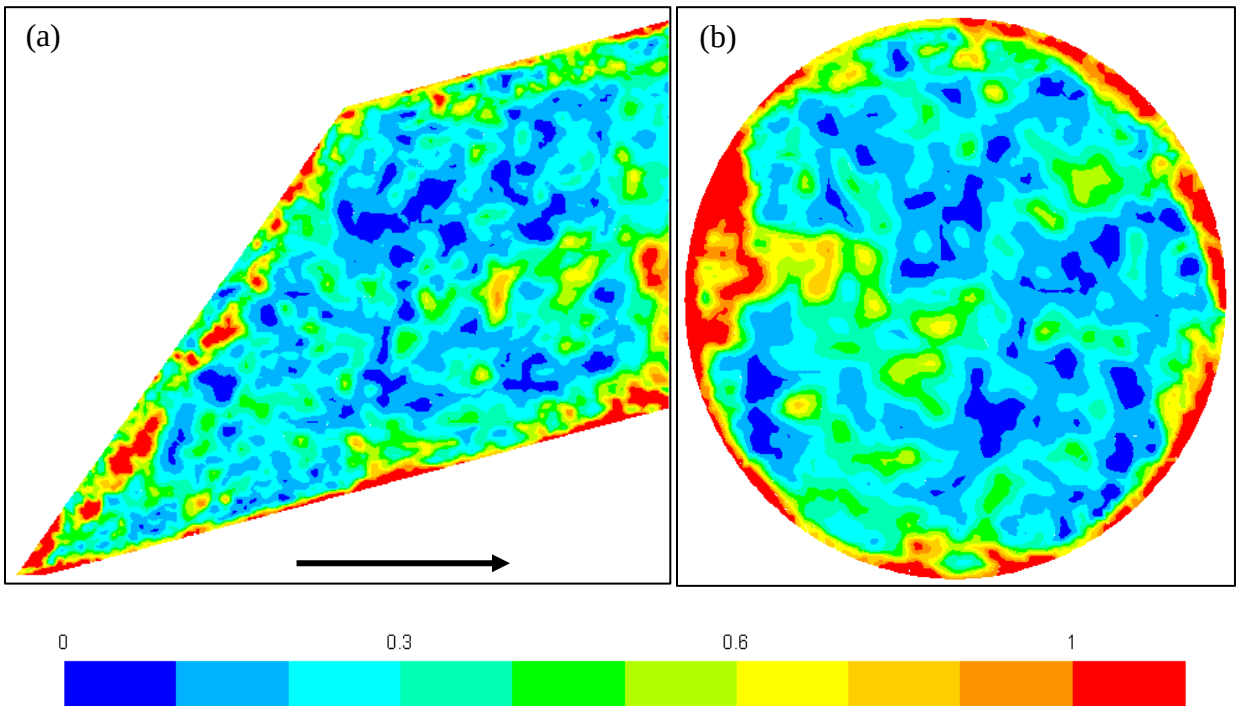

Figure 7.34 – Magnitude of anisotropy tensor invariants in the primary slot 6 in the (a) x = 0 mm and (b) z = 60 mm planes. ΔP = 7 psi, hex 20M LES.

Contours of the magnitude of the anisotropy invariants in the secondary stator slots show similar phenomena as observed in the primary stator. These contours are shown in figure 7.35 below. As the diameter of the secondary stator slots decrease, a larger percentage of the slot is occupied by anisotropic regions. This measure of anisotropy peaks at the secondary stator opening, yet for the primary slot, it peaks some short distance away from the stator opening. This is due to the larger size of the primary stator slot. Both primary and secondary stator slots show high anisotropy farther away from the outer edge wall relative to other regions along the outer edge. This anisotropy occurs because of the interactions between the stator jet and the recirculation region.

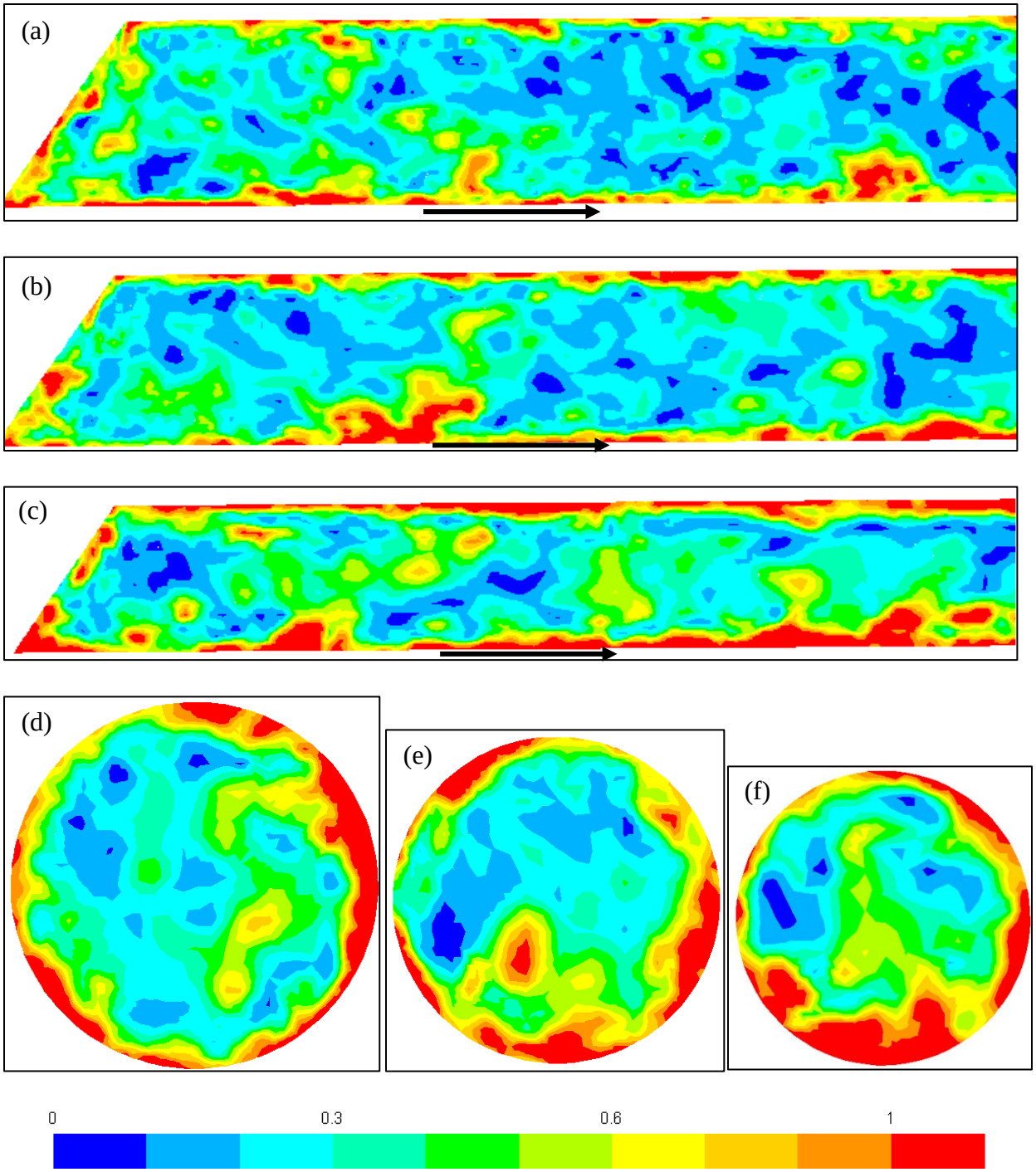

Figure 7.35 – Magnitude of the anisotropy tensor invariants in the x = 0 mm plane for the secondary (a) outer, (b) middle, and (c) inner slots 15, also in the z = 100 plane for the secondary (a) outer, (b) middle, and (c) inner slots 15. ΔP = 7 psi, hex 20M LES.

7.8 Summary of RANS/LES Comparison

Macroscopic properties such as angularly resolved stator slot flow rate and rotor torque were compared between RANS and LES. Turbulence quantities such as mean velocity, turbulent kinetic energy, as well as the production and dissipation rates of turbulent kinetic energy, were compared between RANS and LES. Assumptions made to develop the RANS realizable k-ε model equations, including the Boussinesq approximation, gradient-diffusion hypothesis, and the empirical homogeneous-based turbulent energy dissipation rate equation, were validated using LES results. The turbulent energy dissipation rate was computed from LES using the resolved as well as SGS contributions and by considering each term in the turbulent kinetic energy conservation equation. The invariants of the anisotropy tensor from LES were considered.

The angularly resolved flow rate and torque profiles from RANS agreed well with the ensemble averaged flow rate and torque profiles from LES. This implies that angularly averaged macroscopic properties such as the flow and power number predicted by either turbulence model would be quantitatively similar. Flow rate fluctuations modeled by LES were unaccounted for in RANS. In conclusion, RANS can be used to quickly find flow and power number data. LES can be used to find information on fluctuations and turbulence quantities.

Mean velocity profiles readily available from RANS and ensemble averaged from LES shared similar flow features, such as the stator jet and recirculation region. The location of these regions differed between these two turbulence models. The penetration distance of the high velocity from the rotor blade into the stator slot opening is predicted to be higher for RANS. In the primary and secondary outer slots, RANS predicted a shorter stator jet length, but with a higher height from the outer stator wall. The location of the recirculating vortices at the exit of the secondary middle and inner slots differed between each model.

RANS predicted lower turbulent kinetic energy in the stator slots compared to LES. This was particularly true at the stator entrance due to rotor blade interactions. High turbulent kinetic energy predicted by LES enveloped a larger area than RANS in the stator jet and recirculation region. Higher turbulence energy dissipation rate was predicted by RANS compared to LES. Both models predict high turbulent energy dissipation rate in regions where the rotor blade acts. At the outer stator wall, RANS predicts a significantly higher turbulent energy dissipation rate compared to LES. A higher gradient of the turbulent energy is predicted by LES. The production rate of turbulent kinetic energy predicted by these models also differed. Both models predict high production rates where the rotor blades act and in the stator jet. LES predicts a larger region of high production rate than RANS in the stator slot.

8 Conclusions and Recommendations

This chapter summarizes the work completed in this thesis and summarizes conclusions made from the results provided by the simulations. Aspects of this project that would benefit from further investigation are presented as recommendations for future work.

8.1 Summary

Mean and filtered velocity profiles within the Chemineer Greerco 4-inch tandem shear pipeline mixer were simulated by solving the Reynolds-averaged (RANS) and time-filtered (LES) Navier-Stokes equations in FLUENT. Different operating scenarios were considered, both with and without a backpressure imposed. Fluid flow within this mixer was simulated on coarse and more refined computational grids. The RANS equations were closed using the realizable k-ε model and the SGS of LES was modeled using the WALE SGS eddy viscosity closure.

Stator slot flow rate and rotor torque were presented in the time and frequency domain from RANS and LES. The level of spatial resolution in LES was quantified using the SGS eddy viscosity ratio. Mean velocity, turbulent kinetic energy, and turbulent energy dissipation rate contours were compared between the two models. The adequacy of the Boussinesq approximation was investigated by comparing the turbulent kinetic energy production rate between RANS and LES. Modeling assumptions for the transport of the turbulent kinetic energy were investigated.

8.2 Conclusions

The mean velocity field predicted by RANS shows a high axial velocity stator jet along the outer edge of the stator wall and a recirculation region at the inner edge for both primary and secondary stator slots. The velocity field at the exit of the primary stator is highly influenced by the presence of the secondary rotor, and the exit of the secondary stator slots is influenced by the outlet. The resolved velocity fluctuations simulated by LES show vortices in the recirculation

region and high-intensity stator jet eddies dependent on rotor position. Mean strain rates predicted by RANS are high at the rotor tip and at the edge of the stator where the recirculation vortex is present. The fluctuating component of the filtered strain rate simulated by LES occupies a larger region of the stator opening, especially after the blade has passed the slot.

The mean flow rate in a stator slot showed cyclic behavior, with a period of one rotor blade passage. Based on Fourier analysis, it was found that the number of mean torque oscillations in one rotor blade passage period is dependent on the number of stator slots per rotor blade for a given stage. The angularly resolved flow rate and torque profiles predicted by both RANS and LES agree within 5% for all rotor positions considered. The fluctuating flow rate component simulated by LES was shown to be dependent on small frequencies which are periods larger than one rotor blade pass. The fluctuating torque component is relatively small compared to the mean component. Higher throughput and power were reported for the 0-psi backpressure compared to the 7-psi backpressure. RANS predicted that more mean and turbulent energy is dissipated at the lower backpressure, resulting in a higher power draw.

Results predicted by LES were highly dependent on grid resolution. Vortices in the recirculation region predicted by the refined hex 20M mesh were not observed for the coarse hex 4.2M mesh. Lower filtered strain rates were observed near the stator opening from the coarse hex 4.2M mesh since the fluctuating strain rate field was not as well resolved as it was for the hex 20M mesh. As indicated by the SGS eddy viscosity ratio, more energy was dissipated at the SGS than at the resolved scales, indicating that further grid refinement is required to properly predict the turbulent energy dissipation rate using the LES technique.

Both RANS and LES predict similar mean velocity profiles in the stator slots. LES predicts higher turbulent kinetic energy in the stator slots compared to RANS. RANS predicts higher

turbulent energy dissipation rates near the stator walls and shows a smaller spreading gradient than predicted by LES. The turbulent energy dissipation rate model equation used in RANS, which was derived assuming isotropy, is likely over predicting the turbulent energy dissipation rate in the stator slots. LES is likely under predicting the turbulent energy dissipation rate due to the smaller scales that are improperly modeled by the SGS model.

Both simulations predict high production and transport rates of turbulent kinetic energy near the stator opening and at the stator jet. The production rate of turbulent kinetic energy predicted by LES was higher than that modeled using the Boussinesq approximation in the RANS k-ε model. The transport of turbulent kinetic energy predicted by LES was spread over a larger region than that modeled by eddy diffusion assumed in the RANS k-ε model. These discrepancies between the two models are due to inappropriate modeling of the eddy viscosity. The magnitude of the invariants of the anisotropy tensor were shown highest at the stator opening and along the stator walls.

To predict turbulence quantities such as the turbulent kinetic energy, the strain rate tensor, and the production and dissipation rate of turbulent kinetic energy, spatial and temporal resolution required by LES is more costly than RANS. This is particularly true for energy dissipation rates. Although LES has fewer model equations to solve on a per iteration basis compared to RANS, several realizations are required from LES to gather reliable statistics. Macroscopic quantities such as flow rate and torque require less spatial and temporal resolution. These fluctuations of these quantities can be solved in a time efficient manner on a coarse LES mesh.

8.3 Mesh Resolution Summary

Independent of turbulence model used, the coarse hex 4.2M mesh predicted flow rate and torque profiles that agreed with the refined hex 20M mesh. However mean and turbulent velocity

gradients are less resolved in the hex 4.2M mesh and the energy dissipated is therefore under predicted compared to the hex 20M mesh. With LES, both meshes predict a fluctuating velocity field, however smaller turbulent structures resolved in the hex 20M mesh are not observed in the hex 4.2M mesh. The absence of these structures implies the hex 4.2M mesh would under predict the turbulent kinetic energy, as well as its production and dissipation rate compared to the hex 20M mesh.

8.4 Recommendations for Future Work

Further consideration is necessary to properly quantify the turbulent energy dissipation rate in the stator slots. Results from other closure methods such as the k-ω or Reynolds stress model (RSM) could be compared to the RANS realizable k-ε model results. The parameters in the RANS k-ε model could be tuned to quantify the turbulent kinetic energy and energy dissipation rate properly.

Further grid refinement in the stator slots is necessary for LES to accurately predict the turbulent energy dissipation rate. More realizations should be used to confirm that the reported turbulent energy dissipation rate has converged. To resolve the smaller scales that are required to quantify turbulent energy dissipation, a portion of the rotor-stator mixer could be simulated with appropriate boundary conditions. Other SGS models, such as the Smagorinsky-Lilly or dynamic kinetic energy SGS model, could be considered for future work with LES. A different wall model could be considered or a detached eddy simulation, which solves the filtered Navier-Stokes in regions sufficiently refined and solves the RANS equations where it is not, could be used to simulate the flow within this or other rotor-stator mixers.

If the turbulent energy dissipation rate is better quantified, then it can be used to better predict the power dissipated in the mixer. By integrating the turbulent energy dissipation rate

across the entire volume of the mixer, it can be compared to the power output predicted by the torque. If the power predicted by the volume integral of the turbulent energy dissipation rate is significantly less than the power predicted by the torque, then other contributions must be considered. Flow work and work to accelerate the fluid should be added to the power dissipation term. The modeled equation for the turbulent energy dissipation rate in the RANS k-ε model was derived by assuming homogeneous turbulence. It was shown that flow near the rotor blades and at the stator walls is highly anisotropic. Energy dissipated in these anisotropic regions is unaccounted for when using a model that assumes homogeneous turbulence.

9 Appendix A – RANS/LES 20M 0-psi Comparison Figures

Appendix A contains the mean velocity field turbulent kinetic energy and turbulent energy dissipation rate contours in primary slot 6 and secondary outer slot 15 at the 0-psi backpressure as predicted by RANS and LES. The center plane and corresponding cross view is shown. For more information on these figures, see sections 7.2 and 7.3.

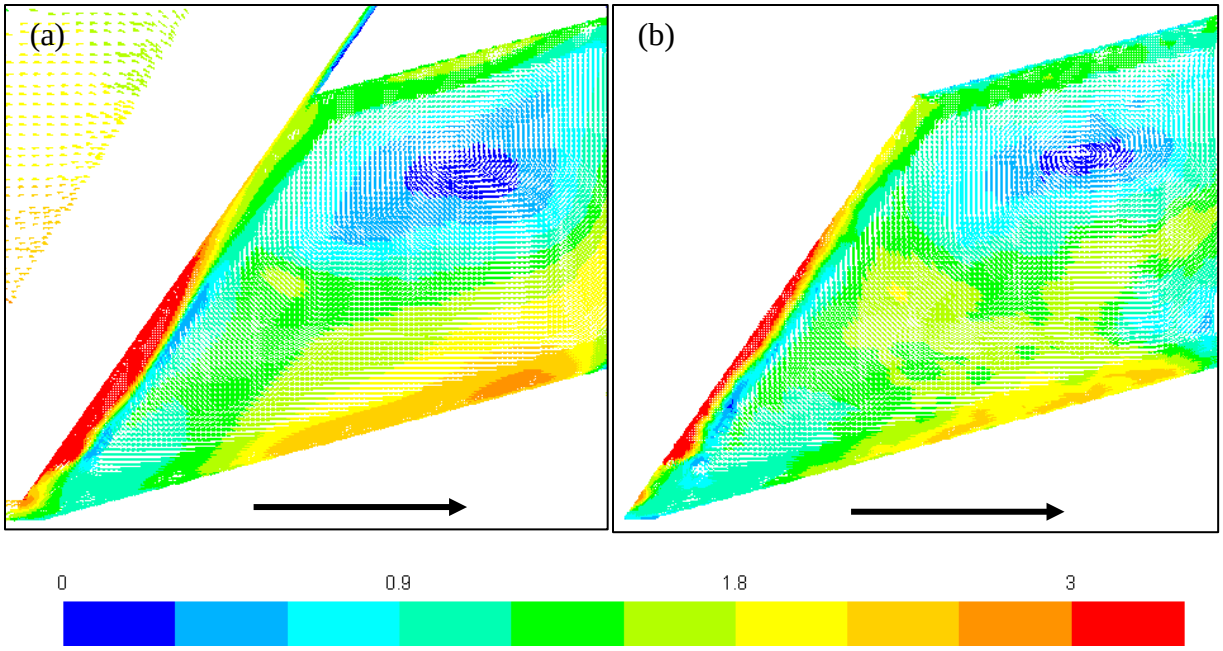

Figure 10.1 – Primary stator slot 6 mean velocity field colored by velocity magnitude in the center plane, x = 0 mm, from (a) RANS and (b) LES. Color legend scaled by (ND) = 5.8 m/s. ΔP = 0 psi, hex 20M.

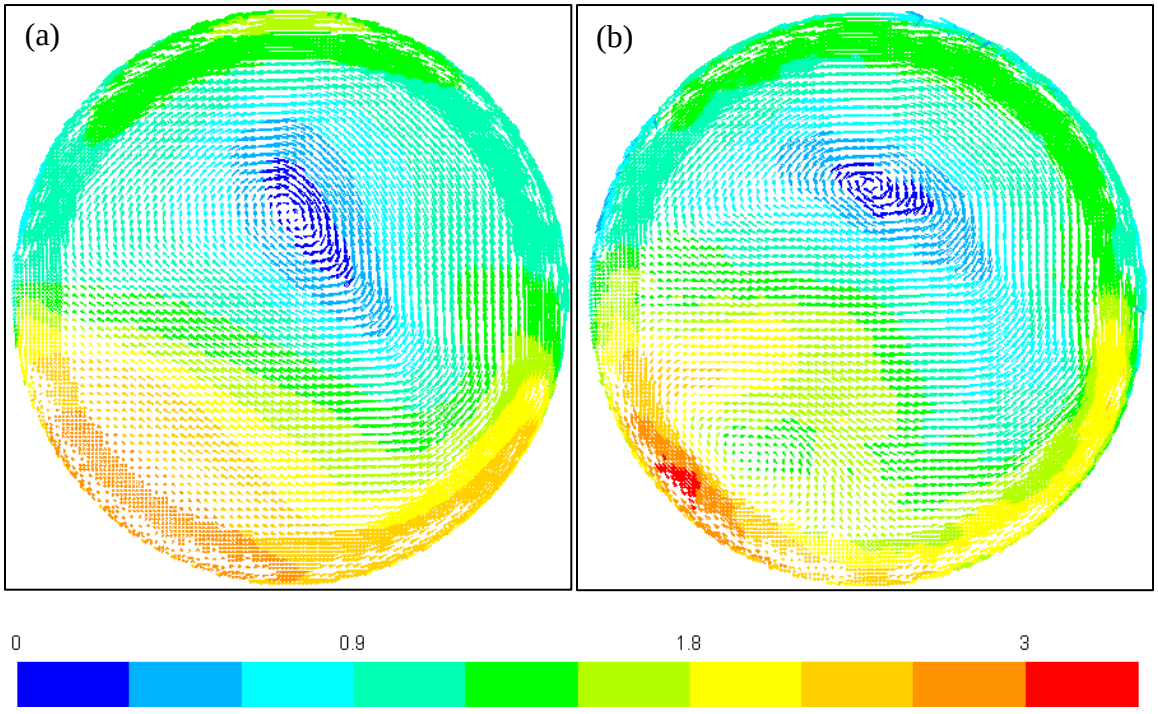

Figure 10.2 – Primary stator slot 6 mean velocity field colored by velocity magnitude in the z = 60 mm plane looking upstream from (a) RANS and (b) LES. Color legend scaled by (ND) = 5.8 m/s. ΔP = 0 psi, hex 20M.

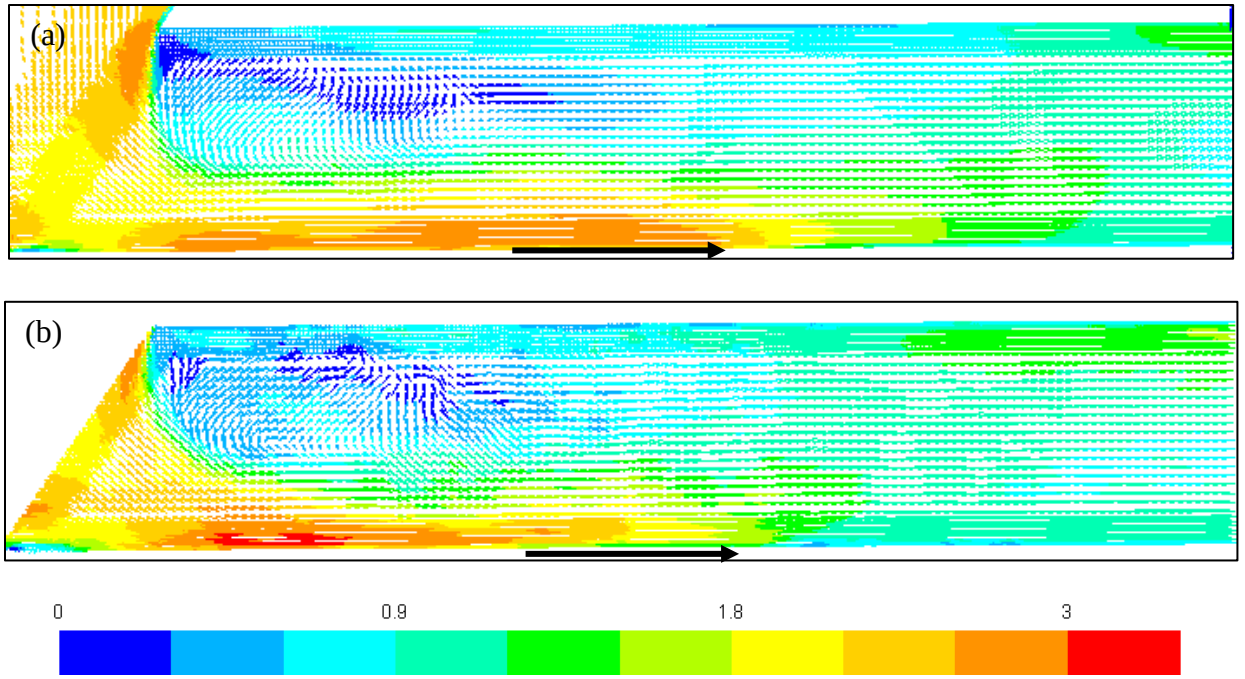

Figure 10.3 – Secondary outer slot 15 mean velocity field colored by velocity magnitude in the center plane, x = 0 mm, from (a) RANS and (b) LES. Color legend scaled by (ND) = 5.8 m/s. ΔP = 0 psi, hex 20M.

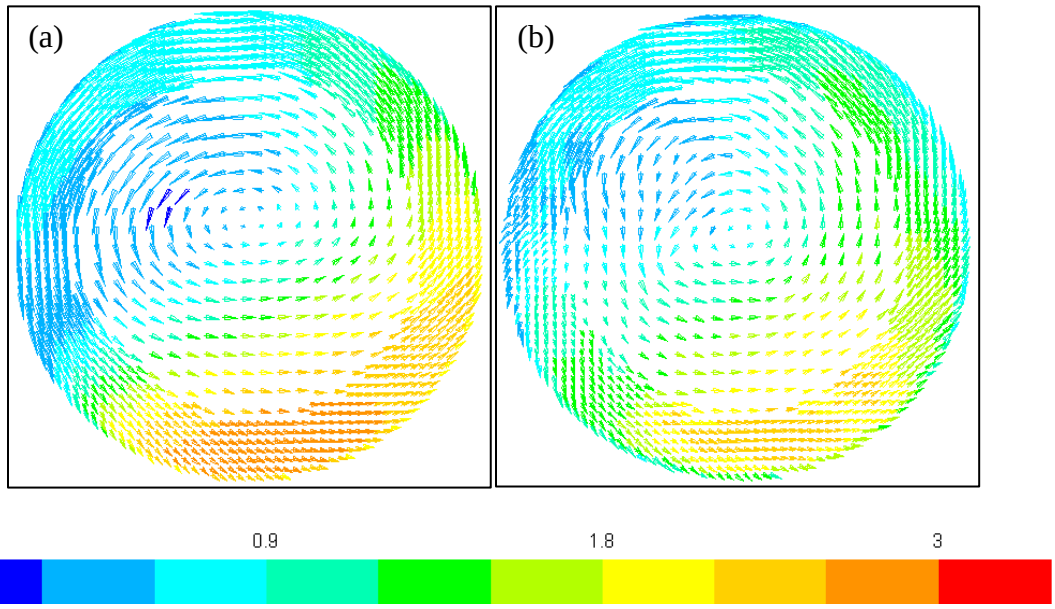

Figure 10.4 – Secondary outer slot 15 mean velocity field colored by velocity magnitude in the z = 100 mm plane looking upstream from (a) RANS and (b) LES. Color legend scaled by (ND) = 5.8 m/s. ΔP = 0 psi, hex 20M.

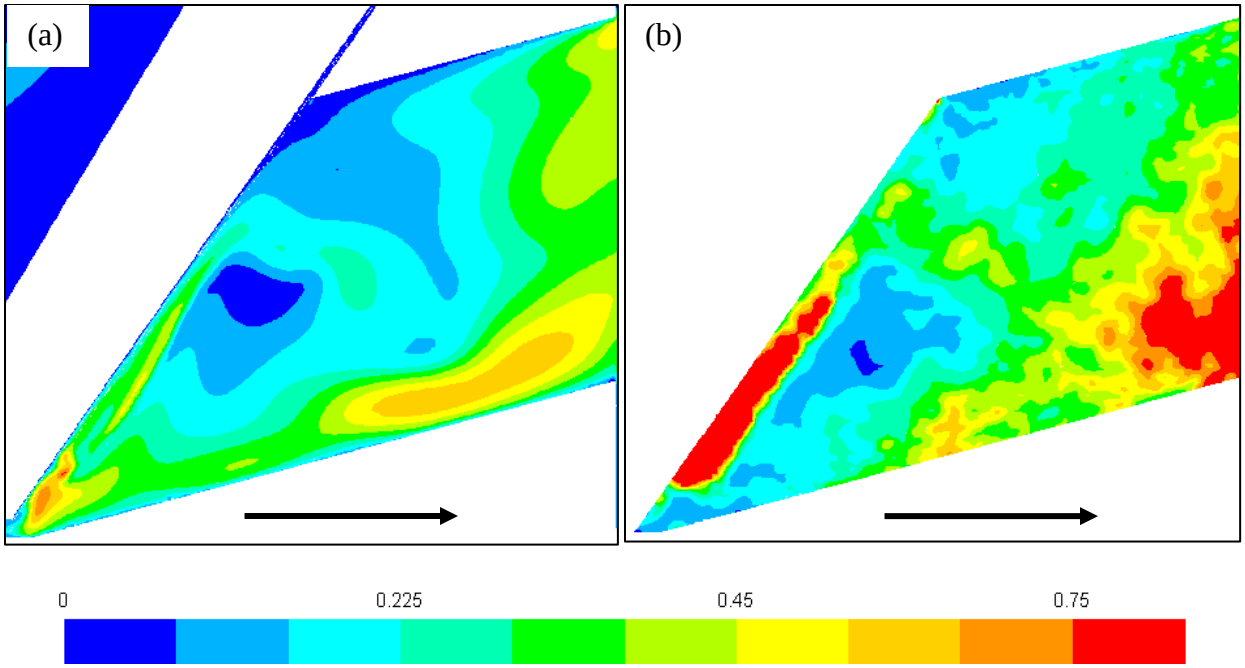

Figure 10.5 – Primary slot 6 turbulent kinetic energy in the x = 0 mm plane from (a) RANS and (b) LES. Color legend scaled by $(ND)^2 = 33.64\ m^2/s^2$. $\Delta P = 0$ psi, hex 20M.

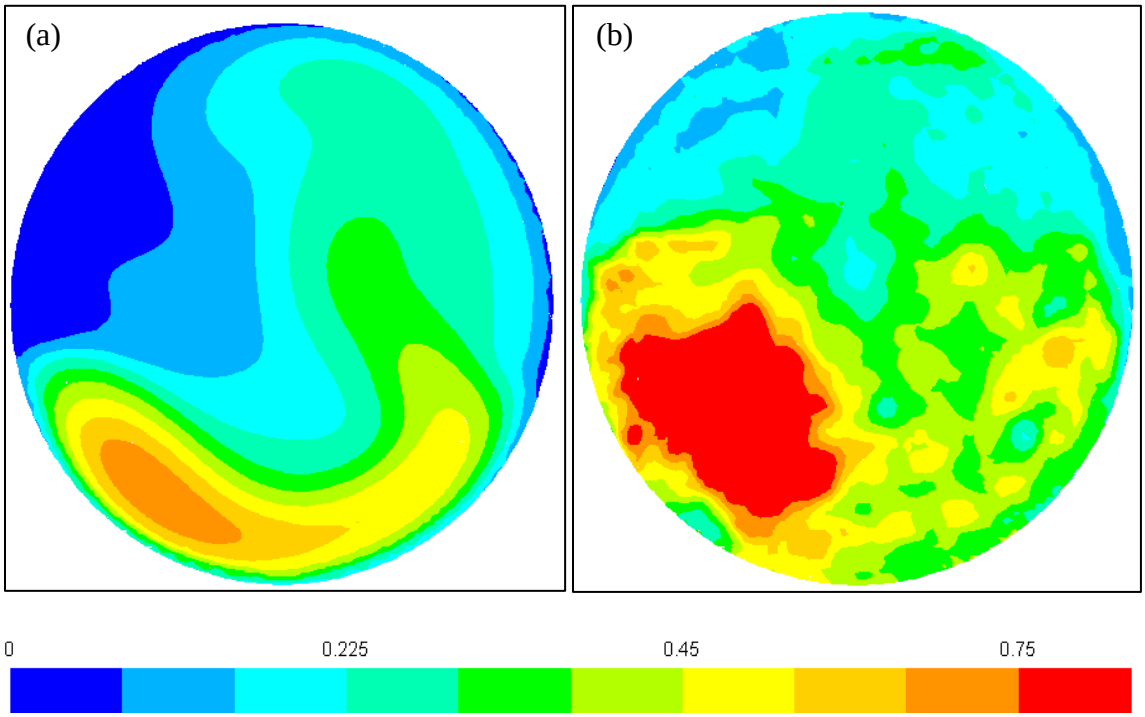

Figure 10.6 – Primary slot 6 turbulent kinetic energy in the z = 60 mm plane looking upstream from (a) RANS and (b) LES. Color legend scaled by $(ND)^2 = 33.64\ m^2/s^2$. $\Delta P = 0$ psi, hex 20M.

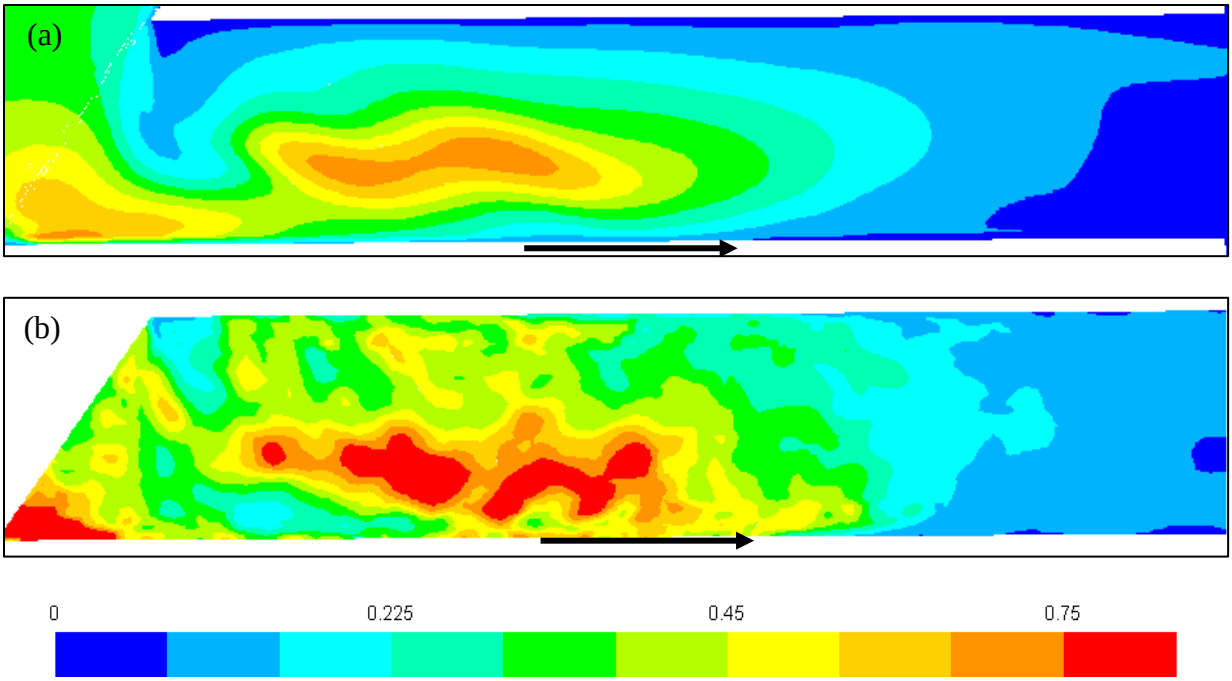

Figure 10.7 – Secondary outer slot 15 turbulent kinetic energy in the x = 0 mm plane from (a) RANS and (b) LES. Color legend scaled by $(ND)^2 = 33.64\ m^2/s^2$. $\Delta P = 0$ psi, hex 20M.

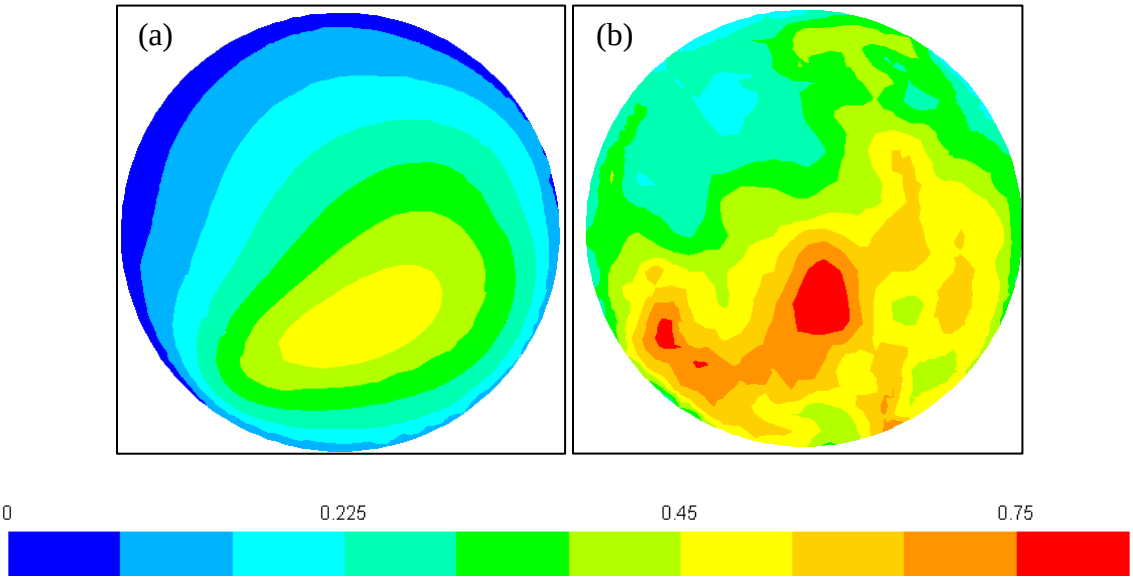

Figure 10.8 – Secondary outer slot 15 turbulent kinetic energy in the z = 100 mm plane looking upstream from (a) RANS and (b) LES. Color legend scaled by $(ND)^2 = 33.64\ m^2/s^2$. $\Delta P = 0$ psi, hex 20M.

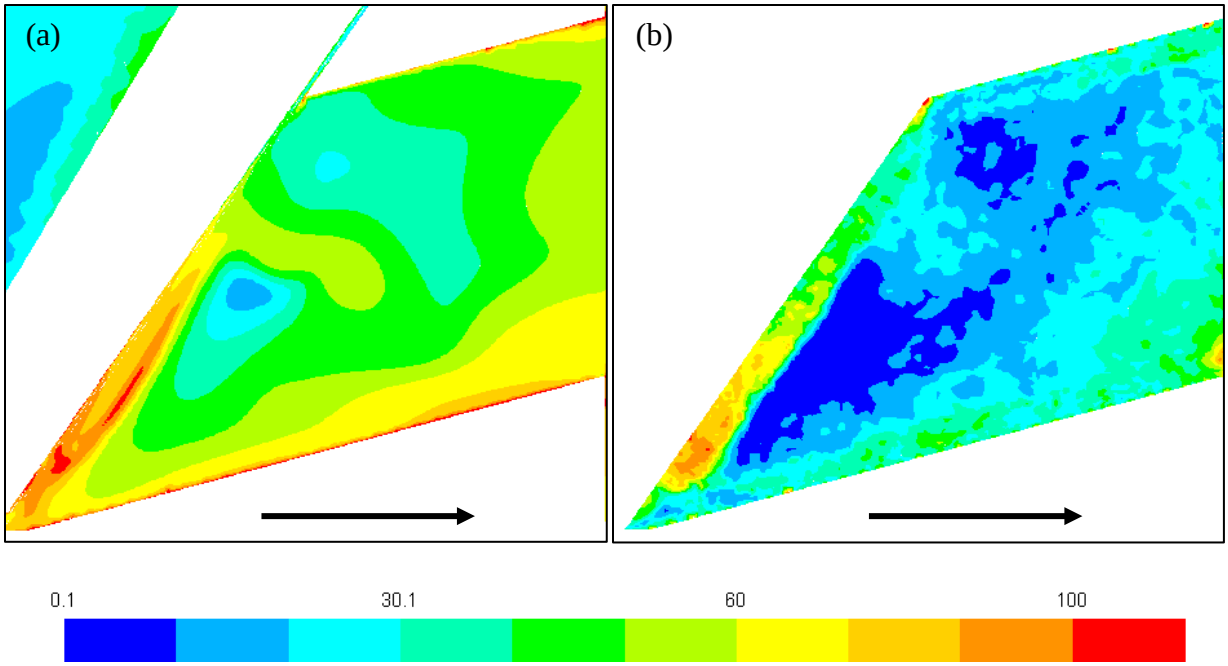

Figure 10.9 – Primary slot 6 turbulent energy dissipation rate in the x = 0 mm plane from (a) RANS and (b) LES. Color legend is logarithmic and scaled by N^3D^2 = 2018.4 m^2/s^3. ΔP = 0 psi, hex 20M.

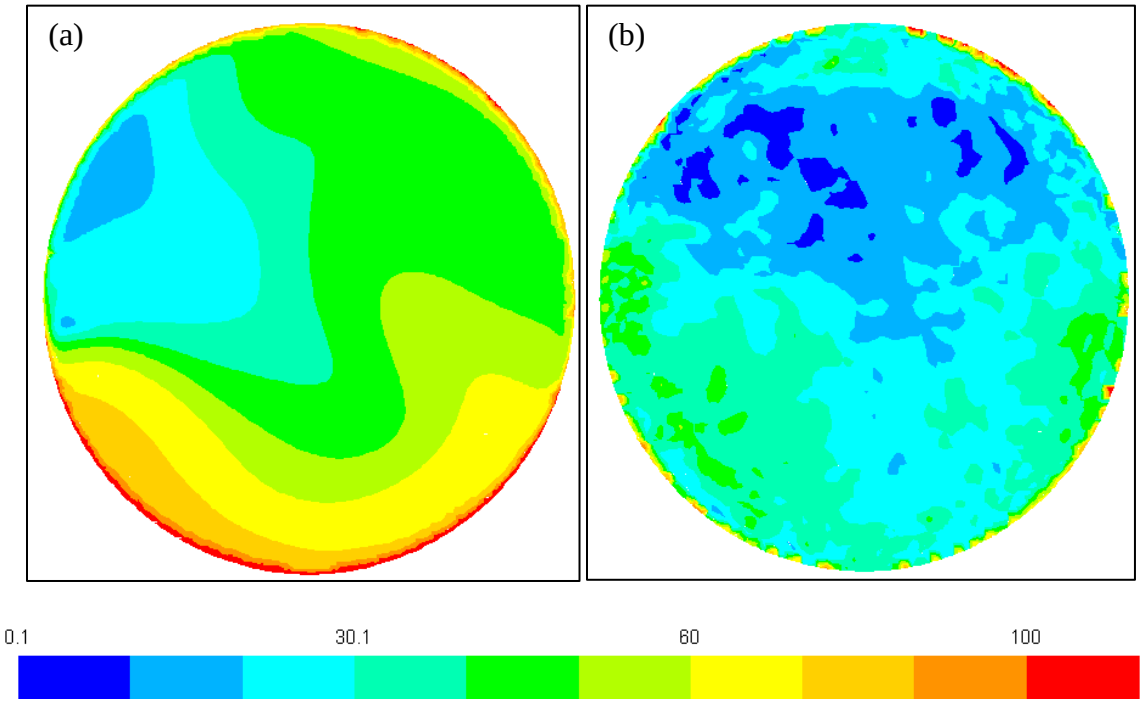

Figure 10.10 – Primary slot 6 turbulent energy dissipation rate in the z = 60 mm plane looking upstream from (a) RANS and (b) LES. Color legend is logarithmic and scaled by N^3D^2 = 2018.4 m^2/s^3. ΔP = 0 psi, hex 20M.

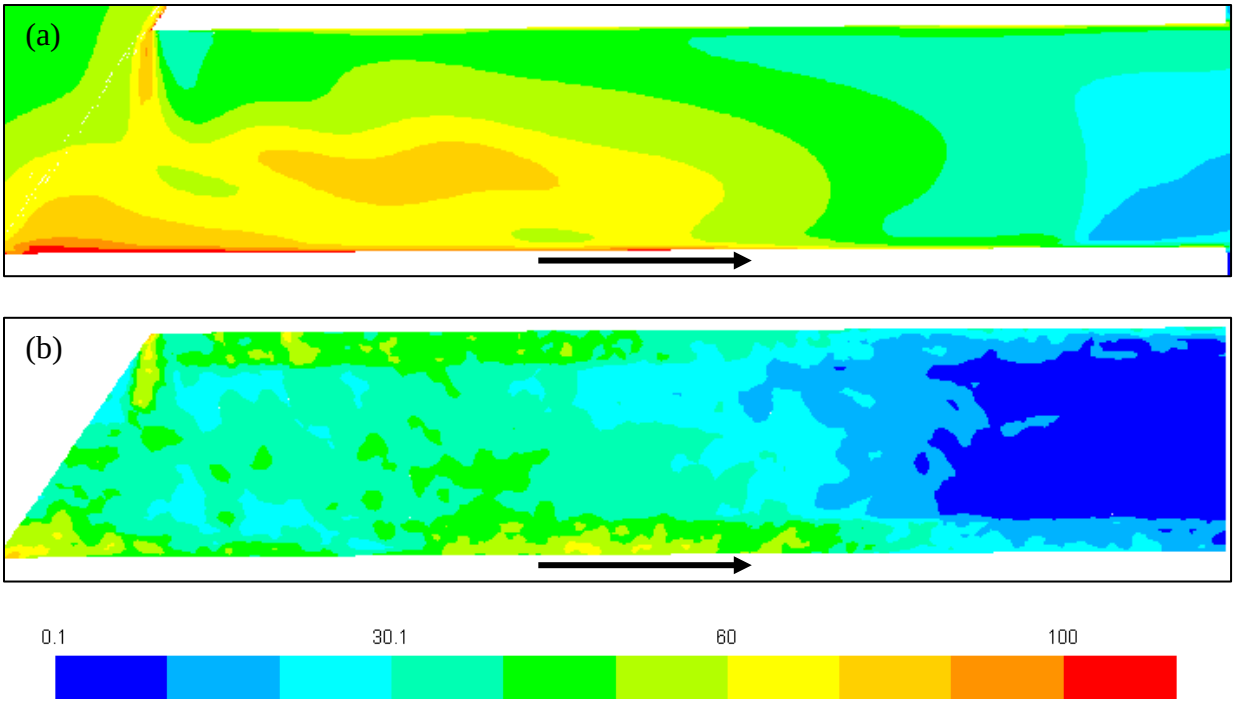

Figure 10.11 – Secondary outer slot 15 turbulent energy dissipation rate in the x = 0 mm plane from (a) RANS and (b) LES. Color legend is logarithmic and scaled by N^3D^2 = 2018.4 m^2/s^3. ΔP = 0 psi, hex 20M.

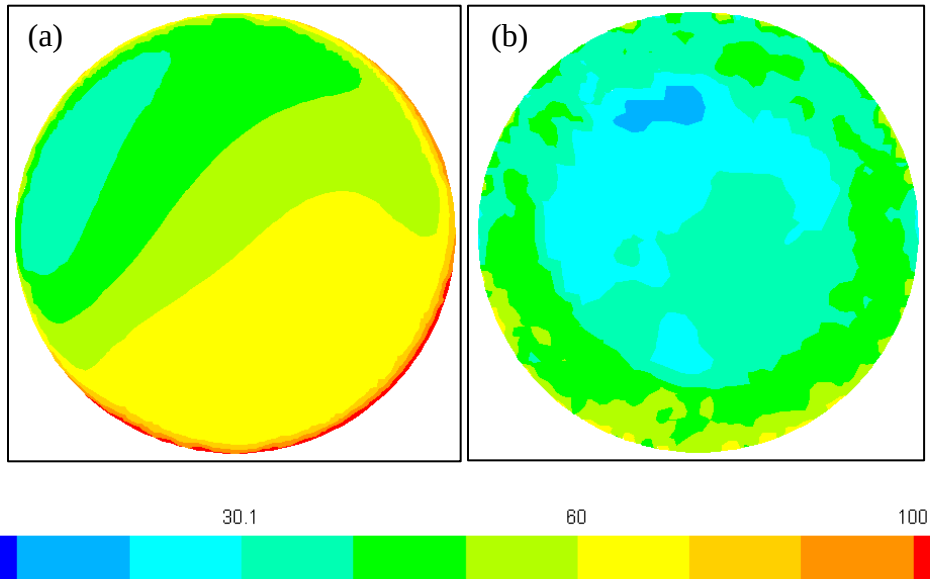

Figure 10.12 – Secondary outer slot 15 turbulent energy dissipation rate in the z = 100 mm plane looking upstream from (a) RANS and (b) LES. Color legend is logarithmic and scaled by N^3D^2 = 2018.4 m^2/s^3. ΔP = 0 psi, hex 20M.

10 Appendix B – Flow Field Animations

Appendix B contains a list of animations which are provided in a CD. The captions to these animations are included here in this appendix. These animations provide information about how the flow field changes in time.

Animation 1 – Mean velocity field colored by velocity magnitude in the primary stage, x = 0 mm. Showing bottom half of the center plane. Color legend scaled by (ND) = 5.8 m/s. Skipped every three arrows. ΔP = 0 psi, hex 20M RANS.

Animation 2 – Mean velocity field colored by velocity magnitude in the secondary stage, x = 0 mm. Showing bottom half of the center plane. Color legend scaled by (ND) = 5.8 m/s. Skipped every three arrows. ΔP = 0 psi, hex 20M RANS.

Animation 3 – Turbulent kinetic energy contour in the primary stage, x = 0 mm. Showing bottom half of the center plane. Color legend scaled by $(ND)^2$ = 33.64 m^2/s^2. ΔP = 0 psi, hex 20M RANS.

Animation 4 – Turbulent kinetic energy contour in the secondary stage, x = 0 mm. Showing bottom half of the center plane. Color legend scaled by $(ND)^2$ = 33.64 m^2/s^2. ΔP = 0 psi, hex 20M RANS.

Animation 5 – Turbulent energy dissipation rate contour in the primary stage, x = 0 mm. Showing bottom half of the center plane. Color legend scaled by N^3D^2 = 2018.4 m^2/s^3. ΔP = 0 psi, hex 20M RANS.

Animation 6 – Turbulent energy dissipation rate contour in the secondary stage, x = 0 mm. Showing bottom half of the center plane. Color legend scaled by N^3D^2 = 2018.4 m^2/s^3. ΔP = 0 psi, hex 20M RANS.

Animation 7 – Filtered velocity field colored by velocity magnitude in the center plane, x = 0 mm, for the outer edge of primary slot 6. Color legend scaled by (ND) = 5.8 m/s. ΔP = 0 psi, hex 20M LES.

Animation 8 – Filtered velocity field colored by velocity magnitude in the center plane, x = 0 mm, for the inner edge of primary slot 6. Color legend scaled by (ND) = 5.8 m/s. ΔP = 0 psi, hex 20M LES.

Animation 9 – Filtered velocity field colored by velocity magnitude in the center plane, x = 0 mm, for the entrance of secondary slot 15. Color legend scaled by (ND) = 5.8 m/s. ΔP = 0 psi, hex 20M LES.

Animation 10 – Mean velocity field colored by velocity magnitude in the primary stage, x = 0 mm. Showing bottom half of the center plane. Color legend scaled by (ND) = 5.8 m/s. Skipped every three arrows. ΔP = 7 psi, hex 20M RANS.

Animation 11 – Mean velocity field colored by velocity magnitude in the secondary stage, x = 0 mm. Showing bottom half of the center plane. Color legend scaled by (ND) = 5.8 m/s. Skipped every three arrows. ΔP = 7 psi, hex 20M RANS.

Animation 12 – Turbulent kinetic energy contour in the primary stage, x = 0 mm. Showing bottom half of the center plane. Color legend scaled by $(ND)^2 = 33.64\ m^2/s^2$. ΔP = 7 psi, hex 20M RANS.

Animation 13 – Turbulent kinetic energy contour in the secondary stage, x = 0 mm. Showing bottom half of the center plane. Color legend scaled by $(ND)^2 = 33.64\ m^2/s^2$. ΔP = 7 psi, hex 20M RANS.

Animation 14 – Turbulent energy dissipation rate contour in the primary stage, x = 0 mm. Showing bottom half of the center plane. Color legend scaled by $N^3D^2 = 2018.4\ m^2/s^3$. ΔP = 7 psi, hex 20M RANS.

Animation 15 – Turbulent energy dissipation rate contour in the secondary stage, x = 0 mm. Showing bottom half of the center plane. Color legend scaled by $N^3D^2 = 2018.4\ m^2/s^3$. ΔP = 7 psi, hex 20M RANS.

Animation 16 – Filtered velocity field colored by velocity magnitude in the center plane, x = 0 mm, for the outer edge of primary slot 6. Color legend scaled by (ND) = 5.8 m/s. ΔP = 7 psi, hex 20M LES.

Animation 17 – Filtered velocity field colored by velocity magnitude in the center plane, x = 0 mm, for the inner edge of primary slot 6. Color legend scaled by (ND) = 5.8 m/s. ΔP = 7 psi, hex 20M LES.

Animation 18 – Filtered velocity field colored by velocity magnitude in the center plane, x = 0 mm, for the entrance of secondary slot 15. Color legend scaled by (ND) = 5.8 m/s. ΔP = 7 psi, hex 20M LES.

11 List of Publications

Below is a list of publications pertaining to the work shown in this thesis. These publications will be will be submitted after the defense. Tentative titles and dates are shown.

1. Minnick, B.A., Kim, J.W., Ko, D.I., Calabrese, R.V. (2017). *Flow and Power Characteristics of an Axial Discharge Rotor-Stator Mixer*. Draft manuscript to be submitted, University of Maryland, Department of Chemical and Biomolecular Engineering, College Park, MD 20742-2111 USA.
2. Minnick, B.A., Calabrese, R.V. (2017). *Computational Fluid Dynamics Simulations of an Axial Discharge Rotor-Stator Mixer*. Manuscript in progress, University of Maryland, Department of Chemical and Biomolecular Engineering, College Park, MD 20742-2111 USA.

12 List of Conference Presentations

Conference presentations pertaining to the work shown in this thesis are listed below. These presentations are divided into two sections, 1. Presentations that have been delivered and 2. Presentations that have been scheduled. The submitted abstract has been accepted for the presentations that have been scheduled.

Presentations that have been delivered:

1. Ko, D.I., Kim, J.W., Minnick, B.A., Prada, R.J., Calabrese, R.V. (2015, November). *Computational Fluid Dynamics Simulation of a Pipeline Rotor-Stator Mixer*. Presented at the American Institute of Chemical Engineers (AIChE) Annual Meeting. Salt Lake City, UT, USA.

Presentations that have been scheduled:

1. Minnick, B.A., Calabrese, R.V. (2017, November). *Computational Fluid Dynamics Simulations of a Pipeline Rotor-Stator Mixer*. Presented at the American Institute of Chemical Engineers (AIChE) Annual Meeting. Minneapolis, MN, USA.

13 References

1. Atiemo-Obeng, V.A. & Calabrese, R.V. (2004). Rotor-stator mixing devices, in *Handbook of Industrial Mixing: Science and Practice*, Paul, E.L., Atiemo-Obeng, V.A., & Kresta, S.M. (eds). (John Wiley & Sons, Hoboken, NJ, USA).
2. ANSYS, (2015). *ANSYS Fluent's User Guide v16.* (Fluent Inc).
3. Kammler, D.W., (2000). *A First Course in Fourier Analysis*. (Prentice Hall, Upper Saddle River, NJ, USA).
4. Pope, S.B. (2000). *Turbulent Flows*. (Cambridge University Press, Cambridge, UK).
5. Bernard, P.S. & Wallace, J.M. (2002). *Turbulent Flow: Analysis, Measurement, and Prediction*. (John Wiley & Sons, Hoboken, NJ, USA).
6. Nicoud, F. & Ducros, F. (1999) Sugbrid-Scale Stress Modelling Based on the Square of the Velocity Gradient Tensor. *Flow, Turbulence and Combustion*, 62(3), 183-200.
7. Piomelli, U. (2008). Wall-layer models for large-eddy simulations. *Progress in Aerospace Sciences*, 44(6), 437-446.
8. Sheng, J., Meng, H., & Fox, R. O. (2000). A large eddy PIV method for turbulence dissipation rate estimation. *Chemical Engineering Science*, 55(20), 4423-4434.
9. Gimbun, J., Rielly, C. D., Nagy Z. K., & Derksen, J. J. (2012). Detached eddy simulation on the turbulent flow in a stirred tank. *AIChE Journal*, 58(10), 3224-3241.
10. Sheng, J. Meng, H. & Fox, R. O. (1998). Validation of CFD simulations of a stirred tank using particle image velocimetry data. *The Canadian Journal of Chemical Engineering*, 76(3), 611-625.

11. Coroneo, M., Montante, G. Paglianti, A. & Magelli, F. (2011). CFD prediction of fluid flow and mixing in stirred tanks: Numerical issues about the RANS simulations. *Computers and Chemical Engineering*, 35(10), 1959-1968.
12. Hartmann, H., Derksen, J. J., Montavon, C., Pearson, J., Hamill, I. S., & van der Akker, H. E. A. (2004). Assessment of large eddy and RANS stirred tank simulations by means of LDA. *Chemical Engineering Science*, 59(12), 2419-2432.
13. Myers, K. J., Reeder, M. F., & Ryan, D. (2001). Power Draw of a High-Shear Homogenizer. *The Canadian Journal of Chemical Engineering*, 79(1), 94-99.
14. Utomo, A. T., Baker, M., & Pacek, A. W. (2008). Flow pattern, periodicity and energy dissipation in a batch rotor-stator mixer. *Chemical Engineering Research and Design*, 86(12), 1397-1409.
15. Utomo, A. T., Baker, M., & Pacek, A. W. (2009). The effect of stator geometry on the flow pattern and energy dissipation rate in a rotor-stator mixer. *Chemical Engineering Research and Design*, 87(4), 533-542.
16. Özcan-Taşkin, G., Kubicki, D. & Padron, G. (2011). Power and flow characteristics of three rotor-stator heads. *Canadian Journal of Chemical Engineering*, 89(5), 1005-1017
17. Xu, S., Cheng, Q. Li, W., & Zhang, J. (2014). LDA measurements and CFD simulations of an in-line high shear mixer with ultrafine teeth. *AICHE Journal*, 60(3), 1143-1155.
18. Lumley, J., (1978). Computational modelling of turbulent flows. *Advances in Applied Mechanics*, 26, 123-176.